UNIVERSIDADE DE LISBOA
FACULDADE DE CIÊNCIAS

Experimental and numerical study on MFI-ZSM-5 zeolite membranes for tritium separation and recovery in nuclear fusion reactors

" Documento Definitivo"

Doutoramento em Engenharia Física

Rodrigo Nuno Mendes Antunes

Tese orientada por:
Prof. Dr. Maria Margarida Cruz
Dr. Laëtitia Frances

Documento especialmente elaborado para a obtenção do grau de doutor

2019

UNIVERSIDADE DE LISBOA

FACULDADE DE CIÊNCIAS

Ciências ULisboa

Experimental and numerical study on MFI-ZSM-5 zeolite membranes for tritium separation and recovery in nuclear fusion reactors

Doutoramento em Engenharia Física

Rodrigo Nuno Mendes Antunes

Tese orientada por:

Prof. Dr. Maria Margarida Cruz

Dr. Laëtitia Frances

Júri:

Presidente:

- Doutor José Manuel de Nunes Vicente Rebordão, Investigador Coordenador e Presidente do Departamento de Física da Faculdade de Ciências da Universidade de Lisboa

Vogais:

- Doutora Laëtitia Frances, Senior Research Engineer, Valduc Centre for Nuclear Studies – CEA/Valduc, França (Orientadora)
- Doutor Magnus Schlösser, Investigador, Karlsruhe Institute of Technology, Alemanha
- Mestre Silvano Tosti, na qualidade de individualidade de reconhecida competência na área científica
- Doutor José António de Carvalho Paixão, Professor Catedrático, Faculdade de Ciências e Tecnologia da Universidade de Coimbra
- Doutor Luís Miguel Palma Madeira, Professor Associado, Faculdade de Engenharia da Universidade do Porto
- Doutor Bruno Miguel Soares Gonçalves, Investigador Principal, Instituto Superior Técnico da Universidade de Lisboa

Documento especialmente elaborado para a obtenção do grau de doutor

In collaboration with the Karlsruhe Institute of Technology

2019

Acknowledgements

My first words are directed to Prof. Dr. Maria Margarida Cruz, who, since the beginning, believed in my capabilities and skills and so kindly accepted to supervise me during the 4-years long PhD project. During this period, you were always very supportive with all administrative aspects and also with many important inputs at both scientific and personal levels, which were very important to me all along. Um muito obrigado.

I want to express my immense gratitude to Dr. Laëtitia Frances, who accepted to supervise my work at KIT one year after the start, requiring extra efforts to swiftly understand and support my work. I am also very thankful for the support you gave me during all the good and difficult moments I have gone through along my PhD. You helped me a lot to keep me focused on my work, while still sending me important messages on what is important and what is not, whether personally or professionally. I thank you a lot for always being there to defend my work but also to criticise it so transparently, which I am convinced it helped me growing as a person and as a scientist. Merci beaucoup.

The whole PhD journey wouldn't have started without Dr. David Demange, who challenged me for a PhD, right after the end of the MSc. I am deeply thankful for your trust and support in helping me defending my project, which was very important for me at such an early stage. Moreover, you also opened up my horizons by challenging me further with an extended work project, the EUROfusion Engineering Grant. I sincerely want to thank you for all the confidence you transmitted to me, which was essential for me to be able to manage my work and believe in my capabilities. Merci beaucoup.

The realisation of my work, especially the experiments with tritium, was only possible due to the very supportive TLK colleagues who demonstrated an exceptionally high level of commitment. To start with, I am very thankful to Eng. Alejandro Muñoz for the CAD drawings of the ZEMTEX setup. In addition, I would like to thank Dr. András Bükki-Deme, who, besides the friendship and help with different tasks, gave a very important contribution to the assembling of the ZEMTEX facility inside the the CAPER glovebox. During this process, Mr. Long-Than Le and Mrs. Eleonore Fanghänel were always tirelessly very supportive, not only in the assembly and commissioning phases, but also during the experimental campaign. I woud also like to thank the commitment and involvement of Mrs. Monika Sirch in providing the calorimetry measurements, and I am also very greateful to Dr. Florian Priester for having provided me with mass spectrometry measurements

in a timely manner. I want to express my imense gratitude to Eng. David Hillesheimer, who very skillfully helped me developing a tritium compatible membrane module, without which the experiments with tritium wouldn't have been possible. I also thank you very much for your commitment during the experimental phase with the processing and preparation of the tritiated mixtures. In this regard, I am indebted to Eng. Stefan Welte, whose excellent engineering skills, prompt cooperation and deep involvement allowed me to carry out all experiments with tritium in an extraordinarily short time. I am also very thankful to Dr. Uwe Besserer, who, in a very crucial moment of my PhD, mobilised the key people to help me realising all required experiments. I also want to express my deep gratitude to Eng. Ester Diaz Alvarez for the friendship, support and availability to discuss my work, which were crucial for me to successfully arrive at the end of my PhD. Last but not least, I want to warmly acknowledge all TLK colleagues, who, in one way or another, gave me the conditions to carry out my research in a friendly and helpful environment. Deshalb, ein großes Danke schön an alle.

I had also the honour to supervise three MSc and BSc students, who gave very important contributions to my PhD, both with simulations and experiments. Therefore, I would like to express my gratitude to you all: Eng. Patrick-Simon Klug, Eng. Máximo Solis and Mr. Alexander Böhmländer. I want to especially acknowledge Mr. Böhmländer who so kindly continued helping me with the experiments at the HyDe loop even after the end of his BSc. In this regard, I want to express also my gratitude to Mr. Bennet Krasch, who, beyond our friendship, so gently provided me with LARA measurements of inactive gas samples.

All the work I developed during my PhD could only be possible by the financial support from both the Karlsruhe Institute of Technology and the EUROfusion consortium. I am very thankful for the extraordinary opportunities I was given, namely the participation in international conferences, where I had the opportunity to discuss my work with experts in the field, helping me establishing my own network of contacts. On top of that, I had the great opportunity to work abroad for some months in the scope of the EUROfusion Engineering Grant. During these missions, I had the pleasure and honour to work in CIEMAT and ENEA, where I was warmly received by the groups of Dr. David Rapisarda and Dr. Alessia Santucci. Beyond that, I am also very lucky to have had the opportunity to earn so many friendships from different cultures and countries during the international events I took part of.

I would also like to the address the Faculty of Sciences of the University of Lisbon, which was very supportive since the beginning of my PhD with all administrative and technical aspects. I would like to especially express my gratitude to the coordinator of the Engineering Physics PhD programme, Prof. Dr. José Rebordão, who was very forthcoming in guaranteeing I had the conditions to do my PhD in Ciências. I also want to acknowledge Mr. Telmo Nunes, who so gently provided me with the SEM pictures of

the tested membranes.

My last words go to my beloved family and longtime friends. Queria agradecer-vos por todo o apoio e confiança nas minhas capacidades. Aos meus amigos, um muito obrigado por todos os momentos divertidos que me proporcionaram durante todo este tempo, sem dúvida foram fundamentais para conseguir levar o meu doutoramento até ao fim. À minha família, primeiro um pedido de desculpas pelas muitas viagens de médico a Portugal e por não ter passado mais tempo convosco. Mas, acima de tudo, eu queria agradecer-vos por todo o inquebrável apoio e pela paciência em ouvir as minhas indecisões, que reconheço terem sido muitas ao longo destes quatro anos. Todas as vezes que voltei a Lisboa foram extraordinariamente importantes para mim, dado que é onde me sinto verdadeiramente em casa.

A todos, um muito obrigado por tudo.

Abstract and keywords

In a fusion reactor, tritium must be continuously produced inside a breeding blanket to ensure its self-sufficiency. For a solid blanket, the tritium is continuously extracted using large flows of helium ($0.4\,\mathrm{kg\,s^{-1}}$) doped either with 0.1 wt% of H_2 ("dry purge") or 0.1 wt% of H_2O ("wet purge"). Downstream of the blanket, the purge gas contains ppm concentrations of tritiated species, which are separated in the Tritium Extraction and Removal System (TERS). In this work, the TERS relying on zeolite membranes and Pd-based membrane reactors is considered. The aim of this thesis is to evaluate experimentally and numerically the feasibility of MFI-ZSM-5 zeolite membranes to pre-concentrate Q_2 or Q_2O in He, where Q = H, D, T. The permeation experiments with inactive and active Q_2 mixtures demonstrated that the permeances are proportional to the inverse of the square root of the molar mass. Hence, the Q_2/He selectivity (ratio of permeances) is highest for H_2 (≈ 1.8) and lowest for T_2 (≈ 1.1). These results are consistent with the separation factors obtained for H_2/He (≈ 1.4) and Q_2/He (≈ 1.0, with 20 at% T in Q). Thus, these membranes are not suitable for a dry purge, since the tritiated isotopologues cannot be efficiently separated from He. In contrast, a larger separation factor of ≈ 2.2 is obtained for Q_2O/He at 303 K, which is explained by the stronger adsorption of Q_2O onto the zeolite, hindering helium permeation. With the proposed values for the enrichment factor $\mathcal{E} \geq 50$ and recovery fraction $\mathcal{R} \geq 90\,\%$, a 7-stages membrane cascade is obtained to pre-concentrate Q_2O in He. The resulting cascade has a tritium inventory of 52 mg, which is much lower than the 12.5 g calculated for the reference technology relying on hydrophilic adsorption columns.

zeolite membrane, MFI-ZSM-5, tritium separation, nuclear fusion

Resumo e palavras-chave

Num reator de fusão, o trítio tem de ser continuamente produzido dentro de uma camada fértil para garantir a sua auto-suficiência. Para uma camada sólida, o trítio é continuamente coletado utilizando caudais de hélio ($0.4\,\mathrm{kg\,s^{-1}}$) dopados com 0.1 wt% de H_2 ("purga seca") ou 0.1 wt% de H_2O ("purga húmida"). A jusante da camada, o gás de purga contém espécies tritiadas em concentrações da ordem das ppm, que são separadas no Sistema de Extração e Remoção de Trítio (SERT). Este trabalho é focado no SERT baseado em membranas de zeólito e reatores de membrana de paládio. O objetivo desta tese é avaliar experimental e numericamente a viabilidade das membranas de zeólito MFI-ZSM-5 para pré-concentrar Q_2 ou Q_2O em He, onde Q = H, D, T. As experiências de permeação com misturas inativas e ativas de Q_2 mostraram que as permeâncias são proporcionais ao inverso da raíz quadrada da massa molar, obtendo-se para a seletividade Q_2/He (razão de permeâncias) o maior valor para H_2 e o menor para T_2. Estes resultados são consistentes com os fatores de separação obtidos para H_2/He (≈ 1.4) e Q_2/He (≈ 1.0, com 20 at% T). Assim, estas membranas não são adequadas para a purga seca, pois a separação dos isotopólogos tritiados não é eficiente. Em contraste, obtém-se um fator de separação de 2.2 para Q_2O/He a 303 K, que é explicado pela maior adsorção de Q_2O no zeólito, dificultando a permeação do hélio. Com os valores pretendidos para o fator de enriquecimento, $\mathcal{E} \geq 50$, e fração de recuperação, $\mathcal{R} \geq 90\,\%$, é proposta uma cascata de membranas com sete estágios. O inventário de trítio nesta cascata é 52 mg, muito menor que os 12.5 g previstos para a tecnologia baseada em colunas hidrofílicas de adsorção.

membrana de zeólito, MFI-ZSM-5, separação de trítio, fusão nuclear

Resumo alargado

O combustível proposto para a primeira geração de centrais de fusão nuclear é uma mistura equimolar de deutério (D) e trítio (T). Dada a sua escassez natural, o trítio tem de ser produzido dentro do reator de fusão para garantir a sua auto-suficiência. Os neutrões, produzidos nas reações de fusão, reagem com o lítio na camada fértil, para gerar trítio. Na metodologia europeia baseada em camada sólida, conhecida como Helium-Cooled Pebble Bed (HCPB), o lítio está presente sob a forma cerâmica Li_4SiO_4 e o trítio é coletado utilizando caudais elevados de hélio ($0.4\,kg\,s^{-1}$). Pequenas quantidades de H_2 (ou D_2) são adicionadas ao hélio ($0.1\,wt\%$) para melhorar a recuperação do trítio através de reações de troca de isótopos. Contudo, devido às quantidades não desprezáveis de trítio que permeiam através da tubagem para o refrigerante do reator, a purga com He + H_2O (ou D_2O) está também sob consideração pela sua vantagem na redução das permeação do trítio. Dependendo do dopante utilizado, o gás a jusante da camada fértil é composto por $Q_2O/Q_2/He$ (purga seca) ou Q_2O/He (purga húmida) com concentrações de espécies tritiadas na ordem das ppm (Q = H, D, T). Este gás é encaminhado para o Sistema de Extração e Remoção de Trítio (SERT), no qual as espécies Q_2 e Q_2O são separadas do hélio.

Diferentes tecnologias de separação têm sido consideradas para o SERT. Esta tese é focada na tecnologia baseada em membranas, que inclui duas etapas divididas por dois sub-sistemas: membranas de zeólito seguidas de reatores de membrana de paládio. Os reatores de membrana são responsáveis pela detritiação do gás que vem da camada sólia. No entanto, de forma a assegurar uma detritiação eficiente e minimização das dimensões e custos associados, é necessária uma redução do caudal e pré-concentração de Q_2 e Q_2O no hélio. Assim, as membranas de zeólito são usadas a montante dos reatores de paládio para reduzir o caudal de hélio e aumentar a concentração de Q_2 e Q_2O. O trabalho desta tese é focado no estudo de viabilidade da utilização de membranas de zeólito MFI-ZSM-5 no primeiro sub-sistema do SERT para as duas metodologias de purga. O trabalho desenvolvido inclui uma componente experimental e uma numérica: os resultados experimentais obtidos nas experiências de permeação e separação foram usados para determinar numericamente as dimensões de um sistema de membranas com eficiência adequada para o SERT.

Duas campanhas experimentais foram realizadas com o objetivo de (i) investigar os mecanismos de transporte de massa dos seis isotópologos do hidrogénio determinando as suas permeâncias a diferentes temperaturas, e (ii) determinar o fator de separação para misturas iniciais de Q_2/He e Q_2O/He com concentrações de hélio até 99 mol%. As experiências foram executadas com dois equipamentos experimentais: o "HyDe loop", para determinar as permeâncias de H_2, D_2 e HD, e o "ZEMTEX", desenhado e construído com o objetivo de determinar as permeâncias dos isotopólogos radioativos e os fatores de separação para as misturas de Q_2/He e Q_2O/He. Os resultados experimentais obtidos resumem-se nos pontos seguintes:

- foram utilizadas duas membranas para determinar as permeâncias de H_2, D_2 e misturas catalizadas de H_2-HD-D_2 a diferentes temperaturas. As permeâncias obtidas são proporcionais a $M_{\text{eff}}^{-0.5}$, onde M_{eff} é a massa efetiva calculada pelas média ponderada das massas dos isótopos de hidrogénio que permeiam o membrana. Assim, a maior permeância é obtida para o H_2 e a menor para o T_2. Estes resultados foram corroborados pelas experiências de permeação realizadas com espécies tritiadas até 55 at% de T em Q com uma amostra de MFI-ZSM-5 adicional. Devido à adsorção semelhante das espécies Q_2, espera-se que as permeâncias sejam idênticas para uma estrutura sem defeitos cristalinos. Assim sendo, as diferenças nas permeâncias são explicadas pela existência de defeitos na estrutura zeolítica. No entanto, uma vez que as seletividades para Q_2/He estão compreendidas nos intervalos $1.8 - 1.9$ para H_2/He e $1.0 - 1.1$ para T_2/He (ou seja, maior que as seletividades de Knudsen), a concentração de defeitos é considerada baixa para as três membranas. Os resultados são explicados pela maior adsorção das espécies Q_2 na estrutura do zeólito, sendo as maiores permeâncias atribuídas à difusão superficial, mecanismo de transporte considerado dominante no intervalo de temperaturas utilizado;

- para a mistura inicial H_2/He, o fator de separação determinado é ≈ 1.4 e, portanto, menor que a seletividade. Além disso, o fator de separação global para Q_2/He, com 20 at% T em D ($M_{\text{eff}} \approx 4.4\,\text{g mol}^{-1}$), é $\approx$ 1 traduzindo-se numa ausência de separação, independentemente da temperatura da membrana. A diminuição dos fatores de separação em relação às estimativas dadas pelas seletividades é explicada pelos motivos seguintes: (i) as espécies Q_2 e He têm diâmetros cinéticos semelhantes e menores do que os diâmetros dos poros da estrutura MFI-ZSM-5, (ii) a separação é determinada por pequenas diferenças no comportamento de difusão (devido às pequenas diferenças de massa) e (iii) a depleção das espécies com maior permeância ao longo da membrane do lado da entrada reduz a diferença de pressão parcial que induz permeação. Para a mistura de Q_2O/He foram obtidos maiores fatores de separação, devido à adsorção preferencial de Q_2O no zeólito o que dificulta a permeação do hélio. O valor médio para o fator de separação é ≈ 2.2 a 303 K com

frações de recuperação elevadas, acima de 70 %. Um aumento da concentração de T em Q_2O (por um fator de 23 %) foi medido no lado do permeado, o que sugere a existência de um efeito isotópico na separação de água tritiada.

Os resultados experimentais demonstram que as membranes MFI-ZSM-5 não são adequadas para o SERT quando a camada fértil é purgada com uma mistura seca, dado que não é possível a separação de hélio dos isotopólogos com massas idênticas ou maiores. No entanto, foram obtidas eficiências razoáveis para a pré-concentração de Q_2O em He. Por conseguinte, usando os resultados experimentais como parâmetros de entrada, o número de estágios de separação necessários para satisfazer os requerimentos do SERT do DEMO foi determinado usando um modelo numérico desenvolvido no contexto deste trabalho. Considerando que a eficiência de separação do SERT tem de ser superior a 80 % e tendo em conta os resultados experimentais disponíveis na literatura obtidos com reatores de membrana de paládio para a detritiação de água, a cascada de membranas adequada tem de assegurar um fator de enriquecimento $\mathcal{E} \geq 50$ e uma fração de recuperação $\mathcal{R} \geq 90\,\%$.

Uma cascata de membranas com sete estágios em série é a configuração encontrada para satisfazer a eficiência necessária. O estágio maior (que recebe a mistura vinda da camada fértil) tem um comprimento de $\approx 2.7\,\mathrm{m}$ e um diâmetro de $\approx 0.3\,\mathrm{m}$ com milhares de canais de permeação, que são necessários para aumentar a razão entre a área de permeação e o volume ocupado. A área de permeação total é $\approx 513\,\mathrm{m}^2$ e a potência necessária para os compressores utilizados na cascada é $\approx 3.7\,\mathrm{MW}$. O inventório de trítio no sistema é estimado ser de 52 mg, representando cerca de 0.2 % da massa total de trítio que chega à cascada durante um dia de operação. Para a metodologia de referência do SERT, foram consideradas três colunas hidrofílicas de adsorção, com $\approx 1.9\,\mathrm{m}$ de comprimento e $\approx 0.9\,\mathrm{m}$ de largura, operadas em modos alternados de adsorção e regeneração. A potência estimada para o aquecimento e arrefecimento das colunas é cerca de $0.7\,\mathrm{MW}$, mas o inventório de trítio é muito elevado (50 % da quantidade total vinda da camada fértil).

Com os resultados obtidos, uma avaliação comparativa entre as duas tecnologias foi feita com o intuito de concluir qual delas satisfaz os critérios relevantes para o SERT. Apesar da importante vantagem da cascata de membranas em minimizar o inventório de trítio, a maturidade tecnológica das colunas de adsorção com preços relativamente baixos supera o estado atual da arte das membranas MFI-ZSM-5 para esta aplicação. No entanto, a seleção de uma destas tecnologias tem de ser re-avaliada de acordo com os desenvolvimentos futuros. Por exemplo, a importância do inventório de trítio poderá tornar-se mais importante devido a considerações relacionadas com o ciclo de combustível do reator ou poderá existir uma evolução significativa na maturidade das tecnologias disponíveis, dado que são esperados progressos no desenvolvimento de membranas de zeólito com capacidade de processamento elevada e consequente decréscimo dos custos de produção.

Contents

List of Figures

List of Tables

List of Acronyms

AV	Automatic Valve
BB	Breeding Blanket
BD	Gas vessel
CPS	Coolant Purification System
DEMO	DEMOnstration reactor
DF	Decontamination Factor
EH	Electrical Heater
EPDM	Ethylene Propylene Diene Methylene
EU	European or European Union
FAU	FAUjasite
FPP	Fusion Power Plant
GB	Glovebox
GC	Gas Chromatograph
GT	Gas Translational (diffusion)
HCCB	Helium-Cooled Ceramic Breeder
HCPB	Helium-Cooled Pebble Bed
HV	Hand Valve
HyDe	Hydrogen Deuterium
IKTS	Institut für Keramische Technologien und Systeme
ISO	International Organization of Standardization
ISS	Isotope Separation System
IUPAC	International Union of Pure and Applied Chemistry
IZA	International Zeolite Association
KP	Circulation Pump
LARA	LAser RAman spectroscopy
LTA	Linde Type A
MFC (or RF)	Mass Flow Controller

MFI	Mordenite Framework Inverted
MM	Membrane Module
MR	Membrane Reactor
MSB (or MS)	Molecular Sieve Bed
PCS	Pre-Concentration Stage
PERMCAT	PERMeator and CATalyst
ppm	part per million
P&ID	Pipe and Instrumentation Diagram
RGA	Residual Gas Analyser
RM	Moisture Sensor
RP	Pressure Sensor
RT	Temperature Sensor
RV	Pressure controller
RX	Ionisation Chamber
R&D	Research and Development
sccm	standard cubic centimeter per minute
SD	Surface-Diffusion
SEM	Scanning Electron Microscope
SI	International System of Units
SOD	SODalite
STP	Standard Temperature and Pressure
TBM	Test Blanket Module
TERS	Tritium Extraction and Removal System
TLA	Technische Liefer- und Abnahmebedingungen
TLK	Tritium Laboratory Karlsruhe
TRL	Technology Readiness Level
TSA	Temperature Swing Adsorption
TTS	Tritium Transfer System
VP	Vacuum Pump
WCCB	Water-Cooled Ceramic Breeder
WCLL	Water-Cooled Lithium-Lead
ZEMTEX	ZEolite Membranes for Tritium EXperiments
ZSM-5	Zeolite Socony Mobil-5

List of Symbols

A	area (m^2)
$\mathcal{A}$	activity (Ci)
b	number of compressors (-)
c	molar concentration ($mol\,m^{-3}$)
c_p	specific heat at constant pressure ($J\,kg^{-1}\,K^{-1}$)
c_V	specific heat at constant volume ($J\,kg^{-1}\,K^{-1}$)
d	diameter (m)
D	diffusivity ($m^2\,s^{-1}$)
E_a	activation energy ($J\,mol^{-1}$)
$\mathcal{E}$	enrichment factor (-)
f	friction factor (-)
F_f	feed flow ($mol\,s^{-1}$ or $mL\,min^{-1}$)
F_p	permeate flow ($mol\,s^{-1}$ or $mL\,min^{-1}$)
F_r	retentate flow ($mol\,s^{-1}$ or $mL\,min^{-1}$)
H_{ads}	enthalpy of adsorption ($J\,mol^{-1}$)
J	flux ($mol\,m^{-2}\,s^{-1}$)
K_{eq}	reaction rate constant (-)
K^L	Langmuir adsorption constant (Pa^{-1})
K_n	Knudsen number (-)
L	length (m)
m	mass (kg)
M	molar mass ($kg\,mol^{-1}$)
$\mathcal{M}$	number of stages in stripping section (-)
n	particle density (m^{-3})
N_{ch}	number of channels (-)
$\mathcal{N}$	number of stages in enriching section (-)
p_f	feed pressure (Pa)

p_p	permeate pressure (Pa)
P	permeability ($\mathrm{mol\,m^{-1}\,s^{-1}\,Pa^{-1}}$)
q	adsorbed concentration ($\mathrm{kg\,mol^{-1}}$)
Q	H, D, T
R	correlation coefficient (-)
R	ideal gas constant ($\mathrm{J\,K^{-1}\,mol^{-1}}$)
$\mathcal{R}$	recovery fraction (%)
S_ads	entropy of adsorption ($\mathrm{J\,K^{-1}\,mol^{-1}}$)
S_h	head separation factor (-)
S_stg	stage separation factor (-)
S_t	tail separation factor (-)
t	time (s)
T	temperature (°C or K)
t_m	membrane thickness (m)
$\mathcal{T}$	total number of stages (-)
v	speed ($\mathrm{m\,s^{-1}}$)
V	volume ($\mathrm{m^3}$)
W	molar work ($\mathrm{J\,mol^{-1}}$)
x_f	feed concentration (-)
x_r	retentate concentration (-)
y_p	permeate concentration (-)
z	direction of permeation (m)
$\alpha_{i/j}$	separation factor (-)
$\alpha_{i/j}^\mathrm{Kn}$	Knudsen selectivity (-)
$\alpha_{i/j}^*$	selectivity (-)
β	coordination number (-)
γ	feed-to-pressure ratio (-)
Δ	variation (units depending on the quantity)
ϵ	porosity (-)
η	efficiency (-)
θ	occupancy (-)
λ	mean free path (m)
λ_d	diffusional length (m)
μ	chemical potential ($\mathrm{J\,mol^{-1}}$)

μ_d	dynamic viscosity (Pa s)
ν	cut (-)
ξ	fractional concentration/area of defects (-)
$\mathit{\Pi}$	permeance ($\mathrm{mol\,m^{-2}\,s^{-1}\,Pa^{-1}}$)
ρ	mass density ($\mathrm{kg\,m^{-3}}$)
σ	stage diameter-to-length ratio (-)
τ	tortuosity (-)
τ_E	energy confinement time (s)
ψ	fractional area of channels (-)

Chapter 1

Introduction

Nowadays, the more frequent devastating effects of climate change can be witnessed at different areas of the planet. A wide consensus in the scientific community exists in connecting these events to the increase of greenhouse gases emissions due to our global dependency on fossil fuels [1]. Therefore, it is urgent to diversify the sources for energy production, promoting a shift towards CO_2-free options. A well-known and reliable energy option to maintain the emissions close to zero is nuclear energy. In particular, nuclear fusion is considered to be very promising due to the resulting short-lived radioactive waste and no risk of meltdown.

Deuterium (D) and tritium (T) are proposed to be the fuels of the first generation of fusion power plants due to the higher probability of reaction at lower temperatures. However, due to its scarcity, tritium has to be bred inside the fusion reactor to ensure fuel self-sufficiency [2, 3]. The production of tritium occurs inside a dedicated breeding blanket (BB) as a result of the neutron bombardment of lithium [4]. In the European Helium-Cooled Pebble Bed (HCPB) solid blanket concept, lithium is present in the form of ceramics Li_4SiO_4 and tritium is recovered by large helium flows ($0.4\,kg\,s^{-1}$) [5, 6]. Small amounts of H_2 (or D_2) are added to the helium ($0.1\,wt\%$) to enhance tritium recovery as a result of isotopic exchange reactions (dry purge). However, the use of H_2O (or D_2O) as dopant (wet purge) is also under consideration to be used as dopant for its benefits in enhancing tritium recovery and mitigating tritium permeation [7, 8]. Downstream of the blanket, the gas mixture is expected to be $Q_2O/Q_2/He$ (dry purge) or Q_2O/He (wet purge) and the concentrations of the tritiated species (HT, HTO) are expected to be at the ppm range (with Q = H, D, T) [9]. This stream is routed into the Tritium Extraction and Removal System (TERS), where Q_2 and Q_2O are separated from helium.

Different separation technologies have been proposed for the TERS [10, 11]. This thesis is focused on the concept that relies on membrane technologies, which includes two steps divided by two sub-systems [12]: zeolite membranes followed by Pd-based membrane reactors. The tritium recovery is ensured by the membrane reactors, which require a reduction of the gas flow coming from the BB and a pre-concentration of Q_2 and Q_2O for an efficient detritiation and minimisation of the dimensions and costs. For this reason,

the zeolite membranes are required upfront to reduce as much as possible the He flows and concentrate the Q_2/Q_2O species.

The main objective of this thesis is to evaluate the feasibility of MFI-ZSM-5 zeolite membranes for the pre-concentration step of the TERS considering the two foreseen purging scenarios. Therefore, experimental and numerical work was carried out to answer the following main questions:

- **What are the isotopic effects on the permeances of Q_2 isotopologues and how do they affect the Q_2/He separation efficiency?**
- **What are the separation performances of the zeolite membranes for DEMO-relevant mixtures, i.e. Q_2/He and Q_2O/He?**
- **How feasible is the scaled-up membrane system in terms of dimensions, power consumption and tritium inventory and how does it compare with the reference technologies?**

These questions are addressed throughout the thesis, which is structured as follows: in chapter 2 the characteristics of the two main TERS concepts currently under consideration for the HCPB of the EU-DEMO are compared and the research strategy followed throughout this work is discussed. Chapter 3 introduces the main quantities to experimentally characterise the separation performance of membranes (permeance, selectivity, separation factor), with the focus on the transport and separation mechanisms of zeolite membranes. In chapter 4 the permeances of the inactive hydrogen isotopologues (H_2, HD, D_2) and Q_2/He selectivities obtained for two MFI-ZSM5 membranes are presented and discussed. The permeances of the tritiated Q_2 mixtures and separation factors for Q_2/He and Q_2O/He are reported in chapter 5. Chapter 6 presents a numerical code developed to determine the number of stages, surface area, power consumption and tritium inventory required for the pre-concentration step of the TERS. Chapter 7 compares the numerical results obtained for the two purge scenarios at DEMO scale, using the separation factors and permeances determined experimentally. In chapter 8, a pairwise study is presented to compare the feasibility of the TERS based on membrane technologies against the reference approach relying on hydrophilic adsorption columns. Finally, the conclusions of the work and perspectives are given in chapter 9.

Chapter 2

Tritium Extraction and Removal System for the solid blanket using membrane technologies

2.1 Characteristics of deuterium-tritium nuclear fusion

2.1.1 Nuclear fusion and energy production

Nuclear reactions are characterised by the interaction of nuclei with particles or other nuclei involving the modification of nuclear states, in general leading to the formation of at least one new nucleus [13]. Nuclear fission consists in the splitting of heavy nuclei producing lighter ones, and nuclear fusion takes place when two light nuclei fuse into a heavier one. Whereas nuclear fission requires one neutron to initiate a cascade of fission reactions of uranium nuclei at low-to-moderate temperatures ($T \sim 10^2\,\mathrm{K}$), nuclear fusion reactions occur only at very high temperatures ($T \sim 10^8\,\mathrm{K}$) for the initial nuclei to overcome the Coulomb repulsion barrier [14, 15]. At these temperatures, the fusion fuel is in plasma state, which is a quasi-neutral cloud of positive ions and electrons [16]. The plasma must be confined well enough at fusion temperatures to guarantee that the power generated by the fusion reactions exceeds the external heating power required to sustain the reactions. The break-even condition, achieved when the fusion power equals the external heating power, is defined by the so-called Lawson criterion, which, for deuterium-tritium fusion reactions, is given by $n\tau_\mathrm{E}T > 1.5\times10^{21}\,\mathrm{keV\,s\,m^{-3}}$, where n is the plasma density and τ_E is the energy confinement time [15]. As a result of this criterion, two different confinement methods exist: high density fusion or inertial confinement with $n \sim 10^{31} - 10^{32}\,\mathrm{m^{-3}}$ and $\tau_\mathrm{E} \sim 10^{-9}\,\mathrm{s}$ and low density fusion or magnetic confinement with $n \sim 10^{21}\,\mathrm{m^{-3}}$ with $\tau_\mathrm{E} \sim 1\,\mathrm{s}$ [17].

The magnetic confinement of the plasma has been proven to be challenging due to various scientific factors such as plasma turbulence [15]. Furthermore, the realisation of fusion as an energy source faces engineering challenges related to the neutron activation of materials or fuel self-sufficiency (in case of deuterium-tritium fusion). Nevertheless, nuclear fusion is a very promising energy source when compared to fossil fuel or nuclear fission due to the following advantages:

- there are no greenhouse emissions or atmospheric release of harmful substances for the human being;
- very small amounts of fuel ($1 - 10\,\mathrm{Pa}$ in a $2000\,\mathrm{m}^3$ vacuum vessel [18, 19]) are expected to be present at the core each time, and thus the release of radioactive substances in case of an accident is kept at minimum;
- studies have demonstrated that the radiotoxicity of the neutron-induced activation of materials inside a fusion power plant decreases by roughly four orders of magnitude within 100 years, whereas in a pressurised water reactor after 500 years the decrease in radiotoxicity remains below one order of magnitude [20];
- the very special conditions to reach fusion (e.g., high temperatures) imply that fusion reactions will stop immediately after a major accident event (no risk of meltdown) [21].

2.1.2 Relevant properties of deuterium and tritium for fusion

Different reactions have been considered for the production of fusion energy. In figure 2.1, the cross sections of different fusion reactions involving different reactants are presented as a function of the kinetic energy. The deuterium (^{2}H or D) and tritium (^{3}H or T) fusion reaction is the one that presents the highest cross-section values for lower temperatures (e.g., $15\,\mathrm{keV} \approx 1.7 \times 10^8\,\mathrm{K}$) and therefore retained for the mainstream fusion research. This reaction produces one neutron with a kinetic energy of 14.1 MeV and one ^{4}He nucleus with a kinetic energy of 3.5 MeV, as presented in equation (2.1).

$$^2\mathrm{H} + {}^3\mathrm{H} \rightarrow {}^4\mathrm{He}\,(3.5\,\mathrm{MeV}) + {}^1\mathrm{n}\,(14.1\,\mathrm{MeV}) \tag{2.1}$$

On the one side, deuterium, with one proton and one neutron, is a widely abundant hydrogen isotope, mainly present in the water resources with an isotopic ratio of one ^{2}H atom per 6700 atoms of ^{1}H [21]. On the other side, tritium, with one proton and two neutrons, decays with a half-life of $4500 \pm 8\,\mathrm{days}$[1], emitting one helium-3 nucleus, one electron, and one electron anti-neutrino [22]. All three isotopes share the following properties: high chemical reactivity, high risk of explosion and high permeation through materials, namely polymers and metals. Due to the differences in masses among the isotopes, isotopic exchange reactions occur when these species interact chemically with each other[2] [23, 26, 28]. Equations (2.2) and (2.3) present two examples of isotopic

[1] Corresponding to a decay rate of around $5.47\,\%\,\mathrm{yr}^{-1}$.

[2] Isotopic exchange reactions are equilibrium reactions whose kinetic constants can be determined from the partition functions of the molecules. The major contribution arises from the molecular vibrational states and the corresponding frequencies (quantum energy states) vary with the masses of the isotopes [23, 24]. These exchange reactions take place regardless of their chemical form, and the rate at which they occur depends on the chemical nature of the species involved (base or acid), temperature, presence of a catalyst and ionising radiation [25–27].

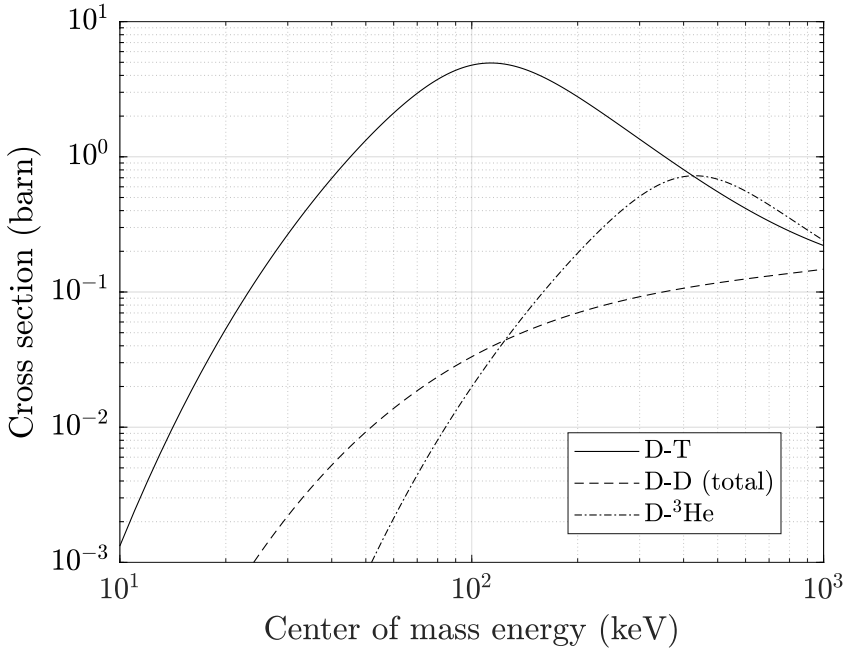

Figure 2.1: Cross sections of different fusion reactions as a function of the center of mass energy. 1 barn = $10^{-28}\,\mathrm{m}^2$, 10 keV $\approx 1.2 \times 10^8$ K. Plotted with data from [30].

exchange reactions among hydrogen isotopes [29].

$$\mathrm{H_2} + \mathrm{D_2} \rightleftharpoons 2\,\mathrm{HD} \tag{2.2}$$

$$\mathrm{HT} + \mathrm{H_2O} \rightleftharpoons \mathrm{H_2} + \mathrm{HTO} \tag{2.3}$$

Table 2.1 presents the molar masses M of all Q_2 and Q_2O molecules (with Q = H, D, T). H_2 and H_2O are the lightest molecules and T_2 and T_2O are the heaviest. As described in the following sections and chapters, the most common forms encountered in a fusion reactor and experimental setups are the molecules with two isotopes (e.g., HT or HTO) due to the isotopic exchange reactions described above.

Table 2.1: Molar masses of Q_2 and Q_2O species. H: 1.008 g mol^{-1}, D: 2.014 g mol^{-1}, T: 3.016 g mol^{-1}, O: 15.999 g mol^{-1}. Data from [31].

Q_2	M (g mol^{-1})	Q_2O	M (g mol^{-1})
H_2	2.016	H_2O	18.015
HD	3.022	HDO	19.021
HT	4.024	HTO	20.023
D_2	4.028	D_2O	20.027
DT	5.030	DTO	21.029
T_2	6.032	T_2O	22.031

2.2 Tritium self-sufficiency of a fusion power plant

2.2.1 The scarcity of tritium as fuel

The natural worldwide inventory of tritium is around 3.5 kg as a result of a balance between tritium production in the atmosphere[3] and its decay [2]. Tritium is also produced anthropogenically as a by-product in heavy-water moderated fission reactors (at a rate of $0.2\,\mathrm{kg\,yr^{-1}}$) [32]. However, for a fusion device with an output power of $1000\,\mathrm{MW\,yr^{-1}}$ tritium consumption rates of $55.6\,\mathrm{kg\,yr^{-1}}$ are required [3]. Therefore, tritium is a scarce fuel for fusion and a deuterium-tritium fusion reactor will require internal breeding systems to ensure tritium self-sufficiency. This aspect is one of the main challenges to tackle in the Roadmap for the Development of Fusion Energy in Europe[4], which aims at building a DEMOnstrator reactor (DEMO) [33].

2.2.2 Breeding blankets for tritium production

A future Fusion Power Plant (FPP) will have to continuously produce electricity to the grid and thus a high availability of the fusion fuel is necessary. The continuous production of tritium takes place in the so-called Breeding Blanket[5] (BB) as a result of the bombardment of lithium with D-T fusion neutrons, schematically represented in figure 2.2.

The neutron-lithium nuclear reactions are given in (2.4) and (2.5) [34]. Although the reaction with ^{7}Li produces one additonal neutron, an energy consumption of 2.50 MeV is required to start it, hence reducing the output power. Thus, tritium breeding shall be accomplished via reaction (2.4). Since the natural isotopic abundance of ^{6}Li/^{7}Li is 7.5/92.5 at%, a ^{6}Li-enriched breeder material up to $60-90$ at% ^{6}Li is required [35]. Furthermore, due to the unavoidable losses of neutrons and tritium atoms inside the reactor, additional neutrons are required to increase the tritium breeding ratio[6]. Beryllium and lead are two neutron multipliers currently under consideration, which produce neutrons according to equations (2.6) and (2.7).

$$^{1}\mathrm{n} + {}^{6}\mathrm{Li} \rightarrow {}^{4}\mathrm{He} + {}^{3}\mathrm{H} + 4.80\,\mathrm{MeV} \tag{2.4}$$

$$^{1}\mathrm{n} + {}^{7}\mathrm{Li} \rightarrow {}^{4}\mathrm{He} + {}^{3}\mathrm{H} + {}^{1}\mathrm{n} - 2.50\,\mathrm{MeV} \tag{2.5}$$

[3] Due to the nuclear reactions between the cosmic rays - mostly high-energy neutrons - and ^{14}N nuclei.

[4] The remaining seven challenges are focused on the study and development of: plasma regimes of operation, heat-exhaust systems, neutron resistant materials, implementation of intrinsic safety features, integrated DEMO design, competitive cost of electricity, stellarator.

[5] Besides the tritium breeding role, the heat generated in the BB is extracted by a dedicated cooling loop for power production. Moreover, the BB contributes to the nuclear shielding of the reactor components.

[6] Defined as the ratio between the number of tritium atoms produced per second in the blanket and the number of neutrons produced per second in the plasma. The tritium self-sufficiency criterion requires that the tritium breeding ratio exceeds 1 [36].

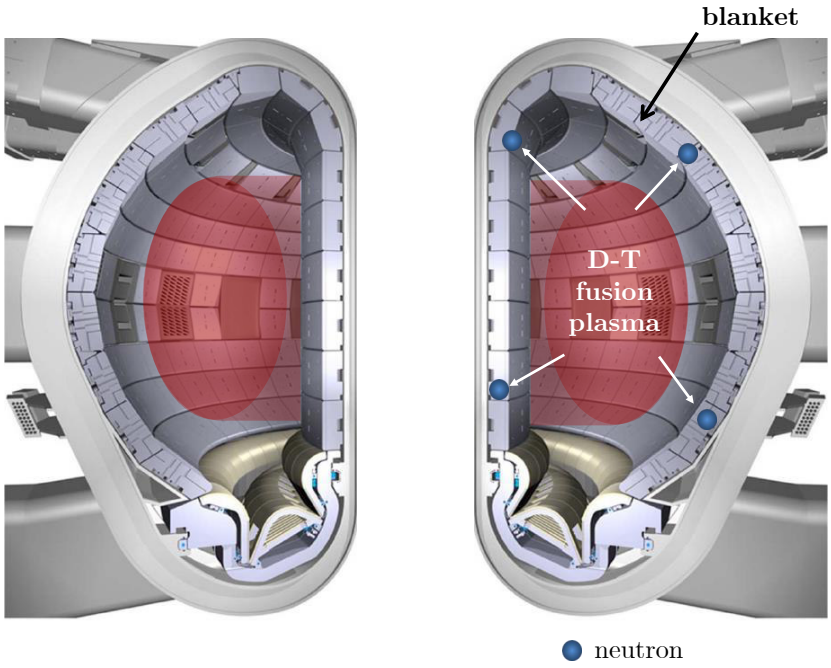

Figure 2.2: Physical representation of the breeding blanket for a magnetically confined plasma. The fusion neutrons will escape from the plasma and react with lithium present in the BB to produce tritium (equation (2.4)). Adapted from [36].

$$^{1}\mathrm{n} + {}^{9}\mathrm{Be} \rightarrow 2\,{}^{4}\mathrm{He} + 2\,{}^{1}\mathrm{n} - 2.50\,\mathrm{MeV} \tag{2.6}$$

$$^{1}\mathrm{n} + {}^{A}\mathrm{Pb} \rightarrow {}^{A\text{-}1}\mathrm{Pb} + 2\,{}^{1}\mathrm{n} - 7.00\,\mathrm{MeV} \tag{2.7}$$

The breeder material can be either in solid or liquid state. Several different solid BB concepts that consider the implementation of lithium-based and beryllium-based pebble beds placed in a sandwich-like configuration have been proposed by different countries [37]. Two examples are the Chinese Water-Cooled Ceramic Breeder (WCCB) and the Indian Helium-Cooled Ceramic Breeder (HCCB) [38, 39]. The European Helium-Cooled Pebble Bed (HCPB) concept, consisting of Li_4SiO_4 and Be ceramic pebble beds, is the reference design for ITER[7] and DEMO [5]. The present work is focused on the development of the tritium extraction system for the DEMO HCPB blanket, presented in section 2.3. The liquid blanket concepts rely on the eutectic mixture 84.3-15.7 at% Pb-Li, with a melting point around 235 °C, for both tritium production and neutron multiplier [37]. The Water-Cooled Lithium-Lead (WCLL) is the reference European design for both ITER and DEMO [41].

Small-scale Test Blanket Modules (TBMs) integrating different breeding blanket concepts will be tested at ITER, under construction in Cadarache, France. The main testing objectives of the TBMs are the validation of tritium breeding predictions and tritium

[7]ITER is a major worldwide effort to construct the largest fusion reactor ever built, which is planned to start operations at the end of 2025 [40]. This project involves seven parties: China, European Union, India, Japan, Korea, Russia and the United States of America.

Table 2.2: Comparison of tritium-related scenarios for ITER and DEMO machines. From the data available in [6, 43].

	ITER	EU-DEMO
Fusion power (MW)	500	1572
T consumption ($g\,d^{-1}$)	76	$\approx$ 240
T burn-up fraction (%)	0.3	$>$ 2
T production ($g\,d^{-1}$)	$<$ 0.4	$\approx$ 252

extraction efficiencies [42]. However, the ITER modules will have limited tritium production rates ($< 0.4\,g\,d^{-1}$) when compared to reactor relevant conditions. In DEMO, which aims at demonstrating the production of electricity with an availability close to a FPP, the expected tritium production rates are $\approx 252\,g\,d^{-1}$. Table 2.2 compares the expected scenarios for ITER and DEMO. The tritium consumption[8] and production rates are considerably higher for the DEMO machine illustrating the challenge of the tritium self-sufficiency. Associated with the need for tritium self-sufficiency is a rather complex fuel cycle.

2.2.3 Fuel cycle of a fusion device

According to table 2.2, a low D-T burn-up fraction is expected inside the fusion reactor core. Therefore, a continuous recycling of the fuel is necessary for further fusion reactions [3]. Moreover, undesirable impurities (for instance, ^{4}He from reaction (2.1)) will be produced inside the fusion reactor and they have to be separated from the unburnt D-T mixture before re-injection into the vacuum vessel. As a consequence, the fuel cycle of a DEMO-like device will be rather complex, as depicted in figure 2.3. Moreover, the implementation of a breeding blanket and interfacing systems increases further the complexity of the fuel processing and management inside a fusion reactor (i.e., DEMO and beyond). The whole fuel cycle of an FPP can be split into two:

- **Inner fuel cycle**: includes all the systems responsible for the removal of the impurities (e.g., helium, water, inert gases [44]) generated inside the toroidal vacuum vessel and for the recovery of the unburnt fuel[9]. The continuous evacuation of the torus removes the molecular hydrogen isotopologues Q_2 together with the impurities. This gaseous mixture is firstly sent to the tritium recovery system to remove

[8] The tritium consumption rate is not given in reference [6], which discusses the 1572 MW DEMO design. However, since in [43] the tritium consumption rate is $412\,g\,d^{-1}$ for a DEMO design with 2700 MW, a value of $240\,g\,d^{-1}$ can be estimated for the 1572 MW DEMO design.

[9] A slightly different fuel cycle has been recently considered for the EU-DEMO machine. In this concept, the fuel cycle is embedded with a "Direct Internal Recycling" (DIR) function which aims at decreasing tritum inventories by adding a short-cut between the torus pumps and the fuelling systems (i.e., by-passing the tritium plant) [45].

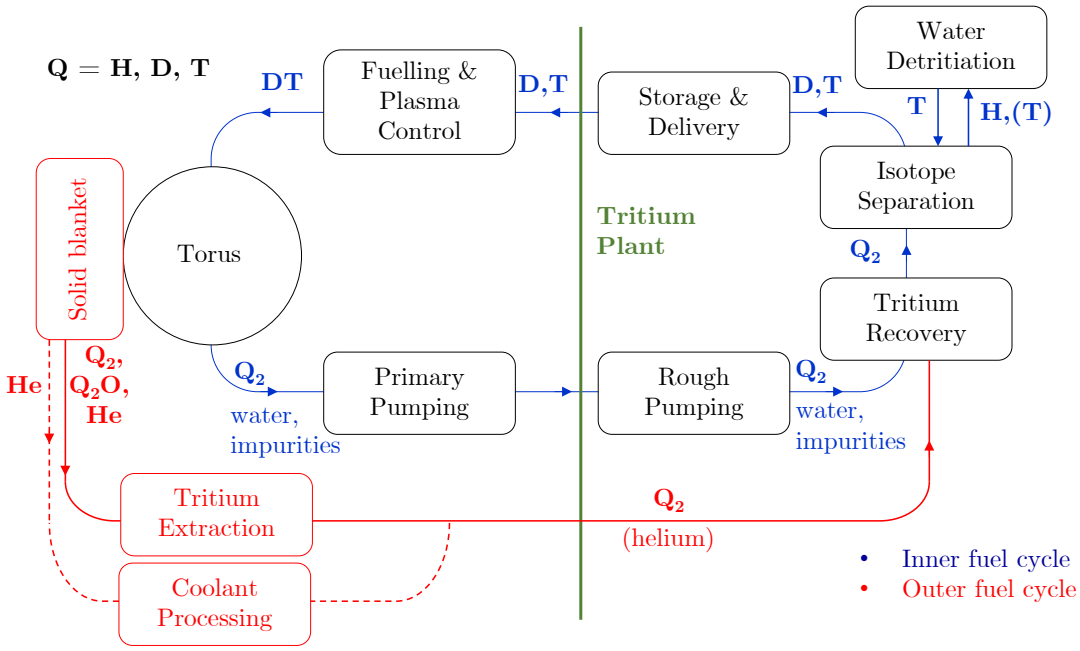

Figure 2.3: Schematic diagram of the fuel cycle of a DEMO-like fusion device. The inner fuel cycle is presented in blue and the outer fuel cycle is presented in red. It should be noted that a solid blanket is depicted for the purposes of this work. Q = H, D, T. Adapted from [43].

the impurities, and the Q_2 mixture is then processed by the Isotope Separation System (ISS) for the removal of protium H. The resulting D-T mixture is then routed into the storage/delivery system before having it available for the fuelling systems;

- **Outer fuel cycle**: includes all the systems dedicated to the extraction, separation, processing and accountancy of the tritium produced in the breeding blanket. Due to the high temperatures expected in the BB ($\approx 300 - 500\,^{\circ}C$ [46]), tritium will unavoidably permeate to the coolant (used for the removal of the heat generated in the blanket), and thus a dedicated Coolant Purification System (CPS) is required for tritium recovery. In addition, the tritium produced in the blanket is recovered using a dedicated Tritium Extraction and Removal System (TERS). For the HCPB, two TERS concepts have been considered.

2.3 Tritium Extraction and Removal Systems for the solid blanket of the EU-DEMO

2.3.1 Purge gas options for tritium recovery from the blankets

The TERS is crucial to guarantee the tritium self-sufficiency of a fusion device, as its extraction efficiency and reliability will impact the availability of tritium for further fusion reactions. The present work is focused on the TERS of the HCPB breeding blanket, which

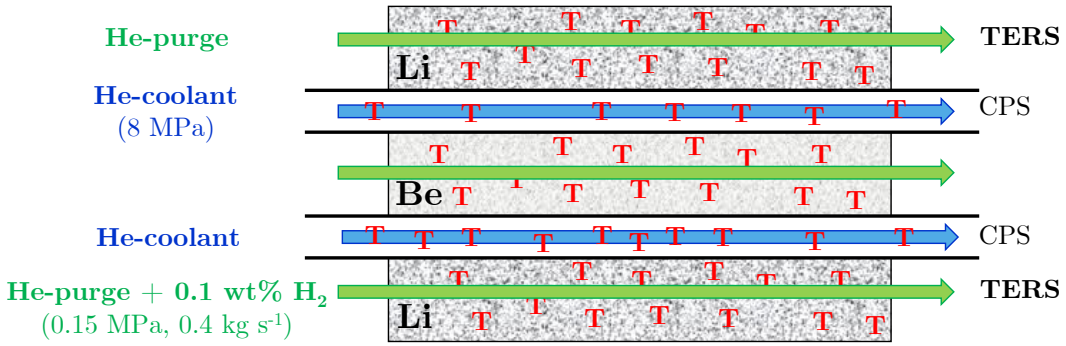

Figure 2.4: Schematic diagram of the HCPB blanket. This blanket consists of a sandwich-like configuration of Li-based and Be-based ceramic beds, with two independent He loops for power extraction and tritium recovery. CPS: Coolant Purification System, TERS: Tritium Extraction and Removal System. Adapted from [43].

is proposed to have a sandwich-like arrangement of Li_4SiO_4 and Be ceramic beds[10], as presented in figure 2.4. Two independent helium loops will be implemented to ensure the cooling of the blanket[11] for power extraction and the tritium recovery from the blanket. The current design specifications for these loops are presented in table 2.3.

Tritium is proposed to be extracted from the blanket by purging it with large flows of helium doped with 0.1 wt% of H_2 to enhance recovery via isotopic exchange reactions. The small partial pressures for protium are required to minimise the tritium permeation through the processing tubes. Downstream of the blanket the purge gas will be essentially $He + 0.1\,wt\%\,H_2$ with small concentrations of HT and HTO on the order of $0.1 - 1$ ppm according to the values reported in [9]. The presence of HTO is unavoidable due to the presence of structural water on the processing lines and the chemical interaction between the atomic tritium produced inside the pebble and the oxygen in the ceramic structure [6]. Alternative purging gas compositions and configurations are presently under consideration [49]. The main difference is whether H_2O is present in the purge gas at the inlet of the blanket. The replacement of H_2 by H_2O would bring several advantages, namely the reduction of tritium permeation to the coolant and higher efficiency of tritium removal from the pebbles [7, 8, 34]. Due to the reactivity of H_2O with Be (resulting in its hydrolisation), this option would require the use of separated purging circuits: dry purge for Be, wet purge for Li_4SiO_4. Alternatively, Be could be replaced with $Be_{12}Ti$ which would allow the use of vapor without hydrolisation [5]. In the perspective of purging it with H_2O, most of the tritiated species in the purge gas downstream of the BB are expected to be in HTO form. Futhermore, the use of D_2 or D_2O as dopant is also

[10]The study of an alternative breeding blanket has been recently started, where liquid lead is proposed as neutron multiplier [47]. This new blanket design is named Molten Lead Ceramic Breeder blanket.

[11]The cooling of the blanket with CO_2 instead of He has been recently proposed [48]. Despite its lower heat capacity and thermal conductivity, CO_2 has the benefit of increasing the net efficiency of the whole plant (one reason for this is that CO_2 is denser than helium which leads to a decrease in the circulation power).

Table 2.3: Characteristics of the two independent helium loops to cool and purge the EU-DEMO HCPB blanket. From the data available in [6].

	Helium coolant loop	Helium purge loop
He flow rate ($kg\,s^{-1}$)	2400*	0.4
Inlet temperature (°C)	300	300
Outlet temperature (°C)	500	500
Absolute pressure (MPa)	8.00	0.15
Dopant	no	H_2 (0.1 wt%)

*Only a small fraction ($\approx$ 1 %) of the total coolant flow rate is routed into the CPS [50].

under consideration since it could bring benefits to the overall fuel management inside the tritium plant.

In sum, two purging scenarios are currently under consideration:

1. "dry purge", where the pebbles are purged with H_2/He and the gas composition at the outlet of the blanket is HTO/HT/H_2/He;

2. "wet purge", where the pebbles are purged with H_2O/He and the gas composition at the outlet of the blanket is HTO/H_2O/He.

After the blanket, the purge gas containing the tritiated species is routed into the TERS for the separation of Q_2 and Q_2O from He. Two different approaches based on adsorption and membrane technologies have been considered for the TERS of the HCPB breeding blanket.

2.3.2 Tritium extraction relying on adsorption technologies

Originally proposed for the tritium extraction system of the HCPB TBM for ITER, the reference TERS approach relies on two trapping stages for the dry purge scenario: an adsorption column to remove the Q_2O molecules from the purge gas followed by a getter bed to remove the Q_2 species [11]. The adsorption column, also known as Molecular Sieve Bed (MSB), operated at $\approx$ 298 K, uses the hydrophilic zeolite LTA, a typical material for the dehydration of tritiated streams [51, 52]. The water molecules remain adsorbed in the zeolite framework, and high temperatures ($>$ 573 K) are required to release them. The getter bed could be either depleted uranium or zirconium-cobalt alloy, inside which the Q_2 species are chemically bond at $\approx$ 298 K as a metal hydride[12] [27, 53]. The Q_2 species are then released upon heating above 573 K.

For DEMO, a recent work has proposed the replacement of the getter beds by cryogenic MSBs as depicted on the top of figure 2.5 [54]. When operated at liquid nitrogen

[12]For instance, tritium is stored inside depleted uranium as UT_3.

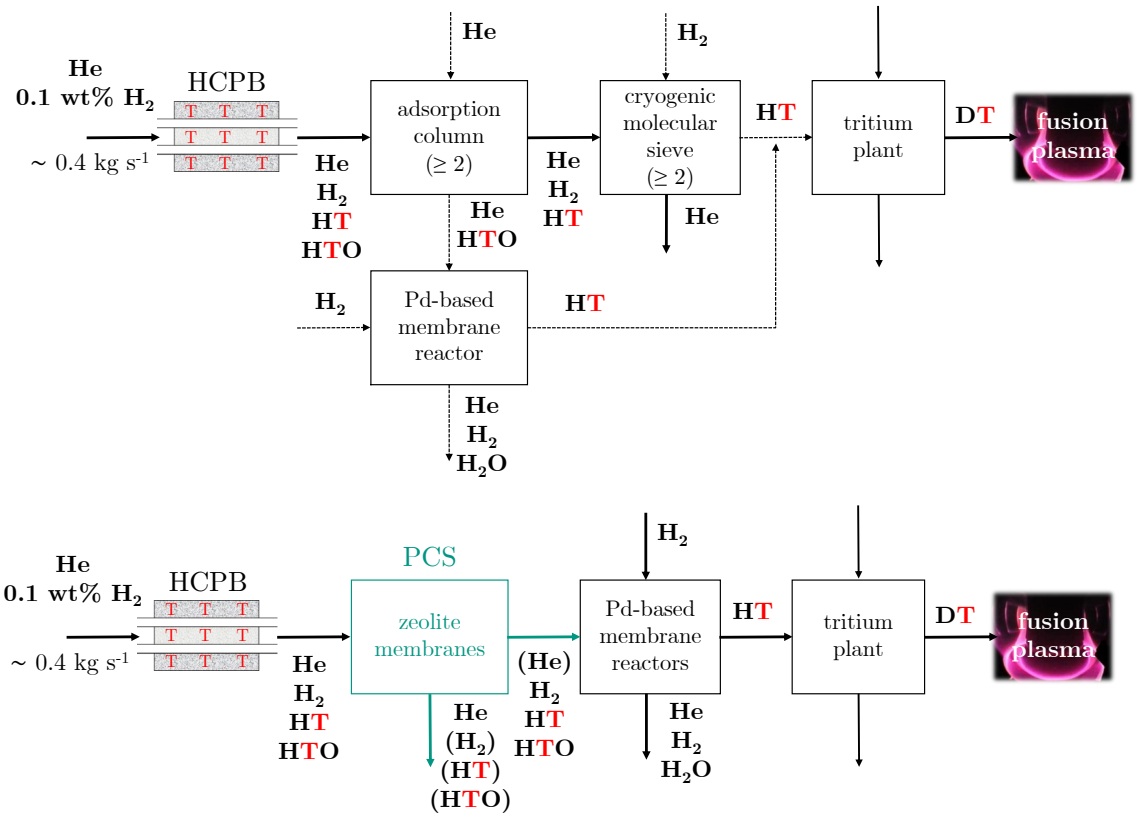

Figure 2.5: Schematic diagram of the two TERS concepts proposed for the HCPB blanket purged with H_2/He. Top: TERS based on adsorption technologies, bottom: TERS based on membrane technologies. The light-dashed lines in the top figure indicate the flows arrangement when the stages are under regeneration. The brackets in the bottom figure indicate the depletion of the species as a result of the membranes separation stage.

temperatures ($\approx$ 77 K), the zeolite framework forms chemical bonds with the hydrogen isotopologues. Its regeneration can be achieved by purging it with H_2 at $\approx$ 370 K. The addition of a catalyst (e.g., platinum) promotes the isotopic exchange among H_2 and the trapped tritiated species.

Due to the trapping of the Q_2O and Q_2 species in the corresponding stages, the tritiated species are temporary unavailable for further fusion reactions. Therefore, at least two parallel stages are required for the trapping stages to achieve a quasi-continuous operation. In this configuration, at least one stage would be operated under "adsorption mode" while the other(s) would work under "regeneration mode". During regeneration, an additional Pd-based membrane reactor, whose working process is described in section 2.3.3, is required to reduce the Q_2O species at the outlet of the adsorption column into Q_2.

Zeolite packed-columns are widespread in the industry for the dehyration of process streams [55, 56]. However, besides being a quasi-continuous process, the need for increasing/decreasing temperatures together with valves switching might penalise the reliability of the system. Moreover, the trapping of tritium in a specific location may raise safety and licensing concerns due to the increased tritium inventory. Last but not least, the need

to cool down large flows to liquid nitrogen temperatures may lead to high-energy requirements.

For the wet purge scenario, the TERS would only consist of adsorption columns and Pd-based membrane reactors for the separation of Q_2O from He.

2.3.3 Tritium extraction relying on membrane technologies

Another approach was proposed several years ago by the Tritium Laboratory Karlsruhe (TLK) to circumvent the issues mentioned above [10]. This concept relies solely on membrane technologies and it also consists of two sub-systems: a Pre-Concentration Stage (PCS) followed by Pd-based membrane reactors, as presented in the bottom diagram of figure 2.5.

Each membrane reactor (also known as PERMCAT) consists of a Pd-based membrane, exclusively permeable to Q_2 species, and a catalyst (for instance, Ni-based) placed in the feed side of the reactor. The removal of the tritiated species from the incoming stream $HTO/HT/H_2/He$ is achieved by operating the PERMCAT under isotope swamping mode as illustrated in figure 2.6. In this operation mode, H_2 purges the permeate side in counter-current. As a result, isotopic exchange reactions between the H_2 and the tritiated species will eventually take place on the catalyst side. At the outlet of the permeate, the flow consists only of HT species, whereas, at the outlet of the feed side, the gas mixture is mostly depleted in tritiated species (i.e., $H_2O/H_2/He$). The so-called decontamination factors of the PERMCAT are highly impacted by the (i) Q_2O flows and concentrations at the feed side, (ii) flow and pressure of H_2 in the shell side, (iii) reactor length and temperature and (iv) catalyst material [57–61].

With the large flows expected at the inlet of the TERS ($0.4\,kg\,s^{-1}$ or $100\,mol\,s^{-1}$, table 2.3) the membrane reactor would reach prohibitive sizes and costs. Moreover, the membrane reactor operates rather inefficiently at very low inlet partial pressures of the tritiated species [10, 12]. Therefore, a PCS is added to reduce as much as possible the flow at the inlet of the membrane reactors and to increase the partial pressures of the tritiated species.

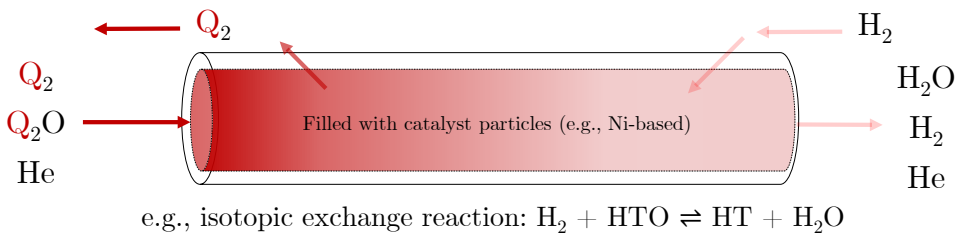

Figure 2.6: Schematic diagram of a membrane reactor operated under isotope swamping mode. H_2 is used as swamping gas in the permeate side of the reactor. The isotopic exchange reactions between H_2 and HT or HTO occur on the catalyst/feed side.

Very good candidates for the PCS are permeable membranes, which allow the continuous separation of two or more gas species due to differences in the mass-transport. Typically, the gas permeation through a membrane is controlled by applying a pressure-gradient across the membrane to promote enough driving force. Conventionally used in the industry, polymer-based membranes are not an option for this application due to the degradation of their properties when in contact with tritium. On the contrary, inorganic membranes have interesting properties in regards to tritium compatibility. In this respect, zeolite membranes have been selected as the most promising candidates due to the following characteristics [10]: (i) long-term stability under tritiated atmosphere, (ii) thermal and chemical stability, (iii) surface tuneability and (iv) molecular-sized pores. The separation of two or more gas species with zeolite membranes is achieved with differences in adsorption, diffusion and/or molecular sizes.

Single-gas permeation measurements with He and H_2 and separation experiments with binary mixtures of H_2/He and H_2O/He were performed at the TLK between 2013 and 2015 with MFI and NaA zeolite-type membranes [62–64]. The single-gas experiments were performed in the temperature range $298 - 398\,\mathrm{K}$ to evaluate the dominant mass-transport mechanism. The results showed a strong dependency of the measured permeances with the temperature explained by the interplay between surface and gas-translational diffusion (introduced and discussed in the following chapter). Moreover, due to the lower mass of H_2 and larger interaction with the zeolite structure, its permeance was larger than that of helium by a factor of 2. The separation experiments were performed with low concentrations of H_2 or H_2O in He (in the range $0.1 - 10\,\mathrm{mol\%}$), as expected in the purge gas of the TERS. The main results and conclusions of these experiments are summarised below:

- Only MFI demonstrated to be selective for H_2/He, and the separation factor was in the range $1.2 - 1.7$ regardless of the feed gas composition. These values were obtained with different membrane geometries (tubular, hollow-fiber) tested under the same conditions;
- The experiments with H_2O/He binary mixtures demonstrated a large dependency of the separation factor with the feeding concentration and membrane temperature. At low concentrations ($0.2 - 1\,\mathrm{mol\%}$) the separation factors measured are below 10 in the whole temperature range. However, with a further increase of the feeding concentration up to $10\,\mathrm{mol\,\%}$, the separation factors obtained for NaA were larger by several orders of magnitude than those measured with MFI. This behavior is consistent with the materials properties since the NaA structure is highly hydrophilic, whereas MFI is usually hydrophobic.

2.4 Objectives of this work

The results gathered in the previous years are important as they provide insights on the performance of zeolite membranes for the separation of Q_2/He and Q_2O/He species. However, no experiments were performed with the heavier hydrogen isotopologues. Their mass-transport is expected to be affected by their masses and the dipole moments of the asymmetric isotopologues (HD, HT and DT) may lead to deviations in their permeances when compared to H_2, D_2 and T_2 (without dipole moments). In addition, the presence of tritium may also influence the permeation and separation performances due to its radioactive decay, since the released energy may effect the adsorption onto the zeolite layer impacting the surface-diffusion contribution in the permeance, which is relevant at the temperatures of interest. Therefore, further experiments are required to evaluate the feasibility of the zeolite membranes for the TERS of the solid breeding blanket.

The strategy followed in this thesis consists in performing permeation and separation experiments with two facilities at the TLK: (i) the HyDe loop setup, for permeation experiments with all inactive isotopologues, and (ii) the ZEMTEX setup, assembled inside a glovebox in the scope of this PhD, for permeation and separation experiments with all tritiated isotopologues and helium. The experimental results are then used to numerically evaluate the feasibility of the zeolite membranes for the pre-concentration stage of the TERS. More specifically, the objectives of this thesis are the following:

- **Isotopic effects on Q_2 permeation:** the HyDe loop setup will be used to study the mass-transport of He, H_2, D_2 and H_2-HD-D_2 at different membrane temperatures. These experiments allow a first estimation of the separation efficiency for Q_2/He using the selectivity, calculated by the ratio of the determined permeances. In these experiments, two MFI-ZSM-5 membranes are going to be compared to evaluate reproducibility. The influence of tritium in the permeation of the Q_2 species will be investigated with the ZEMTEX facility, using a third MFI-ZSM-5 membrane with feeding Q_2 mixtures up to to 55 at% T in Q;

- **Separation performances for Q_2/He and Q_2O/He:** the ZEMTEX setup is equipped with the appropriate instrumentation to allow performing separation experiments with Q_2/He and Q_2O/He mixtures. Taking advantage of the tritium analytics available at the TLK (mainly gas chromatography, mass-spectrometry, laser raman spectroscopy and calorimetry), the concentrations of the gas mixtures upstream and downstream of the membrane are measured to determine the separation factors. The experiments will be performed at relevant conditions for the TERS, with feeding mixtures of 10 mol% Q_2/He (20 at% T in Q) and $1 - 10$ mol% Q_2O/He (1 at% T in Q);

- **Feasibility of the zeolite membranes for the TERS:** a numerical code developed in the context of this thesis is used to calculate the membrane surface area, power consumption, tritium inventory and dimensions of the pre-concentration stage of the TERS using the experimental results as input. The feasibility of the resulting system will be evaluated against the estimations obtained for the TERS reference approach.

Chapter 3

Mass-transport and separation mechanisms of zeolite membranes

3.1 Separation properties of zeolite membranes and transport mechanisms for gas separation

3.1.1 Characteristics of porous membranes

A membrane can be defined as a selective barrier between two phases which is able to separate two or more species as a result of a driving force established across it [65, 66]. The driving force for transport through a membrane is the chemical potential difference $\Delta\mu$ arising due to differences in concentrations, temperatures, pressure or electrical potential [65]. The flux of each species through a membrane is determined by the interaction with the physical structure of the membrane and the competition in permeation with the other species. According to figure 3.1, a gas mixture feeding the membrane is separated

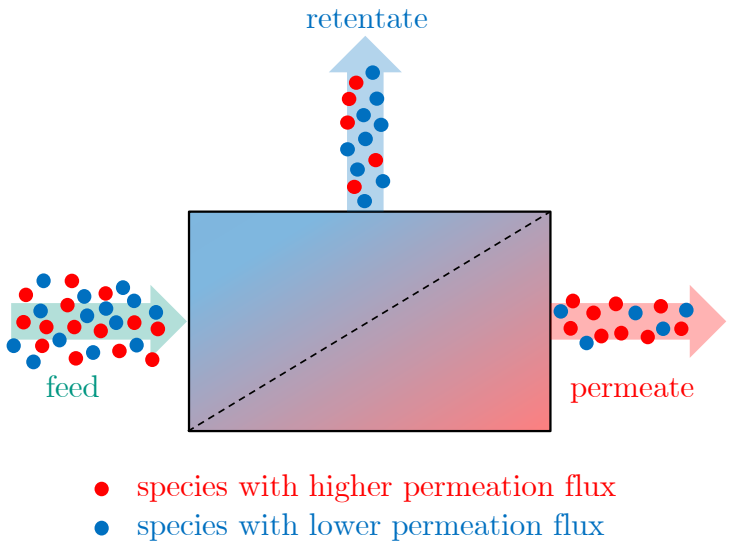

Figure 3.1: Schematic diagram of a membrane for the separation of a binary gas mixture. The feed (inlet), permeate and retentate (both outlet) streams are identified. The red species has higher permeation flux through the membrane, hence its concentration increases in the permeate and decreases in the retentate.

into a permeate stream, which permeates the membrane, and a retentate stream, which does not permeate the membrane. For a binary mixture with species i and j, the membrane is said to be selective towards species i if its flux through the membrane is larger. Consequently, the concentration of species i increases in the permeate and decreases in the retentate.

In gas separation applications, the membranes can be either porous or dense. Porous membranes have a voided structure with a network of interconnected pores and dense membranes are characterised by the inexistence of voids. Examples of porous membranes are ceramics (e.g., α-Al_2O_3) or zeolites (e.g., MFI-ZSM-5), and dense membranes are usually metallic (e.g., Pd-based) or polymeric (e.g., rubber) [67]. According to the IUPAC[1] recommendations, the porous membranes are further divided considering their pore diameters d_p: macroporous ($d_\mathrm{p} > 50\,\mathrm{nm}$), mesoporous ($2\,\mathrm{nm} < d_\mathrm{p} < 50\,\mathrm{nm}$) and microporous ($d_\mathrm{p} < 2\,\mathrm{nm}$) [68, 69]. Zeolite membranes belong to the category of microporous membranes. Depending on the pore sizes, different mass-transport and separation mechanisms arise as a result of different interactions between the permeating molecules and the membrane structure.

3.1.2 Definition of permeance, selectivity and separation factor

The flux J_i of a gas species i permeating through a membrane of thickness t_m is determined by the partial pressure difference established between the feed ($p_{\mathrm{f},i}$) and the permeate ($p_{\mathrm{p},i}$), as presented in equation (3.1). The proportionality constant is the so-called permeance Π_i and quantifies the rate at which species i permeates the material per unit time, area and pressure. The permeance is defined by the ratio between the permeability P_i and the thickness t_m.

$$J_i = \Pi_i(p_{\mathrm{f},i} - p_{\mathrm{p},i}) \equiv \frac{P_i}{t_\mathrm{m}}(p_{\mathrm{f},i} - p_{\mathrm{p},i}) \tag{3.1}$$

The permeance (or permeability) is determined by the interaction between the permeating species and the structure of the membrane and it is usually dependent on the temperature [65, 70]. However, for gas mixtures, the permeance of one gas species may be influenced by the competition in permeation with other species [70].

For a membrane with a known surface area A_m, the permeance Π_i can be calculated experimentally by feeding the membrane with a constant feed flow $F_{\mathrm{f},i}$ at a constant permeate pressure[2] and temperature. With the retentate closed, the feed flow is equal to the permeation flow and the resulting pressure difference is measured. At equilibrium, considered when the pressure difference reaches a constant value, the permeance is calculated with equation (3.2). As detailed in the following chapters, this method and equation are

[1] International Union of Pure and Applied Chemistry.
[2] Established for instance with a continuous evacuation of the permeate.

used to measure the permeances of He and Q_2 through zeolite membranes.

$$\Pi_i = \frac{F_{\mathrm{f},i}}{A_{\mathrm{m}}(p_{\mathrm{f},i} - p_{\mathrm{p},i})} \tag{3.2}$$

The permeances of He and Q_2 are used to estimate the separation of the zeolite membranes along this work using the definition of selectivity $\alpha^*_{i/j}$ given by equation (3.3). The selectivity is calculated by the ratio of the single-gas permeances Π_i and Π_j and it is a first estimation of the ability of a given membrane to separate the gas species i from j [67]. The selectivity is usually defined as $\alpha^*_{i/j} \geq 1$.

$$\frac{J_i}{J_j} = \frac{\Pi_i(p_{\mathrm{f},i} - p_{\mathrm{p},i})}{\Pi_j(p_{\mathrm{f},j} - p_{\mathrm{p},j})} \equiv \alpha^*_{i/j}\frac{(p_{\mathrm{f},i} - p_{\mathrm{p},i})}{(p_{\mathrm{f},j} - p_{\mathrm{p},j})} \tag{3.3}$$

In the presence of a gaseous mixture, $\alpha^*_{i/j}$ may not be representative of the actual membrane separation performance since species i may affect the permeation of species j. For instance, if the gas species i adsorbs more preferentially onto the membrane pores than j, the former can hinder the permeation of the latter leading to a stronger separation. For gas mixtures, the separation factor $\alpha_{i/j}$ defined by equation (3.4) provides an accurate evaluation of the separation performance of a membrane for two gas species [71]. This parameter is calculated by the ratio between the permeate and feed concentrations of the two gas species and it can be highly dependent on the operating conditions (e.g., feed concentrations, pressures, membrane temperature) [67, 70].

$$\alpha_{i/j} \equiv \frac{y_{\mathrm{p},i}/y_{\mathrm{p},j}}{x_{\mathrm{f},i}/x_{\mathrm{f},j}} \tag{3.4}$$

Therefore, to evaluate the application of zeolite membranes for the separation of Q_2 and Q_2O from He in the TERS of the solid blanket, the separation factor is the experimental quantity of interest.

3.1.3 Transport and separation mechanisms in porous membranes

In a porous membrane, the driving force for permeation is the pressure difference established between the feed and permeate [67]. The flux through a porous membrane is given by the so-called Darcy's law according to equation (3.5), where K is an empirical permeation coefficient reflecting the nature of the membrane, μ_{d} is the dynamic viscosity of the permeating fluid, p_i is its partial pressure and z is the direction of permeation.

$$J_i = -\frac{K}{\mu_{\mathrm{d}}}\frac{\mathrm{d}p_i}{\mathrm{d}z} \tag{3.5}$$

The viscous or Poiseuille flow, in which the molecules collide much more frequently with each other than with the pore walls, is described by Darcy's law. Equation (3.6) presents the Poiseuille flux through a pore of diameter d_{p}, where p_i and p are, respectively,

the partial and absolute pressures, T_m is the membrane temperature and R is the ideal gas constant.

$$J_i^\mathrm{vis} = -\frac{\epsilon}{\tau}\frac{p_i}{RT_\mathrm{m}}\frac{d_\mathrm{p}^2}{32\mu_\mathrm{d}}\frac{\mathrm{d}p}{\mathrm{d}z} \tag{3.6}$$

The factor ϵ/τ is introduced to take into account the permeation through a real membrane, with an overall effect of reducing the pemeation fluxes: ϵ is the porosity, which expresses the fraction of the total membrane volume that is porous ($0 < \epsilon < 1$), and τ is the tortuosity, which is a dimensionless parameter reflecting the length of the channels compared with the membrane thickness (for straight channels, $\tau = 1$; for angled paths, $\tau > 1$) [72, 73]. Equation (3.6) does not include any molecule-specific parameter (e.g., molar mass) and thus all gas species permeate with the same flux. Consequently, this transport mechanism does not provide any separation. The viscous flow regime is present for macroporous materials, since the pore diameters (e.g., $d_\mathrm{p} > 200\,\mathrm{nm}$) are larger than the molecules mean free path (typically in the range of $50 - 200\,\mathrm{nm}$, at atmospheric pressure and temperature) [67].

The ratio between the mean free path λ and the pore diameter d_p, defined by equation (3.7), is the so-called Knudsen number K_n and it is an important parameter which defines the dominant transport regime in porous materials. For low values ($K_\mathrm{n} < 0.01$), the viscous flow is the dominant transport mechanism. When the pore diameters are reduced and K_n eventually reaches values above 10, the dominant transport mechanism is the so-called Knudsen diffusion [74, 75]. With $\lambda \gg d_\mathrm{p}$, the molecules collide much more frequently with the pore walls and thus they move essentially independently from each other. Consequently, the transport equation for a continuum medium, as described by Darcy's law, is not applicable [74].

$$K_\mathrm{n} \equiv \frac{2\lambda}{d_\mathrm{p}} \tag{3.7}$$

The Knudsen diffusion is characterised by the transport of molecules that are momentaneously adsorbed on the pore walls and re-directed in a random direction. The Knudsen flux is described by Fick's law according to equation (3.8) [72, 74]. In contrast to the viscous flow, the transport dominated by Knudsen depends on the molar masses of the gas species M and hence separation takes place: the lighter the molecule, the faster it permeates through the membrane. The Knudsen selectivity is given by the inverse of the square-root of the masses of two gas species i and j, according to equation (3.9). Gas separation via Knudsen mechanism is however rather limited, especially for molecules with similar masses (for HT and He, $\alpha_\mathrm{HT/He}^\mathrm{Kn} \approx 1$).

$$J_i^\mathrm{Kn} = -D_i^\mathrm{Kn}\frac{\mathrm{d}c_i}{\mathrm{d}z} = -\frac{\epsilon}{\tau}\frac{d_\mathrm{p}}{3}\sqrt{\frac{8RT_\mathrm{m}}{\pi M_i}}\frac{1}{RT_\mathrm{m}}\frac{\mathrm{d}p_i}{\mathrm{d}z} \tag{3.8}$$

$$\alpha_{i/j}^\mathrm{Kn} = \sqrt{\frac{M_j}{M_i}} \tag{3.9}$$

The separation efficiency of a porous membrane can be improved by further decreasing the pore diameters, and the different transport and separation mechanisms that arise are depicted in figure 3.2 [66, 67]. These mechanisms are not only dependent on the pore diameters, but they are also strongly dependent on the mixture composition, pore sizes and uniformity, and operating conditions (e.g., pressure and temperature) [66, 69, 73].

In general, with the decreasing of the pore diameters, the molecules are subjected to a stronger interaction with the pores surfaces and eventually adsorption occurs. In this case, surface-diffusion of one gas species along the pore surface takes place as a result of a concentration gradient [76]. The gas species exhibiting the strongest adsorption may reduce the effective pore diameter and thus molecular sieving can occur if the kinetic diameter[3] of another molecule in the gas mixture is larger than the space available for permeation. In the range $2\,\text{nm} < d_\text{p} < 50\,\text{nm}$ surface-diffusion may exist together with Knudsen transport [66]. When condensable gases are present in the gas mixture, capillary condensation, characterised by the complete blockage of the pores hindering the permeation of the non-condensable species, may take place.

For materials with $d_\text{p} < 2\,\text{nm}$ such as zeolites, surface-diffusion and capillary condensation are considered to be predominant. For pore diameters d_p in the range of the kinetic

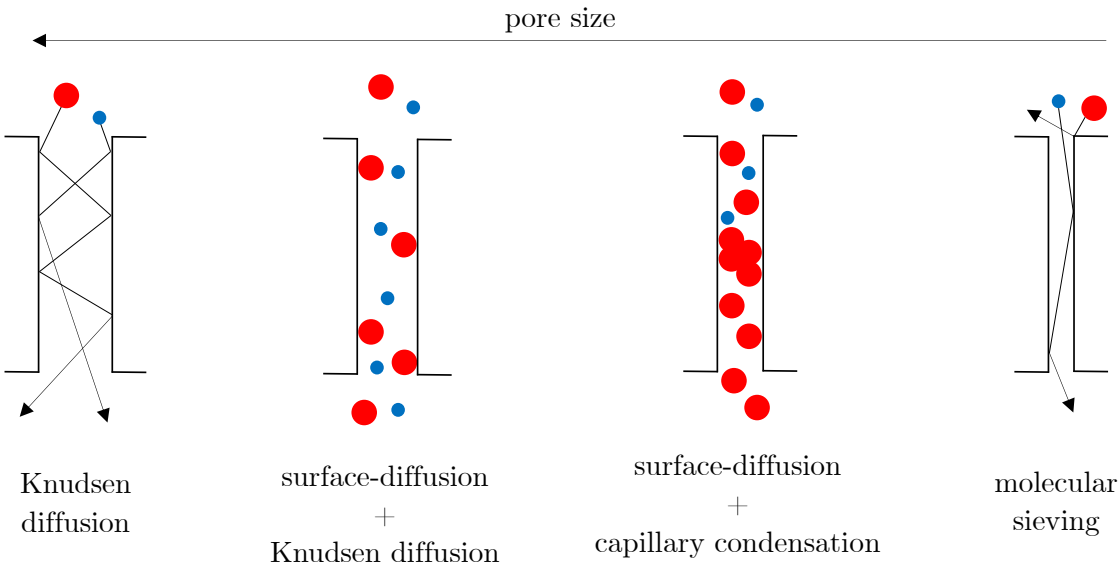

Figure 3.2: Schematic representation of the dominant transport and separation mechanisms for porous membranes. The dominant transport and separation mechanisms are dependent on the pore diameter. Capillary condensation is only present for condensable species. Although the pores are represented as straight channels, in reality they can be rather irregular. The dominant separation and transport mechanisms also depend on the gas mixture composition and operating conditions.

[3]Diameter $d_{\text{k},i}$ of a gas molecule described as a rigid sphere in the kinetic theory of gases. For ideal gases, it is determined by the gas density n_i and the mean free path λ_i according to $d_{\text{k},i} = \sqrt{1/(\pi\lambda_i n_i)}$ [66, 77].

diameters d_k (typically $\sim 10^{-1}$ nm), molecular sieving occurs when the diameter of the pores is in between the kinetic diameters of the molecules facing the membrane and only the molecules with $d_k < d_p$ can permeate through. This gas separation mechanism can be achieved with zeolite membranes due to their molecular-sized pores.

3.1.4 Surface and gas-translational diffusion in zeolite membranes

The main steps for gas permeation through a zeolite layer as a result of an applied pressure difference are presented in figure 3.3 and described in the following points [78]:

1. diffusion of the gas species in the gas phase towards the external surface of the membrane (feed side);
2. adsorption onto the membrane external surface and diffusion towards the pore entrance;
3. intra-crystalline diffusion along the zeolite pores;
4. diffusion out of the zeolite pore to the zeolite external surface;
5. desorption from the membrane surface and diffusion into the gas phase (permeate side).

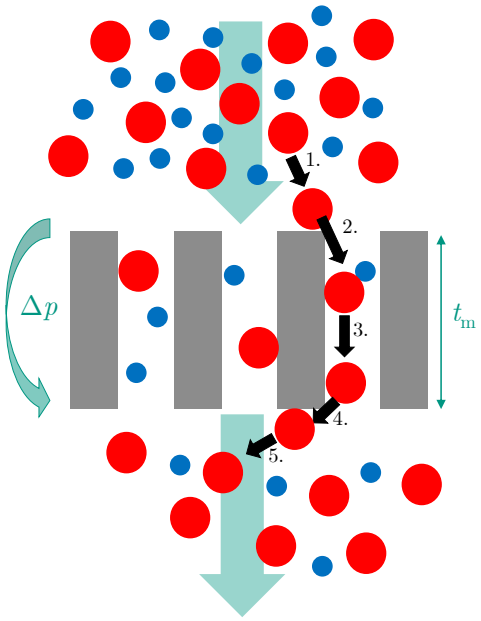

Figure 3.3: Schematic diagram of the mass-transport through microporous, defect-free zeolite membranes. 1. diffusion from gaseous phase towards the membrane external surface, 2. adsorption onto membrane external surface and migration towards the zeolite pore, 3. diffusion along the zeolite pore, 4. migration from the zeolitic pore to the membrane external surface side, 5. desorption into the gaseous bulk phase.

At low temperatures, surface-diffusion is the main permeation mechanism. The adsorbed molecules permeate through the zeolite membrane moving between minima of potential energy imposed by the zeolite lattice [79]. This is an activated process following an Arrhenius-type temperature dependency, with a defined activation energy $E_{\mathrm{a},i}^{\mathrm{SD}}$ for the gas species i. It can be shown that the flux due to surface diffusion is given by equation (3.10) [78, 80, 81]. ρ_{Z} is the zeolite mass density, $q_{\mathrm{sat},i}$ is the saturation concentration of the adsorbed species i (in molar mass units), $D_{0,i}^{\mathrm{SD}}$ is the surface-diffusion coefficient and θ_i is the surface occupancy, defined by the fraction of the adsorption sites which are occupied.

$$J_i^{\mathrm{SD}} = \frac{\epsilon}{\tau}\rho_{\mathrm{Z}} q_{\mathrm{sat},i} D_{0,i}^{\mathrm{SD}} \exp\left(-\frac{E_{\mathrm{a},i}^{\mathrm{SD}}}{RT_{\mathrm{m}}}\right)\frac{1}{1-\theta_i}\frac{\mathrm{d}\theta_i}{\mathrm{d}z} \tag{3.10}$$

The gas adsorption in microporous materials is found to be well described by Langmuir-type isotherms, which considers the adsorption process as a reaction between the molecules in gas phase and the solid according to $A\,(\mathrm{g}) + B\,(\mathrm{s}) \rightleftharpoons AB\,(\mathrm{ads})$ and assumes equilibrium at a given pressure and temperature. The fraction of adsorbed component i depends on the partial pressure p_i according to equation (3.11) [76, 78]. q_i is the adsorbed concentration of species i (in molar mass units) and K_i^{L} is the Langmuir adsorption constant[4], which depends on the temperature [78]. This dependency is established by both the entropy $\Delta S_{\mathrm{ads},i}$ and enthalpy $\Delta H_{\mathrm{ads},i}$ of adsorption[5] via equation (3.12) [81]. p_0 is a reference pressure and equal to 10^5 in SI units.

$$\frac{q_i}{q_{\mathrm{sat},i}} \equiv \theta_i = \frac{K_i^{\mathrm{L}} p_i}{1 + K_i^{\mathrm{L}} p_i} \tag{3.11}$$

$$K_i^{\mathrm{L}} = \frac{1}{p_0}\exp\left(\frac{\Delta S_{\mathrm{ads},i}}{R}\right)\exp\left(-\frac{\Delta H_{\mathrm{ads},i}}{RT_{\mathrm{m}}}\right) \tag{3.12}$$

At higher temperatures, most of the gas molecules retain their gaseous character (negligible adsorption), giving place to a different transport mechanism, the gas-translational diffusion, in which the molecules hop between adsorption sites along the zeolite channels (also called activated Knudsen diffusion). This transport mechanism is pressure independent but it is also thermally activated with an activation energy $E_{\mathrm{a},i}^{\mathrm{GT}}$. The flux due to gas-translational diffusion is given by equation (3.13), where $\lambda_{\mathrm{d},i}$ is the diffusional length

[4] K_i^{L} is defined as the equilibrium constant for the reaction $A\,(\mathrm{g}) + B\,(\mathrm{s}) \rightleftharpoons AB\,(\mathrm{ads})$ where $AB\,(\mathrm{ads})$ represents the A species adsorbed on a vacant site B. Thus, it is given by $K^{\mathrm{L}} = [AB]/([A][B]) = \theta_i/(p_i(1-\theta_i))$ where p_i is the partial pressure of A at equilibrium with the solid surface [82].

[5] Physical adsorption of a gas onto a solid surface is a spontaneous process, provided the total free energy of the system, given by the Gibbs free energy, decreases: $\Delta G_{\mathrm{ads},i} = \Delta H_{\mathrm{ads},i} - T_{\mathrm{m}}\Delta S_{\mathrm{ads},i} < 0$. Upon adsorption, the degrees of freedom of the gaseous phase decrease, i.e. $\Delta S_{\mathrm{ads},i} < 0$. The more negative is $\Delta S_{\mathrm{ads},i}$, the less is the disorder at the gas/solid interface, and thus less molecules are adsorbed. An exothermic adsorption implies that $\Delta H_{\mathrm{ads},i} < 0$, and the more negative this value is the more favourable is the adsorption process (i.e., more energy is released upon adsorption) [83, 84].

and β is the coordination number of the lattice [78, 80, 81, 85]. The GT flux increases monotonously with the temperature.

$$J_i^{\mathrm{GT}} = \frac{\epsilon}{\tau}\frac{\lambda_{\mathrm{d},i}}{\beta}\sqrt{\frac{8RT_{\mathrm{m}}}{\pi M_i}}\frac{1}{RT_{\mathrm{m}}}\exp\left(-\frac{E_{\mathrm{a},i}^{\mathrm{GT}}}{RT_{\mathrm{m}}}\right)\frac{\mathrm{d}p_i}{\mathrm{d}z} \tag{3.13}$$

In sum, gas separation in zeolite membranes occurs due to differences in adsorption and diffusion of the permeating molecules [80]. Besides the operating conditions, the separation expected for a given gas mixture is highly dependent on the type of zeolite materials used and molecules present in the gaseous mixture.

3.2 Properties of zeolite materials and membranes for gas separation

3.2.1 Zeolite Materials

Zeolites are considered to be the most important family of microporous materials [86]. In 2001, there were 133 zeolite structural types and the number of known structures increased to 167 in 2016. By 2018, the number of zeolite materials that have been recognised by the Structure Commission of the International Zeolite Association (IZA) exceeded 220 [87, 88]. These figures demonstrate that research on zeolites is a field in expansion, mainly triggered by their molecular-sized pores, uniform pore size distribution and high surface areas [89]. These properties make these materials interesting for several applications, such as catalysis and separation.

Originally, "zeolite" refers to a crystalline, aluminosilicate material whose regular structure of voids and channels, accessible by molecular-sized pores, is constructed from TO_4 (T = Si or Al) tetrahedral building blocks [90, 91]. Currently, the term "zeolite" is extended to materials whose framework contains other tetrahedrally coordinated atoms, such as P, Ba or Ge [92, 93]. Each T atom is surrounded by four oxygen atoms and each oxygen bridges two T atoms. A pure siliceous structure of SiO_4 blocks is electrically neutral (each positively charged Si^{4+} is cancelled out by four negatively charged O^{2-}). With the addition of Al, the whole aluminosilicate framework is negatively charged, since the valence of aluminum is +3. Thus, extraframework cations are required to guarantee the neutrality of the whole framework. The generic zeolite structure is given by three components, where v is the valence of the extra-framework cations C [88]:

$\mathrm{C}_{n/v}^{v+}$	$[\mathrm{Si}_{1-n}\mathrm{Al}_n\mathrm{O}_2]$	$m\mathrm{H}_2\mathrm{O}$
extra-framework cations	framework	sorbed phase

The zeolites can be classified according to the size of the regular openings enclosed by rings of a given number of T atoms interconnected by oxygen atoms (number of

Table 3.1: Examples of zeolite structures. The number of T atoms per ring, pore diameters and typical Si/Al ratios are given for several zeolite structures. From the data available in [88].

Framework code	Example	Number of T atoms per ring	Pore diameters (Å)	Typical Si/Al ratio
SOD	sodalite	6	2.7	1.0
LTA	NaA	8	4.1	1.0
CHA	Chabazite	8	3.8×3.8	2.0
MFI	ZSM-5	10	(5.3×5.6)/(5.1×5.5)	> 15
FAU	Faujasite	12	7.4	2.5
MTW	ZSM-12	12	5.5×5.9	> 40
VFI	$AlPO_2$	18	11.2	1.0

ring members). These apertures dictate the zeolite molecular-sieving properties. Rings with 6, 8 or 9 members fall within the category of small pore structures. Medium pore frameworks consist of 10 membered rings, and large pore zeolites have rings with 12 members. Ultra-large structures have larger rings, up to 20 members [90]. Table 3.1 presents examples of zeolite structures with different rings sizes, covering a pore diameter range between 0.27 nm for 6-membered rings and 1.12 nm for 18-membered rings. The sodalite with $d_p = 0.27\,\text{nm}$ is an interesting framework since it could provide molecular sieving separation of Q_2 ($d_k = 0.289\,\text{nm}$) from He ($d_k = 0.255\,\text{nm}$).

An additional property of the zeolite structure important for gas separation, also displayed in table 3.1, is the Si/Al ratio. Si/Al varies from 1 to ∞ and the lower limit obeys the so-called Löwenstein's rule, which forbids the link between two successive $(AlO_4)^-$ tetrahedrons [94]. The Si/Al ratio impacts the physical and chemical properties of the zeolites and the following characteristics are usually observed for low and high silica structures [88]:

- **low-silica** (Si/Al = 1 − 1.5): decomposition temperature around 700 °C, unstable in the presence of acids and hydrophilic;
- **high-silica** (Si/Al > 10): decomposition temperature around 1300 °C, unstable in the presence of basic solutions and hydrophobic.

The lower is the Si/Al ratio, the higher is the number of extra-framework cations required for charge compensation. Therefore, for a given guest molecule, stronger electrostatic interactions take place for frameworks[6] with low Si/Al ratio. Furthermore, the strength of the interaction is also dependent on the polarizability of the adsor-

[6]The strength of the interaction is also dependent on the type of cations (e.g., Li^+, Na^+, Cs^+) as reported in the studies [95–100]. For instance, the larger is the cation radius, the weaker is the isosteric heat of adsorption.

bate molecule. In sum, the following properties have a strong impact on the adsorbate-adsorbent interaction [80, 101–104]:

- **adsorbate**: polarizability, electric moments (dipole, quadropole), molecular radius;
- **adsorbent**: polarity, zeolite pore diameter, extra-framework cations.

Table 3.2 presents the properties of various moleules relevant for this work in the perspective of the study of zeolite membranes for the TERS. These properties are important to understand the nature of the interaction between the adsorbate and the adsorbent, ultimately impacting the separation efficiency. The "non-specific" contributions are always present regardless of the adsorbate-adsorbent and they include dispersion, repulsion and polarization interactions, whereas the "specific" contributions depend on the adsorbate-adsorbent pair and they are the dipole, quadrupole and self-potential interactions (a more detailed description is given in Appendix A) [102–104]. In pure siliceous frameworks ($Si/Al = \infty$) the isosteric heats of adsorption are determined by the polarizability of the guest molecules[8]. Experimental and numerical evidence on the direct correlation between the isosteric heat of adsorption and the polarizabilities of non-dipolar molecules has been reported: the higher the polarizablity, the stronger is the adsorption [110, 111].

Table 3.2: Physical characteristics of molecules of interest for this work. From the data available in [31, 88, 105–108].

	Molar mass ($g\,mol^{-1}$)	Kinetic diameter ($10^{-10}\,m$)	Polarizability ($10^{-40}\,C^2\,m^2\,J^{-1}$)	Dipole moment ($10^{-30}\,C\,m$)	Quadrupole moment ($10^{-40}\,C\,m^2$)
H_2	2.016	2.89	0.874	0.0	2.21
HD	3.022	2.89[a]	0.878	0.0027[b]	2.14
D_2	4.028	2.89[a]	0.869	0.0	2.16
He	4.003	2.55	0.231	0.0	0.0
H_2O	18.015	2.64	1.61	6.17	–
N_2	28.014	3.64 – 3.80	1.95	0.0	5.07
Ar	39.948	3.54	1.85	0.0	0.0
CO_2	44.010	3.30 - 3.94	2.94	0.0	14.3

[a]The kinetic diameters of HD and D_2 are assumed to be the same as that of H_2.
[b]The isotopically asymmetric isotopologues (HD, HT, DT) are known to possess a small, but non-negligible, dipole moment.[7]

[7]This observation has been attributed to two effects: (i) a favoring of the ionic configuration H^+D^- due the lower energy of the D(1s) orbital in comparison to H(1s), (ii) the D(1s) orbital is smaller and hence there is a shift of the electron cloud distribution towards H^+D^-. The same applies for HT and DT [109].

[8]In silicalite (SiO_2) the adsorption is determined by the interaction between the adsorbate and the Si-O-Si groups [103].

Moreover, the adsorption of noble gases onto zeolite structures, as a result of their non-zero polarizability, has been widely studied [112–118]. The presence of extra-framework cations enhances the interaction with molecules which possess quadrupole and/or dipole moments [99, 114]. For instance, the separation of H_2O/He with zeolite membranes is one example where high separation factors can be achieved due to the stronger interaction of the dipolar molecule with the zeolite structure (especially with low Si/Al ratios) [64]. A strong supression for the permeation of weakly adsorbing molecules (e.g., He, H_2) in the presence of vapor has been observed for aluminum rich NaA membranes [64, 119, 120].

From the wide variety of zeolite materials, only few zeolites have been synthesized as membranes limiting the number of zeolite membranes available for the separation of Q_2 and Q_2O from He.

3.2.2 Zeolite Membranes

Zeolite membranes have been increasingly studied in the past decades and there are several reviews available in the literature [80, 90, 121–127]. In comparison to the number of zeolite materials available, only a limited number of zeolites have been used as membranes. According to the study presented in [80], MFI is by far the most studied with $\approx$ 800 references indexed in Scopus. The second most studied membrane is LTA with $\approx$ 320. There are less than 200 studies for FAU-type membranes, and for the remaining frameworks (e.g., CHA, T, DDR) the number of publications is less than 100. The prominence of MFI is explained by its relative ease of preparation and its good separation properties for hydrocarbons, of interest for the gas and oil industries [70, 80]. Nevertheless, there are few small-to-medium industrial plants using zeolite membranes[9].

The zeolite membranes are usually available as composite membranes, in which a thin zeolite layer ($\sim$ µm) is synthesized[10] on a thicker supporting porous support layer ($\sim$ mm) for mechanical stability[11]. This configuration ensures high permeation rates through the zeolite layer, and the gas permeance and separation properties are provided by this layer alone (which is in contact with the feeding mixture). Therefore, the pressure difference across the zeolite layer Δp_{zeo} must be much larger than the pressure difference across the support Δp_{sup}, as schematically depicted in figure 3.4. As such, the support should be highly permeable and thus the following relation should be satisfied for the measured pressure difference: $\Delta p_{\text{tot}} = \Delta p_{\text{zeo}} + \Delta p_{\text{sup}} \simeq \Delta p_{\text{zeo}}$. Otherwise, lower permeances are obtained and the selectivities also decrease (towards Knudsen) [80].

[9] For example, the use of NaA membranes for the dehydration of high-purity ethanol in Japan [128].

[10] The so-called secondary growth, in which zeolite seeds or nano-crystals (with dimensions in the range 50 − 100 nm) are deposited as a thin layer on the support surface, is widely used as synthesis method [92, 129].

[11] The mechanical stability of self-supported membranes is considered to be insufficient for industrial applications [130].

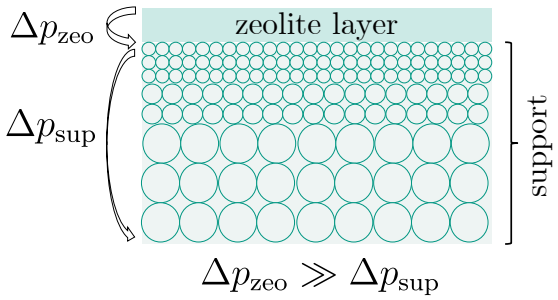

Figure 3.4: Schematic diagram of a zeolite layer synthesized on a ceramic support. The support is an asymmetric membrane where the pore sizes decrease towards the zeolite layer for better synthesis purposes. The pressure difference across the zeolite layer Δp_{zeo} should be much larger than the pressure difference across the support Δp_{sup}.

In practice, the zeolite layers are not free of defects and their presence may have a significant impact on the mass-transport and separation performance. Since the zeolite diameters are usually below 1 nm, intercrystalline defects with few nm can dramatically affect the separation properties of the membrane [131, 132]. As discussed in section 3.3.2, a small percentage of defects in the permeation area is sufficient to considerably increase the flux through the membrane at the expense of a lower separation. Thus, high-quality zeolite membranes are required to ensure high separation.

The membrane supports, which are typically ceramic materials (e.g., α-Al_2O_3, TiO_2), are one of the key aspects that can affect the reproducibility of the zeolite membranes synthesis. One reason for this is the mismatch between the thermal expansions of the zeolite layer and the ceramic support, which may lead to temperature-induced defects [122, 133, 134]. Moreover, the high-quality synthesis of zeolite layers require supports with small pore sizes. For instance, a 1 µm-thick zeolite layer requires a supporting material with 1 µm-wide pore diameters [80]. Thus, asymmetric supports with several layers of different pore sizes and thicknesses are required: the smallest pore size layer for the zeolite synthesis and the larger pore size layers to ensure mechanical stability and high porosity. Moreover, the synthesis of a zeolite membrane can also be impacted by the Si/Al ratio of the framework. A study has reported a higher number of intercrystalline defects (e.g., open grain boundaries in the polycrystalline zeolite layer) for aluminum-rich structures due to repulsion between crystals [135].

3.3 Single-gas permeances through MFI membranes

3.3.1 Defect-free membranes

The following chapters present the singe-gas permeances of Q_2 and He experimentally determined for MFI membranes synthesized on α-Al_2O_3 supports at different temperatures. Therefore, it is relevant to study the expected permeances as a function of the temperature for a defect-free MFI membrane. The permeance at steady-state is calculated

by dividing the total flux J_i^{tot} presented in equation (3.14) with the pressure difference. J_i^{tot} is the sum of the SD and GT fluxes, expressed by equations (3.10) and (3.13), respectively integrated over θ_i and p_i for a thickness t_{m}.

$$J_i^{\mathrm{tot}} = \frac{\epsilon}{\tau t_{\mathrm{m}}}\left[\rho_{\mathrm{Z}} q_{\mathrm{sat},i} D_{0,i}^{\mathrm{SD}} \exp\left(-\frac{E_{\mathrm{a},i}^{\mathrm{SD}}}{RT_{\mathrm{m}}}\right)\log\left(\frac{1-\theta_{\mathrm{p},i}}{1-\theta_{\mathrm{f},i}}\right)+ \frac{\lambda_{\mathrm{d},i}}{\beta}\sqrt{\frac{8RT_{\mathrm{m}}}{\pi M_i}}\frac{1}{RT_{\mathrm{m}}}\exp\left(-\frac{E_{\mathrm{a},i}^{\mathrm{GT}}}{RT_{\mathrm{m}}}\right)(p_{\mathrm{f},i}-p_{\mathrm{p},i})\right] \tag{3.14}$$

The H_2 permeance as a function of the membrane temperature is presented in the top plot of figure 3.5, with the input values displayed in table 3.3 and $M_{\mathrm{H_2}} = 2.016\,\mathrm{g\,mol^{-1}}$, $\epsilon = 0.52$, $\tau = 1$, $t_{\mathrm{m}} = 30\,\mu\mathrm{m}$, $\rho_{\mathrm{Z}} = 1760\,\mathrm{kg\,m^{-3}}$ and $\beta = 4$ (specific for MFI). In this plot, the contributions of the surface and gas-translational diffusions, dominant at low and high temperatures, are also shown. In the same figure, the bottom plot shows the variation of the surface occupancy with the temperature obtained from equations (3.11) and (3.12). Up to $\approx 95\,\mathrm{K}$, the surface occupation on the feed side is very high and the H_2 permeance increases with the temperature due to the increase in mobility (region A-B). A maximum in the permeance is eventually reached at point B, above which the increase in diffusion does not compensate the strong decrease of the amount of adsorbed gas and thus the permeance decreases (region B-C). At point C, a minimum in the permeance is eventually reached due to the increasing contribution of the gas-translational diffusion. At larger temperatures, GT is the dominant transport mechanism and hence the permeance increases (C-D and beyond). This description applies for only one gas species permeating the membrane, and for a gas mixture the Maxwell-Stefan diffusion theory, which takes into account the competition in permeation of the different molecules, is usually applied [136, 137].

Table 3.3: Input parameters used for the calculation of single-gas permeances for several gases. From the experimental data obtained with a MFI membrane reported in [81]. Due to the lack of experimental data, the values for D_2 are assumed to be the same as for H_2.

	H_2	D_2	He	N_2	Ar	CO_2
$q_{\mathrm{sat},i}$ $(\mathrm{mol\,kg^{-1}})$	5.4	5.4	0.0	5.4	5.1	5.0
$E_{\mathrm{a},i}^{\mathrm{SD}}$ $(\mathrm{kJ\,mol^{-1}})$	2.1	2.1	1.0	5.5	4.9	9.6
$-\Delta S_{\mathrm{ads},i}$ $(\mathrm{J\,mol^{-1}\,K^{-1}})$	43	43	0	50	49	58
$-\Delta H_{\mathrm{ads},i}$ $(\mathrm{kJ\,mol^{-1}})$	5.9	5.9	0.0	13.8	13.2	24.1
$D_{0,i}^{\mathrm{SD}}$ $(10^{-8}\,\mathrm{m^2\,s^{-1}})$	1.5	1.5	2.0	1.3	1.9	0.7
$\lambda_{\mathrm{d},i}$ $(10^{-9}\,\mathrm{m})$	0.9	0.9	0.9	0.8	1.1	0.9
$E_{\mathrm{a},i}^{\mathrm{GT}}$ $(\mathrm{kJ\,mol^{-1}})$	8.3	8.3	8.9	8.4	7.1	10.3

The plot of figure 3.6 compares the single-gas permeances of H_2, D_2, N_2, Ar, CO_2 and He for a defect-free MFI membrane as a function of the temperature. The input

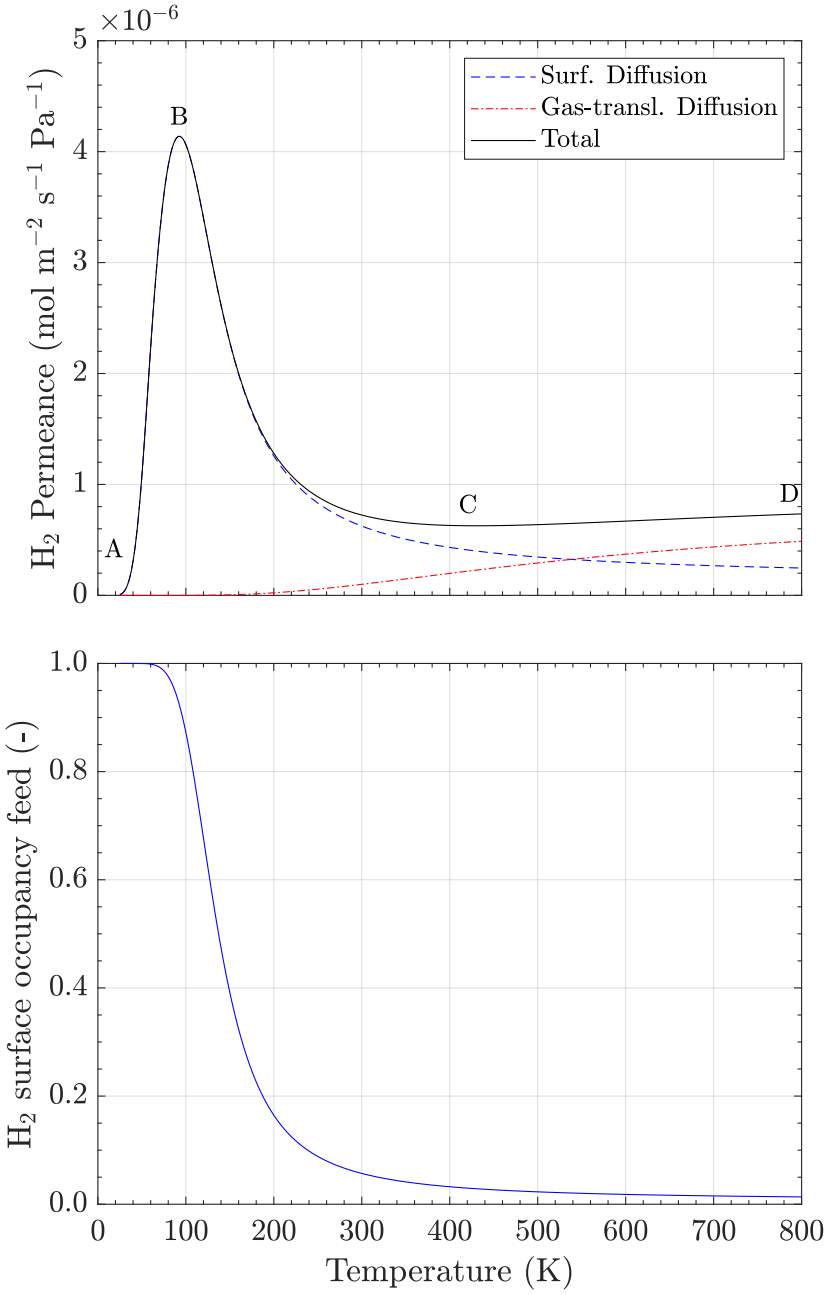

Figure 3.5: H_2 permeance and surface occupancy as a function of the temperature. Top: H_2 permance, bottom: H_2 surface occupancy. A-B: increase in permeance due to high surface occupancy (i.e., adsorption) and increase in activated thermal diffusion at low temperatures, B: maximum above which the diffusion cannot compensate the decrease of adsorption, and thus the overall flux through the membrane decreases with the temperature, C: a minimum in the flux is reached due to the increase of the importance of the gas-translational diffusion, C-D (and beyond): transport dominated by gas-translational diffusion, where the flux through the membrane increases with the temperature. The input data are presented in table 3.3, with $\epsilon = 0.52$, $\tau = 1$, $t_m = 30\,\mu m$ and $\rho_Z = 1760\,kg\,m^{-3}$.

parameters are presented in tables 3.2 (for the molar masses) and 3.3. Except for the molar masses, the input data for D_2 is the same as for H_2 since they have similar quadrupole moments and polarizabilities and hence similar ΔS_{ads} and ΔH_{ads} are expected[12]. The porosity ϵ, tortuosity τ, thickness t_{m} and density ρ_{Z} are the same as used in the plots of figure 3.5.

The different temperature profiles for the permeances are the result from the different adsorption and diffusion properties of the molecules and their different molar masses. H_2 and D_2 are the molecules with the highest permeance up to 140 K since they have the lowest $E_{\text{a},i}^{\text{SD}}$. However, since they have a smaller quadrupole moment than, for instance, N_2, a weaker interaction with the zeolite layer exists, which is reflected by the sharp maximum around 100 K. Moreover, it can be observed that the permeances for H_2 and D_2 overlap in the temperature region where surface-diffusion is dominant. Nevertheless, at temperatures beyond 400 K, where the transport is determined by gas-translational diffusion, the permeance of H_2 is larger due to its lower mass.

It is interesting to compare the curves of N_2 and CO_2. The quadrupole moment of CO_2 is higher (reflected by the higher ΔS_{ads} and ΔH_{ads} absolute values), but N_2 has much higher permeances (by one order of magnitude) in the temperature range where surface-diffusion is the dominant permeation mechanism. The reason for this is the smaller

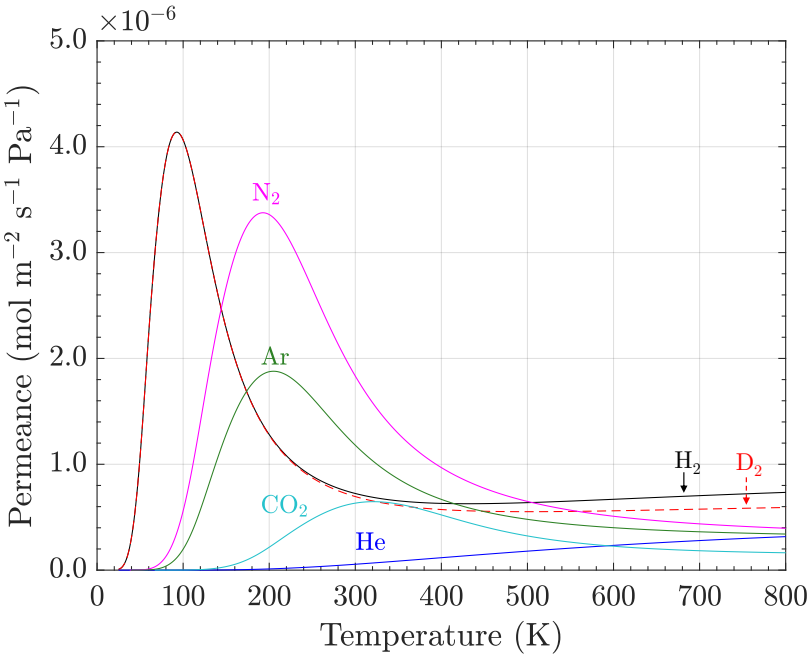

Figure 3.6: Permeance as a function of the temperature for H_2, D_2, N_2, Ar, CO_2 and He. Plot obtained considering a defect-free MFI zeolite membrane, using the input data presented in table 3.3, with $\epsilon = 0.52$, $\tau = 1$, $t_{\text{m}} = 30\,\mu\text{m}$ and $\rho_{\text{Z}} = 1760\,\text{kg}\,\text{m}^{-3}$.

[12]To the best knowledge of the author, there are no experimental results available for D_2 on MFI.

(roughly by a factor of 2) activation energy for surface-diffusion $E_{a,i}^{SD}$ for N_2. Moreover, it should be noted that while Ar shows a profile with a maximum in permeance for lower temperatures, He has no adsorbed phase. In fact, in the reference used for the input parameters, both entropy and enthalpy of adsorption are zero for helium and hence this gas only exhibits gas-translational diffusion.

3.3.2 Impact of defects in real membranes

The plots of figures 3.5 and 3.6 were obtained for defect-free membranes. However, as discussed in section 3.2.2, the synthesis of defect-free zeolite membranes is challenging and non-selective intercrystalline channels larger than the zeolitic channels are always present [132]. The transport through these defects can be viscous or Knudsen depending on their diameter [138].

Even at small concentrations, defects with few nm have an important impact on the overall transport through a zeolite membrane. To illustrate this, the contribution of Knudsen diffusion through defects in the total flux of H_2 was estimated for different diameters at 300 K. Following the approach presented in [139], the total flux J_{real} through a "real" zeolite layer is proposed to be a linear combination of the fluxes J_{zeo} and J_d through the zeolitic and non-zeolitic channels, calculated respectively with equations (3.14) and (3.8). The fractional area occupied by the defects $\xi_{A,d}$ is given by equation (3.15), where ξ_d is the concentration of defects with diameter d_d and $1 - \xi_d$ is the concentration of zeolite channels with diameter d_{zeo}. Therefore, the total flux J_{real} is calculated by equation (3.16).

$$\xi_{A,d} = \frac{\xi_d \pi d_d^2}{\xi_d \pi d_d^2 + (1 - \xi_d)\pi d_{zeo}^2} \tag{3.15}$$

$$J_{real} = (1 - \xi_{A,d}) J_{zeo} + \xi_{A,d} J_d \tag{3.16}$$

The top plot of figure 3.7 presents the contribution of the Knudsen flux in % of the total H_2 flux through a MFI membrane up to 10^4 ppm of defects with different diameters. The plot shows the strong impact of the defects concentration and diameters on the Knudsen contribution. For a MFI layer containing 10^2 ppm of defects with a diameter of 3.0 nm, equivalent to only 0.3 % of the total permeation area, the Knudsen contribution for the whole transport is around 5 %. The H_2/He selectivity, given by the ratio of permeances, is presented in the bottom plot of figure 3.7 as a function of the defects concentration. For 3.0 nm, the selectivity drops from $\approx$ 13 to $\approx$ 3.5 when the concentration of defects increases to 10^4 ppm. A larger concentration of defects would decrease further the selectivity down to the Knudsen selectivity $\approx$ 1.41. Therefore, the selectivity of a MFI membrane can be a good indicator of its synthesis quality. Permeation experiments with H_2 and He through MFI membranes were carried out along this work allowing such assessment.

The contribution of the Knudsen transport is highly dependent on the type of zeolite

framework. For NaA membranes, with $d_{zeo} = 0.41\,nm$, the contribution to the overall flow is 8 % for 10^2 ppm of defects with a diameter of 3.0 nm. For SOD membranes, with $d_{zeo} = 0.27\,nm$, the Knudsen contribution increases to 18 %. The Knudsen contribution to the overall transport also depends on the nature of the gas. Weakly adsorbing gases such as helium do not exhibit preferential interaction with the zeolite pores and thus a considerable amount of its permeation will be done through the larger non-zeolitic pores.

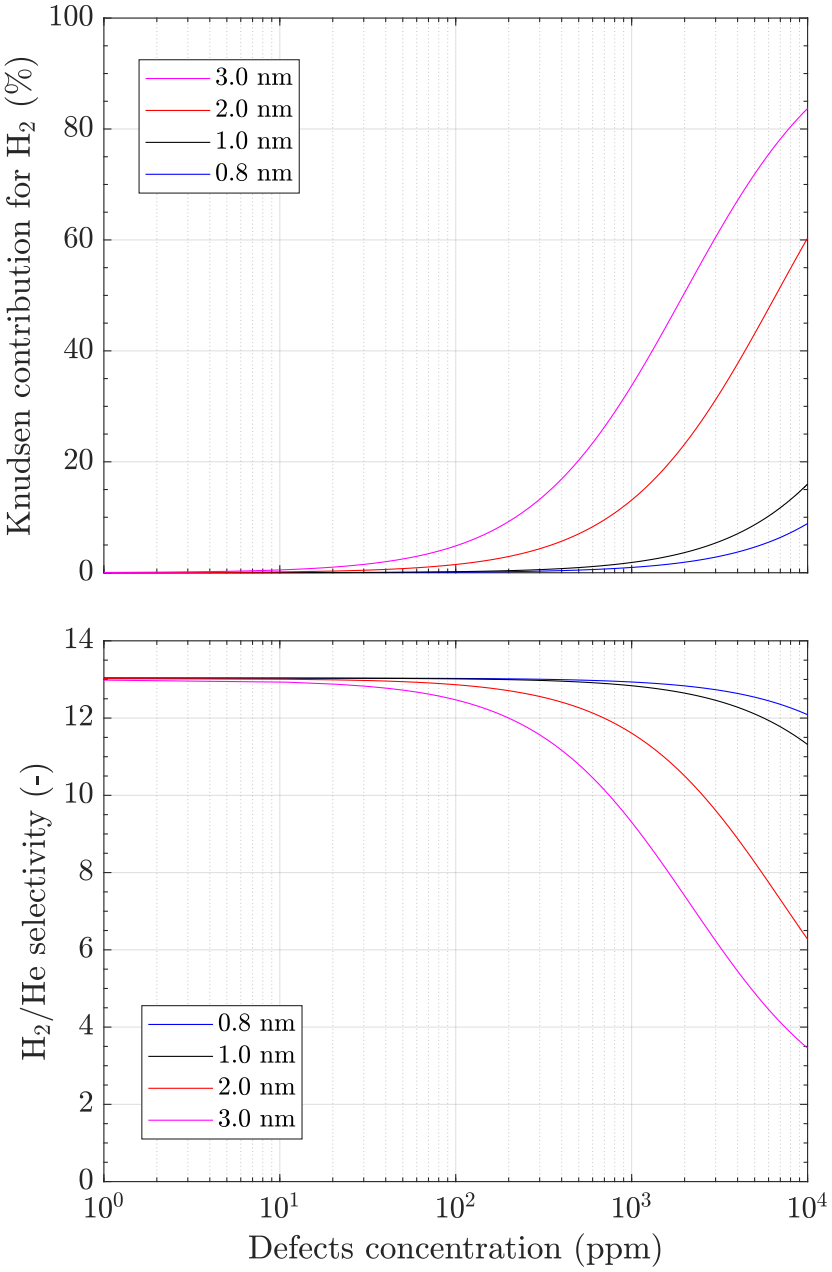

Figure 3.7: Contribution of the Knudsen flux to the total H_2 flux and H_2/He selectivity as a function of the defects concentration for a MFI membrane. Top: contribution of the Knudsen flux in %, bottom: H_2/He selectivity. The plots are presented for different pore diameters at 300 K. The input data is given in tables 3.2 and 3.3.

Experimental evidence of this phenomenon is reported in [131].

3.4 Summary

The main parameters of interest to experimentally characterise the separation performance of membranes are the gas permeance, selectivity and separation factor. These quantities are highly dependent on the gas mixture feeding the membrane, the operation conditions (e.g., temperature) and the physical structure of the membrane, which determines the mass-transport through it. Due to their molecular-sized pore diameters $< 1\,\text{nm}$ and uniform pore size distribution, zeolite membranes are studied for gas separation applications. Thin layers of zeolites ($\sim$ µm) are usually synthesized on the surface of thicker ceramic supports ($\sim$ mm) to ensure high permeances. The mass-transport and separation mechanisms of the zeolite membranes are based on differences in adsorption and diffusion properties of the permeating molecules. At low temperatures adsorption is dominant and surface-diffusion is the main permeation mechanism. At high temperatures the adsorbed phase is negligible and the molecules diffuse retaining their gaseous character. Nevertheless, Knudsen diffusion through non-zeolitic, intercrystalline defects is also present. Their presence at the ppm range has a great impact on the separation of the membrane. The larger is the number of defects in the zeolite layer, the larger is the Knudsen contribution to the transport hence decreasing the selectivity.

Chapter 4

Permeation experiments through two MFI membranes without tritium

4.1 Characteristics of the zeolite membranes used for the experiments

The experimental results presented in this thesis were obtained with MFI-ZSM-5 zeolite membranes supplied from the Fraunhofer Institute for Ceramic Technologies and Systems (IKTS[1]). These membranes are synthesized using the secondary-growth technique where zeolite crystals are grown on the inner surface of a cylindrical ceramic support (e.g., α-Al_2O_3, TiO_2) with: length = 250 mm, inner/outer diameter = 7/10 mm. A schematic diagram of the geometry is presented in figure 4.1. Typical thicknesses of the zeolite layers manufactured by IKTS are on the order of $1 - 100\,\mu m$ [140, 141].

Permeation experiments with He, H_2, D_2 and H_2-HD-D_2 were performed at the HyDe loop facility with two MFI-ZSM-5 membranes A and B. Figure 4.2 presents Scanning Electron Microscope (SEM) pictures of membrane A, in which the thin zeolite layer can be clearly distinguished from the thick porous ceramic support. Figure 4.2c) shows the zeolite crystals used for the synthesis of the layer (i.e., inner surface of the tube). Similar

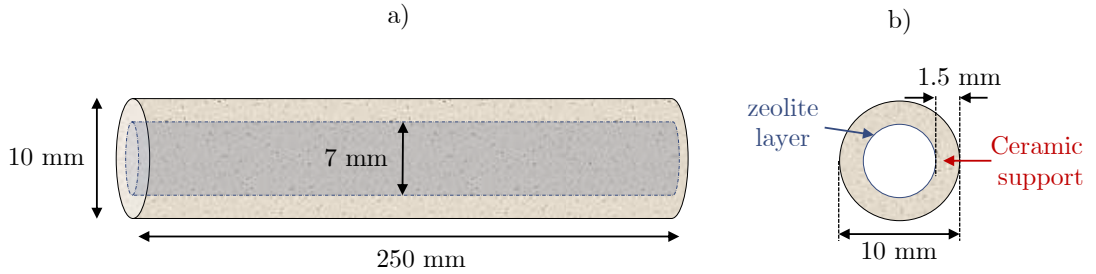

Figure 4.1: Schematic diagram of the tubular membranes used in the experiments. a) lateral view, b) front view.

[1]From the German, "Institut für Keramische Technologien und Systeme".

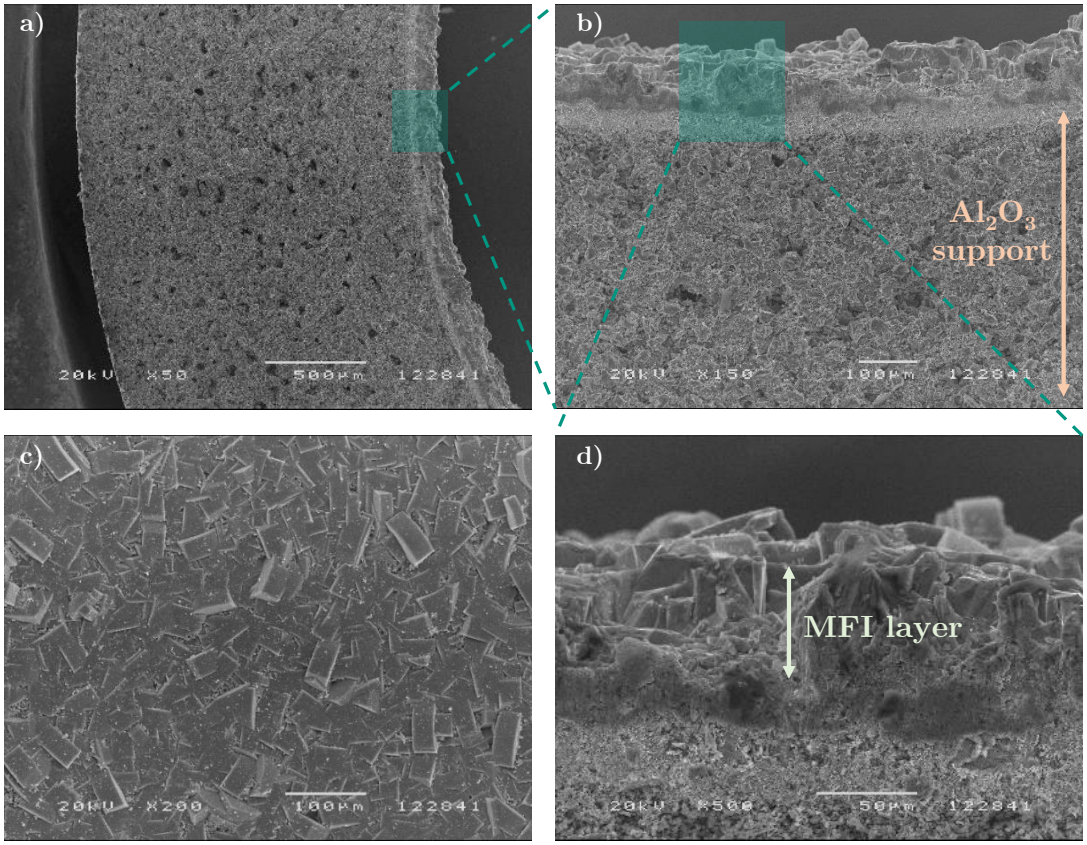

Figure 4.2: Scanning Electron Microscope pictures of membrane A. a) cross-section of the membrane, b) close-up of MFI zeolite layer with α-Al_2O_3 support, c) zeolite crystals on the inner surface, d) close-up of MFI zeolite layer.

micrographs were obtained for membrane B[2]. Nevertheless, the thicknesses of the zeolite layers were found to be different: $t_{m,A} = 67.3 \pm 1.3\,\mu m$ and $t_{m,B} = 55.3 \pm 1.2\,\mu m$. Consequently, it is expected that, for the same gas and temperature, the permeances obtained for membrane A are lower than those obtained for membrane B.

4.2 Procedure for the permeation experiments at the HyDe loop facility

4.2.1 The HyDe loop facility

The HyDe (Hydrogen Deuterium) loop facility was originally assembled at the TLK to prepare gas mixtures with different concentrations of H_2, HD and D_2 for the calibration of different analytical devices (gas chromatography, laser raman spectroscopy) [142]. The setup is presented in the top of figure 4.3 and the pipe and instrumentation diagram (P&ID) is shown in Appendix B.1. The gas supply used for the HyDe loop, the instru-

[2]For each membrane, post-experiment SEM pictures were taken from three sections (both ends and middle) and no differences were found in the thickness of the layer, which also demonstrates the homogeneity of the samples.

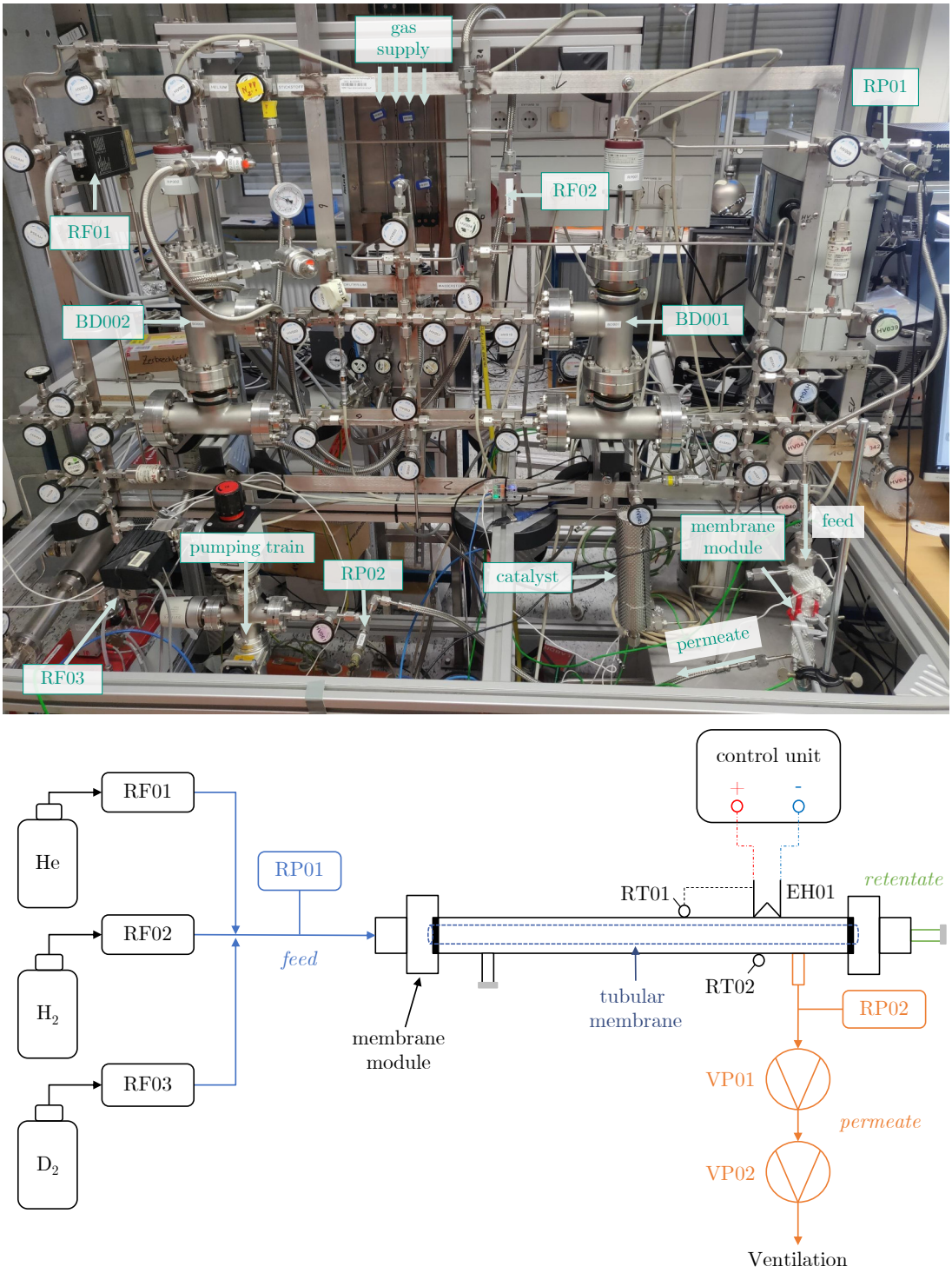

Figure 4.3: HyDe loop facility. Top: photograph of the setup, bottom: schematic diagram with all components used for the permeation experiments. BD: vessel, RF: mass-flow controller, RP: pressure sensor, RT: temperature sensor (thermocouple), EH: electrical heater, VP: vacuum pump.

mentation available (i.e., mass-flow controllers, pressure sensors, thermocouples, vacuum pumps), and the flexibility of the facility allow performing permeation experiments with membranes with minimum efforts for extension. The membrane was accommodated inside a stainless steel module using two EPDM rubber O-rings on the both ends of the

tube. The feed side of the module was connected to the gas supply manifold, and the permeate side was connected to the pumping train. Two additional pressure sensors were installed in the feed (RP01) and permeate (RP02) lines. The schematic diagram of the setup with all the instrumentation used for the permeation experiments is displayed in the bottom of figure 4.3.

4.2.2 Procedure and typical run

The permeation experiments are carried out with the retentate closed and therefore all the feeding gas permeates through the membrane. The driving force for permeation is ensured by the diaphragm-type pump VP02[3] which continuously evacuates the permeate side. With a constant feed/permeate flow $F_{\mathrm{f},i}$, set with a dedicated mass-flow controller (RF01 for He, RF02 for H_2, RF03 for D_2), a pressure difference is established across the membrane. At equilibrium, the feed and permeate pressures, respectively measured with RP01 and RP02, are used to calculated the permeance Π_i expressed by (3.2 revisited). The membrane surface area A_{m} is given by equation (4.1) and it was determined using a ruler for the length (accuracy $\pm 0.5\,\mathrm{mm}$) and a Vernier scale for the inner diameter (accuracy $\pm 0.005\,\mathrm{mm}$)[4].

$$\Pi_i = \frac{F_{\mathrm{f},i}}{A_{\mathrm{m}}(p_{\mathrm{f},i} - p_{\mathrm{p},i})} \qquad \text{(3.2 revisited)}$$

$$A_{\mathrm{m}} = (484 \pm 1) \times 10^{-5}\,\mathrm{m}^2 \qquad (4.1)$$

The temperature of the membrane is set with a control unit associated to a heating wire (EH01) evenly wrapped around the module to ensure uniform heating using glass-fiber as thermal insulator. Two thermocouples are placed on the module surface for control (RT01) and measurement (RT02). The instrumentation list and further information related to the measuring principle of each device and errors are presented in Appendix B.1.

The experimental conditions of the entire experimental program are summarised in table 4.1. Different feed flows were used to investigate the linearity with the pressure difference at 298 K to investigate the presence of large diameter defects. Moreover, permeation experiments with H_2, D_2 and catalysed mixtures of H_2-HD-D_2 were carried out to study the isotopic effects on the permeance. The experiments were performed at different temperatures to investigate the mass-transport mechanisms for permeation. The results presented in the following sections are partly published in a recent publication [144].

An example of a typical plot obtained for the permeation of H_2 at $100\,\mathrm{mL\,min^{-1}}$ at different membrane temperatures is given in figure 4.4. This plot shows the raw values of

[3] VP01 is a turbo-molecular pump which is used only for the evacuation of the setup.

[4] Considering a length of 250 mm and an inner diameter of 7 mm, the expected surface area is around $550 \times 10^{-5}\,\mathrm{m}^2$. However, the membranes manufactured by Fraunhofer have 15 mm-long glass sealing on both sides, which decreases the effective permeation length to 220 mm [143].

Table 4.1: Experimental conditions of flows, pressures and temperatures for the permeation experiments at the HyDe loop. Flows given at standard conditions of temperature and pressure.

Measuring device	Value
RF01 / RF02 / RF03 ($F_{\mathrm{f},i}$)	10 - 100 mL min^{-1}
RP01 ($p_{\mathrm{f},i}$)	$<$ 1100 hPa
RP02 ($p_{\mathrm{p},i}$)	$<$ 30 hPa
RT01/RT02 (T_{m})	298 - 410 K

pressures measured with RP01 (feed) and RP02 (permeate). While the permeate pressure slightly increases with the membrane temperature (variation $\approx$ 2 hPa), the feed pressure varies significantly. These variations are due to the non-linear changes in permeance when the membrane temperature is changed, as a result of the interplay between surface and gas-translational diffusion. For each temperature, the permeance is determined using the average of flows and pressures at steady-state (typically reached within few minutes).

All the experimental results presented in the following sections are supported by the values presented in Appendix D. In addition, the calculation of the uncertainties for each data point follows the recommendations presented in the "EA-4/02 M: 2013" document, as detailed in Appendix C.

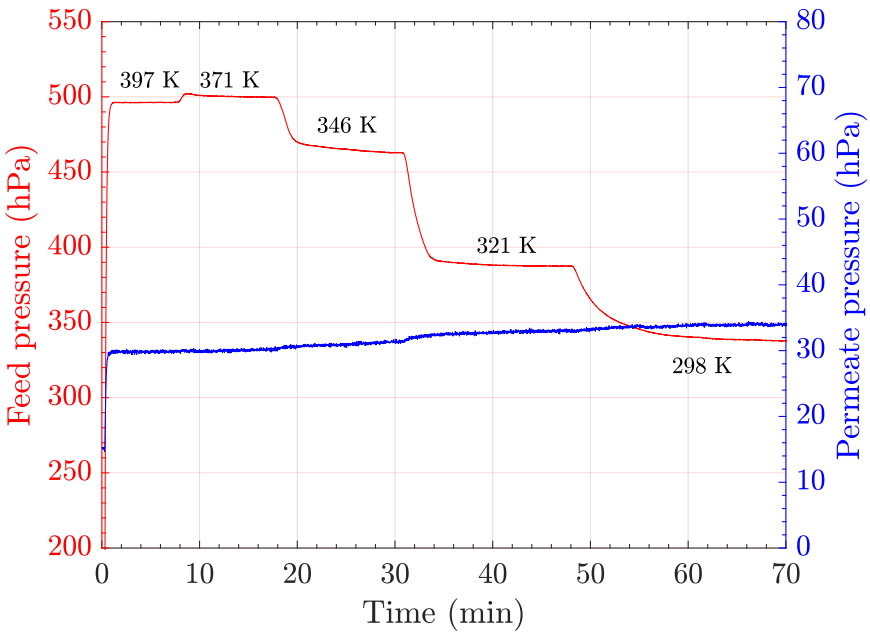

Figure 4.4: Typical measurement run obtained for 100 mL min^{-1} of H_2 as feed flow in the temperature range of 298 – 397 K. In red and left y-axis: feed pressure (RP01), in blue and right y-axis: permeate pressure (RP02).

4.3 Investigation of the presence of large diameter defects in the zeolite layer

The presence of large diameter defects in the zeolite layer was investigated with permeation experiments with different feed flows at 298 K. For large diameter defects (on the order of 10^2 nm), in which the mean free path of the molecules is lower than the defects diameter, the transport is viscous and the permeance is dependent on the applied pressures (equation (3.6)), implying that the feed flow and the pressure difference do not follow a linear relation. The plot of figure 4.5 presents the results obtained for membrane A, for a feed flow between $7.44 - 74.4\,\text{in}\,10^{-6}\,\text{mol}\,\text{s}^{-1}$ (or $10 - 100\,\text{mL}\,\text{min}^{-1}$ at STP). The linear fitting obtained for the plotted data demonstrates the high-degree of correlation between the two quantities and the same conclusions can be drawn for membrane B, whose plot is presented in Appendix D. Therefore, the zeolite layers of membranes A and B are considered to be deprived of large-diameter defects.

4.4 Single-gas permeances for different membrane temperatures

In the plot of figure 4.6, the single-gas permeances of He, H_2 and D_2 obtained for both membranes A (solid symbols) and B (empty symbols) are presented as a function of the membrane temperature. The calculated uncertainties are below 4 % relative.

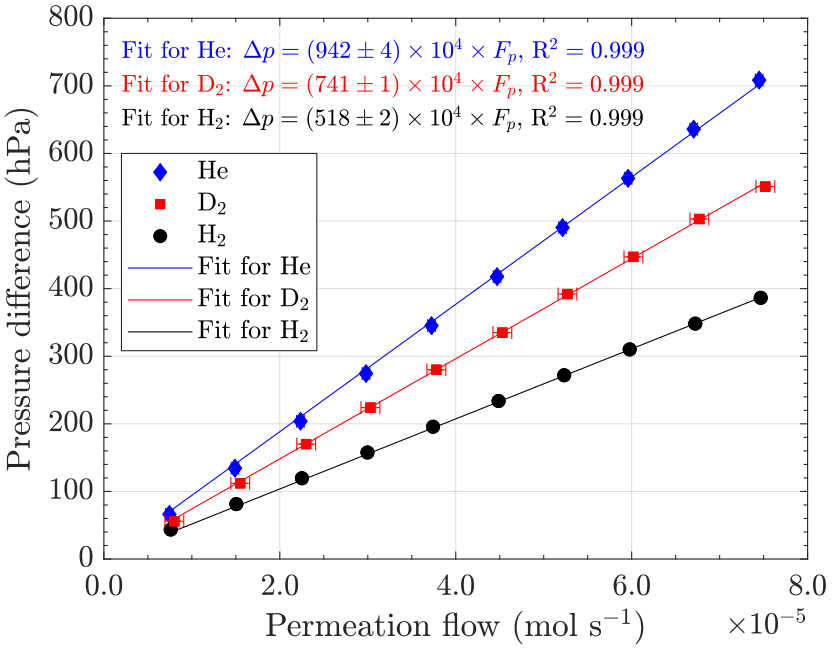

Figure 4.5: Linearity between the imposed flow and the measured pressure difference across membrane A. He: blue diamonds, H_2: black circles, D_2: red squares. Obtained at 298 K. The solid lines are linear fits for the corresponding data.

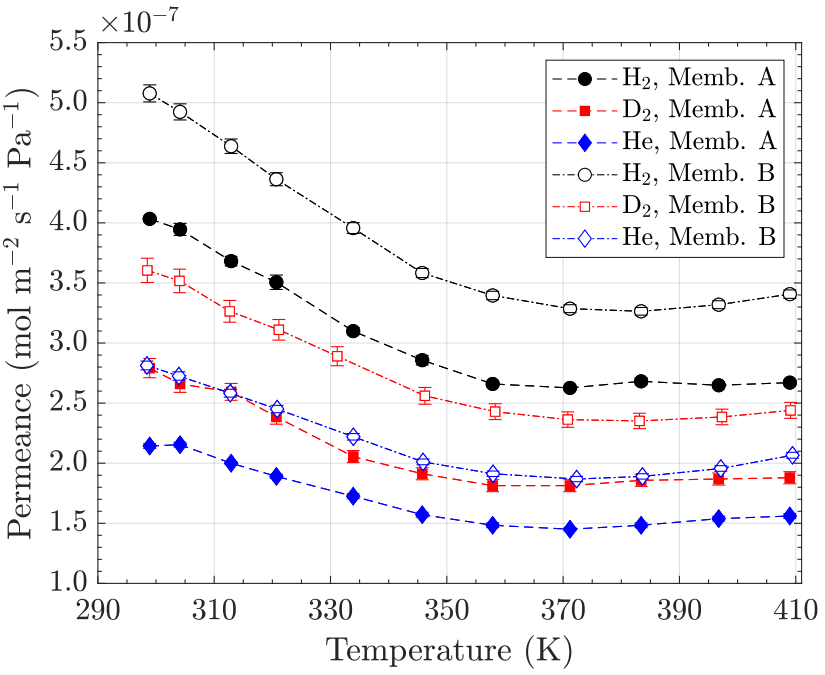

Figure 4.6: Experimental single-gas permeances as a function of the membrane temperature for He, H_2 and D_2. He: blue diamond, H_2: black circles, D_2: red squares. Solid symbols for membrane A and empty symbols for membrane B. The dashed and dot-dashed lines are shown to guide the eye.

The permeances obtained with membrane A are lower than those obtained with membrane B for all gases. The average of the ratio between the permeances calculated for each gas and for all temperatures is 1.28 ± 0.03. Consequently, membrane A is expected to be thicker by a factor of 28 %, which is consistent with the ratio of the thicknesses estimated using the SEM pictures: 1.22 ± 0.04.

For both membranes and for the whole temperature range, H_2 has the highest permeance since it is the lightest molecule. However, despite He and D_2 have similar masses (differing by 0.6 %), the deuterium permeance is higher for for all temperatures. This difference is attributed to the physical properties of the molecules: H_2 and D_2 possess a non-zero quadrupole moment, while He is non-polar. Moreover, the polarizabilities of H_2 and D_2 ($\approx 0.9 \times 10^{-40}\,C^2\,m^2\,J^{-1}$) are higher than the polarizability of He ($\approx 0.2 \times 10^{-40}\,C^2\,m^2\,J^{-1}$). Hence, D_2 is more strongly adsorbed than He and the surface-diffusion component of the permeance is higher.

For the three gases a continuous decrease of the permeance with the temperature can be observed until ≈ 360 K for membrane A and ≈ 384 K for membrane B, where a minimum is reached. The minima in the H_2 and D_2 permeances are attributed to a transition in the transport mechanism from surface-diffusion (dominant at low temperatures) to gas-translational diffusion (dominant at high temperatures). These temperatures are similar to those predicted by the theoretical calculations displayed in figure 4.7 for a defect-free membrane with a thickness of 67 µm (equation (3.14)). The transition temperatures

for H_2 are also consistent with the experimental results obtained by other authors and summarised in table 4.2. The two membranes with the highest transition temperatures ($> 650\,K$) have an exceptionally low Si/Al ratio (around 10), yielding strong adsorption sites and therefore surface-diffusion is the dominant transport mechanism for a wider range of temperatures [62, 145].

For helium, the theoretical calculations predict no minimum in the permeance since, according to the data reported in [81], the surface-diffusion contribution is zero. However, consistently with the results given in figure 4.6, other authors have also observed a minimum for the helium permeance [146, 147]. This minimum is attributed to a combination of (i) Knudsen flux through non-zeolitic channels (i.e., defects) and surface-diffusion through zeolitic channels at lower temperatures and (ii) gas-translational diffusion at higher temperatures. In fact, although helium is a non-polar molecule, a slight interaction with the zeolite matrix is expected due to its non-zero polarizability and it has been proposed that the adsorption process is described by Henry's law (instead of Langmuir's).

Overall, a good agreement between the order of magnitude of the experimental permeances presented in figure 4.6 and the values predicted theoretically in figure 4.7 can be observed within the range of temperature tested. However, the helium permeances calculated theoretically are at least one order of magnitude lower due to the Knudsen and surface-diffusion contributions in the experimental permeances (not considered in the model). Consequently, the experimental selectivities for H_2/He and D_2/He, calculated by

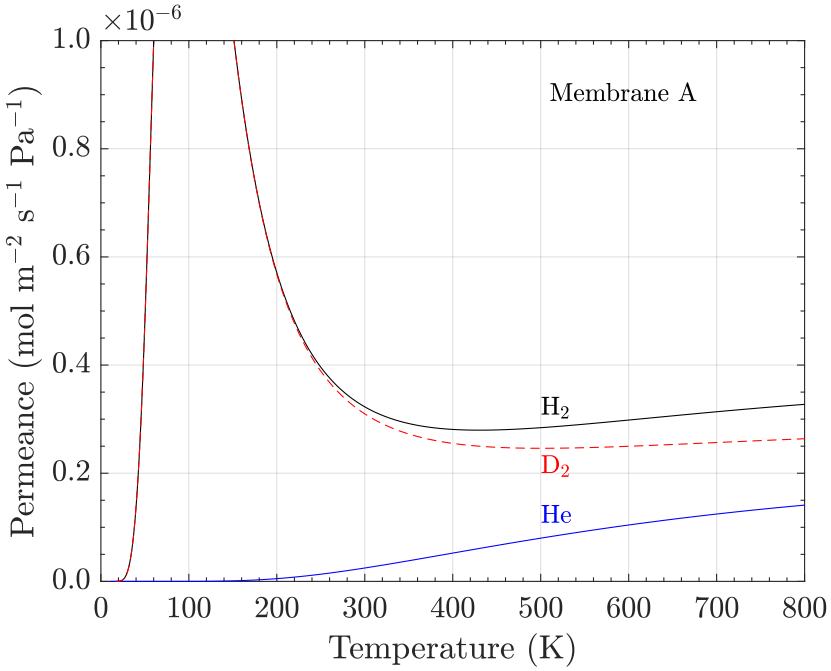

Figure 4.7: Calculated single-gas permeances as a function of the membrane temperature for He, H_2 and D_2. Plot obtained for membrane A ($t_m = 67\,\mu m$ given as input). The input parameters are given in table 3.3, with $\epsilon = 0.52$, $\tau = 1$, and $\rho_Z = 1760\,kg\,m^{-3}$.

Table 4.2: Summary of the data available in the literature concerning H_2 and He permeances obtained with MFI zeolite-type membranes. Silicalite-1 is the pure siliceous form of ZSM-5 (i.e., $Si/Al = \infty$).

Active layer	Thickness (µm)	Temperature for minimum in Π_{H_2} (K)	Π_{H_2} at 300 K (10^{-7} mol m^{-2} s^{-1} Pa^{-1})	Π_{He} at 300 K (10^{-7} mol m^{-2} s^{-1} Pa^{-1})	Π_{H_2}/Π_{He} (-)	Ref.
Silicalite-1	5	350	34	-	-	[148]
Silicalite-1	$30-50$	310	2.5	0.8	3.12	[81]
ZSM-5	-	< 300	18	-	-	[149]
ZSM-5	-	375	36	-	-	[149]
Silicalite-1	0.550	-	215.5 ± 8.8	83.2 ± 6.4	2.59 ± 0.23	[150]
ZSM-5	0.550	-	156.8 ± 14.7	58.2 ± 3.8	2.69 ± 0.31	[150]
ZSM-5	1	> 650	11.0	4.7	2.34	[62]
ZSM-5	30	> 723	0.8	-	-	[145]
ZSM-5 (A)	67.3 ± 1.3	360	4.03 ± 0.06	2.14 ± 0.02	1.88 ± 0.03	this work
ZSM-5 (B)	55.3 ± 1.2	384	5.07 ± 0.07	2.80 ± 0.03	1.81 ± 0.03	this work

the ratio of the permeances, are considerably lower as discussed in the following section.

4.5 Selectivities for H_2/He and D_2/He

The selectivities for H_2/He and D_2/He, obtained by the ratio of the permeances, are plotted in figure 4.8 for both membranes. The values for H_2/He are in the range $1.85-1.70$ and $1.30-1.20$ for D_2/He (relative uncertainties below 4 %). These values are larger than the expected ratio of Knudsen-dominated selectivities (1.41 for H_2/He and 0.99 for D_2/He, as calculated by the inverse of the square root of the mass ratio). Therefore, the zeolite layers of membranes A and B should have a low defect concentration and the surface-diffusion (through zeolitic channels) is important in the separation of the two species. Moreover, the consistency between both membranes demonstrates that their synthesis quality is similar.

The H_2/He selectivities obtained in this thesis have the same order of magnitude as the values reported by other authors (table 4.2), but are lower by a factor of 20 %. These differences may be attributed to the different Si/Al ratios of the MFI layers (above 15, according to table 3.1) leading to different contributions of the surface-diffusion to the transport. Moreover, differences in the concentration of defects (non-zeolitic channels)

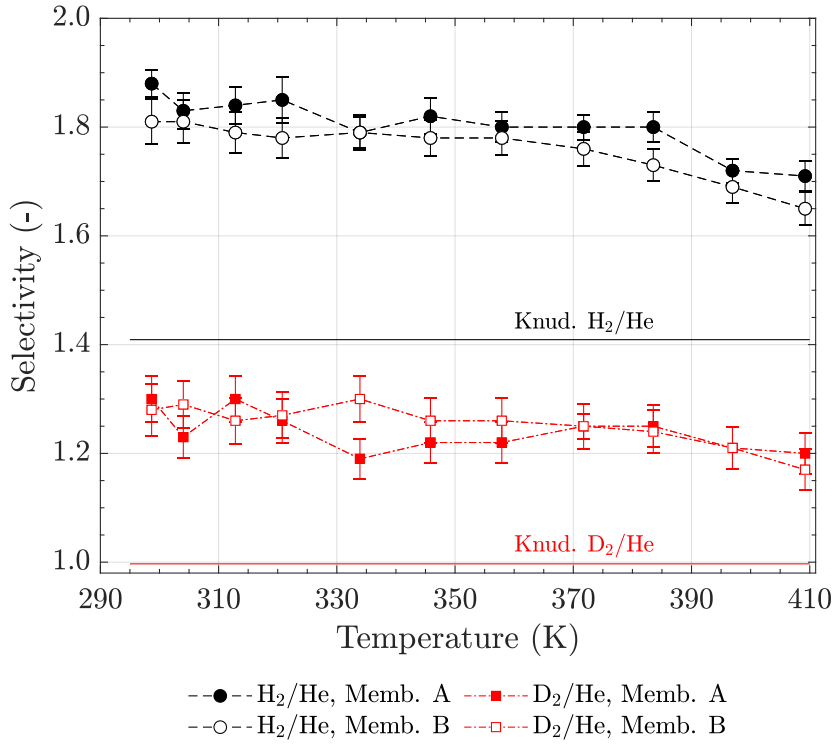

Figure 4.8: H_2/He and D_2/He selectivity as a function of the membrane temperature. Black circles: H_2/He selectivity, red squares: D_2/He selectivity. Solid symbols for membrane A and empty symbols for membrane B. The dashed and dot-dashed lines are shown to guide the eye.

have also a strong impact on the selectivity. For instance, the H_2/He selectivity obtained from the permeances displayed in figure 4.7 would be around 13 at 298 K for a defect-free membrane. However, due to the unavoidable presence of defects in the zeolite layers of real membranes, the reported values in the literature are lower than 4. Furthermore, the H_2/He and D_2/He selectivities exhibit a decrease for high membrane temperatures. This behaviour is also reported in [62] for H_2 and it is attributed to the lesser role of the adsorption in the transport when the temperature increases. No data for D_2/He has been found in the literature but the consistent results obtained with membranes A and B support the existence of an important contribution of surface-diffusion to the selectivity of D_2/He.

4.6 Isotopic effects on the permeance and extrapolation towards tritiated species

4.6.1 Selectivity for H_2/D_2

The ratio between the H_2 and D_2 permeances is plotted as a function of the temperature for membranes A and B in figure 4.9. There is no measurable dependency with the temperature in the range tested and the average values for membranes A and B are 1.46 ± 0.04 and 1.40 ± 0.05, respectively. These values are larger than the ratio between the H_2 and D_2 permeances presented in figure 4.7 for a defect-free MFI layer (between 1.0

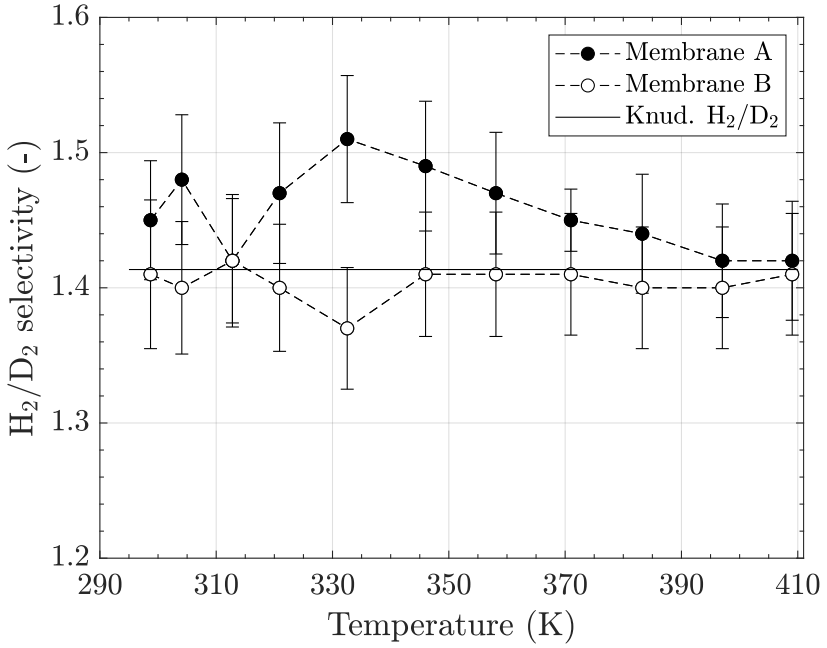

Figure 4.9: H_2/D_2 selectivity as a function of the membrane temperature. Solid symbols for membrane A and empty symbols for membrane B. The dashed lines are shown to guide the eye.

Table 4.3: Comparison of typical Si/Al ratios and pore sizes for FAU, SOD and ZSM-5 frameworks with H_2/D_2 selectivities. The Si/Al values presented are from table 3.1. All selectivity values were obtained at 298 K.

Zeolite	Typical Si/Al ratio	Pore diameters (nm)	H_2/D_2 selectivity (-)	Ref.
SOD	1.0	0.27	0.9	[151]
FAU	2.5	0.74	0.9	[151]
ZSM-5 (A)	> 15	0.55	1.46 ± 0.04	this work
ZSM-5 (B)	> 15	0.55	1.40 ± 0.05	this work

and 1.1 in the same temperature range). Because H_2 and D_2 exhibit similar adsorption properties, the differences in the experimental permeances cannot be explained by the transport through zeolitic channels. Instead, since the Knudsen selectivity for H_2/D_2 is close to 1.41 (given by the inverse of the square root of the masses), these results suggest that the isotopic effects in MFI layers are determined by the transport through defects, always present in real membranes.

It is interesting to compare these results with those reported in [151], where the selectivity for H_2/D_2 was measured with other zeolite frameworks at around 298 K (given in table 4.3). Lower H_2/D_2 selectivities (around 0.9) were measured for the FAU and SOD zeolites, which implies that ZSM-5 is selective for H_2 whereas SOD and FAU are slightly selective for D_2. These differences are not explained by the pore diameters, since $d_p\,(\text{SOD}) < d_p\,(\text{ZSM-5}) < d_p\,(\text{FAU})$ and the selectivities for SOD and FAU are similar. However, SOD and FAU are zeolite frameworks known for their high polarity (i.e., low-to-intermediate Si/Al values) and ZSM-5 is typically a high-silica material[5] [88]. Thus, with a selectivity close to 1, these results suggest that, in contrast to ZSM-5, the transport of H_2 and D_2 is mainly through the zeolitic channels of SOD and FAU, evidencing the similar adsorption properties of H_2 and D_2.

4.6.2 Measurement of global permeances of H_2/D_2 and H_2/He mixtures

The single-gas permeances obtained with H_2 and D_2 suggest that the transport through real ZSM-5 membranes is governed by the mass of the permeating hydrogen isotopologue due to the presence of defects. However, further experiments are required to investigate whether this effect extends to all Q_2. Therefore, the global permeance of the H_2/D_2 feeding mixture was measured in the whole concentration range of H_2 in D_2, equivalent to $M_{\text{eff}} \approx 2 - 4\,\text{g mol}^{-1}$, where M_{eff} is the effective mass of the permeating mixture determined by the

[5]The Si/Al ratio was not provided by the manufacturers of the ZSM-5 membranes tested in this thesis.

weighted average of the molar concentrations x of each species according to equation (4.2). These experiments allow the determination of a function for the permeance $\Pi(M_{\text{eff}})$, which could be used to estimate the permeances of the remaining isotopologues HD, HT, DT and T_2. The single-gas experiments suggest that a dependency of the type $\Pi \propto M_{\text{eff}}^{-0.5}$ should be expected. For comparison, the global permeance of H_2/He was also evaluated for $H_2/He = 0 - 100\,\text{mol}\%$. Since these species have different adsorption properties, the permeance is rather determined by surface-diffusion than by M_{eff} and thus it is expected that $\Pi \propto M_{\text{eff}}^{b}$ with $b < -0.5$.

$$M_{\text{eff}} = x_{H_2} M_{H_2} + x_{D_2} M_{D_2} \tag{4.2}$$

In these experiments the two gases species are sent simultaneously into the membrane. The molar concentration of each species is determined by the ratio of the feed flows F_f set with the mass-flow controllers, according to equation (4.3). The experiments were carried out at $298 - 398\,\text{K}$ with a total feed flow of $100\,\text{mL}\,\text{min}^{-1}$ at STP.

$$x_i = \frac{F_{f,i}}{F_{f,i} + F_{f,j}} \tag{4.3}$$

The permeances obtained for H_2/D_2 are plotted in figure 4.10 for membrane A as a function of the effective molar mass. For each temperature, the data points were fitted

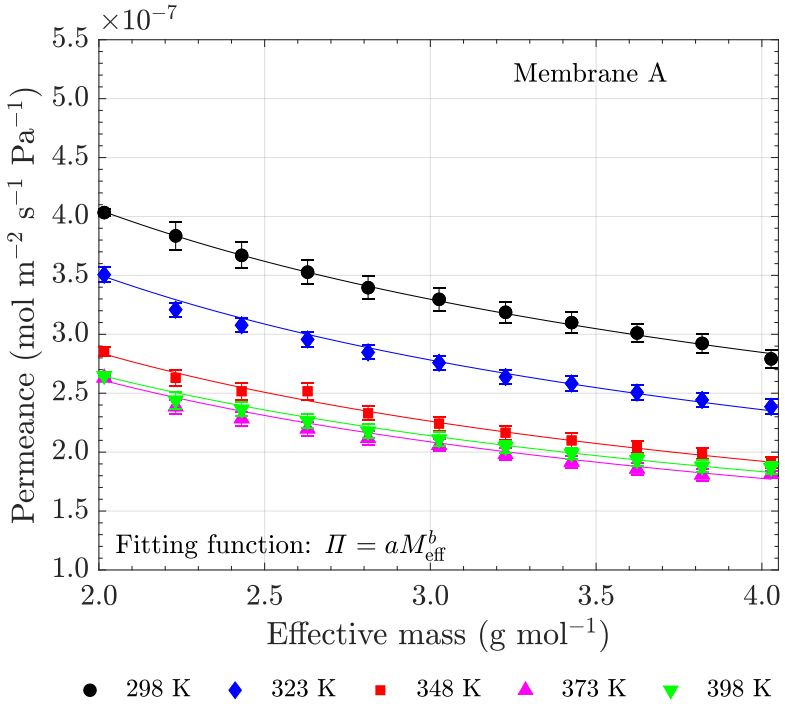

Figure 4.10: Permeance of the H_2/D_2 mixture as a function of M_{eff} for different membrane temperatures. Plot obtained for membrane A. The solid lines present the fits using an allometric function and the fitting parameters are given in table 4.4.

Table 4.4: Parameters obtained in the fitting of the permeances of H_2/D_2 as a function of M_{eff} for membranes A and B. The corresponding plot is presented in figure 4.10. Units: $[a] = 10^{-9}\,\mathrm{mol\,m^{-2}\,s^{-1}\,Pa^{-1}}$, b is dimensionless.

			Membrane A		
	298 K	323 K	348 K	373 K	398 K
a	578 ± 2	474 ± 5	521 ± 4	386 ± 6	385 ± 4
b	-0.511 ± 0.005	-0.571 ± 0.011	-0.565 ± 0.011	-0.559 ± 0.018	-0.534 ± 0.013
R^2	0.999	0.997	0.996	0.991	0.995
			Membrane B		
	298 K	323 K	348 K	373 K	398 K
a	732 ± 6	618 ± 2	505 ± 3	467 ± 3	466 ± 1
b	-0.522 ± 0.008	-0.499 ± 0.004	-0.491 ± 0.006	-0.500 ± 0.005	-0.488 ± 0.002
R^2	0.998	0.999	0.999	0.999	0.999

with an allometric function to obtain an expression of the type $\Pi = aM_{\mathrm{eff}}^{b}$ and the fitting parameters a and b are given in table 4.4. The ranges of values for the exponent $(-b)$ are $0.511 - 0.571$ for membrane A and $0.488 - 0.522$ for membrane B (plot displayed in figure D.3 in Appendix D). The exponents are close to -0.5 and rather independent of the temperature, confirming the hypothesis formulated above that the permeance for Q_2 is mainly governed by the square-root of the mass of the permeating gas. Since no measurable competition in the permeation of H_2 and D_2 is observed, it can be concluded that the permeating mixture behaves macroscopically as one hydrogen isotopologue gas with an effective mass determined by the molar concentrations of the molecules (equation (4.2)). In contrast, the exponents $(-b)$ for the permeance of H_2/He are: $0.919 - 0.808$ for membrane A and $0.865 - 0.758$ for membrane B (table D.13 in Appendix D). The permeance plots for H_2/He are given in figure D.2 for membrane A and figure D.3 for membrane B (Appendix D).

The fitting functions obtained for the H_2/D_2 are of major importance as they provide a simple extrapolation for all hydrogen isotopologues presented in the following section.

4.6.3 Extrapolation of the Q_2 permances and Q_2/He selectivities

The dependency obtained for the permeance of H_2/D_2 as a function of the effective molar mass presented in the previous section was used to extrapolate the permeances of the remaining isotopologues: HD ($3.022\,\mathrm{g\,mol^{-1}}$), HT ($4.024\,\mathrm{g\,mol^{-1}}$), DT ($5.030\,\mathrm{g\,mol^{-1}}$), T_2 ($6.032\,\mathrm{g\,mol^{-1}}$). This extrapolation is a key result to estimate the Q_2/He selectivities and thus evaluate the ability of the membrane to separate the different hydrogen isotopologues from helium.

The top plot of figure 4.11 depicts the extrapolated permeances for HD, HT, DT and T_2 as a function of the molar mass using the fitting functions (4.4) and (4.5) obtained for

membranes A and B at 298 K. This plot illustrates that the permeance of T_2 is reduced by 40 % when compared to H_2.

$$\Pi_{Q_2,A} = 5.78 \times 10^{-7}\, M_{eff}^{-0.511} \tag{4.4}$$

$$\Pi_{Q_2,B} = 7.32 \times 10^{-7}\, M_{eff}^{-0.522} \tag{4.5}$$

The plot for the Q_2/He selectivity as a function of the molar mass is displayed in

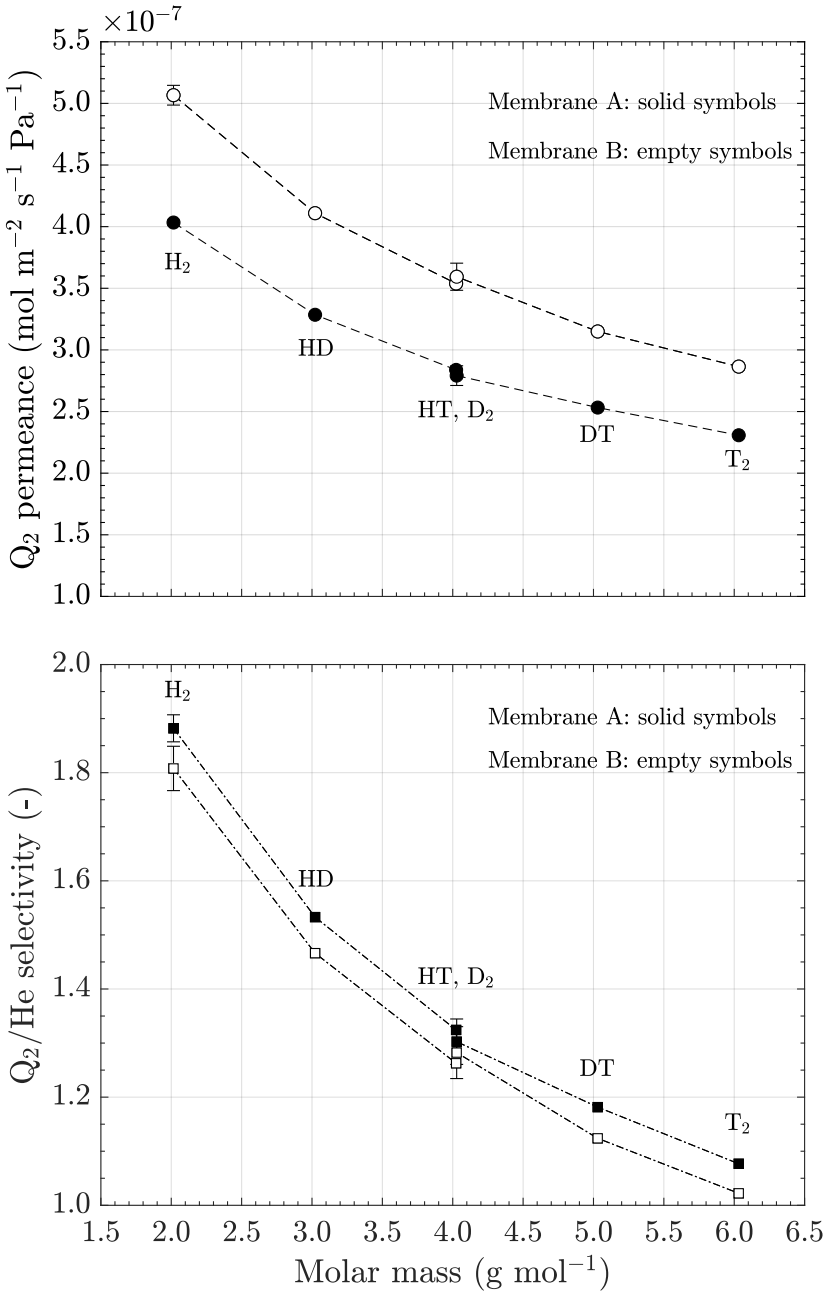

Figure 4.11: Q_2 permeance and Q_2/He selectivity as a function the molar mass of the hydrogen isotopologues for membranes A and B. Top: Q_2 permeance, bottom: Q_2/He selectivity. Solid symbols for membrane A and empty symbols for membrane B. The permeances for H_2 and D_2 are experimental, while the values for the other hydrogen isotopologues are extrapolated.

the bottom of figure 4.11, obtained from the ratio between the Q_2 permeances and the He permeance at 298 K ($\Pi_{\mathrm{He,A}} = 2.14 \times 10^{-7}\,\mathrm{mol\,m^{-2}\,s^{-1}\,Pa^{-1}}$, $\Pi_{\mathrm{He,B}} = 2.81 \times 10^{-7}\,\mathrm{mol\,m^{-2}\,s^{-1}\,Pa^{-1}}$). A monotonic decrease of the selectivity is obtained from ≈ 1.8 for H_2/He down to ≈ 1.1 for T_2/He. The selectivities are larger than 1.0 even for DT and T_2 with larger molar masses than He. This fact is explained by the stronger adsorption of the Q_2 species onto the zeolite structure, which is assumed to be similar to all isotopologues. The plot for the selectivities shows consistent results between membranes A and B.

Without sending the H_2/D_2 mixture through a catalyst at elevated temperatures, no production of HD takes place. However, since the HyDe loop facility is equipped with a catalyst (1/6" Al_2O_3 pebbles coated with Pt), the permeance of an equilibrated mixture of H_2-HD-D_2 with 50 mol% HD was also determined to validate further the extrapolation proposed (the experimental procedure for the production of HD is given in Appendix B.1.3). With an effective mass around $3\,\mathrm{g\,mol^{-1}}$, these experiments allow obtaining equivalent permeances for HD. The measured permeances obtained at 298 K are: $\Pi_{\mathrm{HD,A}} = (3.02 \pm 0.07) \times 10^{-7} \times \mathrm{mol\,m^{-2}\,s^{-1}\,Pa^{-1}}$ and $\Pi_{\mathrm{HD,B}} = (4.06 \pm 0.11) \times 10^{-7}\,\mathrm{mol\,m^{-2}\,s^{-1}\,Pa^{-1}}$. These values are well in agreement with the extrapolation for the HD give in figure 4.11: $\approx 3.3 \times 10^{-7}\,\mathrm{mol\,m^{-2}\,s^{-1}\,Pa^{-1}}$ (membrane A) and $\approx 4.1 \times 10^{-7}\,\mathrm{mol\,m^{-2}\,s^{-1}\,Pa^{-1}}$ (membrane B).

The results obtained with H_2/D_2 mixtures showed no competition in the permeation of these two isotopologues. The results with H_2-HD-D_2 demonstrate that this conclusion can be extended to more Q_2 isotopologues in the permeating mixture. These results are also noticeable for the fact that, contrary to the symmetric H_2 and D_2 molecules, HD has a dipole moment ($0.0027 \times 10^{-30}\,\mathrm{C\,m}$, table 3.2). However, the results show that the dipole moment influence on the permeation is negliglible when compared to the mass effect.

4.7 Summary of the results

Single-gas permeation experiments with He, H_2 and D_2 were performed through two identical MFI-ZSM-5 membranes with the HyDe loop facility in the temperature range $298 - 398\,\mathrm{K}$. The results show a higher contribution of the surface-diffusion on the permeances of H_2 and D_2 when compared to He. This behavior is explained by the quadrupole moments of H_2 and D_2 and their higher polarizabilities resulting in a higher adsorption onto the zeolite layer. Consequently, despite their similar masses, the D_2 permeance is higher than the He permemance by $20 - 30\,\%$. The ratio between the H_2 and D_2 permeances $\Pi_{H_2} \approx 1.4\Pi_{D_2}$ suggests that the differences in the permeation are due to the transport through defects, consistent with their similar adsorption properties (providing a similar contribution for the surface-diffusion through zeolitic channels). These results enabled an extrapolation towards the remaining Q_2 isotopologues and the HD permeance

was validated with the permeation of catalysed mixtures of H_2-HD-D_2 (50 mol% HD) at 298 K. The extrapolation presented in this chapter, verified with experiments for H_2, HD and D_2, requires further validation for HT, DT and T_2, since the tritium decay could possibly affect the kinetics of adsorption. In addition, in view of its application for a fusion reactor, actual separation experiments with these membranes are required since the selectivities only provide a first estimation. Therefore, a dedicated facility was assembled inside a glovebox at the Tritium Laboratory Karlsruhe to perform separation and permeation experiments with tritiated species.

Chapter 5

Permeation and separation experiments with an MFI membrane under tritiated atmosphere

5.1 Requirements for tritium handling at the Tritium Laboratory Karlsruhe

Tritium is radioactive and hence confinement is necessary to avoid contamination. Moreover, due to its hydrogen-like properties (e.g., high reactivity and permeation), special safety equipment and measures are required. Therefore, at the Tritium Laboratory Karlsruhe, as well as in other major tritium laboratories (e.g., the Tritium Process Laboratory in Japan), different levels of protection are implemented [152, 153].

The principle of operation of TLK is illustrated in figure 5.1. Since tritium permeation through metallic surfaces is unavoidable, all tritium processing pipework and components are installed inside a glovebox (GB) with an inert atmosphere (N_2 + few mol% of O_2) constantly renewed at a rate of $5 - 10$ times per hour, providing a static and dynamic tritium confinement. The renewing of the atmosphere is accomplished with the local tritium retention system associated with each glovebox, which separates the tritiated

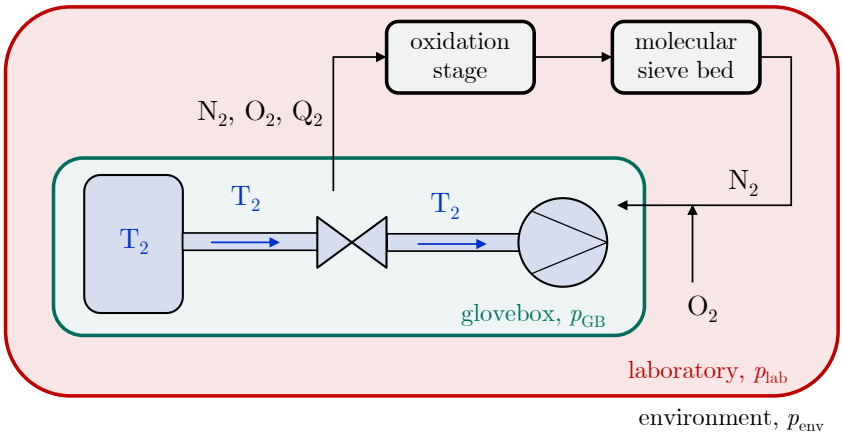

Figure 5.1: Schematic diagram illustrating the principle of tritium handling at the Tritium Laboratory Karlsruhe. In blue: experimental facility; in green: glovebox; in red: laboratory area. O_2 is added to N_2 for the catalytic oxidation of Q_2 into Q_2O and subsequent trapping in the local retention system. $p_{GB} < p_{lab} < p_{env}$.

species in the $N_2 + O_2$ mixture using an oxidation stage that converts all Q_2 into Q_2O (Q = H, D, T) and a molecular sieve bed to trap Q_2O (e.g., hydrophilic zeolite 3A). The minimisation of leaks through the glovebox is ensured by operating the glovebox with a pressure lower than that of the laboratory area ($p_{lab} > p_{GB}$), which in turn is also lower than the pressure of the outside environment p_{env} (pressure cascade concept).

The components installed in the primary system of TLK must comply with the regulations presented in the so-called "Technical Conditions of Delivery and Acceptance" (TLA[1]) document [154]. For instance, each component (e.g., tubes, pressure sensors, mass-flow controllers) has to present a helium leak-rate on the order of 10^{-9} mbar L s^{-1} and must be accompanied by materials certificates. In addition, the integral leak-rate of the whole tritium handling experimental rig must not exceed 10^{-8} mbar L s^{-1}. All components must be metal sealed and no polymers should be in contact with tritium, since the replacement of protium with tritium atoms in the hydrocarbons may alter considerably the properties of these materials[2]. Hence, oil-free pumps must be used for instance. Also, all the welds must pass in quality tests with X-ray and whenever a component has to be operated above 150 °C an enclosing outer vacuum jacket must be used to minimise tritium permeation. This set of regulations is applicable to all facilities and experiments handling tritium at the TLK. Thus, the new setup assembled to perform permeation and separation experiments with zeolite-ceramic membranes has to comply with these requirements.

5.2 Objectives of the experiments and selection of the host glovebox

5.2.1 Objectives of the experiments with tritium

In the previous chapter, the permeances of H_2, HD and D_2 were correlated with their molar masses and extrapolation functions were found for the tritiated isotopologues. However, a deviation may exist due to the energy released upon decay, which may influence the energy-activated mass-transport and/or degrade the material (e.g., amorphisation of the ZSM-5 structure), and thus the measurement of Q_2 permeances with different tritium concentrations is needed. Furthermore, the selectivities obtained from the single-gas experiments (ratio of permeances) are only a first estimation for the separation of Q_2 from He since no competition in permeation is considered. Therefore, further experiments with relevant mixtures of Q_2/He are required to determine the separation factor, which is the key parameter for accurate scaling-up studies for the pre-concentration of the TERS. In addition, the He stream purging the solid breeding blanket has been proposed to be

[1] From the German, "Technische Liefer- und Abnahmebedingungen".

[2] For example, the presence of tritium in the polymeric chains will induce creation of free-radicals as a result of its decay, which impacts the stiffness and elasticity of the sealant materials [155, 156].

doped with H_2O or D_2O (with 0.1 wt% or 0.02 mol%) to reduce tritium permeation into the coolant (section 2.3.1). The presence of the dipolar molecule Q_2O is expected to increase the separation factor, as previous results with H_2O/He have demonstrated [64], and thus separation experiments with different isotopologues of water, including tritiated water, are also required.

In sum, a new MFI-ZSM-5 membrane (referred to as "Membrane C") was tested in a newly developed tritium setup with the following experimental objectives:

1. extend the study of isotopic effects on the permeation to the tritiated hydrogen isotopologues;

2. perform binary separation experiments with Q_2/He and Q_2O/He mixtures.

These objectives were the starting point to design the ZEMTEX facility (ZEolite Membranes for Tritium EXperiments) and define its location. This new setup should enable (i) measuring the permeances of all six hydrogen isotopologues, (ii) producing Q_2/He and Q_2O/He gas mixtures and (iii) measuring gas compositions in feed and permeate to calculate the separation factor.

5.2.2 CAPER as host facility

Since ZEMTEX was erected to carry out tritium experiments, this setup was installed inside an existing glovebox, which was selected according to the experimental objectives to minimise efforts and resources for extension. CAPER was found to be the most suitable host facility due to the following features (more details given in [157, 158]):

- connection to the tritium supply systems (e.g., Tritium Transfer System);
- tritium compatible pumping system;
- production and storage of Q_2 and Q_2/He mixtures (with different isotopic concentrations of T in Q);
- production and safe handling of tritiated water (using a CuO reactor for water production and MSBs for trapping) [57];
- connection to analytical techniques for online and offline compositional analysis (e.g., gas chromatography, mass spectrometry) and activity measurements (ionisation chambers) [159];
- process of waste streams and delivery to other systems for further processing (e.g., Isotope Separation System) [160].

Therefore, CAPER provides all key components and features for the permeation experiments with Q_2 and separation experiments with Q_2/He and Q_2O/He. Nevertheless,

new components, such as mass-flow controllers and moisture sensors, were still required to guarantee the quality of the ZEMTEX experimental campaign. Consequently, the CAPER setup was extended to accommodate the membrane module and additional measuring devices.

5.3 Description of the ZEMTEX-CAPER setup

The simplified process flow diagram of the ZEMTEX-CAPER facility is presented in figure 5.2. In this picture only the devices used for the ZEMTEX experimental campaign are shown. The membrane module is identified as MM001 and the components installed in the feed (blue), permeate (orange) and retentate (green) are described below[3]:

- **Gas bottles**: the gas bottles of He (Air Liquide, $\leq 99.9999\,\text{mol\%}$), H_2 (Air Liquide, $\leq 99.9999\,\text{mol\%}$) and D_2 (Air Liquide, $\leq 99.8\,\text{mol\%}$) are installed outside of the glovebox and are used to supply CAPER;
- **Storage vessels**: the vessels BD807 ($\approx 54.9\,\text{L}$) and BD808 ($\approx 123\,\text{L}$) are used for the preparation and storage of Q_2 and Q_2/He gas mixtures;
- **Circulation and vacuum pumps**: the circulation pump KP803 is typically used to circulate the Q_2 mixture stored in BD807 to promote a balanced tritiated Q_2 mixture and KP802 is used to feed the gas into MM001. The pumping train VA851/VA852 is used to keep the permeate at low pressures ($< 100\,\text{mbar}$) to ensure a pressure difference across the membrane for permeation. It should be mentioned that CAPER is equipped with a vacuum manifold system (not shown in figure 5.2) allowing the evacuation of all ZEMTEX-CAPER lines;
- **Ionisation chambers**: these devices are small custom-made cross-piece chambers ($< 5\,\text{cm}^3$), whose aim is to provide a real-time and inline monitoring of the streams activity[4] [162, 163]. These devices cannot provide accurate measurements of activity as their output signals are highly dependent on the gas mixtures and they suffer from memory effect. Thus, they are used to evaluate whether the steady-state for permeation/separation has been reached, thanks to devices placed upstream (e.g., RX1002) and downstream (e.g., RX3005 and RX3006) of the membrane. The composition of the streams is measured using mass-spectrometry and gas chromatography;

[3]Detailed specifications given in table B.3 in Appendix B.2.

[4]The current produced by these devices is usually in the nA range, which requires high-accuracy amperimeters for signal measurement. At the TLK, Keithley Series 6400 picoammeters are typically used (refer to [161]).

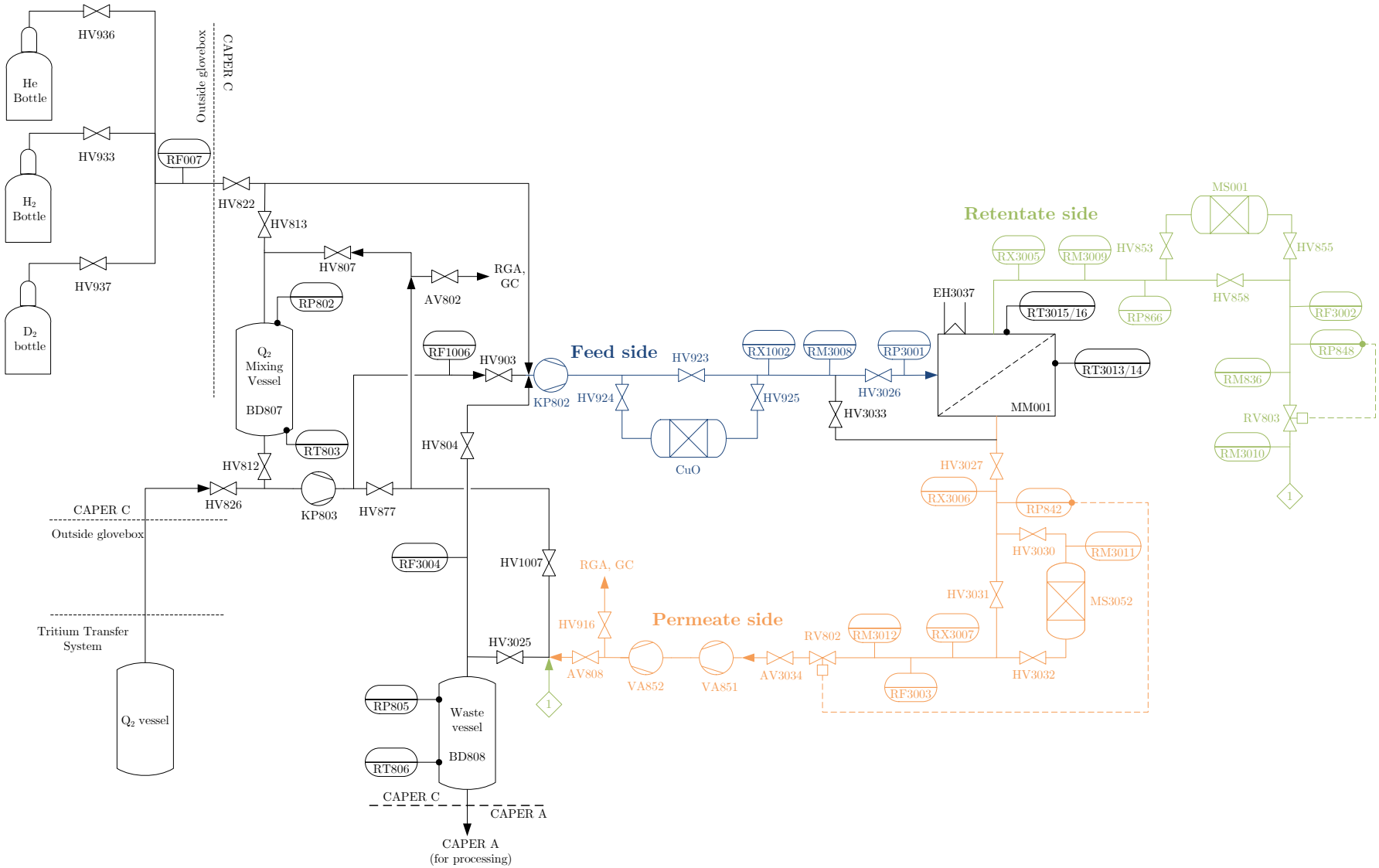

Figure 5.2: Simplified process flow diagram of the ZEMTEX-CAPER experimental rig. AV: automatic valve, BD: vessel, CuO: copper oxide reactor, HV: hand valve, KP: circulation pump, MM: membrane module, MS: molecular sieve bed, RF: flow controller, RM: moisture sensor, RP: pressure sensor, RV: regulation valve (pressure), RX: ionisation chamber, VA: vacuum pump.

- **Mass-flow controllers and meters**: the flow controllers/meters are used to regulate/measure the mass-flow of the gases in the feed, permeate and retentate. RF007 (MKS 1749A) is used to supply He, H_2 or D_2 into CAPER, while RF1006 is used to keep a constant Q_2 flow from BD807 into the membrane inlet. RF3003 and RF3002 (GF80 by Brooks) are used to measure the flows in the permeate and retentate sides of the membrane, respectively. RF3004 (GF80 by Brooks) can be used to feed the membrane with helium stored in BD808. All these devices are crucial for the determination of the gas permeances;

- **Pressure sensors and controllers**: the measurement of pressures along the feed/retentate with RP3001 (EFE PTA225) or RP848 (MKS Baratron) and permeate with RP842 (MKS Baratron) is used to determine the pressure difference across the membrane and calculate the permeance at equilibrium. For the separation experiments, the feed pressure is kept constant using the pressure-controller RV803, associated with RP848, installed in the retentate side;

- **Moisture sensors**: the moisture content is expected to be low along an experimental run (dew-point[5] values below $+10\,°C$) and hence devices especially designed for dry atmospheres were selected (working range: $-100 - +20\,°C$). These sensors (PURA model, Michell Instruments) provide a real-time information of the moisture content in in the feed (RM3008), permeate (RM3011/RM3012) and retentate (RM3009/RM3010) streams. However, due to their limited accuracy, they are used to evaluate whether the steady-state has been reached (similarly to the role of the ionisation chambers). The accurate measurement of the water content in the streams is accomplished with water trapping with MSBs;

- **CuO reactor and MSBs**: for the Q_2O/He separation experiments, the CuO reactor ($300\,cm^3$ vessel filled with $\approx 830\,g$ of CuO) is used to continuously oxidise the incoming Q_2/He stream. Downstream of the membrane module MM001, two molecular sieve beds (MS3052 in the permeate, MS001 in the retentate) are used to dry the wet mixtures. They are $150\,cm^3$ vessels filled with $\approx 120\,g$ of hydrophilic zeolite pebbles (e.g., 3A) [164]. The MSBs are key components since the mass of water stored at the end of an experimental run is used to determine the separation factor;

- **Tritium analytics**: the LAser RAman spectroscopy (LARA) technique, described in [165, 166], is used to measure the composition of the prepared Q_2 mixtures[6]. Mass-spectrometry (i.e., Residual Gas Analyser, RGA) and gas chromatography (GC),

[5]The dew point is the temperature at which the processing gas is saturated with vapor and below which condensation occurs. It is highly dependent on the vapor partial pressure.

[6]The Q_2 mixtures were routinely prepared in the Tritium Transfer System, which is equipped with a LARA system [160], and then sent to CAPER (vessel BD807).

described in [167–169], are used to measure the gas composition of the feed and permeate streams for the calculation of the separation factor in the Q_2/He separation experiments. Despite the higher accuracy of the RGA ($< 5\,\%$), the mass-to-charge ratio of He^+, D_2^+ and HT^+ is 4, which does not allow a distinction between these species. Therefore, since all Q_2 isotopologues can be measured with GC, the results obtained with both techniques are used complementarily. The activity of the water stored in the MSBs is measured with the large volume calorimeter described in [170] to evalute the existence of isotopic effects in the separation of Q_2O from He;

- **Heaters and thermocouples**: a resistive heating wire (EH3037) and four K-type thermocouples (RT3013-16) are installed on the surface of the membrane module to allow the heating of the membrane up to 130 °C (or 403 K). RT3015 is used to control the temperature set with the heater, and safety functions are implemented to ensure that the temperature remains below 150 °C (or 423 K). More heating wires and self-regulating heating tapes (with associated thermocouples for control and safety) are installed on the surfaces of the tubing between the CuO reactor and the MSBs to prevent the condensation of water inside the lines. With a proper heating and insulation, all water is trapped inside the hydrophilic MSBs, which ensures both the safe handling of tritiated water and the quality of the experiments.

The control of all the instrumentation and data acquisition is done with the Siemens PCS7 software, guaranteeing the safe operation of the whole experimental rig as required by the TLK regulations.

5.4 Development of tritium compatible sealings

Each tubular membrane used along the inactive experiments was accommodated inside a stainless steel module using two polymeric O-rings (EPDM-type) placed at both ends. These sealings are required to ensure that the feed side is isolated from the permeate side, ensuring a constant pressure difference across the membrane, which is essential for gas permeation/separation experiments. However, as highlighted in section 5.1, one of the requirements for the components installed in the primary system of TLK is the tritium compatibility, which implies that no polymers can be in direct contact with the tritiated gas. Therefore, a fully tritium compatible solution is necessary to have a membrane module that complies with the TLK regulations. Furthermore, the development of tritium compatible sealings is also relevant for its application at DEMO scale.

Hermetic seals between ceramic and metallic surfaces for high temperature applications (beyond temperatures at which polymers can be used) have been reported in the literature [171–173]. A typical solution is the use of ceramic-to-metal brazing where a filler material (Ti- or Zr-based) is melted to fill the gaps between both ceramic and metallic

surfaces. Although this technique is inherently tritium compatible, thermal stresses shall be expected due to the mismatch of the thermal expansion coefficients of the different materials, resulting in the loss of tightness. Moreover, the brazing solution would require the involvement of third parties with different expertises leading to the increase of the costs and time needed to have a final, tritium compatible product. Hence, a cheaper and faster in-house solution relying on $50 - 50\,\mathrm{wt}\%$ InPb alloy sealings was found with successful results (details on the manufacturing of the sealings and tests given in Appendix B.2.2).

5.5 Commissioning of the ZEMTEX-CAPER setup

Besides the membrane module with InPb sealings, three new mass-flow controllers, one pressure sensor, three ionisation chambers, five moisture sensors, and several heaters and thermocouples were installed in CAPER for the construction of the ZEMTEX setup, with more than 10 new valves and additional pipework. After the full assembly of the new rig, safety and scientific commissioning tests were necessary to ensure the:

- **Safe operation of the setup:** the leak-tightness of the facility was found to be within the TLK requirements (integral leak-rate $< 10^{-8}\,\mathrm{mbar\,L\,s^{-1}}$) and the safety features implemented in the newly updated software of CAPER properly working. These tests are mandatory prior to any experimental activity;
- **Quality of the experiments:** circulation tests at the relevant range of flows and pressures were carried out to compare the values provided by the new instrumentation with previously installed devices. Moreover, moisturised atmosphere was also used to compare the dew-points measured by the moisture sensors, and tritiated mixtures were prepared to evaluate the current measured with the ionisation chambers.

Overall, the results obtained during the commissioning phase provided a consistent agreement between all installed devices. The reliability of the tritium measurements along the experimental campaign was ensured by comparing the gas composition of Q_2 and Q_2/He mixtures measured with LARA, GC and RGA[7].

5.6 Isotopic effects on the permeation of tritiated Q_2 isotopologues

5.6.1 Preparation and composition of the Q_2 mixtures

The preparation of the Q_2 mixtures without tritium is done by mixing H_2 and D_2 inside BD807 (previously emptied) and the partial pressure of each gas species p_i is used

[7]LARA was only used for the measurement of Q_2 mixtures since it is not sensitive to noble gases.

Table 5.1: Atomic concentrations of the gas mixtures prepared for the investigation of isotopic effects on Q_2 permeances. The concentrations presented for the tritiated mixtures were measured with LARA with uncertainties $< 5\,\%$ relative.

Mix. #	H (at%)	D (at%)	T (at%)	M_{eff} (g mol^{-1})
1	50.9	49.1	–	3.022
2	30.2	69.8	–	3.424
3	–	≥ 99.8	–	4.028
4	0.5	92.0	7.3	4.152
5	0.6	79.6	20.6	4.423
6	5.8	59.1	35.1	4.607
7	4.9	48.4	46.6	4.859
8	4.2	41.1	54.6	5.034

to determine its molar fraction. No catalyst is used and hence the presence of HD can be neglected.

$$x_i = \frac{p_i}{\sum_i p_i} \tag{5.1}$$

The Q_2 mixtures with tritium are prepared in the Tritium Transfer System (TTS) of TLK to take advantage of the associated LARA system, allowing a continuous inline monitoring of the gas composition with a relative accuracy up to few % [160]. Each mixture is prepared by initially adding into an empty vessel a specific amount of H_2, D_2 and T_2 so that the desired atomic composition x_i, calculated according to equation (5.1), is obtained. Since tritium is radioactive, the production of the hybrid isotopologues (e.g., DT) can be achieved without a catalyst [26] and closed-circulation using pumps, which offer a relatively high surface area, decreases the time required to obtain a fully equilibrated mixture with constant concentrations of D_2-DT-T_2. Each Q_2 mixture is sent from TTS to CAPER (vessel BD807) where further circulation is done with KP803 and the gas composition measured with GC and RGA.

In total, eight Q_2 mixtures, including three without tritium, were prepared for the permeation experiments with Q_2. Since the objective is to extend the molar mass range to values beyond $4\,\text{g mol}^{-1}$ (to validate the extrapolation found in the last chapter), five mixtures with large concentrations of D and T were prepared up to 54.6 at% of T. The atomic concentrations of the three isotopes for all eight mixtures are displayed in table 5.1. All tritiated mixtures were measured with LARA (higher accuracy) and successfully cross-checked with RGA and GC (refer to Appendix F for detailed comparison).

5.6.2 Procedure to measure Q_2 permeances

The aim of the single-gas permeation experiments is to validate the extrapolation for the Q_2 permeances presented in the previous chapter with tritiated mixtures. The

experimental approach is similar to the procedure used for the inactive experiments: operation in dead-end mode (retentate closed), constant permeation flow, measurement of pressure difference between feed and permeate at steady state and calculation of the permeance at different membrane temperatures. Nevertheless, small differences exist: (i) the feeding gas is previously stored in the vessel BD807 and (ii) the experiments are performed in closed-cycle (BD807 → MM001 → BD807). These differences in the procedure are not expected to have any influence in the results since the pressure difference across the membrane is kept constant thanks to the pumping train VA851/852.

5.6.3 Permeances of Q_2 and selectivities for Q_2/He

The membrane is fed with a constant flow of Q_2 set with RF1006 (from vessel BD807) and the pressure difference established across the membrane at steady-stated is measured with RP3001 (feed) and RP842 (permeate). Hence, dividing the flow by the pressure difference and surface area ($\approx 4.84 \times 10^{-3}\,\mathrm{m}^2$), the permeance is calculated. The experimental permeances obtained for the eight Q_2 mixtures as a function of the effective molar mass, given by equation (5.2), are presented in figure 5.3 for five different temperatures.

$$M_{\mathrm{eff}} = x_{\mathrm{H_2}} M_{\mathrm{H_2}} + x_{\mathrm{D_2}} M_{\mathrm{D_2}} + x_{\mathrm{T_2}} M_{\mathrm{T_2}} \tag{5.2}$$

For each temperature, the experimental permeances were fitted with an allometric function and the corresponding fitting parameters a and b are presented in table 5.2. The average value for the exponents ($-b$) is 0.504 ± 0.021 for all temperatures tested. This value is consistent with the average values obtained with membranes A (0.548 ± 0.012) and B (0.500 ± 0.005) in the previous chapter. Therefore, the extrapolation presented before for the six hydrogen isotopologues (figure 4.11) is confirmed experimentally, and it can be concluded that the Q_2 permeance is proportional to $M_{\mathrm{eff}}^{-0.5}$. Thus, the isotopic effect on the permeation of these species is due to Knudsen diffusion through defects, which is supported by the similiar adsorption properties of the Q_2 species.

The helium permeance was also determined for the same temperature range and the results are given in table 5.3. The Q_2/He selectivity is thus determined by dividing the corresponding permeances for each temperature. Figure 5.4 compares the Q_2/He selectivity as a function of the effective mass M_{eff} obtained with membranes A, B and C at room

Table 5.2: Parameters obtained in the fitting of the permeances of Q_2 mixtures as a function of M_{eff} for membrane C. The corresponding plot is presented in figure 5.3. Units: $[a] = 10^{-9}\,\mathrm{mol\,m^{-2}\,s^{-1}\,Pa^{-1}}$, b is dimensionless.

	291 K	318 K	326 K	349 K	371 K
a	714 ± 25	637 ± 26	591 ± 16	517 ± 12	473 ± 13
b	-0.520 ± 0.024	-0.529 ± 0.028	-0.505 ± 0.018	-0.492 ± 0.016	-0.473 ± 0.019
R^2	0.986	0.982	0.991	0.993	0.989

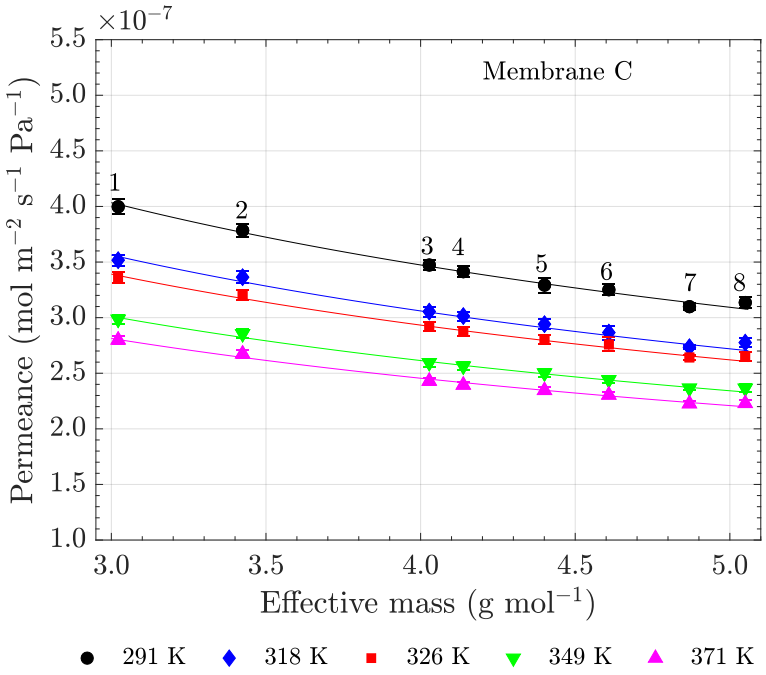

Figure 5.3: Permeances of Q_2 mixtures without and with tritium as a function of M_{eff} for different membrane temperatures. Without tritum: $\#\,1-3$, with tritium: $\#\,4-8$ (table 5.1). The fitting parameters are presented in table 5.2.

Table 5.3: Permeance of He as a function of the membrane temperature.

Π_{He} ($10^{-7}\,\text{mol}\,\text{m}^{-2}\,\text{s}^{-1}\,\text{Pa}^{-1}$)	Temperature (K)
2.62 ± 0.04	293
2.46 ± 0.03	318
2.28 ± 0.03	326
2.05 ± 0.02	371
1.96 ± 0.01	394

temperature[8] using the corresponding extrapolation functions for the Q_2 permeances:

$$\Pi_{Q_2,A} = 5.78 \times 10^{-7}\, M_{\text{eff}}^{-0.511} \qquad \text{(4.4 revisited)}$$

$$\Pi_{Q_2,B} = 7.32 \times 10^{-7}\, M_{\text{eff}}^{-0.522} \qquad \text{(4.5 revisited)}$$

$$\Pi_{Q_2,C} = 7.14 \times 10^{-7}\, M_{\text{eff}}^{-0.520} \qquad (5.3)$$

The selectivity is highest for H_2/He and lowest for T_2/He and thus the separation of the heavier isotopologues from helium is expected to be less efficient. Nevertheless, due to the role of the adsorption (surface-diffusion) on the Q_2 permeance, the selectivity is larger

[8]The experiments with membranes A and B (HyDe loop setup) were carried out at 298 K, whereas the experiments with membrane C (ZEMTEX setup) were carried out at 291 K. However, since the uncertainty of the temperature measurements is 1 % relative, the experiments are considered to have been performed at similar temperatures and no temperature correction of the permeance is necessary.

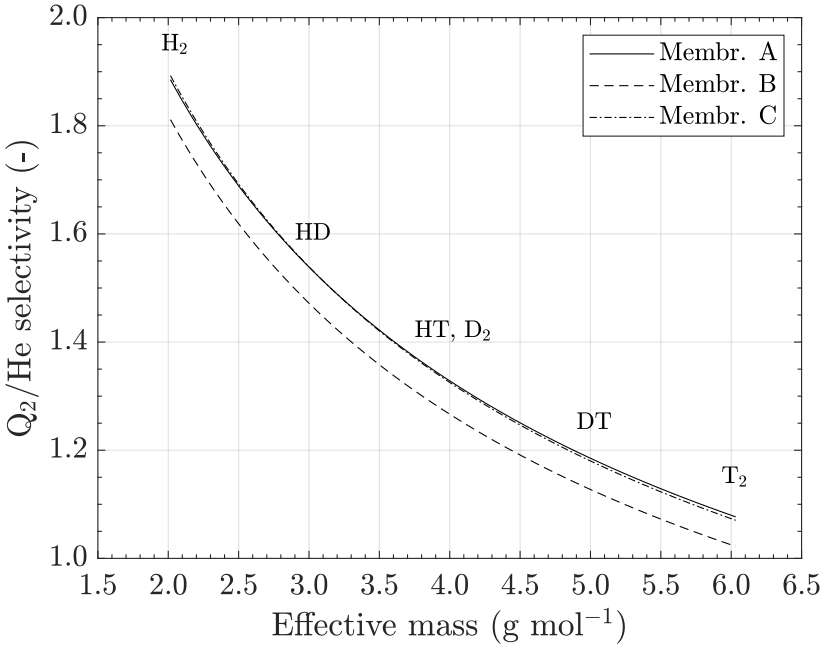

Figure 5.4: Comparison of the Q_2/He selectivity as a function of the Q_2 effective mass obtained with membranes A, B and C at room temperature. Solid line: membrane A, dashed line: membrane B, dashed-point line: membrane C. The associated uncertainties of the extrapolated values are below 4 % relative.

than 1 for all isotopologues. The results obtained for the three MFI-ZSM-5 membranes are consistent, suggesting that the synthesis quality of the zeolite layers is similar, despite their different thicknesses[9] ($t_{\mathrm{m,A}} < t_{\mathrm{m,C}} \approx t_{\mathrm{m,B}}$).

The selectivities displayed in figure 5.4 are a first estimation of the separation efficiency using the permeances measured with single gases. The effect of competition in the permeation is not considered and, as reported in [63] for H_2/He mixtures, the Q_2/He selectivity is expected to be an overestimation of the separation factor obtained with separation experiments. In addition, due to the presence of the radioactive tritium it is difficult to extrapolate the separation factor from the selectivities. Hence, to accurately evaluate the feasibility of a separation system based on membranes at reactor scale, separation experiments with tritiated Q_2/He mixtures were performed.

5.7 Separation experiments with Q_2/He

5.7.1 Procedure to determine the separation factor

Separation experiments with Q_2/He binary mixtures were carried out to obtain the separation factor $\alpha_{i/j}$, which is calculated using the measured permeate (y_{p}) and feed (x_{f})

[9]The thickness of membrane C was not measured, but can be estimated to be around 55 µm considering the proportionality between the measured permeances and thicknesses ($t_{\mathrm{m,A}} \approx 67$ µm, $t_{\mathrm{m,B}} \approx 55$ µm).

concentrations of both Q_2 and He as follows:

$$\alpha_{Q_2/He} = \frac{y_{p,Q_2}/y_{p,He}}{x_{f,Q_2}/x_{f,He}} \tag{5.4}$$

Q_2 stored in BD807 and high-purity He are sent simultaneously into the membrane feed side with constant flows set with RF1006 for Q_2 and with RF007 for He. The flow for each gas $F_{f,i}$ is chosen so that the desired molar concentration $x_{f,i}$, calculated according to equation (5.5), is obtained.

$$x_{f,i} = \frac{F_{f,i}}{\sum_i F_{f,i}} \tag{5.5}$$

These experiments are carried out with the retentate side open to ensure gas separation. The pressure in the feed/retentate side is kept constant with the pressure controller RV803, whereas the permeate is continuously evacuated. The pressure set with RV803 impacts the permeate and retentate flows and hence the cut, which is defined as the ratio between the permeate and feed flows (equation (5.6)). The cut is known to influence the separation performance of a membrane [63, 67]. Previous experiments with H_2/He have demonstrated that the highest separation factor is obtained with $\nu \approx 0.3$ and this was the value chosen for this work [63]. The cut is kept constant along an experimental run.

$$\nu = \frac{F_p}{F_f} \tag{5.6}$$

Along an experimental run, the permeate and retentate streams are directed into BD808 (initally empty). At steady-state[10], the permeate mixture is measured with RGA by expanding the gas mixture after the pumping train (with AV808 closed to avoid mixing with the retentate stream). The permeate mixture was also sampled into small vessels of ≈ 10 mL for offline measurements with GC. No measurements of the retentate concentrations were done[11]. At the end of an experimental run, the Q_2/He mixture stored in BD808, with the same composition as the feed, is analysed with RGA and GC to obtain a more accurate measurement of x_{f,Q_2} and $x_{f,He}$ (initially set with the mass-flow controllers).

The separation factor determined with equation (5.4) considers only two gas species. However, in these experiments more than two species are present in the feed (e.g., D_2, DT, T_2, He, also as expected downstream of the breeding blanket), and therefore multiple separation factors are required to fully characterise the separation performance of the membrane.

[10] Considered to be reached when the values of the flows, pressures and activity upstream and downstream of the membrane are constant. Each sample was taken after roughly 30 min of operation.

[11] With the current setup, the sampling of the retentate stream for RGA and GC analysis is not straightforward. Therefore, only the feed and permeate concentrations were measured, as required for the calculation of the separation factor.

The enrichment factor ($\mathcal{E}$) and recovery fraction ($\mathcal{R}$) are two additional important parameters to characterise the separation of a membrane [69]. $\mathcal{E}_i$ quantifies the increase in concentration of the species i in the permeate side in respect to the feed, whereas $\mathcal{R}_i$, typically given in %, is the fraction of the flow of species i collected in the permeate side in respect to the feed. They are defined by equations (5.7) and (5.8). Besides giving a complete information of the separation performance of a single membrane, $\mathcal{E}$ and $\mathcal{R}$ are also used in this work as design parameters to scale-up membrane separation systems for DEMO.

$$\mathcal{E}_i = \frac{y_{\mathrm{p},i}}{x_{\mathrm{f},i}} \tag{5.7}$$

$$\mathcal{R}_i\,(\%) = 100 \times \frac{y_{\mathrm{p},i} F_{\mathrm{p}}}{x_{\mathrm{f},i} F_{\mathrm{f}}} \tag{5.8}$$

In DEMO, the concentration of helium at the inlet of the zeolite membranes subsystem is expected to be higher than 99 mol%. Reproducing these conditions with the ZEMTEX setup would reduce the accuracy of the results. And from previous experiments with H_2/He mixtures, no dependency of the feeding concentration on the separation factor in the range $0.1 - 10$ mol% is expected [63]. Therefore, the experiments were done with 10 mol% Q_2 and 90 mol% He. Two sets of experiments were carried out using two feeding mixtures with different isotopic concentrations:

1. > 99 at% H in Q with $M_{\mathrm{eff}} \approx 2.0\,\mathrm{g\,mol^{-1}}$ (referred to as H_2/He);
2. 20 at% T and 80 at% D in Q with $M_{\mathrm{eff}} \approx 4.4\,\mathrm{g\,mol^{-1}}$ (referred to as Q_2/He).

The total feed flow ($F_{\mathrm{f,He}} + F_{\mathrm{f,H_2}}$) was kept constant and equal to $200\,\mathrm{mL\,min^{-1}}$ at STP along all experiments. The mass-flow controllers installed in the permeate (RF3003) and retentate (RF3002) are helium calibrated and they were used to measure the total Q_2/He permeate (F_{p}) and retentate (F_{r}) flows. Nevertheless, since the helium concentration along the experimental campaign is > 80 mol%, the effect of the hydrogen isotopologues in the reading is expected to be small and hence neglected. The experiments were done at four different membrane temperatures in the range $293 - 373$ K to study the influence of the mass-transport in the separation efficiency.

5.7.2 Results for 10 mol% H_2/He and Q_2/He

The permeate concentrations were measured with RGA and cross-checked with GC and a good consistency between both techniques was obtained for all experiments. The concentration of the feed gas collected in BD808 at the end of each experimental run was also measured with RGA/GC and used for the calculation of the separation factor. Table 5.4 displays the measured feed and permeate concentrations and the calculated separation factor α, enrichment $\mathcal{E}$ and recovery fraction $\mathcal{R}$.

The separation factor is plotted as a function of the temperature in figure 5.5 for both H_2/He and Q_2/He mixtures. The values for H_2/He are consistent with previous results obtained with similar membranes [63] in which the separation factor is lower than the selectivity obtained from the single-gas experiments. This effect has been attributed to the depletion of H_2 along the membrane feed side, reducing the driving force for permeation [63, 174]. Furthermore, the H_2/He separation factors are larger than those obtained for Q_2/He, supporting the conclusions presented before that the separation of heavier isotopologues from helium is less efficient with MFI-ZSM-5 membranes. In fact, with $\alpha \approx 1$,

Table 5.4: Permeate concentrations, separation factor, enrichment factor and recovery fraction obtained for the separation experiments with dry mixtures. $x_{f,i}$ and $y_{p,i}$ are the feed and permeate concentrations of H_2 or Q_2 in He.

T_m (K)	$x_{f,H_2} \mid x_{f,Q_2}$ (mol%)	$y_{p,H_2} \mid y_{p,Q_2}$ (mol%)	α (-)	$\mathcal{E}$ (-)	$\mathcal{R}$ (%)
		H_2/He			
293 ± 3	12.7 ± 0.4	17.3 ± 0.5	1.44 ± 0.12	1.36 ± 0.06	68.4 ± 2.7
326 ± 4		17.1 ± 0.5	1.42 ± 0.12	1.35 ± 0.06	59.7 ± 2.4
349 ± 6		17.3 ± 0.5	1.43 ± 0.12	1.36 ± 0.06	54.5 ± 2.2
371 ± 9		18.0 ± 0.5	1.51 ± 0.13	1.42 ± 0.06	53.8 ± 2.3
		Q_2/He			
293 ± 3	11.2 ± 0.3	11.7 ± 0.3	1.03 ± 0.09	1.02 ± 0.04	44.0 ± 1.6
326 ± 4		10.9 ± 0.3	0.99 ± 0.08	0.97 ± 0.04	36.7 ± 1.3
349 ± 6		10.9 ± 0.3	0.99 ± 0.08	0.97 ± 0.04	33.0 ± 1.3
371 ± 9		10.8 ± 0.3	0.98 ± 0.08	0.97 ± 0.04	31.3 ± 1.2

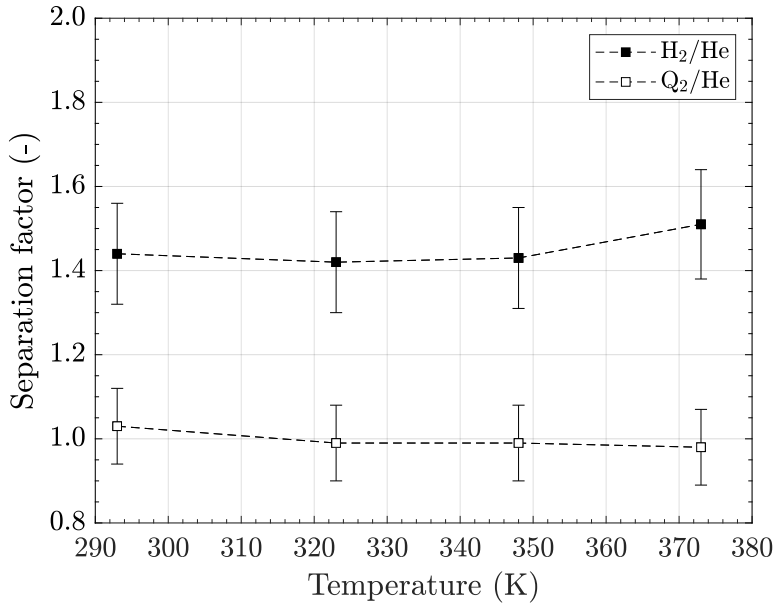

Figure 5.5: H_2/He and Q_2/He separation factor as a function of the membrane temperature.

no separation is obtained for the Q_2/He mixture with $M_{\text{eff}} \approx 4.4\,\text{g mol}^{-1}$.

Within the tested temperature range, α and $\mathcal{E}$ are rather independent of the membrane temperature. However, the temperature does affect the throughput of the membrane: the higher the temperature, the lower is the permeation flow as presented in figure 5.6 for H_2/He (refer to table F.4 in Appendix F for average values from all experiments). With the increase of the temperature, the permeances decrease[12] and hence the measured permeation flow F_{p} decreases and the retentate flow F_{r} increases. Consequently, the recovery fraction given in table 5.4 also decreases with the temperature.

The isotopic effects on the separation can be further investigated for the Q_2/He mixture with the calculation of the separation factor for D_2/He, DT/He and T_2/He (feed composition: 7.03 mol% D_2, 3.66 mol% DT, 0.48 mol% T_2). The measured concentrations and separation factors are displayed in table 5.5. The differences in the α values are within the experimental uncertainty and therefore more accurate measurements are necessary to evaluate whether the separation factor differs for the different isotopologues. Nevertheless, these results suggest that no separation takes place for Q_2 isotopologues with masses similar or larger than He.

In sum, the recovery of tritiated species with DEMO-relevant mixtures, such as T_2/DT/D_2/He, is challenging using MFI-ZSM-5 membranes since the separation is highly impacted by the mass of the species. These conclusions have important consequences for the application of this technology at reactor-scale for the dry purge scenario as discussed

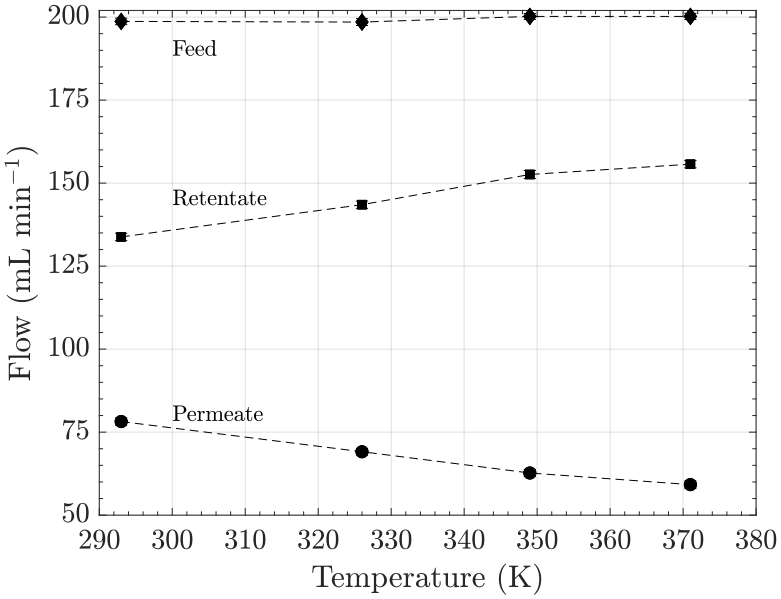

Figure 5.6: Average permeate and retentate flows measured along the H_2/He separation experiments as a function of the membrane temperature. The feed flow is given by $F_{\text{f,He}} + F_{\text{f,H}_2}$.

[12]Since the transport is dominated by surface-diffusion at this temperature range.

Table 5.5: Permeate concentrations and separation factors for D_2/He, DT/He and T_2/He. Feed concentrations: (7.03 ± 0.21) mol% D_2, (3.66 ± 0.11) mol% DT, (0.48 ± 0.01) mol% T_2.

T_m (K)	y_{p,D_2} (mol%)	$\alpha_{D_2/He}$ (-)	$y_{p,DT}$ (mol%)	$\alpha_{DT/He}$ (-)	y_{p,T_2} (mol%)	$\alpha_{T_2/He}$ (-)
293 ± 3	7.21 ± 0.22	1.03 ± 0.08	3.67 ± 0.11	1.00 ± 0.07	0.47 ± 0.01	0.98 ± 0.07
326 ± 4	6.95 ± 0.21	0.99 ± 0.07	3.49 ± 0.10	0.95 ± 0.07	0.44 ± 0.01	0.92 ± 0.07
349 ± 6	6.95 ± 0.21	0.99 ± 0.07	3.49 ± 0.10	0.95 ± 0.07	0.44 ± 0.01	0.92 ± 0.07
371 ± 9	6.92 ± 0.21	0.98 ± 0.07	3.49 ± 0.10	0.94 ± 0.07	0.43 ± 0.01	0.90 ± 0.07

in chapter 7.

5.8 Separation experiments with Q_2O/He

5.8.1 Procedure to determine the separation factor

Separation experiments with Q_2O/He binary mixtures were carried out to obtain the separation factor $\alpha_{i/j}$, which is calculated using the measured permeate (y_p) and feed (x_f) concentrations of both Q_2O and He as follows:

$$\alpha_{Q_2O/He} = \frac{y_{p,Q_2O}/y_{p,He}}{x_{f,Q_2O}/x_{f,He}} \tag{5.9}$$

Figure 5.7 presents the simplified process flow diagram for the Q_2O/He separation experiments. As for the dry experiments, the separation of vapor from helium is done with both permeate and retentate open, and the Q_2 and He flows are set to reach the desired concentration in the feed with $F_{f,Q_2}/(F_{f,Q_2} + F_{f,He})$. F_{f,Q_2} is set with RF1006 (from BD807) and $F_{f,He}$ is set with RF3004 (from BD808).

The Q_2/He stream is oxidised before reaching the membrane inlet using the CuO reactor heated at 400 °C and the vapor is collected in the permeate and retentate molecular sieve beds (MS3052 for permeate, MS001 for retentate). Downstream of the MSBs the remaining helium is sent to BD808 and, at the end of each experimental run, the gas collected in the vessel is analysed with GC. For all experiments, no Q_2 or Q_2O was detected, demonstrating that all Q_2 was oxidised with the CuO reactor and all Q_2O was trapped in the MSBs, ensuring the quality of the experiments.

The amount of water collected in the MSBs during an experimental run was measured after disconnecting them from the primary system (following the procedure and recommendations for the handling of components that were in contact with tritium). These measurements are of major importance to estimate the average permeate and retentate flows. Equation (5.10) is used to calculate the permeate vapor flow F_{p,Q_2O}, where M_{Q_2O} is the molar mass of Q_2O and m_p is the mass of Q_2O trapped in the MSB installed in

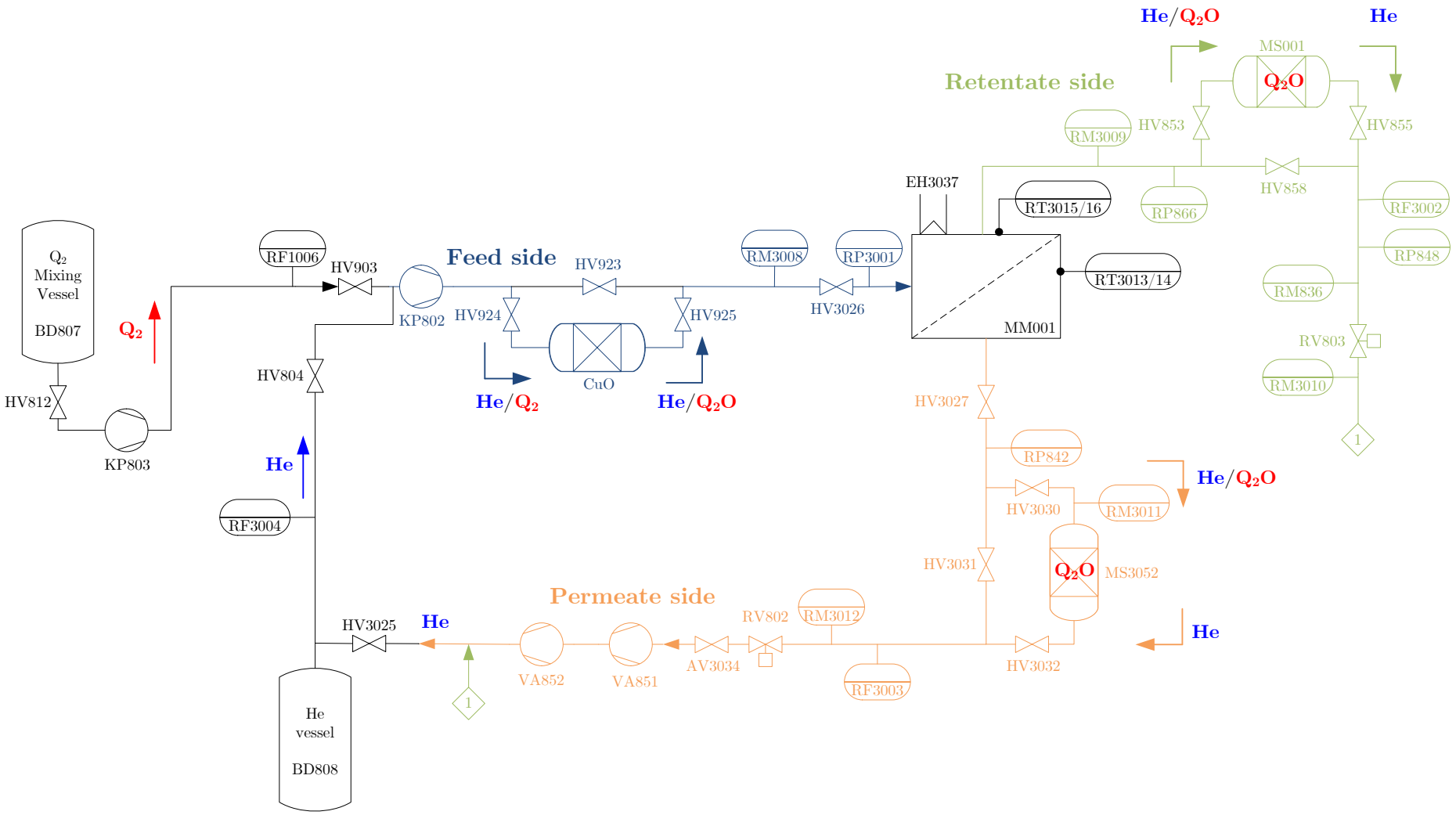

Figure 5.7: Simplified process flow and diagram for the Q_2O/He separation experiments. AV: automatic valve, BD: vessel, CuO: copper oxide reactor, HV: hand valve, KP: circulation pump, MM: membrane module, MS: molecular sieve bed, RF: flow controller, RM: moisture sensor, RP: pressure sensor, RV: regulation valve (pressure), RX: ionisation chamber, VA: vacuum pump.

the permeate along the time of the experiment Δt_{run} (weighed with a balance, Sartorius TE1502S). The gases are considered to behave as ideal and hence the molar volume 22400 mL mol^{-1} (valid at STP) is used. The mass-flow meters RF3003 (permeate) and RF3002 (retentate), installed downstream of the MSBs, measure the flow of the dried helium. Therefore, the concentration of water in the permeate is determined using equation (5.11). Likewise, the flow and concentration of Q_2O in the retentate were obtained with equations equivalent to (5.10) and (5.11). The permeate and feed concentrations were used to determine the separation factor given by equation (5.9).

$$F_{\text{p,Q}_2\text{O}} = \frac{1}{\Delta t_{\text{run}}} \frac{m_{\text{p}}}{M_{\text{Q}_2\text{O}}} \times 22400 \tag{5.10}$$

$$y_{\text{p,Q2O}} = \frac{F_{\text{p,Q}_2\text{O}}}{F_{\text{p,Q}_2\text{O}} + F_{\text{p,He}}} \tag{5.11}$$

Since the resolution of the scale available inside the glovebox is 0.01 g, the duration of the each experimental run (initially estimated with the set flow of Q_2) is chosen to allow the measurement of the weight of the trapped water with good accuracy, targetting a total Q_2O mass of ≈ 1 g for each run. The isotopic effect on the separation was also investigated by measuring the activity of the tritiated water stored in the MSBs using the TLK large-volume calorimeter with a detection limit of 0.1 Ci (equivalent to 0.010 mg of T) [170]. Hence, the T concentration in Q was chosen so that the expected activities for 1 g of generated water were > 10 Ci. The measurement of the activity of water stored inside the MSBs requires their removal from the glovebox with additional procedures required for the safe handling of tritiated components. In addition, for each MSB, roughly one week of calorimeter measurements are required.

In DEMO, the content of vapor in the helium purge is proposed to be around 0.02 mol%. Since the minimum Q_2 flow that can be set with RF1006 is 2 mL min^{-1}, the DEMO-relevant concentrations could be achieved with large helium flows ($\sim 10^4$ mL min^{-1}), beyond the full-scale of the installed devices[13]. Instead, consistently with the previous experiments, the total feed flow was kept constant and equal to 200 mL min^{-1} at STP and the lowest concentration achieved was 1 mol% of Q_2O in He.

Two sets of separation experiments were carried out using different isotopic and molar concentrations of Q_2 in He:

1. > 99 at% D in Q, with $1 - 10$ mol% in He to investigate the effect of the feeding concentration (referred to as D_2O/He, runs $\#1 - 4$);
2. 1.1 at% T, 10.0 at% H and 88.9 at% D in Q, with 2 mol% in He to investigate the influence of diluted T in the separation (referred to as Q_2O/He, run #5).

Due to the heaters used in the feed (between the CuO reactor and the membrane) and in the permeate/retentate (between the membrane and the MSBs) to avoid water

[13] In addition, large pressures above the safety levels of 1500 hPa would be achieved.

condensation inside the processing lines, the average temperature of the membrane module was measured to be around 303 K.

5.8.2 Discussion of the raw data

The plots displayed in figure 5.8 present a complete experimental run with raw data from the relevant flow (top), pressure (middle) and moisture (bottom) sensors obtained for 5 mol% D_2O/He. These experiments started by feeding the membrane with a constant He flow of 190 mL min^{-1} using RF3004 (at $t \simeq 7$ min). The steady-state is reached within ≈ 2 min (i.e., constant flows and pressures). During this period, with helium alone in closed circulation, the values of the moisture sensors consistently decrease due to the drying effect of helium in the tubing (bottom plot of figure 5.8). With values below $-45\,°C$, the vapor concentrations are estimated to be lower than 0.02 mol%[14] and hence negliglible when compared to the target vapor concentrations. At $t \simeq 25$ min, a constant D_2 flow of 9.9 mL min^{-1} was set with RF1006 and directed into the CuO reactor (top plot of figure 5.8). Consequently, the moisture measured by RM3008 after the CuO increased suddenly from -48 to $-5\,°C$ (bottom plot of figure 5.8). Shortly after, the moisture sensors placed at the permeate (RM3011) and retentate (RM3009) sides also measured a drastic increase of moisture.

The adsorption of water molecules onto the zeolite pores lead to a decrease of the helium permeate flow (RF3003) and hence an increase of helium in the retentate side (RF3002), as observed in the top plot of figure 5.8. As a result, the feed and permeate pressures increase and decrease, respectively (middle plot figure 5.8). This effect is stronger when the water content increases, as presented in table 5.6.

The dew points measured by RM3012 and RM3010, installed after the permeate and retentate MSBs, did not exceed $-80\,°C$, confirming that all water molecules remain trapped in the MSBs. At $t \simeq 170$ min the vessel BD807 was closed and thus the D_2

Table 5.6: Variation of the flows and pressures in the feed, permeate and retentate for the D_2O/He separation experiments. The positive/negative signs reflect an increase/decrease of the flows and pressures after water production. The flows are given in standard conditions of temperature and pressure.

#	x_{f,D_2O} (mol%)	$\Delta F_{p,He}$ (mL min^{-1})	$\Delta F_{r,He}$ (mL min^{-1})	Δp_f (hPa)	Δp_p (hPa)
1	0.95 ± 0.15	-6	$+6$	$+5$	-2
2	1.95 ± 0.17	-4	$+6$	$+5$	-2
3	4.95 ± 0.15	-11	$+9$	$+5$	-4
4	10.00 ± 0.17	-14	$+16$	$+8$	-6

[14] Calculated for a pressure of 530 hPa and 80 °C.

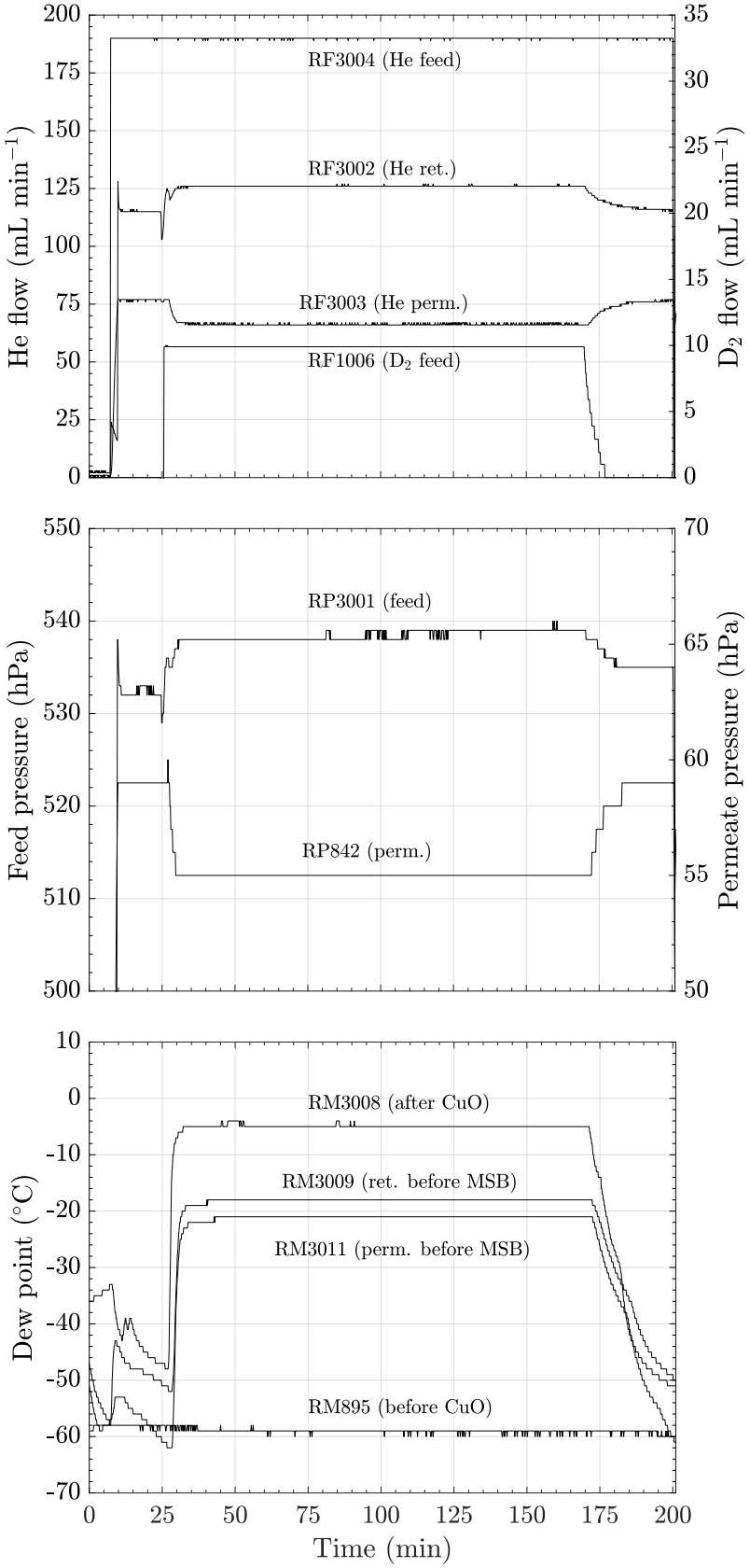

Figure 5.8: Example of raw data obtained for the 5 mol% D_2O/He binary separation experiments. Top plot: He (left axis) and D_2 (right axis) flows; middle plot: absolute pressures in the feed (left axis) and permeate (right axis); bottom plot: dew point in the feed, permeate and retentate. The flows are given in standard conditions of temperature and pressure.

flow decreased. This led to a decrease in moisture measured by RM3008, RM3009 and RM3011. The initial conditions of flows and pressures with helium alone were restored within 18 min.

The behaviour presented and discussed here for 5 mol% D_2O/He was observed for all experiments. At the end of the experimental runs the MSBs were weighed to determine the average vapor flows in the permeate and retentate to calculate the separation performance of the membrane. The average values measured with the flow, pressure and humidity sensors are summarised in Appendix F.4 for all D_2O/He and Q_2O/He separation experiments.

5.8.3 Results for 1 - 10 mol% D_2O/He

Table 5.10 displays the total mass of water injected in the feed and adsorbed in the permeate and retentate MSBs. From these values, the average permeate and retentate vapor flows can be calculated (equation (5.10)) and they are presented in table 5.11 together with the average of the measured helium flows. The vapor concentrations in the permeate, calculated with $F_{p,D_2O}/(F_{p,D_2O} + F_{p,He})$, are given in table 5.7. The permeate concentrations and flows are used to calculate the separation factor α, the enrichment factor $\mathcal{E}$ and recovery fraction $\mathcal{R}$, presented in the same table. The uncertainties associated with α, $\mathcal{E}$ and $\mathcal{R}$ increase with the decrease of the vapor concentration due to the lower imposed D_2 flows (the total flow is kept constant).

The separation factors are larger than 2 for runs $\#1-4$ and thus considerably higher than the values obtained for the separation of Q_2/He ($\alpha \approx 1$). This fact is explained by the water dipole moment that promotes electrostatic interactions absent for non-polar molecules. Consequently, the strong adsorption of the water molecules onto the zeolite surface hinders the permeation of helium. Although the values for α, $\mathcal{E}$ and $\mathcal{R}$ are highest at 2 mol% D_2O/He (explained by the collection of all feeding water in the permeate), the results obtained with the three remaining concentrations suggest that there is no observable dependency with the feeding concentration.

H_2O/He separation experiments performed at similar conditions ($0.2-10$ mol%) are reported in [64] for a similar membrane (from the same manufacturer) and the results are summarised in table 5.8. The same order of magnitude was obtained for α and $\mathcal{R}$. Nevertheless, consistently higher separation factors and lower recoveries were obtained for the H_2O/He experiments. At 10 mol%, a complete exclusion of helium from the permeate side was observed (hence $\alpha = \infty$). These differences are not expected to be due to isotopic effects, since H_2O and D_2O have equal dipole moments (6.17×10^{-30} C m [105]). Instead, these differences are attributed to the considerably lower cut of the experiments reported in [64] ($F_p/F_f < 0.1$) when compared to the one used for the D_2O/He experiments ($F_p/F_f \approx 0.3$). With lower cut values, the enrichment is expected to be higher (due to higher driving force) at the expense of lower recoveries (due to lower throughput) [67, 69].

Table 5.7: Permeate concentrations, separation factor, enrichment factor and recovery fraction obtained for all experimental runs.

#	$x_{f,D_2O} \mid x_{f,Q_2O}$ (mol%)	$y_{p,D_2O} \mid y_{p,Q_2O}$ (mol%)	α (-)	$\mathcal{E}$ (-)	$\mathcal{R}$ (%)
			D_2O/He		
1	0.95 ± 0.15	2.13 ± 0.05	2.27 ± 0.36	2.24 ± 0.35	82 ± 13
2	1.95 ± 0.17	6.13 ± 0.10	3.28 ± 0.30	3.14 ± 0.28	111 ± 10
3	4.95 ± 0.15	11.52 ± 0.33	2.50 ± 0.11	2.33 ± 0.10	87 ± 3
4	10.00 ± 0.17	19.56 ± 0.54	2.19 ± 0.09	1.96 ± 0.06	75 ± 2
			Q_2O/He		
5	1.95 ± 0.14	3.65 ± 0.14	1.91 ± 0.16	1.88 ± 0.16	74 ± 6

Table 5.8: Comparison with the data available in the literature for the separation of vapor from helium with MFI-ZSM-5 membranes. Only the values reported in [64] with similar H_2O/He feeding concentrations and at $\approx 303\,K$ are presented.

x_f (mol%)	α (-)	$\mathcal{R}$ (%)	Ref.
1	3.5 ± 0.6	12.3 ± 0.7	[64]
	2.27 ± 0.36	82 ± 13	this work
5	6.7 ± 1.1	24.8 ± 0.4	[64]
	2.50 ± 0.11	87 ± 3	this work
10	∞	56.8 ± 0.9	[64]
	2.19 ± 0.09	75 ± 2	this work

Table 5.9: Vapor and helium permeances calculated for all experimental runs.

#	$\Pi_{D_2O} \mid \Pi_{Q_2O}$ ($10^{-7}\,mol\,m^{-2}\,s^{-1}\,Pa^{-1}$)	Π_{He} ($10^{-7}\,mol\,m^{-2}\,s^{-1}\,Pa^{-1}$)
	D_2O/He	
1	6.39 ± 0.36	2.39 ± 0.04
2	10.16 ± 1.36	2.29 ± 0.04
3	6.53 ± 0.31	2.20 ± 0.04
4	5.46 ± 0.18	2.20 ± 0.02
	Q_2O/He	
5	5.93 ± 0.61	2.73 ± 0.01

The calculated permeances for D_2O and He given in table 5.9, determined by the ratio between the permeate flow, partial pressure difference and surface area. Consistently with α, $\mathcal{E}$ and $\mathcal{R}$, the permeance for 2 mol% D_2O is highest when compared to the remaining values, which is explained by the complete recovery of the feed in the permeate (i.e., $F_{p,D_2O} \approx F_{f,D_2O}$). A slight decrease of the helium permeance with the increase of the

Table 5.10: Feed, permeate and retentate masses of water measured along all experimental runs. Runs #1 − 4 were performed with D_2O/He (≈ 100 at% D in Q) and run #5 was performed with Q_2O/He (≈ 1.1 at% T in Q). m_f: total mass of water produced, m_p: mass of water trapped in the permeate MSB, m_f: mass of water trapped in the retentate MSB.

#	$x_{f,D_2O} \mid x_{f,Q_2O}$ (mol%)	$m_{f,D_2O} \mid m_{f,Q_2O}$ (g)	$m_{p,D_2O} \mid m_{p,Q_2O}$ (g)	$m_{r,D_2O} \mid m_{r,Q_2O}$ (g)
		D_2O/He		
1	0.95 ± 0.15	0.84 ± 0.13	0.68 ± 0.01	0.27 ± 0.02
2	1.95 ± 0.17	0.92 ± 0.08	1.01 ± 0.01	0.00 ± 0.03
3	4.95 ± 0.15	1.48 ± 0.04	1.07 ± 0.03	0.44 ± 0.02
4	10.00 ± 0.17	1.43 ± 0.02	1.03 ± 0.02	0.30 ± 0.02
		Q_2O/He		
5	1.95 ± 0.14	1.00 ± 0.07	0.69 ± 0.02	–

Table 5.11: Average helium and vapor flows measured along all experimental runs. Runs #1 − 4 were performed with D_2O/He (≈ 100 at% D in Q) and run #5 was performed with Q_2O/He (≈ 1.1 at% T in Q). $F_{f,i}$: feed flow of species i, F_p and F_r: permeate and retentate flows (helium), Δt_{run}: time of the experiment (while vapor produced). The flows are given in standard conditions of temperature and pressure.

#	$x_{f,D_2O} \mid x_{f,Q_2O}$ (mol%)	Δt_{run} (min)	$F_{f,D_2O} \mid F_{f,Q_2O}$ ($mL\,min^{-1}$)	$F_{f,He}$ ($mL\,min^{-1}$)	$F_{p,D_2O} \mid F_{p,Q_2O}$ ($mL\,min^{-1}$)	$F_{p,He}$ ($mL\,min^{-1}$)	$F_{r,D_2O} \mid F_{r,Q_2O}$ ($mL\,min^{-1}$)	$F_{r,He}$ ($mL\,min^{-1}$)
				D_2O/He				
1	0.95 ± 0.15	485.3 ± 0.2	1.9 ± 0.3	198.5 ± 3.1	1.57 ± 0.03	72.1 ± 1.0	0.62 ± 0.05	128.5 ± 1.1
2	1.95 ± 0.17	253.2 ± 0.2	4.0 ± 0.3	200.8 ± 1.7	4.46 ± 0.06	68.3 ± 1.1	–	132.4 ± 1.3
3	4.95 ± 0.15	139.2 ± 0.2	9.9 ± 0.3	190.0 ± 3.0	8.62 ± 0.21	66.2 ± 1.1	3.51 ± 0.14	126.0 ± 1.0
4	10.00 ± 0.17	76.7 ± 0.2	20.0 ± 0.3	180.0 ± 3.0	15.07 ± 0.35	62.0 ± 0.5	4.37 ± 0.26	120.8 ± 1.4
				Q_2O/He				
5	1.95 ± 0.14	271.5 ± 0.2	3.9 ± 0.3	196.4 ± 3.1	2.88 ± 0.10	76.0 ± 0.2	–	123.0 ± 0.3

vapor content in the feed was obtained, which is attributed to the higher occupation ratio of water molecules in the zeolite channels which hinders the helium permeation. Moreover, the permeances of D_2O are larger than those obtained for the Q_2 molecules in single-gas mode ($\Pi_{H_2,C} \approx 5.0 \times 10^{-7}\,\mathrm{mol\,m^{-2}\,s^{-1}\,Pa^{-1}}$) even though the former has a larger molar mass. This fact is explained by the stronger interaction between D_2O and the zeolite structure, which increases the permeance due to surface-diffusion.

These results demonstrate the superior efficiency of the MFI-ZSM-5 membranes to separate vapor from helium, showing the advantage for the pre-concentration of the TERS when the gas purging the blanket is doped with vapor. Further experimental results are nevertheless necessary with DEMO-relevant mixtures containing diluted tritium in vapor.

5.8.4 Results for 2 mol% Q_2O/He

Due to the larger efforts required to measure MSBs with the calorimeter, only one experimental run was carried with a selected feeding mixture of 2 mol% Q_2O in He to allow a comparison with run #2 for reproducibility. The Q_2 mixture was prepared with a concentration of T around 1.1 at%. This corresponds to ≈ 200 ppm of T in the feeding gas, whereas in a fusion reactor ≈ 1 ppm (or lower) should be expected. This very low T concentration would correspond to 0.2 Ci (for 1 g of collected water) and hence close to the limit of detection of the calorimeter (0.1 Ci). Instead, with the selected tritium concentration, the activity produced in one run is on the order of 30 Ci.

Tables 5.10 and 5.11 present the masses and flows obtained for the experiment with tritiated water (run #5). Only the mass accumulated in the MSB placed in the permeate is given[15]. The total activity of tritiated water produced along this experiment was: $\mathcal{A}_f = (32.21 \pm 0.97)$ Ci. This value was calculated from the total moles of Q_2 (0.05 mol) sent to the CuO reactor according to equation (5.12), where c_T is the tritium concentration in Q (1.1 at%) and $\mathcal{A}_T = 29000\,\mathrm{Ci\,mol^{-1}}$ is the molar activity of atomic tritium [27]. The activity of the water accumulated in the permeate MSB measured with calorimeter was: $\mathcal{A}_p = (27.48 \pm 0.22)$ Ci.

$$\mathcal{A}_f = 2 \times \frac{F_{f,Q_2}}{22400} \Delta t_{run} c_T \mathcal{A}_T \tag{5.12}$$

From the total mass of water sent to the membrane, 69 % was recovered in the permeate. However, based on the activity measurements, 85 % of the tritium was collected in the permeate. This implies that the tritium concentration in the water increased by a factor of 23 %. Furthermore, the separation factor, enrichment factor, recovery fraction and permeances calculated for run #5 (tables 5.7 and 5.9) are in the range of the values obtained with runs #1, 3, 4. Thus, these results support the conclusion that the

[15]The mass of the MSB in the retentate decreased 1.5 g between the beginning and the end of the experiment. This surprising result was attributed to an improper regeneration of the MSB, previously used for other purposes in the CAPER glovebox.

separation is rather independent of the feeding concentration of vapor in helium.

In sum, within the experimental uncertainties, no strong isotopic effects in the overall separation performances were observed. Nevertheless, more experiments with tritiated water should be performed towards DEMO-relevant conditions with lower T concentrations in Q (although limited by the available analytics and duration of the experiment). In addition, the observed effect of tritium enrichment in water upon separation should be further investigated as it would benefit the recovery efficiencies of tritium in the TERS.

5.9 Summary of the results

The ZEMTEX facility was assembled inside the CAPER glovebox to perform gas permeation with Q_2 and separation experiments with tritiated mixtures of Q_2/He and Q_2O/He. The tubular membrane was accommodated inside a fully tritium compatible membrane module with $50 - 50\,wt\%$ InPb alloy sealings. The gas permeation experiments with tritiated molecules Q_2 were performed in the range $290 - 371\,K$ and validated the correlation between the effective mass and the permeance proposed in chapter 4. The permeance of the Q_2 mixture is proportional to $M_{eff}^{-0.5}$, which implies that the higher is the T concentration in Q, the less efficient is the separation from helium. This result is consistent with the results from the Q_2/He separation experiments: while the H_2/He separation factor is around 1.4, a separation factor of 1 for Q_2/He (with 20 at% T in D) was obtained. Higher separation factors above 1.9 were determined for D_2O/He at 303 K in the range $1 - 10\,mol\%$, which is consistent with the higher amount of adsorbed vapor molecules (dipolar) onto the zeolite hindering the permeation of helium (non-polar). One experiment with 2 mol% tritiated water (1 at% T in Q) in helium was also carried out at the same temperature. The Q_2O/He separation factor was consistent with the results obtained with D_2O, suggesting the absence of strong isotopic effects (contrary to the dominant role of the mass in the separation of Q_2/He). An interesting effect of tritium enrichment (around 23 %) in Q_2O at the permeate side was also observed, which would be beneficial for the separation of T in the TERS.

These results demonstrate that the applicability of the MFI-ZSM-5 membranes is highly impacted by the purge gas composition chosen for the solid blanket. Small-to-none separation is expected when the ceramics are purged with a dry mixture. Instead, when the ceramics are purged with a wet mixture, higher separation efficiencies are obtained leading to higher tritium recoveries. These results are reinvested for the scaling-up studies discussed in the following chapters.

Chapter 6

Numerical code for the simulation of ideal membrane cascade systems

6.1 The need for membrane cascade systems

The experimental permeances of gases Π_i and Π_j, the selectivity $\alpha^*_{i/j}$ (ratio of permeances) and the separation factor $\alpha_{i/j}$ (for a gas mixture) are highly impacted by the interaction between the gas species and the membrane at certain operating conditions. In addition, since permeation is a pressure-driven process, the ratio between the feed and permeate pressures ($\gamma = p_\mathrm{f}/p_\mathrm{p}$) limits the enrichment $\mathcal{E}$ that can be attained for a given species in the permeate (equation (5.7 revisited)). Moreover, the trade-off between the enrichment $\mathcal{E}$ and recovery $\mathcal{R}$ (equation (5.8 revisited)) is impacted by the cut, defined by the ratio between the permeate and feed flows ($\nu = F_\mathrm{p}/F_\mathrm{f}$).

$$\mathcal{E}_i = \frac{y_{\mathrm{p},i}}{x_{\mathrm{f},i}} \qquad \text{(5.7 revisited)}$$

$$\mathcal{R}_i\,(\%) = 100 \times \frac{y_{\mathrm{p},i} F_\mathrm{p}}{x_{\mathrm{f},i} F_\mathrm{f}} \qquad \text{(5.8 revisited)}$$

The variation of one of the parameters mentioned above has an impact on the enrichment and recovery of the desired product [67], which are used as performance requirements to scale-up the membrane separation system for the DEMO Tritium Extraction and Removal System. Equation (6.1) shows the explicit dependency of the permeate concentration $y_{\mathrm{p},i}$ on $\alpha^*_{i/j}$ and γ (the derivation can be found in [67]). Thus, a short sensitivity analysis is conducted to analyse the impact of $\alpha^*_{i/j}$ and γ on $\mathcal{E}$. The range selected is $\alpha^*_{i/j} = 1.5 - 10$, simulating different membranes, and $\gamma = 1 - 10^3$, simulating different compression/pumping systems. The results are plotted in figure 6.1.

$$y_{\mathrm{p},i} = \frac{\gamma}{2}\left[x_{\mathrm{f},i} + \frac{1}{\gamma} + \frac{1}{\alpha^*_{i/j}-1} - \sqrt{\left(x_{\mathrm{f},i} + \frac{1}{\gamma} + \frac{1}{\alpha^*_{i/j}-1}\right)^2 - 4\frac{\alpha^*_{i/j} x_{\mathrm{f},i}}{(\alpha^*_{i/j}-1)\gamma}}\right], \qquad (6.1)$$

The top plot of figure 6.1 depicts the enrichment factor as a function of the pressure-ratio for different $\alpha^*_{i/j}$ values. As expected, for a given selectivity, when γ increases, $\mathcal{E}$ also

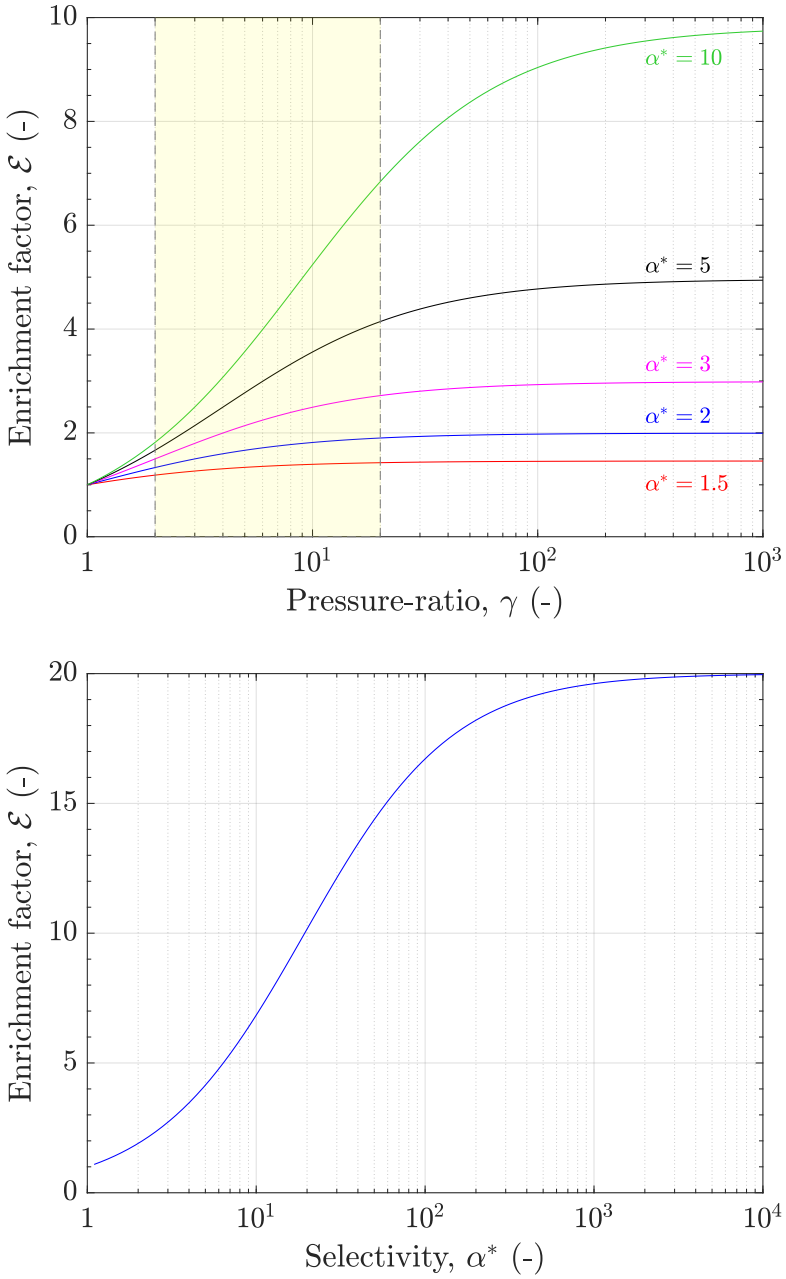

Figure 6.1: Impact of the selectivity and pressure-ratio on the enrichment factor. Top: effect of the pressure-ratio for different selectivities, bottom: impact of the selectivity for $\gamma = 20$.

increases until a plateau is reached, limited by $\alpha^*_{i/j}$. The higher the selectivity, the wider the region of γ-values that impact the value of $\mathcal{E}$. Hence, there is a "pressure-limited" regime when $\alpha^*_{i/j} \gg \gamma$ and a "selectivity-limited" regime when $\alpha^*_{i/j} \ll \gamma$. The yellow region depicted in the plot corresponds to the practical pressure-ratio range ($\gamma = 2 - 20$) considering the available pumping systems and economical viability [67, 175]. Therefore, although membranes with higher selectivities enrich the permeate stream further, membranes with selectivities above 100 are of limited advantage. This fact can be clearly observed in the bottom plot of figure 6.1 ($\mathcal{E}$ reaches saturation for $\alpha^*_{i/j} > 100$ with $\gamma = 20$).

The cut regulates the amount of product recovered in the permeate side. Therefore, it impacts the partial pressure difference across the membrane. High cut values provide large recoveries at the expense of a low enrichment, whereas low stage-cut values imply low recoveries with high-enrichment. This effect is displayed in figure 6.2 for $\alpha^* = 5$. This plot was obtained with the numerical code described in [174], which was developed to simulate the separation performance of a tubular membrane in the scope of this work. As discussed in [176], this trade-off in enrichment and recovery is expected for membranes with low-to-moderate selectivities[1] ($\alpha^* < 20$), and thus applicable for the separation of Q_2/He and Q_2O/He with MFI-ZSM-5 zeolite membranes. To circumvent this limitation, multi-stage systems with recycle streams must be implemented to obtain products with both high enrichment and recovery to be competitive with conventional technologies (e.g., cryogenic distillation columns) in industrial processes [177–179]. For the TERS of DEMO, the proposed performance requirements to scale-up the front-end stage relying on zeolite membranes are $\mathcal{E} \geq 20$ and $\mathcal{R} \geq 90\,\%$, which exceed the experimental performances reported in the previous chapter [180].

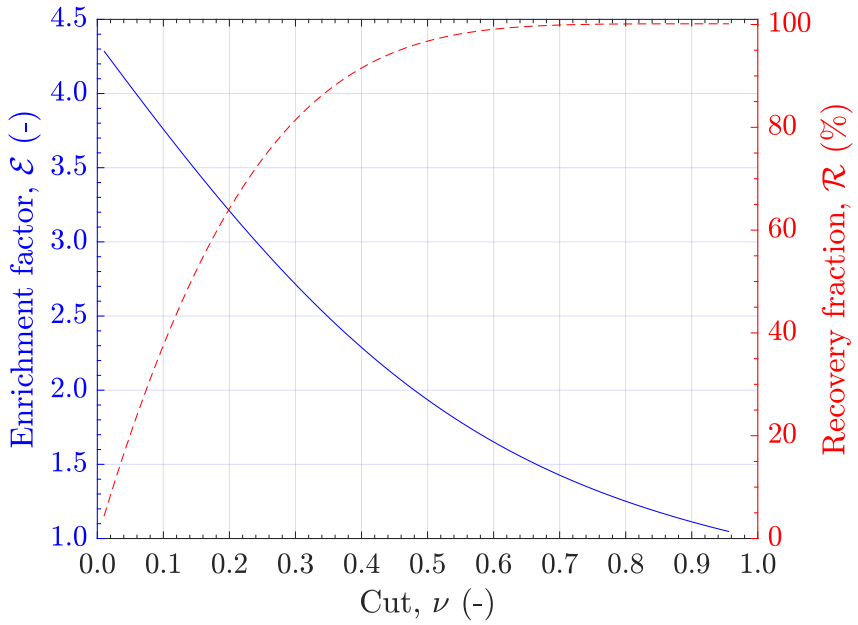

Figure 6.2: Impact of the cut on the enrichment factor and recovery fraction of a single membrane. Plot obtained for $\alpha^*_{i/j} = 5$ and $\gamma = 20$. Enrichment factor: solid blue line (left y-axis), recovery fraction: dashed red line (right y-axis).

[1] For higher selectivities, the trade-off is less pronounced since a relatively high enrichment can be achieved for a relatively high recovery.

6.2 Membrane cascade with classical arrangement

6.2.1 Configuration of the cascade

A generic scheme of a membrane cascade with a classical arrangement is depicted in figure 6.3. In this configuration, several stages[2] are placed in series, with compressors placed in between the permeate of stage k and the feed of $k+1$. Due to the pressure difference applied across the injection stage, the feed flow $F_{\mathrm{f}}^{\mathrm{inj}}$ is splitted into a permeate and retentate streams. The permeate flow $F_{\mathrm{p}}^{\mathrm{inj}}$ feeds the first stage of the so-called "enriching section", dedicated to enrich the most permeable species (with $\mathcal{N}$ stages), and the retentate flow $F_{\mathrm{r}}^{\mathrm{inj}}$ is used to feed the first stage of the so-called "stripping section" where the most permeating species is depleted (with $\mathcal{M}$ stages). Therefore, the whole cascade has a total number of stages $\mathcal{T}$, with $\mathcal{T} = \mathcal{N} + \mathcal{M} + 1$. Overall, the feed flow of stage k F_{f}^{k} is the sum of the retentate stream F_{r}^{k+1} and permeate stream F_{p}^{k-1} from stages $k+1$ and $k-1$, respectively, in agreement with equation (6.2).

$$F_{\mathrm{f}}^{k} = F_{\mathrm{f}}^{\mathrm{inj}} \delta_{\mathrm{k}}^{\mathrm{inj}} + F_{\mathrm{r}}^{k+1} + F_{\mathrm{p}}^{k-1} \tag{6.2}$$

6.2.2 Simulation codes in the literature

There are several numerical codes available in the literature that simulate the separation of gas mixtures using membrane cascades with a classical arrangement (e.g., isotope separation of $^{235}UF_6$ from $^{238}UF_6$) [181–185]. These models consider each separating stage as a "black-box" with input and output flows and concentrations, which are conserved using mass-balance equations. The flows and concentrations are calculated throughout the cascade by taking into account the selectivity $\alpha_{i/j}^{*}$, the cut ν and the pressure-ratio γ attributed to each stage.

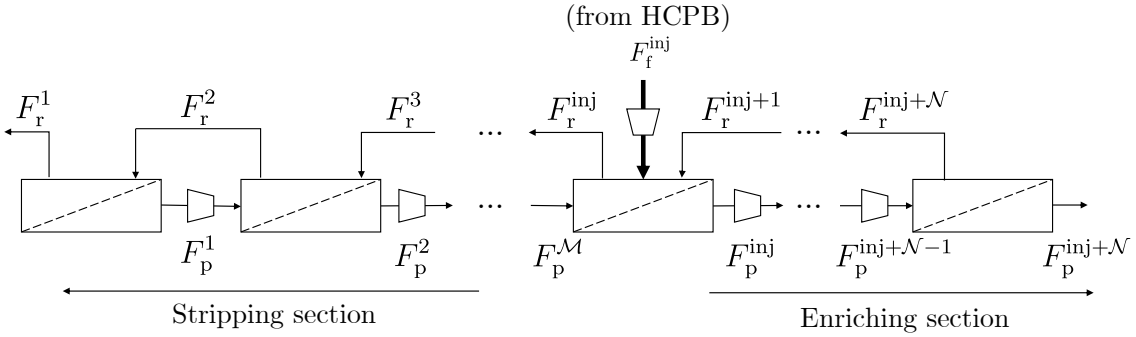

Figure 6.3: Classical arrangement of a membrane cascade. Enriching section with $\mathcal{N}$ stages and stripping section with $\mathcal{M}$ stages. Total number of stages: $\mathcal{T} = \mathcal{N} + \mathcal{M} + 1$.

[2] A "stage" is defined in this work as a separating element (i.e., membrane) in the cascade dedicated to perform a given separation (i.e., with a defined feed flow and gas species concentration).

An important criterion considered in these studies is that of an ideal cascade in which the permeate (y_{p}^{k-1}) and retentate (x_{r}^{k+1}) concentrations are equal to the feed concentration of stage k (x_{f}^{k}) according to equation (6.3). This condition minimises the separation power required, since the mixing of streams with different concentrations would lead to an extra production of entropy[3] and thus leading to a waste of the invested separation energy [186–188]. Consequently, more stages and power would be required to ensure that $\mathcal{E}$ and $\mathcal{R}$ (given as input) are fulfilled[4]. In this work, the condition of an ideal cascade is used to find the minimum number of stages.

$$y_{\mathrm{p}}^{k-1} = x_{\mathrm{f}}^{k} = x_{\mathrm{r}}^{k+1} \tag{6.3}$$

Other studies investigated the process of multi-stage systems by calculating the separation peformance of each stage individually (i.e., using finite volume permeation models) [175, 190, 191]. These approaches allow a larger flexibility in the arrangement of the different stages, which could lead to more energy and process efficient configurations. Nevertheless, these studies consider membranes with moderate selectivities and thus cascades with a few number of stages (not more than 3).

6.3 Objectives and assumptions of the model

6.3.1 Objectives of the model and desired outputs

According to the discussions presented in section 2.3, two configurations are considered for the TERS inlet depending on the doping agent: (i) Q_2/He for a purge gas with H_2 (or D_2) in He[5], (ii) Q_2O/He for a wet purge gas with H_2O (or D_2O) in He. For both configurations, the doping concentration of the purge gas is proposed to be 0.1 wt%, which corresponds to ≈ 0.2 mol% for Q_2/He and ≈ 0.02 mol% for Q_2O/He. The results of the separation experiments with Q_2/He and Q_2O/He carried out in this work and reported in [63, 64] are used as reference to evaluate the feasibility of a membrane cascade for the pre-concentration stage of the TERS to meet the performance requirements $\mathcal{E}$ and $\mathcal{R}$ given as input. This evaluation is based on the following aspects:

- **number of stages and surface area**: the complexity of operating a membrane cascade increases with the number of stages and the space occupation is highly impacted by the required surface area per stage;

[3] The streams are assumed to have the same phase, pressure and temperature. Hence a more general form of equation (6.3) would be obtained using the chemical potential μ: $\mu_{\mathrm{p}}^{k-1} = \mu_{\mathrm{f}}^{k} = \mu_{\mathrm{r}}^{k+1}$ [186].

[4] Recent studies demonstrate that cascades with mixing losses can be optimised (e.g., with a variable separation factor) to be as economical as the no-mixing losses process [176, 188, 189].

[5] An adsorption column is implemented before the membrane cascade to remove the Q_2O component with ppm concentrations [192].

- **power consumption**: the energy required to run the cascade is strongly related with the number of compressor units, which are the most energy-intensive equipments to operate the cascade as described in the following sections;

- **tritium inventory**: the minimisation of the tritium inventory of a given system inside the DEMO power plant is of paramount importance for safety and environmental reasons [193–195]. Therefore, despite the membrane cascade being a separation technology working under continuous mode (and thus not leading to immobilisation of tritiated molecules such as with adsorption technologies), the potential need for several stages may lead to a constant, non-negligible amount of tritium in the streams processed by the cascade.

Therefore, the desired outcomes of the numerical code are the total number of stages $\mathcal{T}$, permeate and retentate flows and concentrations along the cascade (F_{p}^{k}, F_{r}^{k}, y_{p}^{k}, x_{r}^{k}), membrane surface area per stage A_{m}^{k} and the power required to compress the permeate streams in each stage $\mathcal{P}^{k}$.

6.3.2 Assumptions

The temperature of the gas at the outlet of the blanket is expected to be around 773 K according to the HCPB design parameters given in table 2.3. However, regardless of the TERS concept (membranes or adsorption based), this gas must be cooled down to ensure higher efficiency in separation. For instance, the trapping of Q_2O is done with hydrophilic zeolite at around 300 K. Thus, it is also assumed that the cascade is operated at 300 K, favouring the adsorption-dominant separation mechanism of MFI-ZSM-5 membranes. Furthermore, the absolute pressure of the purge gas is expected to be 150 kPa (table 2.3). However, assuming a permeate pressure of 101.3 kPa, a rather low pressure-ratio is obtained ($\gamma \approx 1.5$). Thus, in this work a compressor is used to isentropically increase the feeding pressure to 2026 kPa targetting the highest practical γ-value ($\gamma = 20$). The same compression factor is assumed for the compressors placed at the permeate of each stage integrating the cascade.

The concentrations of the gas species feeding each stage vary along the cascade. As discussed in the previous chapters, due to the hydrophobicity of MFI-ZSM-5 membranes no dependency on the separation factor with the feeding concentration has been observed for Q_2O/He up to 10 mol%. Such behaviour was also reported in [64] for H_2O concentrations down to 0.2 mol%. Moreover, previous experiments also demonstrated that the separation factor for H_2/He (and therefore Q_2/He) is independent of the feeding concentration (in the range $0.1 - 10$ mol%) [63]. These ranges are within those expected inside the membrane cascade and hence the separation factors and permeances are kept constant throughout the system.

Currently, DEMO is in its pre-conceptual phase of development [196] and thus the aim of this work was to develop a model that allows a rather expedit evaluation and dimensioning of the system under various conditions (e.g., performance requirements, selectivities, flows). Therefore, the numerical code treating the cascade as ideal, with "black-box" stages and mass-balance equations, was found to be the most suitable. This approach relies on six major assumptions:

- **ideal gas approximation**: within the range of pressures ($\leq 2026\,\mathrm{kPa}$) used in the membrane cascade, deviations in respect to the ideal gas behaviour are expected[6] to be lower than 2 %;

- **homogeneous concentrations**: the concentrations in the permeate and retentate streams are considered homogeneous along each stage (well-mixed flows);

- **constant stage separation factor**: all stages are assumed to be equal with the same separation factor. In particular, the so-called "stage separation factor" $S_{\mathrm{stg}} = [y^k_{\mathrm{p},i}/(1-y^k_{\mathrm{p},i})]/[x^k_{\mathrm{r},i}/(1-x^k_{\mathrm{r},i})]$ is used for the calculation of the concentrations in the permeate and retentate (refer to Appendix G);

- **no pressure drops**: the feed/retentate and permeate pressures are considered constant along the stage and hence the pressure drops along the axis of the membrane channels are neglected (i.e., the pressure-ratio is considered constant for all stages);

- **isentropic compression**: the work performed to increase the pressure of the permeate stream with a compressor is assumed to be isentropic (i.e., adiabatic and reversible), which is a typical approximation for reciprocating compressors [198]. The minimum molar work W_{min} required to increase the pressure of a gas from p_{p} to p_{f} is calculated with equation (6.4), where c_p and c_V are the gas specific heat constants, T_{g} is the gas temperature and R is the constant for ideal gases [198].

$$W_{\mathrm{min}}(p_{\mathrm{p}}) = RT_{\mathrm{g}}\frac{bc_p}{c_p - c_V}\left[\left(\frac{p_{\mathrm{f}}}{p_{\mathrm{p}}}\right)^{\frac{c_p-c_V}{bc_p}} - 1\right] \tag{6.4}$$

  The specific heat constants are given for helium ($c_p = 5190\,\mathrm{J\,kg^{-1}\,K^{-1}}$, $c_V = 3118\,\mathrm{J\,kg^{-1}\,K^{-1}}$), since it is the major component in the streams ($> 90\,\mathrm{mol\%}$). b is the number of compressors required for isentropic compression[7]. In this work the

[6] The van der Waals equation of state $\left[p + a_1(n^2/V^2)\right](V/n - a_2) = RT_{\mathrm{g}}$ accounts for the fact that the molecules of a real gas are not point particles and attraction forces between molecules do occur (a_1 and a_2 are experimentally measured gas constants) [197]. For ideal gases, $pV/(nT_{\mathrm{g}}) = R = 8.314\,\mathrm{J\,K^{-1}\,mol^{-1}}$. Considering helium at 2000 kPa at 298 K, the deviation in respect to the ideal gas constant is estimated to be around 1.88 % (for helium: $a_1 = 3.457 \times 10^{-3}\,\mathrm{m^6\,Pa\,mol^{-2}}$, $a_2 = 2.370 \times 10^{-5}\,\mathrm{m^3\,mol^{-2}}$).

[7] Multi-stage compression with intercooling stages is required to avoid the decrease in compression efficiency due to heating of the gas [198, 199]

compression ratio is fixed to $\gamma = 20$ (corresponding to the highest practical value) and thus three compression stages are required[8];

- **no time transient**: the equations presented in the following section provide calculations of a cascade under steady-state operation. Thus, the time evolution of the concentrations and flows until the steady-state values is not considered.

6.4 Mathematical description and algorithm

Table 6.1 summarises the inputs and outputs of the developed model, whose numerical implementation follows the computations steps displayed in figure 6.4 and described below:

1. the input values for $\mathcal{E}$, $\mathcal{R}$ and $F_{\mathrm{f}}^{\mathrm{inj}}$ are used to calculate the flows at the last stages of both enriching ($F_{\mathrm{p}}^{\mathcal{N}}$) and stripping ($F_{\mathrm{r}}^{1}$) sections according to equations (6.5) and (6.6)

$$F_{\mathrm{p}}^{\mathcal{N}} = \frac{1}{\mathcal{E}} \frac{\mathcal{R}}{100} F_{\mathrm{f}}^{\mathrm{inj}} \tag{6.5}$$

$$F_{\mathrm{r}}^{1} = F_{\mathrm{f}}^{\mathrm{inj}} - F_{\mathrm{p}}^{\mathcal{N}} \tag{6.6}$$

2. using $F_{\mathrm{p}}^{\mathcal{N}}$, F_{r}^{1} and $x_{\mathrm{f},i}^{\mathrm{inj}}$, the concentrations $y_{\mathrm{p},i}^{\mathcal{N}}$ and $x_{\mathrm{r},i}^{1}$ are calculated with equations (6.7) and (6.8)

$$y_{\mathrm{p},i}^{\mathcal{N}} = x_{\mathrm{f},i}^{\mathrm{inj}} \mathcal{E} \tag{6.7}$$

$$x_{\mathrm{r},i}^{1} = \frac{F_{\mathrm{f}}^{\mathrm{inj}} x_{\mathrm{f},i}^{\mathrm{inj}} - F_{\mathrm{p}}^{\mathcal{N}} y_{\mathrm{p},i}^{\mathcal{N}}}{F_{\mathrm{r}}^{1}} \tag{6.8}$$

3. using the experimental permeances Π_i and Π_j (whose ratio is $\alpha_{i/j}^{*}$), the γ-value and $y_{\mathrm{p},i}^{\mathcal{N}}$, the stage separation factor S_{stg} is calculated with equation (6.9) [183], whose derivation is given in Appendix G

$$S_{\mathrm{stg}} = \frac{\alpha_{i/j}^{*} - y_{\mathrm{p},i}^{\mathcal{N}} (\alpha_{i/j}^{*} - 1) \gamma^{-1}}{1 + (1 - y_{\mathrm{p},i}^{\mathcal{N}})(\alpha_{i/j}^{*} - 1)\gamma^{-1}} \tag{6.9}$$

Table 6.1: Input and output parameters of the numerical code simulating the separation performance of a membrane cascade.

Inputs	Outputs
separation requirements ($\mathcal{E}$, $\mathcal{R}$)	number of stages ($\mathcal{N}$, $\mathcal{M}$)
concentrations stage inj ($x_{\mathrm{f},i}^{\mathrm{inj}}$, $x_{\mathrm{f},j}^{\mathrm{inj}}$)	concentrations stage k ($x_{\mathrm{r},i}^{k}$, $y_{\mathrm{p},i}^{k}$)
feed flow stage inj ($F_{\mathrm{f}}^{\mathrm{inj}}$)	flows stage k (F_{r}^{k}, F_{p}^{k})
permeances (Π_i, Π_j)	surface area stage k (A_{m}^{k})
pressures ratio (γ)	total power consumption ($\mathcal{P}_{\mathrm{tot}}$)
specific heat constants (c_p, c_V)	

[8] With $b = 3$ and $\gamma = 20$, the compression ratio per stage is $\gamma^{1/3} \approx 2.71$ [198, 199].

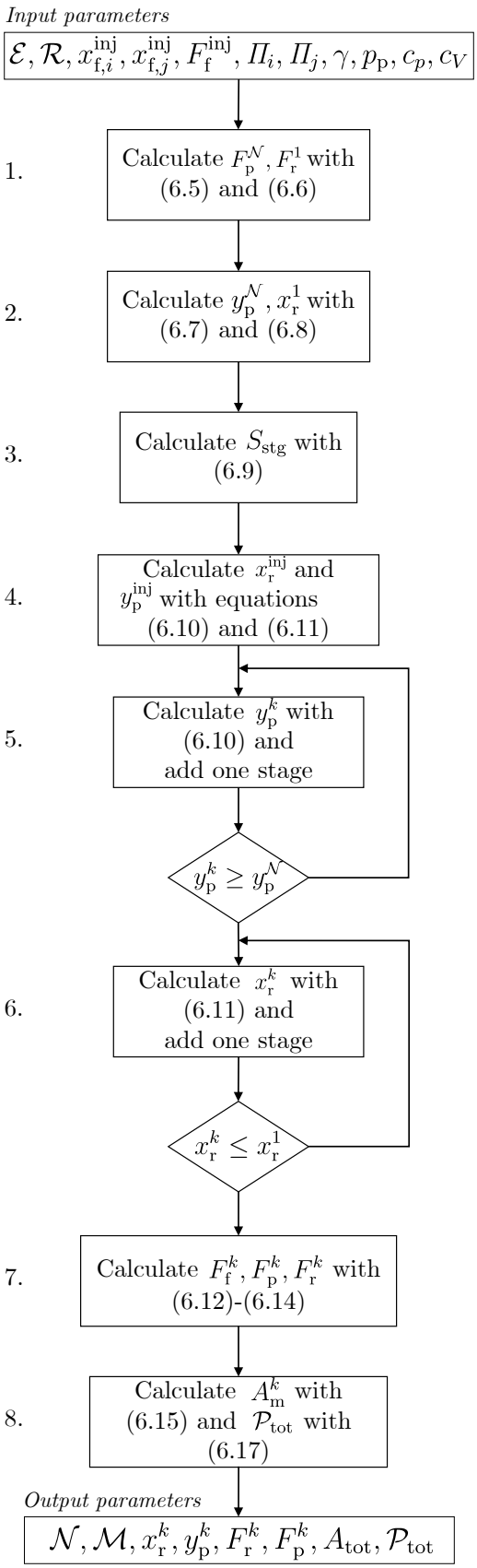

Figure 6.4: Algorithm for the numerical code developed to simulate the separation performance of a membrane cascade.

4. with the feed concentration $x_{\mathrm{f},i}^{\mathrm{inj}}$ and stage separation factor S_{stg}, the permeate and retentate concentrations of the injection stage $y_{\mathrm{p},i}^{\mathrm{inj}}$ and $x_{\mathrm{r},i}^{\mathrm{inj}}$ are calculated with equations (6.10) and (6.11), where $X_{\mathrm{f},i}^{k} = x_{\mathrm{f},i}^{k}/(1 - x_{\mathrm{f},i}^{k})$

$$y_{\mathrm{p},i}^{k} = \frac{\sqrt{S_{\mathrm{stg}}} X_{\mathrm{f},i}^{k}}{1 + \sqrt{S_{\mathrm{stg},i}} X_{\mathrm{f},i}^{k}} \tag{6.10}$$

$$x_{\mathrm{r},i}^{k} = \frac{X_{\mathrm{f},i}^{k}/\sqrt{S_{\mathrm{stg}}}}{1 + X_{\mathrm{f},i}^{k}/\sqrt{S_{\mathrm{stg}}}} \tag{6.11}$$

5. according to the definition of ideal cascade (equation 6.3)), $y_{\mathrm{p}}^{\mathrm{inj}}$ is equal to the feed concentration of the first stage of the enriching section (i.e., $k = \mathrm{inj} + 1$). Thus, $y_{\mathrm{p},i}^{\mathrm{inj}+1}$ and $x_{\mathrm{r},i}^{\mathrm{inj}+1}$ are calculated with equations (6.10) and (6.11). If $y_{\mathrm{p},i}^{k} < y_{\mathrm{p},i}^{\mathcal{N}}$, one stage is added to the cascade, and the calculations are repeated until $y_{\mathrm{p},i}^{\mathrm{k}} \geq y_{\mathrm{p},i}^{\mathcal{N}}$. The number of iterations is equal to the number of stages $\mathcal{N}$ in the enriching section

6. using the same procedure as in the previous step, the number of stages in the stripping section $\mathcal{M}$ is found using $x_{\mathrm{r},i}^{\mathrm{inj}}$ as feed concentration of stage $k = \mathrm{inj} - 1$ (according to the condition of ideal cascade). The calculations are repeated until $x_{\mathrm{r},i}^{\mathrm{k}} \leq x_{\mathrm{r},i}^{1}$. The total number of stages is $\mathcal{T} = \mathcal{N} + \mathcal{M} + 1$

7. in Appendix G it is demonstrated that the following equality holds for the cut: $\nu = F_{\mathrm{p}}/F_{\mathrm{f}} = (x_{\mathrm{f},i} - x_{\mathrm{r},i})/(y_{\mathrm{p},i} - x_{\mathrm{r},i})$. Thus, the cut values ν^{k} for all stages can be determined from the feed, permeate and retentate concentrations calculated in the previous steps. Then, the feed, permeate and retentate flows for all stages are calculated with (6.12)-(6.14), where $\boldsymbol{F}$ and $\boldsymbol{\nu}$ are column matrices and $\boldsymbol{A}^{\nu}$ is a square matrix dependent on the cut values (derivation presented in Appendix G)

$$\boldsymbol{F}_{\mathrm{f}} = \boldsymbol{A}^{\nu^{-1}} \boldsymbol{F}_{\mathrm{f}}^{\mathrm{inj}} \tag{6.12}$$

$$\boldsymbol{F}_{\mathrm{p}} = \boldsymbol{\nu} \boldsymbol{F}_{\mathrm{f}} \tag{6.13}$$

$$\boldsymbol{F}_{\mathrm{r}} = \boldsymbol{F}_{\mathrm{f}} - \boldsymbol{F}_{\mathrm{p}} \tag{6.14}$$

8. with the permeate flows determined in the previous step and the experimental permeances Π_i and Π_j, the surface area A_{m}^{k} for each stage is calculated with equation (6.15), where Π is the average permeance to take into account the permeation of both gases through the membrane (equation (6.16)). The total surface area A_{tot} is calculated by summing A_{m}^{k} over all stages

$$A_{\mathrm{m}}^{k} = \frac{F_{\mathrm{p}}^{k}}{\Pi^{k} p_{\mathrm{p}} (\gamma - 1)} \tag{6.15}$$

$$\Pi^{k} = \Pi_i x_{\mathrm{f},i}^{k} + \Pi_j x_{\mathrm{f},j}^{k} \tag{6.16}$$

The total compression power is calculated with equation (6.17), which is the sum of two contributions: (i) compression of the feeding gas coming from the blanket, and

(ii) compression of the permeate stream from stage k to feed $k+1$. η_e is the electrical-to-mechanical conversion efficiency, with $\eta_e \approx 82\,\%$ for a three-stages compressor with a compression ratio of ≈ 2.71 per stage (so that the overall compression is $\gamma \approx 2.71^3 \approx 20$) [198].

$$\mathcal{P}_{tot} = \frac{1}{\eta_e}\left(W_{min}(p_p)\sum_{k=1}^{\mathcal{N}-1} F_p^k + W_{min}(p_{blanket})F_f^{inj}\right) \tag{6.17}$$

6.5 Selected results

6.5.1 Impact of α, $\mathcal{E}$ and $\mathcal{R}$ on $\mathcal{T}$

The selectivity ($\alpha^*_{i/j}$) and the design requirements ($\mathcal{E}$, $\mathcal{R}$) have a direct impact on the number of stages of the whole cascade. For a given $\mathcal{E}$ and $\mathcal{R}$, the higher is the selectivity, the higher is the enrichment per stage of the desired product and thus less stages are required. As described in the previous section, the selectivity $\alpha^*_{i/j}$ is used to calculate S_{stg} (equation (6.9)), which relates with the separation factor α calculated from the separation experiments according to $\alpha = \sqrt{S_{stg}}$ (derivation given in Appendix G).

Figure 6.5 presents the total number of stages as a function of the separation factor α for $\mathcal{E} \geq 20$, $\mathcal{R} \geq 90\,\%$ and $\gamma = 20$. The range selected for α covers the values obtained experimentally: $\lesssim 1.44$ for Q_2/He and $\gtrsim 1.91$ for Q_2O/He. A strong dependency of the number of stages with α can be observed. For the range relevant for the Q_2/He mixtures,

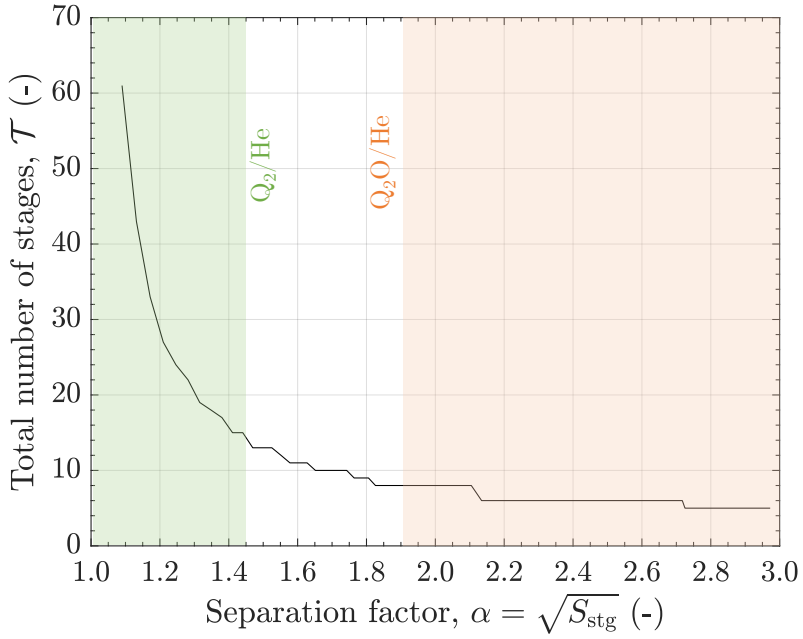

Figure 6.5: Number of required stages as a function of the selectivity for $\gamma = 20$, $\mathcal{E} \geq 20$, $\mathcal{R} \geq 90\,\%$. The two shaded regions indicate the range of separation factors obtained with Q_2/He (green, $\lesssim 1.44$) and Q_2O/He (orange, $\gtrsim 1.91$) mixtures.

the minimum number of stages is 15 (corresponding to the separation of H_2/He). For a Q_2 mixture including D and T, as expected at the outlet of the blanket, the separation factor decreases (since the separation is determined by the molar mass) and the number of stages increases dramatically. On the contrary, for Q_2O/He, with $\alpha > 1.9$, the required number of stages should not exceed 8. Using the average value $\alpha \approx 2.2$ obtained along the D_2O/He and Q_2O/He separation experiments[9], 6 stages are found to be necessary to meet the performance requirements $\mathcal{E} \geq 20$ and $\mathcal{R} \geq 90\,\%$. Thus, the number of stages required for the pre-concentration stage of the TERS is highly impacted by the composition of the gas initially purging the solid blanket.

The number of stages as a function of $\mathcal{E}$ for $\mathcal{R} \geq 80 - 99\,\%$ and $\gamma = 20$ is plotted in figure 6.6. This plot was obtained for $\alpha = 1.44$, which corresponds to the separation factor obtained in the H_2/He separation experiments. The increase of both $\mathcal{E}$ and $\mathcal{R}$ leads to an increase of the number of stages as expected. A highly efficient system ($\mathcal{E} \geq 90$, $\mathcal{R} \geq 99\,\%$) would require 25 stages (10 more than for $\mathcal{E} \geq 20$, $\mathcal{R} \geq 90\,\%$). As discussed in more detail in [200], the increase of $\mathcal{E}$ leads to an increase of the number of stages in the enriching section. Consequently, the flow $F_p^{\mathcal{N}}$ at the outlet of the cascade also decreases, which is beneficial to keep the next stage (Pd-based membrane reactors) within reasonable sizes. It should be noted that the higher is $\mathcal{R}$, the stronger is its impact on the number of

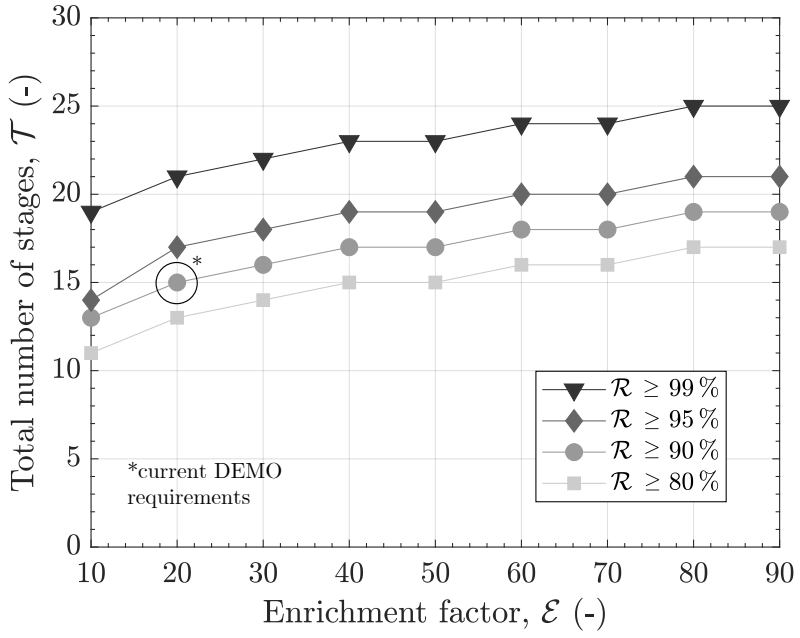

Figure 6.6: Number of required stages as a function of the enrichment factor for different recovery fractions. $\gamma = 20$ and $\alpha = 1.44$ (obtained for H_2/He).

[9]Run #2 was not considered for the average due to its higher values when compared to the remaining 4 runs (table 5.7).

stages[10]. For higher selectivities, the increase of $\mathcal{E}$ and $\mathcal{R}$ has less impact on the number of stages since the membranes separate more efficiently.

6.5.2 Impact of α on A_{tot} and $\mathcal{P}_{\text{tot}}$

The dependency of $\mathcal{P}_{\text{tot}}$ and A_{tot} on α is presented in figure 6.7, considering a helium permeance of $\Pi_{\text{He}} = 2.5 \times 10^{-7}\,\text{mol}\,\text{m}^{-2}\,\text{s}^{-1}\,\text{Pa}^{-1}$ (typical value measured in the experiments) and a permeate pressure of $p_{\text{p}} = 101.3\,\text{kPa}$. For $\alpha < 1.4$, the power consumption can largely exceed 100 MW and the required surface area could reach almost $10^5\,\text{m}^2$. For the region of separation factor values obtained for Q_2O/He, the power consumption should be lower than 4 MW and the surface area below $10^3\,\text{m}^2$. It should be noted that the power required to compress the whole stream coming from the blanket (i.e., before feeding the injection stage) is more than 1.8 MW.

The required surface area and power consumption increase with the number of stages for two reasons: (i) a larger number of separating elements increases the surface area and number of compressors, (ii) a larger number of stages increases the recycling of

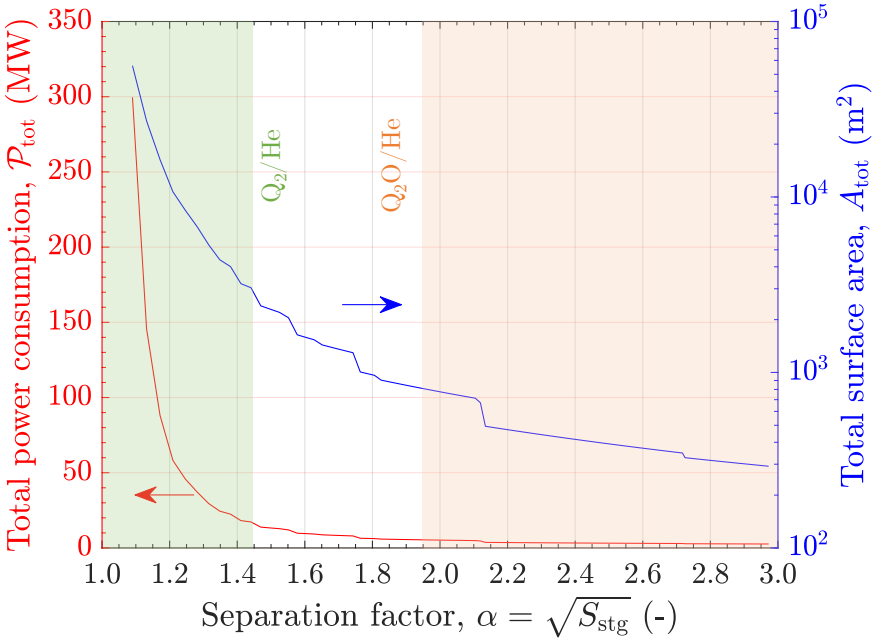

Figure 6.7: Total power consumption and surface area as a function of the separation factor $\alpha = \sqrt{S_{\text{stg}}}$. $\mathcal{E} \geq 20$, $\mathcal{R} \geq 90\,\%$, $\gamma = 20$, $\Pi_{\text{He}} = 2.5 \times 10^{-7}\,\text{mol}\,\text{m}^{-2}\,\text{s}^{-1}\,\text{Pa}^{-1}$ and $p_{\text{p}} = 101.3\,\text{kPa}$. The two shaded regions indicate the range of separation factors obtained with Q_2/He (green, $\lesssim 1.44$) and Q_2O/He (orange, $\gtrsim 1.91$) mixtures.

[10]When $\mathcal{R} \to 100\,\%$, $\mathcal{T} \to \infty$ since the membranes are not completely selective towards one species and thus a complete recovery of the desired product in the last stage of the enriching section is not possible.

flows between stages leading to a larger build-up of flows[11] [200]. Moreover, the order of magnitude of A_{tot} and $\mathcal{P}_{\text{tot}}$ is directly impacted by the flow feeding the cascade, which is considered to be equal to the flow required for the purging of the HCPB blanket: $F_{\text{f}}^{\text{inj}} = 0.4\,\text{kg}\,\text{s}^{-1}$ or $F_{\text{f}}^{\text{inj}} \approx 100\,\text{mol}\,\text{s}^{-1}$.

6.6 Diagram of dependencies

In the previous section, the strong impact of the selectivity, $\mathcal{E}$ and $\mathcal{R}$ on the number of stages, surface area and power consumption has been discussed. Furthermore, the pressures-ratio γ has also an important impact on these quantities. For the calculations, $\gamma = 20$ was considered since it is the most favorable scenario with the maximum value that can be achieved in practice at the expense of higher levels of compression power. However, a decrease in γ would not necessarily lead to a lower power consumption, since more stages could be required to compensate the decrease in α.

A thorough sensitivity analysis was conducted to identify the influence of $\mathcal{E}$, $\mathcal{R}$, γ, Π, p_{p} and $F_{\text{f}}^{\text{inj}}$ on the number of stages, surface area and compression power [200]. An overview of the dependencies among the different input/output parameters is given in the diagram of figure 6.8. The total number of stages $\mathcal{T}$ is directly impacted by $\mathcal{E}$, $\mathcal{R}$ and the separation factor S_{stg}, which, in turn, is determined by the pressure-ratio γ and selectivity given by the ratio of permeances Π_i and Π_j. The permeances, together

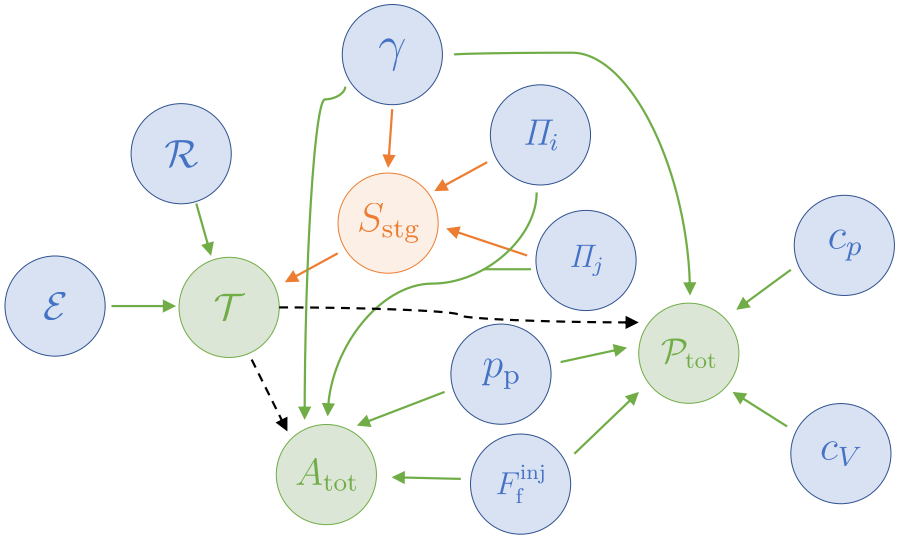

Figure 6.8: Diagram of dependencies between the input and output parameters of the membrane cascade code. Input parameters: blue, output parameters: green. The stage separation factor S_{stg} calculated using equation (6.9) is highlighted in orange.

[11] The mass-balance condition $F_{\text{f}}^{\text{inj}} = F_{\text{r}}^{1} + F_{\text{p}}^{\mathcal{N}}$ is valid under steady-state operation. However, due to the recycling between stages, the flows inside the cascade will eventually exceed $F_{\text{f}}^{\text{inj}}$.

with γ and permeate pressure p_{p}, have a strong impact on the stage surface area. The power consumption is impacted by γ, p_{p} and the specific heat constants c_p and c_V of the compressed gas. A_{tot} and $\mathcal{P}_{\mathrm{tot}}$ are both directly impacted by the feeding flow $F_{\mathrm{f}}^{\mathrm{inj}}$, which determines the order of magnitude of the permeating flows along the cascade. Last but not least, since A_{tot} and $\mathcal{P}_{\mathrm{tot}}$ are cumulative values they are also impacted by the number of stages taking part in the cascade, especially due to the build-up of flows as previously discussed.

6.7 Summary of the chapter

The limited separation performances for Q_2/He and Q_2O/He obtained with one single MFI-ZSM-5 membrane in the previous chapter do not meet the requirements for the TERS of the solid blanket. Hence, a cascade of membranes is required to increase both enrichment factor ($\mathcal{E}$) and recovery fraction ($\mathcal{R}$) to fulfill the DEMO requirements. In a membrane cascade, several stages are placed in series with compressors in between to ensure constant pressures-ratio across each stage (guaranteeing driving force for permeation). For the TERS, the most important figures to evaluate the feasibility of the cascade are the number of stages, membrane surface area, power consumption and tritium inventory. Thus, a numerical code was developed for the separation of binary mixtures with input parameters such as the performance requirements $\mathcal{E}$ and $\mathcal{R}$, and gas permeances $\mathit{\Pi}$ (providing a selectivity α^* for each stage). In this code, each stage is considered as a "black-box" with input flows and concentrations.

The model was used to investigate the impact of different parameters (e.g., $\mathcal{E}$, $\mathcal{R}$, α) on the number of stages, surface area and compression power based on the purging scenarios proposed for the solid blanket. The total number of stages was found to be highly impacted by the separation factor α, enrichment $\mathcal{E}$ and recovery $\mathcal{R}$. For instance, with $\mathcal{E} \geq 20$, $\mathcal{R} \geq 90\,\%$ and $\gamma = 20$, the number of stages decreases from 15 to separate H_2 from He ($\alpha \approx 1.4$) down to 6 to separate Q_2O from He ($\alpha \approx 2.2$) The higher the number of stages, the higher is the power consumption necessary to run it and the higher is the required membrane surface area. Due to the higher separation factor for Q_2O/He, a more compact system with no more than 6 stages, operated with less than 4 MW and requiring $\sim 10^2\,\mathrm{m}^2$ of total surface area could be sufficient. These results demonstrate the high impact of the purge gas composition on the configuration of the required membrane cascade, ultimately impacting the applicability of using zeolite membranes in the pre-concentration stage (first TERS sub-system).

The feasibility of the membrane cascade in terms of number of stages, power consumption and tritium inventory for the two purge gas scenarios is discussed in the following chapter with the focus on the recovery of Q_2O from He.

Chapter 7

Membrane cascade for the separation of Q_2O from He in the TERS

7.1 Required separation performances for the membrane cascade in the TERS

The Tritium Extraction and Removal System (TERS) aims at recovering the tritium produced in the blanket to ensure a continuous delivery (e.g., in HT or DT form) to the tritium plant. Several publications have discussed the importance of having an efficient TERS with high throughputs for a fusion reactor with high tritium production rates such as DEMO to ensure the tritium self-sufficiency [43, 201–203]. For whichever blanket design under development in the EUROfusion consortium, tritium extraction efficiencies of at least 80 % have been considered [6, 204, 205].

The diagram of figure 7.1 displays a system level view of the TERS for the solid

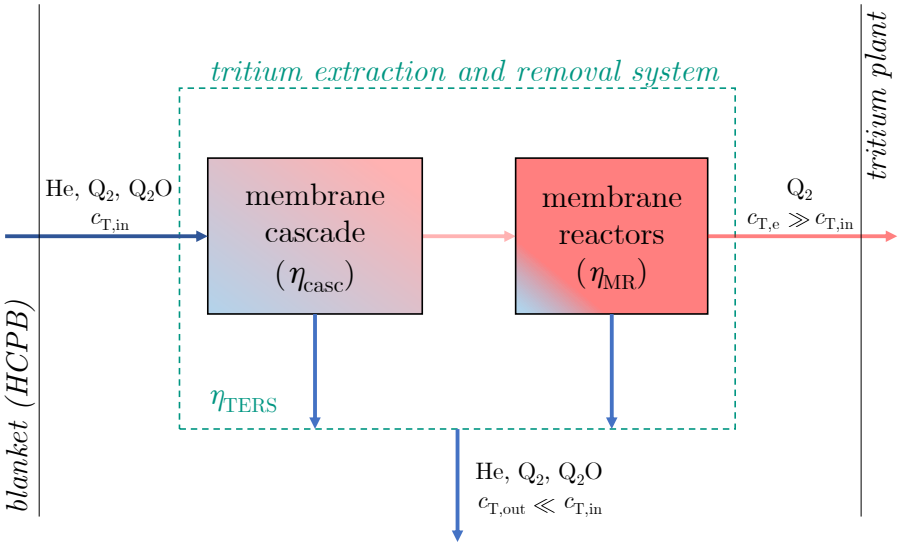

Figure 7.1: Diagram of the tritium extraction and removal system for the solid blanket, evidencing the separation efficiencies of the sub-systems. Q = H, D, T.

blanket (i.e., HCPB) for the approach relying on membrane technologies with two sub-systems: (i) zeolite-based membrane cascade and (ii) Pd-based membrane reactors. The purge gas coming from the blanket arrives at the inlet of the TERS with an initial tritium concentration $c_{\mathrm{T,in}}$. Then, the membrane cascade separates the tritiated species from helium with an efficiency η_{casc} and the downstream flow[1] is detritiated by the membrane reactors operated with an efficiency η_{MR}. The tritium concentration in the detritiated stream $c_{\mathrm{T,out}}$ is related with the overall TERS efficiency $\eta_{\mathrm{TERS}} = \eta_{\mathrm{casc}}\eta_{\mathrm{MR}}$ according to equation (7.1).

$$c_{\mathrm{T,out}} = (1 - \eta_{\mathrm{TERS}})c_{\mathrm{T,in}} \tag{7.1}$$

An extraction efficiency $\eta_{\mathrm{casc}}\eta_{\mathrm{MR}} > 80\,\%$ implies that $\eta_{\mathrm{casc}} \geq 90\,\%$ and $\eta_{\mathrm{MR}} \geq 90\,\%$. Thus, the minimum recovery fraction $\mathcal{R}$ of the membrane cascade is 90 % and the enrichment factor $\mathcal{E}$ is defined by the desired concentrations and flows at the inlet of the MR to allow its operation with reasonable costs and efficiencies. According to the discussions presented in the previous chapter, the increase of $\mathcal{E}$ leads to higher concentrations of Q_2 or Q_2O and lower total flows at the outlet of the last stage, improving the operation of the membrane reactors[2]. However, the number of stages increases with $\mathcal{E}$, hence increasing the size and operation complexity of the membrane cascade. Therefore, a trade-off exists to find an optimised design of the sub-systems ingrating the TERS.

There are two main options currently under consideration for the composition of the purge gas used to recover tritium from the ceramic pebbles (detailed discussion given in section 2.3). For the purging with H_2/He (or D_2/He) the gas downstream of the blanket is expected to contain ppm levels of tritiated species in both molecular and oxidised forms. For the purging with H_2O/He (or D_2O/He) the gas composition at the inlet of the TERS is expected to be Q_2O/He with ppm levels of T in Q. Hence, the number of stages integrating the membrane cascade and its feasibility are highly impacted by the dopant (e.g., H_2 or H_2O) and its concentration in the helium flow purging the solid blanket. These aspects are discussed in detail in the following section.

7.2 Feasibility evaluation for the recovery of tritium with a dry purge gas

The recovery of the tritiated species from the ceramics is enhanced by the isotopic exchange reactions between the dopant agent (H_2 or D_2) and the tritiated species at the surface of the pebbles. Consequently, the purge gas composition at the inlet of TERS is expected to be[3]: He (99.8 mol%) + H_2 (0.2 mol%) + HT (few ppm) + H_2O (< 1 ppm) +

[1] Permeate flow from the last stage ($\mathcal{N}$) of the cascade.

[2] Larger Q_2/Q_2O concentrations and lower flows increase the detritiation efficiency of the membrane reactors [57, 58]. Moreover, lower flows imply smaller Pd-based surface areas and hence lower costs.

[3] For the case where H_2 is used as dopant.

HTO (< 1 ppm) [9]. The water molecules are removed from this gas mixture using an hydrophilic adsorption column before the membrane cascade, as proposed in [192]. Thus, the stream feeding the membrane cascade consists of He + Q_2 and the objective is to increase the concentration of Q_2 before the membrane reactors[4].

As discussed in chapters 4 and 5, the separation of Q_2 from He is highly dependent on the mass of the hydrogen isotopologues. From the permeation experiments, selectivities of $\alpha^*_{H_2/He} \approx 1.8$ for H_2/He and $\alpha^*_{HT/He} \approx 1.3$ for HT/He were obtained. However, in actual separation experiments, the separation factor for H_2/He was found to be $\alpha_{H_2/He} \approx 1.4$, and, although no separation experiments were carried out for HT/He, it is expected that $\alpha_{HT/He} \approx \alpha_{D_2/He} \approx 1$ due to the similar masses of HT and D_2 (table 5.5). Consequently, the cascade of MFI membranes would increase the concentration of H_2 in the permeate while the relative concentration for [HT]/[He] would be the same on both permeate and retentate flows (figure 7.2a)). For D_2/He as purge gas, the gas mixture at the inlet of the membrane cascade would be He + D_2 + DT. Since $\alpha_{D_2/He} \approx \alpha_{DT/He} \approx 1$, no separation would take place and thus the concentrations [DT], [D_2] and [He] would be roughly the same in the feed, permeate and retentate streams of the cascade (figure 7.2b)).

The separation of Q_2 from He with zeolite membranes having pores larger than the kinetic diameters of the molecules is challenging since they are weakly adsorbing gases and the separation is determined by the small differences in diffusion (due to their similar masses). Instead, molecular sieving is an interesting alternative separation mechanism which explores the differences in the kinetic diameters of the molecules facing the membrane. Since the kinetic diameter of Q_2 is 0.289 nm, Q_2 could be separated via molecular sieving from He (with a kinetic diameter of 0.255 nm) using a structure with pore diameters d_p in between (0.255 nm < d_p < 0.289 nm). The SOD structure with d_p = 0.27 nm

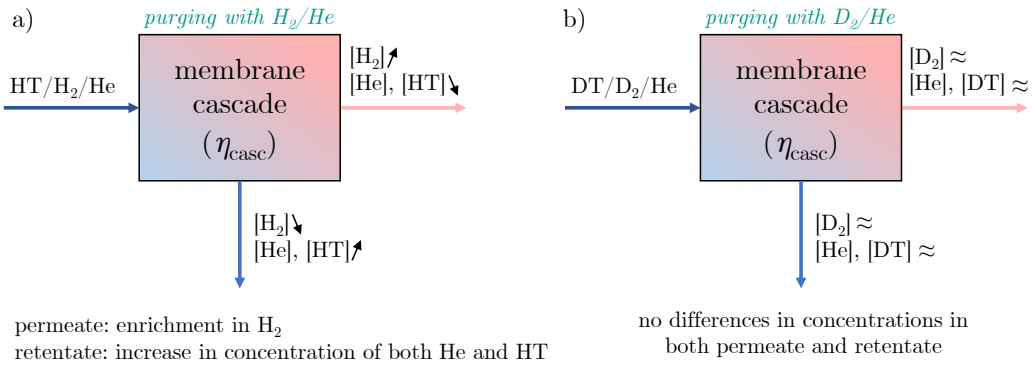

Figure 7.2: Scheme for the separation of Q_2 from He with a MFI-based membrane cascade for a dry purge gas. a) He purge gas with H_2 as dopant, b) He purge gas with D_2 as dopant.

[4]Since no Q_2O is present in the stream, Pd-based permeators without catalyst would suffice for the separation of the enriched Q_2/He stream [192].

(table 3.1) offers a quite interesting possibility for high recovery and enrichment of the Q_2 species in the retentate stream. Although considerably less experimental data is available for SOD membranes[5], H_2 permeances below $10^{-12}\,\mathrm{mol\,m^{-2}\,s^{-1}\,Pa^{-1}}$ have been reported for a 2 µm-thick H-SOD membrane in [206]. These permeances are considerably lower than the values reported for H_2O on the order of $10^{-8}\,\mathrm{mol\,m^{-2}\,s^{-1}\,Pa^{-1}}$. Thus, even though no values are given in this paper for the helium permeance, very high selectivities towards He are expected due to the similar kinetic diameters of He and H_2O (which differ by 4 %). Assuming a selectivity $\alpha^*_{\mathrm{He/Q_2}}$ on the order of $\sim 10^3$ and He permeance of $2.5\times10^{-9}\,\mathrm{mol\,m^{-2}\,s^{-1}\,Pa^{-1}}$, only 5 SOD membrane stages with a total area of $4.3\times10^4\,\mathrm{m^2}$ would suffice to completely separate Q_2 from He ($[Q_2] > 99.9\,\mathrm{mol\%}$ in the retentate flow of the first stage). Therefore, the Q_2-enriched stream with a total flow of $\approx 0.2\,\mathrm{mol\,s^{-1}}$ could be directly sent to the tritium plant, drastically reducing the complexity of the TERS.

In sum, the pre-concentration of tritiated species with MFI-ZSM-5 membranes is not feasible for the scenario with a dry purge. Nevertheless, SOD zeolite membranes offer an interesting option for a compact TERS and they should be further investigated for the separation of Q_2 from He.

7.3 Feasibility evaluation for the recovery of tritium with a wet purge gas

7.3.1 Definition of the input parameters

The results of the separation experiments with D_2O/He and Q_2O/He (with 1 at% T in Q) were presented in chapter 5. With an average value of $\alpha \approx 2.2$, the MFI membranes are capable of enriching Q_2O in He before the membrane reactors in the TERS (figure 7.3). Moreover, the experiment with tritiated water was carried out with similar partial pressures than those expected in the membrane cascade at DEMO conditions. On the one side, the concentrations used for the experiments (2 mol% of Q_2O in He and 200 ppm of tritium) are different from the concentrations expected at the inlet of the TERS (0.02 mol% of Q_2O in He with ppm levels of tritium). On the other side, the experimental pressures were around 1 hPa for Q_2O and 0.01 hPa for the T species[6], which are similar to 4 hPa for Q_2O and 0.02 hPa for the T species at the inlet of the TERS[7].

The performance requirements $\mathcal{R}$ and $\mathcal{E}$ are defined according to: (i) the overall TERS efficiency $\eta_{\mathrm{TERS}} = \eta_{\mathrm{casc}}\eta_{\mathrm{MR}} > 80\,\%$ which gives the condition $\mathcal{R} \geq 90\,\%$, and (ii) the detritiation efficiency of the membrane reactors, highly impacted by the concentration

[5] Due to the small pore diameters of the SOD zeolite, their separation performances are highly impacted by small diameter defects (section 3.3.2). Hence, the synthesis of high-quality SOD membranes is more challenging and the number of experimental studies with these membranes is relatively low.

[6] The absolute feed pressure in the experiment was around 500 hPa.

[7] Assuming a feed pressure of 20260 hPa, for $\gamma = 20$ and $p_{\mathrm{p}} = 1013$ hPa, and 1 ppm of T.

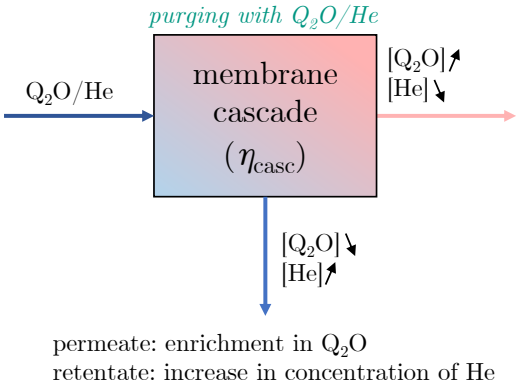

Figure 7.3: Scheme for the separation of Q_2O from He with a membrane cascade with a MFI-based membrane cascade for a wet purge gas.

of Q_2O at the inlet, which sets a minimum value for $\mathcal{E}$. Therefore, the objective of the membrane cascade is to increase the Q_2O concentration at the last stage of the enriching section so that the membrane reactors can efficiently detritiate the incoming water.

Several experimental studies have been published by the TLK during the past decade to investigate the decontamination efficiencies of Pd-based membrane reactors at various conditions (e.g., inlet concentration) [58–60]. Large decontamination factors[8] on the order of 5000 were reported in [60] for 1 mol% Q_2O in He with $5-7$ at% T in Q. Hence, using these results as reference and considering that the stream feeding the membrane cascade has a composition of 0.02 mol% of Q_2O in He, the number of stages will be calculated using $\mathcal{E} \geq 50$, which is a stricter condition than $\mathcal{E} \geq 20$ considered in the previous chapter.

The resulting number of stages, surface area, power consumption and tritium inventory are presented in the following section using the input parameters displayed in table 7.1. The Q_2O/He separation factor and corresponding permeances are the average of the exprimental values: $\alpha = 2.2$, $\Pi_{Q_2O} = 6.08 \times 10^{-7}\,\mathrm{mol\,m^{-2}\,s^{-1}\,Pa^{-1}}$, $\Pi_{He} = 2.38 \times 10^{-7}\,\mathrm{mol\,m^{-2}\,s^{-1}\,Pa^{-1}}$ (runs #1, 3, 4, 5 in table 5.9). Furthermore, consistently with the input values considered in chapter 6, the total feed flow is equal to $F_f^{inj} = 0.4\,\mathrm{kg\,s^{-1}} \approx 100\,\mathrm{mol\,s^{-1}}$ and the pressure of the permeate flows (initially at 1.013×10^5 hPa) is in-

Table 7.1: Input values for the dimensioning of the membrane cascade for the recovery of Q_2O from He.

	Values		Values		Values
x_{f,Q_2O}	0.02 mol%	F_f^{inj}	$100\,\mathrm{mol\,s^{-1}}$	η_e	82 %
$x_{f,He}$	99.8 mol%	Π_{He}	$2.38 \times 10^{-7}\,\mathrm{mol\,m^{-2}\,s^{-1}\,Pa^{-1}}$	c_p	$5190\,\mathrm{J\,kg^{-1}\,K^{-1}}$
$\mathcal{E}$	≥ 50	Π_{Q_2O}	$6.08 \times 10^{-7}\,\mathrm{mol\,m^{-2}\,s^{-1}\,Pa^{-1}}$	c_V	$3118\,\mathrm{J\,kg^{-1}\,K^{-1}}$
$\mathcal{R}$	≥ 90 %	γ	20	b	3
α^*	6.2 ($\alpha \approx 2.2$)	p_p	1.013×10^5 hPa		

[8] Defined as the ratio of the concentrations at the inlet/outlet of the reactor ($DF = x_{f,Q_2O}/x_{r,Q_2O}$).

creased with three-stages compressors ($b = 3$) to ensure $\gamma = 20$ with an efficiency of $\eta_e = 82\,\%$.

7.3.2 Number of stages and surface area

A 7-stages membrane cascade is required to fulfill the design requirements ($\mathcal{E} \geq 50$, $\mathcal{R} \geq 90\,\%$) and the flows, concentrations, surface area and power consumption throughout are given in table 7.2. From the feeding flow of $100\,\mathrm{mol\,s^{-1}}$ with 0.02 mol% Q_2O (stage 3), the cascade produces two outlet streams (at the end of both stripping and enriching sections): $98.3\,\mathrm{mol\,s^{-1}}$ with 0.002 mol% Q_2O (stage 1) and $1.7\,\mathrm{mol\,s^{-1}}$ with 1.070 mol% Q_2O (stage 7). The surface area and power consumption per stage is directly related with the corresponding processing flows. For instance, stage 3 is the feeding stage and hence it has the largest throughput, surface area and power consumption. The power associated with the injection stage is the sum of the compression of the incoming purge gas flow $F_\mathrm{f}^\mathrm{inj}$ (1.11 MW) and the permeate flow F_p^3 (0.81 MW). The total required surface area is $\approx 513\,\mathrm{m^2}$, which is roughly two orders of magnitude lower than the SOD-based cascade for the dry purge scenario (section 7.2). The total power to run the cascade would be around 4 MW, which is 0.8 % of the 500 MW output net power of the 2015 EU-DEMO design [19].

7.3.3 Tritium inventory

The values given in table 7.2 are expected to be reached at steady-state, and the corresponding inlet and outlet tritium mass-flows of the cascade can be estimated assuming a Q_2O mixture mainly consisting of D_2O with 1 ppm of DTO[9] ($M_{Q_2O} = 20.02\,\mathrm{g\,mol^{-1}}$).

Table 7.2: Concentrations, flows, surface area and power consumption for the 7-stages membrane cascade. The input values are given in table 7.1. Stage 3 is the injection stage.

	stage k	y_{p,Q_2O} (mol%)	x_{r,Q_2O} (mol%)	F_p ($\mathrm{mol\,s^{-1}}$)	F_r ($\mathrm{mol\,s^{-1}}$)	A_m ($\mathrm{m^2}$)	$\mathcal{P}$ (MW)
	1	0.009	0.002	44.3	98.3	96.6	0.49
	2	0.020	0.004	64.2	142.6	140.2	0.71
	3	0.044	0.009	73.2	162.5	159.8	0.81+1.11
	4	0.098	0.020	32.2	65.9	71.5	0.36
	5	0.218	0.044	13.8	26.7	30.5	0.15
	6	0.484	0.098	4.5	10.1	12.1	0.06
	7	1.070	0.218	1.7	3.0	3.7	–
Σ						512.6	3.69

[9] Although there are no studies on the expected tritium concentration in the wet purge gas downstream of the blanket, it is assumed to be similar to the values estimated for a dry purge (few ppm) [9].

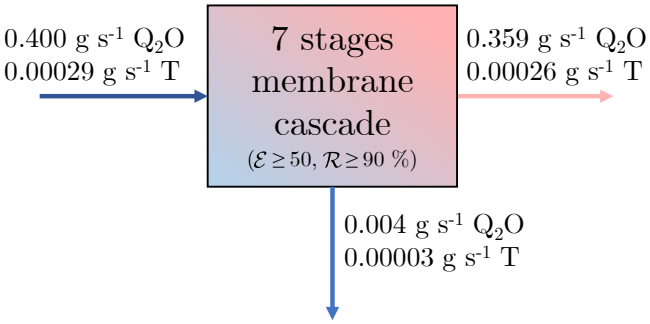

Figure 7.4: Scheme for the input/output Q_2O and T flows of the membrane cascade designed to separate Q_2O from He.

The DTO molar-flow is $1 \times 10^{-4}\,\mathrm{mol\,s^{-1}}$ which is equivalent to a mass-flow of $2 \times 10^{-3}\,\mathrm{g\,s^{-1}}$, and since $M_\mathrm{T}/M_\mathrm{DTO} \approx 0.143$, the mass-flow of atomic tritium at the inlet is estimated to be $2.87 \times 10^{-4}\,\mathrm{g\,s^{-1}}$. With the same reasoning, the tritium mass-flows at the outlet of the cascade are $2.61 \times 10^{-4}\,\mathrm{g\,s^{-1}}$ (enriching section) and $0.26 \times 10^{-4}\,\mathrm{g\,s^{-1}}$ (stripping section), as schematically represented in figure 7.4.

The inventory of the whole cascade is the amount of tritium that remains inside the cascade at all time and it is calculated by the product of the T mass-flow at the inlet with the time t_eq after which the steady-state is reached. According to the Q_2O/He separation experiments, the steady-state conditions were reached within 3 min (figure 5.8). Hence, a simple estimation of the tritium inventory is provided here by assuming that this equilibration time is the same for all stages integrating the cascade since they are dimensioned proportionally to the processing flows. As a result, the tritium inventory of the cascade is estimated to be $m_\mathrm{T} = 2.9 \times 10^{-4} \times 180 \approx 52\,\mathrm{mg}$, neglecting the time for the gas to flow between stages and non-linearities introduced by the operation of the cascade.

7.3.4 Physical configuration of the stages

The membranes used in the experiments were of tubular shape with a single channel, suitable for lab scale throughputs (on the order of $10^{-5}\,\mathrm{mol\,s^{-1}}$). However, for larger throughputs up to large scale applications, multi-channel membranes are necessary to maximise the ratio between the permeation area and membrane volume. The schematic diagram of a multi-channel membrane integrating N_ch channels with a diameter of d_ch is displayed in figure 7.5. In each channel the feed flow is equal to $F_\mathrm{f}^k/N_\mathrm{ch}^k$, where F_f^k is the total feed flow at the stage inlet. This configuration is used in this work to determine the physical dimensions for each stage k: the number of channels N_ch^k, stage diameter d_stg^k and length L_stg^k.

Recent studies have reported the scaling-up of tubular ceramic membranes in which the membrane tubes are placed inside a ceramic element (so-called monolithic structure) [207,

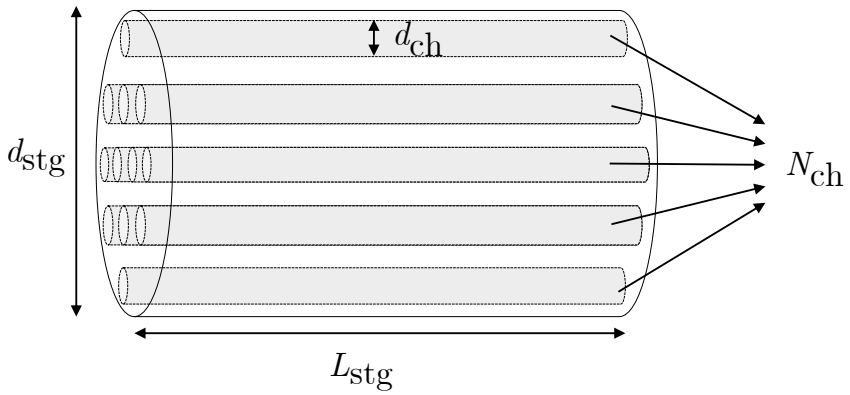

Figure 7.5: Scheme of a multi-channel membrane used as reference for scaling-up. Length: L_{stg}, outer diameter: d_{stg}, number of channels: N_{ch}, channels diameter: d_{ch}.

208]. The geometrical values provided in these two works are summarised in table 7.3. On the one side, the work [208] presents a 12 m^2 DDR zeolite-type membrane element for gas separation but does not explicitly mention the number of channels and their diameters. On the other side, the work [207] presents a 10 m^2 ceramic membrane for nanofiltration and therefore some differences in the design may arise when used for gas separation. Nevertheless, the more complete information from [207] was used as reference for the sizing of the stages in this thesis as follows:

- each channel has a diameter of $d_{\mathrm{ch}} = 3\,\mathrm{mm}$;
- the ratio between the cross-section of all channels ($N_{\mathrm{ch}}^k \pi d_{\mathrm{ch}}^2/4$) and the cross-section of the stage ($\pi d_{\mathrm{stg}}^{k^2}/4$) is constant and given by:

$$\psi = N_{\mathrm{ch}}^k \left(\frac{d_{\mathrm{ch}}}{d_{\mathrm{stg}}^k} \right)^2 \approx 0.48 \tag{7.2}$$

- the ratio between the diameter and length of the stage is constant and given by:

$$\sigma = \frac{d_{\mathrm{stg}}^k}{L_{\mathrm{stg}}^k} \approx 0.125 \tag{7.3}$$

N_{ch}^k, L_{stg}^k and d_{stg}^k are determined iteratively: with an initial guess for L_{stg}^k, the number of channels N_{ch}^k and the diameter of the stage d_{stg}^k are calculated with equations (7.4) and (7.2), respectively. Then, $d_{\mathrm{stg}}^k/L_{\mathrm{stg}}^k$ is compared to $\sigma = 0.125$ and L_{stg}^k is varied until condition (7.3) is verified.

$$N_{\mathrm{ch}}^k = \frac{A_{\mathrm{m}}^k}{\pi d_{\mathrm{ch}} L_{\mathrm{stg}}^k} \tag{7.4}$$

The physical dimensions for each stage are presented in table 7.4. Stage 3 is the largest with a diameter of 341 mm and a length of 2730 mm, whereas stage 7 is the smallest with $d_{\mathrm{stg}}^7 = 97\,\mathrm{mm}$ and $L_{\mathrm{stg}}^7 = 777\,\mathrm{mm}$. The footprint of the space required to accommodate this

Table 7.3: Physical dimensions of membrane modules available in the literature for large throughput applications. L_{stg}: module length, d_{stg}: module diameter, d_{ch}: channels diameter, N_{ch}: number of channels, A_{stg}: membrane area, V_{stg}: module volume. The entries with − are not provided by the manufacturer.

L_{stg} (m)	d_{stg} (m)	d_{ch} (mm)	N_{ch} (-)	A_{stg} (m^2)	A_{stg}/V_{stg} ($m^2\ m^{-3}$)	Ref.
1.200	0.150	2 − 3	1200	10	640	[207]
1.000	0.180	−	−	12	472	[208]

Table 7.4: Physical dimensioning of the stages integrating the membrane cascade presented in table 7.2. Δp_f is the fractional decrease of the pressure along a stage calculated with equation (7.5).

stage k	L_{stg} (m)	d_{stg} (m)	N_{ch} (-)	V_{stg} (m^3)	v_f ($m\,s^{-1}$)	Re (-)	Δp_f (%)
1	2.310	0.289	4400	0.151	111.1	26802	0.19
2	2.620	0.326	5678	0.219	126.0	30399	0.26
3*	2.730	0.341	6211	0.250	131.3	31677	0.29
4	2.080	0.259	3588	0.110	100.1	24137	0.14
5	1.560	0.196	2043	0.047	75.1	18106	0.06
6	1.150	0.143	1096	0.019	55.4	13353	0.03
7	0.777	0.097	505	0.006	37.4	9030	0.01

membrane cascade considering also ancillary equipment (e.g., compressors) was estimated to be around 19.4 m^2 (refer to Appendix H). Table 7.4 also presents the relative pressure drops expected along the feed/retentate side of the channels calculated using the Darcy-Weisbach relation, expressed by equation (7.5) [209]. ρ is the density of the gas (assumed to be that of helium, equal to 3.2 $kg\,m^{-3}$ at 2.0 MPa and 298 K [210]) and $\langle v_f^k \rangle$ is the time averaged speed of the gas along each membrane channel[10].

$$p_f(0) - p_f(L_{stg}^k) = 4f\frac{\rho}{2}\langle v_f^k \rangle^2 \frac{L_{stg}^k}{d_{ch}} \tag{7.5}$$

The Blasius formula, given by equation (7.6), was used to estimate the friction factor f since the flow is turbulent under these speed and geometry conditions (i.e., Reynolds number[11] Re > 2100) [209].

$$f = \frac{0.0791}{\mathrm{Re}^{1/4}} \tag{7.6}$$

The pressure drops at the end of each stage are not expected to exceed 0.3 % of the feed pressure (20.26×10^5 Pa), which validate the initial assumption that the use of compressors

[10]For simplification, the fraction of the feed that permeates was not considered. As a result, the Reynolds number and pressure drop values presented in table 7.4 are considered to be conservative.

[11]The values for the Reynolds number were calculated with $\mathrm{Re} = v_f^k d_{ch}\rho/(2\mu_d)$, where $\mu_d \approx 1.99 \times 10^{-5}$ Pa s is the dynamic viscosity of the gas mixture (assumed to be equal to the viscosity of helium) at 2.0 MPa and 298 K [209, 210].

for the permeate streams is sufficient to ensure enough driving force for permeation along the cascade. The dimensions for each stage could be reduced by decreasing the diameter of the channels d_{ch} at the expense of larger pressure drops. For instance, with $d_{\mathrm{ch}} = 1\,\mathrm{mm}$, the volume occupied by each stage is decreased by 67 % but the pressure drops would increase by a factor of 10.

The sizing estimations presented are preliminary and consist in a methodology proposal. Further studies are required towards an optimised design, considering different aspects neglected here such as manufacturing constraints (e.g., the construction and implementation of equally sized stages would lead to lower costs). Fluid dynamic studies would also be required to accurately simulate the flows profiles and distribution inside the module channels. Due to the relatively large number of channels, the physical distribution of the channels per stage element could differ from those presented in [207, 208], to ensure that the permeate streams of the inner channels can be efficiently removed. Last but not least, the unprecedented dimensions of these stages would raise the need for high-quality synthesis of large surface areas of MFI zeolite layers on the large ceramic monolithic structure.

7.4 Summary of the results

The number of stages of the membrane cascade for the TERS of DEMO is highly dependent on the purge gas scenario. For a dry purge gas (He with H_2 or D_2), the enrichment of Q_2 in He is not feasible with MFI-ZSM-5 membranes since the molar masses are too similar to allow separation by diffusion and the MFI pore diameters are larger than the kinetic diameters of the molecules. On the contrary, very high separation factors are expected with SOD membranes with pore diameters smaller than the kinetic diameters of Q_2. Hence, only helium permeates through the membrane and all Q_2 molecules remain on the feed/retentate. Consequently, this Q_2 stream could be sent directly to the tritium plant for isotope separation. Nevertheless, high-quality synthesis of SOD zeolite layers is challenging due to the presence of defects.

With a wet purge (He with H_2O or D_2O), higher separation factors are obtained due to the strong adsorption of water onto the zeolite structure. Using $\mathcal{E} \geq 50$ and $\mathcal{R} \geq 90\,\%$ with the experimental value for $\alpha \approx 2.2$ as input, the resulting cascade consists of 7 stages for the enrichment of Q_2O in He. This cascade has a total permeation area of $513\,\mathrm{m}^2$, a total compression power of 4 MW and a tritium inventory of 0.36 g at steady-state. These reasonable values suggest that the MFI-ZSM-5 membranes are interesting for the TERS with a wet purge. Nevertheless, physically large stages (up to 2.73 m-long with thousands of channels) would be necessary. These results are compared with those obtained for the reference TERS technology based on hydrophilic adsorption columns in the next chapter.

Chapter 8

Comparison between membrane and adsorption technologies for the TERS

8.1 Dimensioning of the adsorption columns for Q_2O removal

8.1.1 The Temperature Swing Adsorption process

The baseline technology for the TERS relies on adsorption columns filled with hydrophilic zeolite pellets through which the Q_2O/He mixture coming from the blanket flows. The typical storage capacities of these materials are around 20 wt%[1] [211]. The adsorption efficiency is dependent on several factors such as operation temperature, moisture content, flows distribution, residence time and amount of water adsorbed on the zeolite [56, 211, 212]. Due to the low content of moisture present in the purge gas feeding the adsorption column (0.02 mol% or 0.03 kPa at 298 K), the maximum loading ratio is expected to be around 13 wt%[2] [213]. A quasi-continuous tritium extraction from the purge gas is attained by implementing two or more adsorption colums in parallel. In this process, one (or more) vessel dries the incoming stream at 298 K ("adsorption mode") whereas another one is regenerated with a heated gas at 573 K ("regeneration mode"). This process is designated "Temperature Swing Adsorption" (TSA) and it is widely used in the industry for the dehydration of streams [55, 56].

Figure 8.1 presents a schematic diagram of the TSA with three adsorption columns. With this configuration, two columns are always drying the incoming stream while the third one is under regeneration. For a 24 h-long cycle, each bed is in "adsorption mode" for 16 h and in "regeneration mode" for 8 h [214]. The regeneration of one column starts when the loading ratio reaches 13 wt%, which is done by purging the zeolite pellets with clean helium slowly heated up to the desired temperatures (typically 573 K with 1 h ramping time [56]). At these conditions, Q_2O is desorbed from the zeolite structure and continuously purged out of the vessel. This Q_2O/He stream is routed to a Pd-based membrane

[1] Given by the ratio between the mass of stored water and mass of zeolite.

[2] From the adsorption isotherms for zeolite 4A obtained at different vapor partial pressures in [213].

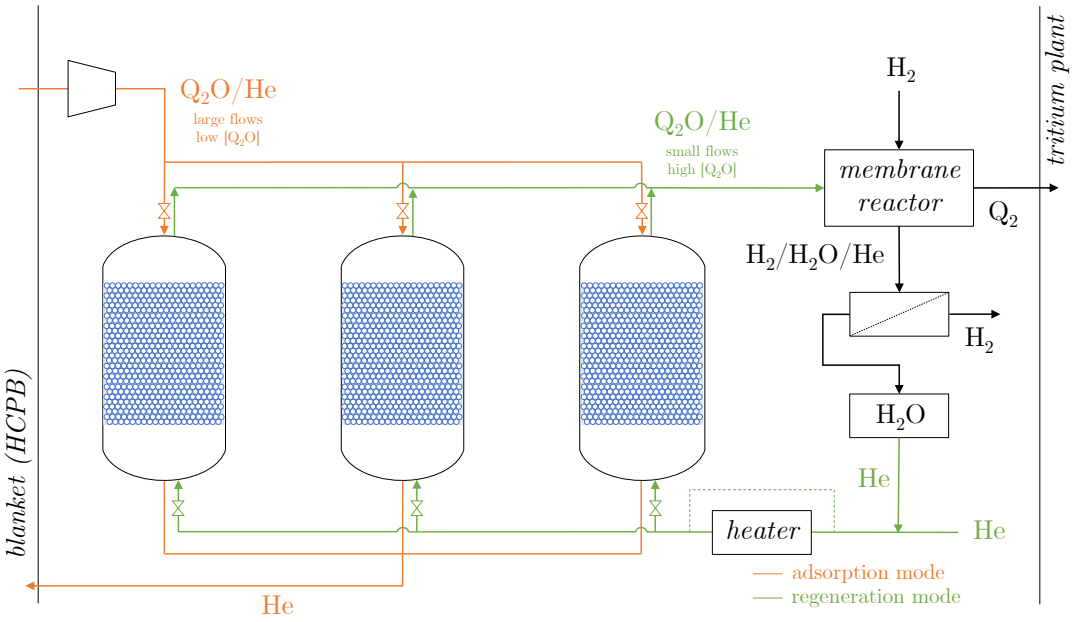

Figure 8.1: Scheme of the Temperature Swing Adsorption process for the extraction of Q_2O from He. Three adsorption columns filled with zeolite pellets are presented. Two columns are operated under "adsorption mode" (shown in orange), while the third one is operated under "regeneration mode" at elevated temperatures (shown in green). A membrane reactor is used to produce continuous Q_2 flows out of the incoming Q_2O/He mixture (during regeneration). The heater is by-passed for the cooling of the columns.

reactor operated under isotope swamping mode with H_2 in counter-current. As a result of isotopic exchange reactions, a tritium enriched Q_2 stream is continuously produced and sent to the tritium plant, where the hydrogen isotopes are separated for the recovery of D and T for plasma re-fueling. The decontaminated mixture downstream of the MR is sent to a permeator for H_2 removal and the H_2O is removed with an additional drying step. The helium flow used to regenerate each column is chosen to ensure an efficient Q_2O removal, but also to guarantee that the membrane reactor can be operated with reasonable dimensions and high decontamination factors (high Q_2O concentrations). At the end of the regeneration step, the adsorption column is cooled with helium down to its original temperature (for the next adsorption phase).

8.1.2 Sizing and operation of the adsorption columns

Using the same input vapor and tritium flows as used in the previous chapter for the membrane cascade (Q_2O: $4 \times 10^{-1}\,g\,s^{-1}$, T: $2.9 \times 10^{-4}\,g\,s^{-1}$), simple calculations were performed to estimate the dimensions of the zeolite 4A adsorption columns, the power consumption required to operate them and the tritium inventory, with the following assumptions:

1. maximum storage capacity before regeneration set to 13 wt% and no isotopic effects on the adsorption process considered;

2. typical packing density values for zeolites are in the range $690 - 720\,\mathrm{kg\,m^{-3}}$ [55]. In these estimations, the value of $\rho_{\mathrm{zeo}} = 700\,\mathrm{kg\,m^{-3}}$ is used;

3. the ratio between the length and diameter of the vessel is set to a minimum of 2 to promote a favourable flow distribution [56, 215];

4. the adsorption of water onto zeolites is exothermic (with typical values around $60\,\mathrm{kJ\,mol^{-1}}$ [211, 213]) and 1 % of the adsorbable component in the stream could lead to an increase of 50 °C in the temperature [216]. Consequently, the equilibrium is disturbed and the adsorption is expected to decrease. Nevertheless, since the estimation of the temperature increase and its impact on the adsorption requires a detailed modelling of the flows distribution inside the vessel, the increase in temperature is neglected;

5. the vessels are usually designed with two dome-like sections at the top/bottom with a cylindrical section in the middle where the zeolite pellets are placed (refer to figure 8.1). For simplicity, only cylindrical vessels (without domes) are considered in the calculations below.

During one day, the total amount of Q_2O sent to the TERS is 34.6 kg. Thus, in a TSA system with three columns, each bed should be regenerated after accumulating 11.5 kg (which corresponds to 16 h under adsorption mode). Thus, a zeolite mass of $m_{\mathrm{zeo}} \approx 88.7\,\mathrm{kg}$ (assumption 1.), corresponding to a volume of $V_{\mathrm{zeo}} \approx 0.13\,\mathrm{m^3}$ (assumption 2.), is required for each bed. The volume V_{zeo} is used to estimate the diameter and length of the vessel accommodating the zeolite pellets. The cross-section of the column A_{col} is determined with equation (8.1), where $F_{\mathrm{f}} = 100\,\mathrm{mol\,s^{-1}} = 2.24\,\mathrm{m^3\,s^{-1}}$ at STP is the inlet flow (from the blanket) and $v_{\mathrm{typ}} = 0.15 - 0.6\,\mathrm{m\,s^{-1}}$ is the typical speed recommended for reasonable residence times and uniform flow distribution inside the vessel [212].

$$A_{\mathrm{col}} = \frac{F_{\mathrm{f}}}{v_{\mathrm{typ}}} \tag{8.1}$$

With an average value of $v_{\mathrm{typ}} = 0.38\,\mathrm{m\,s^{-1}}$, $A_{\mathrm{col}} = 5.97\,\mathrm{m^2}$ and thus the diameter of the vessel is $d_{\mathrm{col}} = 2.8\,\mathrm{m}$ with a minimum lenght of $L_{\mathrm{col}} = V_{\mathrm{zeo}}/A_{\mathrm{col}} = 0.021\,\mathrm{m}$. Thus, the ratio between the length and diameter of the column would be around 0.03, much lower than the recommended value of 2 (assumption 3.). Therefore, the diameter of the vessel should be decreased, at the expense of higher gas speeds (to keep the throughput constant). Consequently, the adsorption efficiency is expected to decrease due to the lower residence times, which is proposed to be compensated by increasing L_{col} proportionally

to $v_{\text{actual}}/v_{\text{typ}}$, where v_{actual} is the actual speed through the lower diameter column. With this approach, the resulting dimensions of the column are $d_{\text{col}} = 0.90\,\text{m}$ and $L_{\text{col}} = 1.9\,\text{m}$. Thus, the column has a volume of $1.2\,\text{m}^3$, which corresponds to 833 kg of zeolite with a water storage capacity of 108 kg (assumption 2.).

The pressure drop across the adsorption column can be estimated with the so-called Ergun equation typically used for packed columns [209]. This equation is presented in (8.2), where ϵ is the zeolite porosity, d_{pe} is the diameter of the pellets and $g = \rho v_{\text{actual}}$. With $\epsilon = 0.39$, $d_{\text{pe}} = 0.3\,\text{mm}$ (as considered in [217]) and $\rho = 0.24\,\text{kg}\,\text{m}^{-3}$ (density of helium at 150 kPa and 298 K), the pressure drop across the adsorption column is estimated to be 47.0 kPa. Since the dried helium at the exit of the column will be used for further purging (at 150 kPa), a compressor before the inlet of the adsorption column should be used to increase the gas pressure up to 200 kPa[3] (also depicted in figure 8.1).

$$\Delta p = \frac{1-\epsilon}{\epsilon^3}\frac{g^2}{\rho d_{\text{pe}}}\left[150\left(\mu\frac{1-\epsilon}{d_{\text{pe}}g}\right)+\frac{7}{4}\right]L_{\text{col}} \tag{8.2}$$

The major power consumption to run this system is the energy required to compress the feeding gas up to 200 kPa and to regenerate the adsorption column at 573 K. The power required for a one-stage compressor is estimated to be[4] 125 kW. The power provided to the regeneration gas is estimated with equation (8.3), where m_{ads} is the mass of adsorbent and $c_{p,\text{ads}}$ its specific heat capacity; m_{vessel} is the mass of the stainless steel vessel[5] and $c_{p,\text{vessel}}$ its specific heat; $m_{\text{Q}_2\text{O}}$ mass of adsorbed Q_2O and $\Delta H_{\text{ads,Q}_2\text{O}}$ the enthalpy of adsorption/desorption. The values of these quantities are given in table 8.1.

$$\mathcal{P}_{\text{reg}} = 1.2 \times \frac{2 \times (m_{\text{ads}}c_{p,\text{ads}} + m_{\text{vessel}}c_{p,\text{vessel}})\Delta T_{\text{g}} + m_{\text{Q}_2\text{O}}M_{\text{Q}_2\text{O}}\Delta H_{\text{ads,Q}_2\text{O}}}{\Delta t_{\text{ramp}}} \tag{8.3}$$

The factor of 2 in equation (8.3) takes into account the power required for the cooling of the column (i.e., after the Q_2O removal). A heating losses factor of 20 % is also included and $\Delta t_{\text{ramp}} = 1\,\text{h}$ is the heating/cooling ramping time. The total power for the complete regeneration step is estimated to be 200 kW. Since in a 24 h cycle each column is regenerated once, the total power required to operate the TSA process for the TERS is $125 + 3 \times 200 = 725\,\text{kW}$.

As mentioned previously, each adsorption column is under adsorption mode for 16 h and hence, for a 24 h cycle, two adsorption columns are always operated simultaneously (with an overlap time frame of 8 h). This means that the tritium inventory in steady-state

[3] An excess in the pressure is introduced to compensate for pressure losses along the processing pipework connecting the adsorption column and the blanket.

[4] Estimated with equation (6.4) using $b = 1$, $c_p = 5190\,\text{J}\,\text{kg}^{-1}\,\text{K}^{-1}$, $c_V = 3118\,\text{J}\,\text{kg}^{-1}\,\text{K}^{-1}$, $T_{\text{g}} = 298\,\text{K}$, $\eta_{\text{e}} = 82\,\%$ with a pressure ratio of 1.33.

[5] Calculated assuming a wall thickness of 10 mm. With this value, the volume of the stainless steel hollow cylindrical column is estimated to be $0.067\,\text{m}^3$. Therefore, using the density value for the stainless steel 316 ($7960\,\text{kg}\,\text{m}^{-3}$ [218]), a mass of 532 kg of steel is required per column.

Table 8.1: Values used for the calculation of the heating/cooling power of the adsorption columns. Specific heat values given at 298 K.

	Value	Ref.
m_{ads} (kg)	833	
$c_{p,\text{ads}}$ (J kg K^{-1})	910	[219]
m_{vessel} (kg)	532	
$c_{p,\text{vessel}}$ (kJ kg K^{-1})	510	[218]
m_{Q_2O} (kg)	11.5	
$\Delta H_{\text{ads},Q_2O}$ (kJ mol^{-1})	63	[211]
M_{Q_2O} ($10^{-3}\,\text{kg mol}^{-1}$)	20.02	
ΔT_g (K)	275	

operation is equivalent to 1.5 columns. Since one column is designed to store 11.53 kg of Q_2O, the amount of water inventory in steady-state is 17.30 kg, which corresponds to 12.4 g of tritium (half of the total amount of tritium sent to the TERS during 1 day).

Although these estimations are based on several assumptions and simplifications, a comparison with the results obtained for the membrane cascade can be done in view of evaluating their feasibility for the TERS.

8.2 Comparison of the feasibility of membrane-based and adsorption-based technologies for the TERS

Table 8.2 summarises the most relevant results concerning the application of a membrane cascade and adsorption columns for the TERS of DEMO. As expected, the main advantage of the membrane cascade is its very low tritium inventory (around 0.2 % of the total amount feeding the cascade) due to its inherent continuous processing. In steady-state the inventory of the adsorption columns is 50 % of the total amount of tritium extracted from the ceramics per day, which may raise concerns on safety and fuel man-

Table 8.2: Comparison of major parameters of interest to run the TERS in steady-state. The tritium inventory is also given as a fraction of the total amount of tritium $m_{\text{T,tot}}$ sent to the columns per day. During a 24 h cycle each adsorption column is regenerated once.

	Membrane cascade	Adsorption (TSA)
$m_{\text{T,inv}}$ (g)	0.052 (0.2 %)	12.411 (50 %)
Regeneration steps (-)	0	3
$\mathcal{P}_{\text{tot}}$ (MW)	3.69	0.72
$\mathcal{P}_{\text{tot}}/m_{\text{T,tot}}$ (MW g^{-1})	0.164	0.058
A_{room} (m^2)	19.4	15.7
V_{room} (m^3)	63.6	59.7

agement inside the reactor. On the other side, the need to use compressors throughout the cascade to increase the feed pressure up to 2.0 MPa (ensuring enough driving force for permeation and suitable separation performances) leads to a power consumption almost 4 times higher than for the TSA process[6]. Dividing the total power by the mass of tritium delivered to the membrane reactors[7] in one day (22.5 g for the cascade, 12.4 g for the TSA), the specific power to run the cascade is 3 times lower. Rough estimations of the area (footprint) and volume of the room to accommodate the membrane cascade and adsorption columns are given in Appendix H. A larger area and a slightly larger room volume is required to install the membrane cascade together with the compressors.

Furthermore, the applicability of these technologies at DEMO scale should also take into consideration the following aspects:

- manufacturing issues and costs;
- complexity of operation;
- waste production;
- Technology Readiness Level (TRL).

The scaling-up of zeolite membranes towards large-scale applications is an identified issue in the membranes community. On the one side, the manufacturing of high-quality zeolite membranes (i.e., "defect-free") is challenging and therefore only a few suppliers exist for technical-to-industrial scale applications (mainly NaA membranes). On the other side, the cost of the membranes[8] is very high, on the order of $35000\,€\,m^{-2}$. Consequently, with a total surface area of $513\,m^2$, the membrane costs associated with the cascade would be $18 \times 10^6\,€$, considerably higher than the $9 \times 10^4\,€$ required to fill three adsorption columns with 833 kg of zeolite 4A each[9]. Indeed, the reduction of the surface area has been identified as a key factor for the integration of zeolite membranes in industrial processes [221]. In this publication, a reduction of the currently achievable thicknesses of zeolite layers down to 50 nm is proposed[10] to drive down the capital costs (and sizes) and hence increasing the competitivity of the technology. Thus, considerable efforts have yet to be done for the process intensification of zeolite membranes.

The continuous operation of the membrane cascade with 7 stages seems to be simpler when compared with the monitor and control of water required to switch between adsorption and regeneration steps. In fact, if a column is switched to adsorption mode while

[6]Such high pressures may also result in non-negligibe tritium permeation through the piping towards the coolant.

[7]Placed downstream for the detritiation of Q_2O.

[8]Estimated from the price of the tubular membranes used for the experiments presented in this thesis ($0.0048\,m^2$), with a cost of $170\,€$ per piece (without considering the stainless steel module).

[9]Using a price tag of $35\,€\,kg^{-1}$ for 4A zeolite pellets, according to the information available on the website of Brounell Limited [220].

[10]In contrast with the thicknesses of the zeolilte membranes used in the experiments ($\approx 55 - 67\,\mu m$).

still in regeneration, a forced shutdown on the TERS may be required. Furthermore, the temperature cycles degrade the uptake capacity of the adsorbent. It is recommended that the replacement of the adsorbent (column) must be done after 1000 cycles or every 3 years (at the end of a regeneration step) [56]. For a fusion reactor, the degradation in adsorption capacity with the regeneration cycles may have important impacts on the fuel cycle and therefore more frequent replacements of the columns should be considered. After replacement, an adsorption column is not usable any longer and should be safely disposed as radioactive waste [222].

The TRLs indicate the maturity of the technology to be operated under relevant environments. Using the scale from 1 to 9 adopted by the European Commission[11] [223], the TRL for the zeolite membranes / membrane cascade is 3 ("experimental proof of concept"). On the one side, experiments have been performed with MFI membranes with and without tritium, with and without water at relevant concentrations and partial pressures. On the other side, the experiments were carried out with limited flows (up to 7 orders of magnitude lower than expected for the TERS) and no membrane cascade has been tested yet to demonstrate that 7 stages are sufficient to reach the design performances. Furthermore, few large scale zeolite membranes have been produced. In contrast, the TSA technology with zeolite pellets have been used in the industry for years and this material is routinely used to dry tritiated atmosphere in major tritium labs (technical scale). However, no protoype has been tested yet under relevant DEMO conditions (TRL 7). Therefore, it is suggested that the TRL for the TSA process is 6 ("technology demonstrated in relevant environment").

8.3 Technology assessment: membrane cascade vs adsorption columns

Based on these discussions, the membrane cascade can be compared with the adsorption columns using a list of requirements relevant for the use of these technologies in DEMO. The applied methodology consists in a pairwise comparison between requirements, also used in other technology assessment studies for DEMO [18]. Table 8.3 presents the 10 criteria retained for this comparison. Two criteria are directly compared with each other and a factor 2, 0 or 1 is attributed depending on whether the requirement displayed horizontally is, respectively, "more", "less" or "equally" important than the requirement displayed vertically. The sum of all factors (column "Sum") reflects the importance of a

[11] TRL 1: "basic principle observed", TRL 2: "technology concept formulated", TRL 3: "experimental proof of concept", TRL 4: "technology validated in lab", TRL 5: "technology validated in relevant environment", TRL 6: "technology demonstrated in relevant environment", TRL 7: "system prototype demonstration in operational environment, TRL 8: "system completed and qualified", TRL 9: "actual system proven in operational environment".

Table 8.3: Pairwise comparison between requirements for the technologies integrating the TERS. "2" means that the horizontal criterion is more important than the vertical one; "0" means that the horizontal criterion is less important than the vertical one; "1" means that the horizontal criterion is as important as the vertical one.

	Tritium inventory	Power consumption	Space occupation	Waste production	Complexity of operation	Manufacturing / scalability	Capital costs	R&D investment	Technology Readiness Level	Synergy with fuel cycle / tritium management	Sum	Ranking
Tritium inventory		2	2	1	2	1	2	2	1	1	14	1
Power consumption	0		0	0	1	1	2	0	0	0	4	7
Space occupation	0	2		1	1	0	2	0	0	0	6	5
Waste production	1	2	1		1	0	2	1	0	1	9	4
Complexity of operation	0	1	1	1		0	1	1	0	0	5	6
Manufacturing / scalability	1	1	2	2	2		2	1	1	1	13	2
Capital costs	0	0	0	0	1	0		0	0	0	1	8
R&D investment	0	2	2	1	1	1	2		1	0	10	3
Technology Readiness Level	1	2	2	2	2	1	2	1		1	14	1
Synergy with fuel cycle / tritium management	1	2	2	1	2	1	2	2	1		14	1
										SUM	90	

given criterion and it will be used as weighting or ponderation factor w. Column "Ranking" highlights the importance of each criterion, briefly described below:

1. **"Tritium inventory", "Technology Readiness Level", "Synergy with fuel cycle / tritium management"**: all these three aspects directly influence the feasibility of the tritium extraction and removal system. High tritium inventory raises concerns on safety, impacting the licensing of the technology; a low TRL system has a limited maturity level and hence not DEMO relevant; the interface with the fuel cycle should be flexible enough to guarantee a continuous delivery of tritiated species required for the operation of the fusion reactor;

2. **"Manufacturing / scalability"**: impact the construction of a system with large throughputs, as required for DEMO. The easier the manufacturing process, the more relevant the TERS is;

3. **"R&D investment"**: closely related to the TRL and scalability, the need to develop infrastructures to test a technology for the validation of its performances requires R&D activities, leading to an increase of the costs and the time required to develop a DEMO-relevant process;

4. **"Waste production"**: the minimisation of the radioactive waste produced by a given technology reduces the efforts for its decontamination, decreasing the load on

waste disposal sites (which are planned to handle other components activated along DEMO operation [222]);

5. **"Space occupation"**: the attractiveness of the TERS increases with its modularity and lower footprint;

6. **"Complexity of operation"**: a TERS with a low complexity of operation has a reduced number of devices and parameters to control and monitor;

7. **"Power consumption"**: the power to run a given system with relevant performances should be minimised to reduce its impact on the net power of DEMO;

8. **"Capital costs"**: a cost-efficient TERS is desirable. Nevertheless, the capital costs appear as the least relevant criterion because, in a complex machine such as DEMO ("first-of-a-kind"), the capital costs of large-scale systems are expected to be high (especially those processing tritium, never used at such scale).

The membrane cascade and adsorption columns were evaluated against the requirements given above and the results are presented in table 8.4. The weighting factor found for each requirement is multiplied with a mark p between 0 and 4, where 0 means "unsatisfactory", 1 means "acceptable", 2 means "satisfactory", 3 means "good" and 4 means "very good / ideal". $p \times w$ is the score obtained by a technology for a given criterion, and the

Table 8.4: Ranking matrix for the membrane cascade and adsorption columns.

	Weighting	Membrane cascade		Adsorption columns	
		p	$p \times w$	p	$p \times w$
Tritium inventory	14	3	42	1	14
Technology Readiness Level	14	1	14	3	42
Synergy with fuel cycle / tritium management	14	3	42	1	14
Manufacturing / scalability	13	1	13	4	52
R&D investment	10	1	10	4	40
Waste production	9	4	36	2	18
Space occupation	6	3	18	3	18
Complexity of operation	5	3	15	2	10
Power consumption	4	2	8	4	16
Capital costs	1	0	0	3	3
SUM	90	198		227	

overall sum gives the final score for this technology. The adsorption columns obtained the highest score, benefiting mainly from its maturity. The membrane cascade only scored better in four requirements: "Tritium inventory", "Synergy with the fuel cycle / tritium management", "Waste production", "Complexity of operation". The low TRL of zeolite membranes and the current issues on reproducibility and large-scale manufacturing are highly penalizing for the membranes, despite the important benefits in respect to tritium inventory and management.

The methodology used in this work was followed to correct for subjectivity. Nevertheless, the ranking matrix was found on basis of the knowledge gained during the course of this work and it should be re-evaluated periodically, since (i) the relative importance of the requirements for the TERS technologies (given by w, table 8.3) may change over time and (ii) the marks p attributed to the membranes (table 8.4) should be inline with the latest progresses and developments of this field.

8.4 Summary of the results

The charateristics of the TERS reference process for the separation of Q_2O from He were evaluated with regard to the number of adsorption columns, dimensions, power consumption and tritium inventory. The results were compared with those obtained in the previous chapter for the membrane cascade. This comparison was done by defining and using 10 relevant criteria with a weighting factor associated. The most important requirements were found to be: "Tritium inventory", "Technology Readiness Level", "Synergy with fuel cycle / tritium management". The grid of criteria was applied to the membrane cascade and adsorption columns, with the resulting scores of 198 and 227, respectively. The adsorption columns are thus more suitable mainly due to its maturity, while the membranes are penalised by their low TRL. From this evaluation, the membranes scored lower than the adsorption columns, but they are nevertheless an interesting and promising option. The ranking of the technologies should be re-assessed according to the developments in the coming years. For instance, the relative importance of tritium inventory may change due to considerations on the interface with the fuel cycle and maturity of available technologies. On the other side, progresses on the development of zeolite membranes towards large throughputs should be expected, thus decreasing production costs.

Chapter 9

Conclusions and perspectives

Conclusions In the European DEMOnstration fusion reactor (EU-DEMO), tritium will be produced inside the breeding blanket and recovered by purging the blanket with large flows of He ($\approx 0.4\,\mathrm{kg\,s^{-1}}$) doped with ≈ 0.1 wt% of either H_2 (dry purge) or H_2O (wet purge). The tritiated gas mixture is sent afterwards to a Tritium Extraction and Removal System (TERS) where the separation of Q_2/Q_2O from He should have efficiencies higher than 80 %. The TERS based on membrane technologies considers zeolite membranes for the pre-concentration of Q_2/Q_2O in He to reduce the sizes and costs of the Pd-based membrane reactors placed downstream.

The main objective of this project was to determine experimentally the performances of MFI-ZSM-5 zeolite membranes for the separation of Q_2/He and Q_2O/He, covering both purging scenarios. After two experimental campaigns, the mass-transport mechanisms of the six hydrogen isotopologues were clarified by evaluating their permeances at different membrane temperatures, and the separation factors for feed mixtures of Q_2/He and Q_2O/He, with helium concentrations up to 99 mol%, were determined. The main experimental results are summarised below:

- The permeances of the inactive isotopologues H_2, D_2 and HD were found to be correlated to their molar masses. These results are consistent with the similar adsorption properties of Q_2 species onto the zeolite (with similar surface-diffusion) and the isotopic effects arise due to permeation through defects. This correlation was validated with the permeation of tritiated mixtures of D_2-DT-T_2. The resulting Q_2/He selectivities were found to be $1.8 - 1.9$ for H_2/He and $1.0 - 1.1$ for T_2/He, and hence the separation from helium is less efficient for heavier isotopologues;

- The separation factor for H_2/He and Q_2/He (with 20 at% T in D) was found to be around 1.4 and 1.0, respectively, in the range $293 - 373\,\mathrm{K}$. Higher separation factors and recoveries above 70% were obtained for Q_2O/He, due to the preferential adsorption of Q_2O onto the zeolite. With an average of ≈ 2.2, the separation factor was found to be independent of the feeding concentration in the range $1 - 10$ mol% at 303 K. Experimental evidence for the increase of T concentration in Q_2O by

a factor of 23 % in the permeate suggests the existence of isotopic effects upon separation of tritiated water, which would benefit the separation of tritated species in the pre-concentration step of the TERS.

With experimental separation factors around 1.0 for D_2/He and DT/He, our results suggest that the MFI-ZSM-5 membranes cannot efficiently separate tritiated isotopologues from He. Therefore, these membranes are considered to be not suitable for the pre-concentration step of the TERS for a dry purge. For a wet purge, the MFI-ZSM-5 membranes exhibit interesting separation performances, although not enough to meet the proposed performance requirements ($\mathcal{E} \geq 50$ and $\mathcal{R} \geq 90\,\%$) and therefore a membrane cascade should be used to pre-concentrate Q_2O in He. The resulting membrane cascade consists of 7 stages, with a total surface area of 513 m^2, a total operating power of $\approx$ 3.7 MW and a total tritium inventory of $\approx$ 52 mg. This membrane cascade was compared with the adsorption columns, currently envisioned for the TERS. The membrane cascade has interesting advantages when compared with adsoprtion columns (currently envisioned for the TERS), namely in terms of the reduced tritium inventory due to continuous operation, but they are penalised by the lower level of technological maturity.

Perspectives To propose the most suitable separation system for the pre-concentration step of the TERS, three lines of R&D are identified as important:

- **Development and test of new membranes**: due to the limited availability of commercial zeolite membranes, only MFI-ZSM-5 and NaA membranes have been studied for the pre-concentration stage of the TERS. However, it is important to extend the database of the tested materials. One example is the study of high-quality SOD membranes, with pore diameters (0.270 nm) in between the kinetic diameters of Q_2 (0.289 nm) and He (0.255 nm), which could be used for the separation of He from Q_2 with very high separation factors due to molecular-sieving, resulting in a compact TERS;

- **Optimisation of the purge gas flow and composition**: the purge gas flows (0.4 kg s^{-1}) and dopant concentrations (0.1 wt%) should be re-discussed in the future to reduce the constraints on the TERS, regardless of the technology. The use of lower He flows and higher concentrations of HT/HTO would result in a more compact and cost-efficient TERS. On the other side, higher H_2 concentrations in He would lead to an increased tritium permeation into the coolant. Therefore, the flows and concentrations should be optimised considering this trade-off. Moreover, the pre-concentration of Q_2/Q_2O with zeolite membranes could be improved by using other purge gases. For instance, due to its larger mass and kinetic diameter, the use of Ar instead of He would lead to higher separation factors for Q_2/Ar;

- **Extension of experiments towards low concentrations of tritiated species**: separation experiments with tritium are scarce in the literature for all separation technologies considered for DEMO. In addition, despite this work was devoted to first experiments with tritiated mixtures, more experiments should be performed towards low tritium concentrations as expected at the inlet of the TERS (few ppm, which is at least two orders of magnitude lower than the experimental conditions used in this work). These experiments are of particular importance for pressure-driven processes because the decrease in partial pressure differences results in a lower driving force for permeation and hence the separation factor is expected to decrease.

Bibliography

[1] N. Oreskes, "The scientific consensus on climate change," *Science*, vol. 306, p. 1686, 2004.

[2] P. Guetat, "Tritium and the environment: Sources, measurement and transfer," EU scientific seminar on emerging issues on tritium, 2007. Available in `https://ec.europa.eu/energy/sites/ener/files/documents/tritium_and_environment.pdf`.

[3] M. Abdou, "Overview of the tritium fuel cycle and conditions for tritium fuel self- sufficiency and other tritium issues," (Karlsruhe, Germany), 4$^{\text{th}}$ IAEA DEMO Programme Workshop, 2016. URL: `https://nucleus.iaea.org/sites/fusionportal/Technical%20Meeting%20Proceedings/4th%20DEMO/website/talks/November%2015%20Sessions/Abdou.pdf`.

[4] M. Abdou *et al.*, "Blanket/first wall challenges and required R&D on the pathway to DEMO," *Fusion Engineering and Design*, vol. 100, pp. 2–43, 2015.

[5] F. Hernández *et al.*, "A new HCPB breeding blanket for the EU DEMO: Evolution, rationale and preliminary performances," *Fusion Engineering and Design*, vol. 124, pp. 882–886, 2017.

[6] E. Carella *et al.*, "Tritium modelling in HCPB breeder blanket at system level," *Fusion Engineering and Design*, vol. 124, pp. 687–691, 2017.

[7] K. Munakata *et al.*, "Tritium release from lithium silicate pebbles produced from lithium hydroxide," *Fusion Engineering and Design*, vol. 83, no. 7-9, pp. 1317–1320, 2008.

[8] H. Yamasaki *et al.*, "Effect of water vapor on tritium permeation behavior in the blanket system," *Fusion Engineering and Design*, vol. 87, no. 5-6, pp. 525–529, 2012.

[9] F. Franza *et al.*, "Tritium transport analysis in HCPB DEMO blanket with the FUS-TPC code," *Fusion Engineering and Design*, vol. 88, no. 9-10, pp. 2444–2447, 2013.

[10] D. Demange *et al.*, "New combination of membranes and membrane reactors for improved tritium management in breeder blanket of fusion machines," *Fusion Engineering and Deisgn*, vol. 86, no. 9, pp. 2312–2316, 2011.

[11] A. Ciampichetti *et al.*, "Conceptual design of tritium extraction system for the European HCPB test blanket module," *Fusion Engineering and Design*, vol. 87, no. 5-6, pp. 620–624, 2012.

[12] D. Demange *et al.*, "Zeolite membranes and palladium membrane reactor for tritium extraction from the breeder blankets of ITER and DEMO," *Fusion Engineering and Design*, vol. 88, no. 9, pp. 2396–2399, 2013.

[13] K. S. Krane, *Introductory Nuclear Physics*. John Wiley & Sons, 1988.

[14] G. Kessler, *Nuclear fission reactors: potential role and risks of converters and breeders*. Springer-Verlag, 1983.

[15] M. Kikuchi *et al.*, eds., *Fusion Physics*. IAEA, 2012.

[16] F. F. Chen, *Introduction to Plasma Physics and Controlled Fusion (2^{nd} edition)*. Plenum Publising Corp., 1984.

[17] A. A. Harms *et al.*, *Principles of Fusion Energy*. World Scientific, 2002.

[18] T. K. Giegerich, *Novel vacuum pumping concepts for fusion power plants*. PhD thesis, Karlsruhe Institute of Technology, 2016.

[19] G. Fedirici *et al.*, "European DEMO design strategy and consequences for materials," *Nuclear Fusion*, vol. 57, p. 092002 (26pp), 2017.

[20] T. Hamacher and A. M. Bradshaw, "Fusion as future power source: recent achievments and prospects," in *Proceedings of the 18^{th} World Energy Congress*, 2001. URL: `https://fire.pppl.gov/energy_eu_wec01.pdf`.

[21] J. Freidberg, *Plasma Physics and Fusion Energy*. Cambridge University Press, 2007.

[22] L. L. Lucas and M. P. Unterweger, "Comprehensive review and critical evaluation of the half-life of tritium," *Journal of Research of the National Institute of Standards and Technology*, vol. 105, no. 4, pp. 541–549, 2000.

[23] J. Biegeleisen, "Chemistry of isotopes," *Science*, vol. 147, no. 3657, pp. 463–471, 1965.

[24] J. A. Kaye, ed., *Isotope Effects in Gas-Phase Chemistry*, ch. 1. Isotope Effects in Gas-Phase Chemical Reactions and Photodissociation Processes, pp. 1–14. American Chemical Society, 1992.

[25] A. I. Shatenshtein, *Isotope exchange and the replacement of hydrogen in organic compounds*. Consultants Bureau, 1962.

[26] P. C. Souers, *Hydrogen Properties for Fusion Energy*. University of California Press, 1986.

[27] F. Mannone, ed., *Safety in Tritium Handling Technology*. Kluwer Academic Publishers, 1993.

[28] J. Biegleisen *et al.*, "Calculation of equlibrium constants for isotopic exchange reactions," *The Journal of Chemical Physics*, vol. 15, no. 5, pp. 261–267, 1947.

[29] V. Gold *et al.*, "The principles of hydrogen isotope exchange reactions in solution," *Quarterly Reviews, Chemical Society*, no. 1, pp. 55–72, 1955.

[30] J. D. Huba, "NRL plasma formulary," tech. rep., Naval Research Laboratory, 2013.

[31] National Institute of Standards and Technology, "NIST Chemistry WebBook, SRD 69." Visited on 21/07/2018. URL: `https://webbook.nist.gov/chemistry/`.

[32] M. Kovari *et al.*, "Tritium resources available for fusion reactors," *Nuclear Fusion*, vol. 58, p. 026010 (10pp), 2018.

[33] T. Donné, "European Roadmap to Fusion Energy," in *30th Symposium on Fusion Technologies*, 2018. URL: `https://www.euro-fusion.org/fileadmin/user_upload/EUROfusion/Documents/180917.Donne.SOFT.Roadmap.v2.pdf`.

[34] T. Tanabe, ed., *Tritium: Fuel of Fusion Reactors*. Springer-Verlag, 2017.

[35] U. Fischer *et al.*, "Neutronic design optimisation of modular HCPB blankets for fusion power reactors," *Fusion Engineering and Design*, vol. 75-79, pp. 751–757, 2005.

[36] F. Cismondi *et al.*, "Basics of breeding blanket technology," 9$^{\text{th}}$ International School on Fusion Technologies, 2015. URL: `http://summerschool.fusion.kit.edu/124.php`.

[37] I. Ricapito, "Liquid metal breeding blankets," 9$^{\text{th}}$ International School on Fusion Technologies, 2015. URL: `http://summerschool.fusion.kit.edu/124.php`.

[38] D. Sharma and P. Chadhuri, "Design and analysis of manifolds for Indian HCCB blanket module," *Fusion Engineering and Design*, vol. 129, pp. 40–57, 2018.

[39] K. Jiang *et al.*, "Development of neutronic-thermal hydraulic-mechanic-coupled platform for WCCB blanket design for CFETR," *Fusion Engineering and Design*, vol. 137, pp. 312–324, 2018.

[40] ITER Organization website. Visited on 22/03/2018. URL: `https://www.iter.org`.

[41] A. D. Nevo *et al.*, "WCLL breeding blanket design and integration for DEMO 2015: status and perspectives," *Fusion Engineering and Design*, vol. 124, pp. 682–686, 2017.

[42] L. Giancarli *et al.*, "Test blanket modules in ITER: An overview on proposed designs and required DEMO-relevant materials," *Journal of Nuclear Materials*, vol. 367-370, no. Part B, pp. 1271–1280, 2007.

[43] B. Bornschein *et al.*, "Tritium management and safety issues in ITER and DEMO breeding blankets," *Fusion Engineering and Design*, vol. 88, no. 6-8, pp. 466–471, 2013.

[44] R. J. Walker and M. R. Gilbert, "Neutron activation of impurity seeding gases within a DEMO environment," *Fusion Engineering and Design*, vol. 124, pp. 892–895, 2017.

[45] C. Day and T. Giegerich, "The Direct Internal Recycling concept to simplify the fuel cycle of a fusion power plant," *Fusion Engineering and Design*, vol. 88, pp. 616–620, 2013.

[46] G. Federici *et al.*, "Overview of EU DEMO design and R&D activities," *Fusion Engineering and Design*, vol. 89, pp. 882–889, 2014.

[47] F. A. Hernández and P. Pereslavtsev, "First principles review of options for tritium breeder and neutron multiplier materials for breeding blankets in fusion reactors," *Fusion Engineering and Design*, vol. 137, pp. 243–256, 2018.

[48] S. Wang *et al.*, "Comparative analysis of the efficiency of a CO_2-cooled and a He-cooled pebble bed breeding blanket for the EU DEMO fusion reactor," *Fusion Engineering and Design*, vol. 138, pp. 32–40, 2019.

[49] F. Hernández *et al.*, "HCPB design report 2015," tech. rep., Karlsruhe Institute of Technology, 2016. Eurofusion report, IDM reference: EFDA_D_2MNBH9.

[50] A. Santucci *et al.*, "The coolant purification system in DEMO: Interfaces and requirements," *Fusion Engineering and Design*, vol. 124, pp. 744–747, 2017.

[51] U. Besserer *et al.*, "Tritium confinement, retention and releases at the Tritium Laboratory Karlsruhe," *Fusion Science and Technology*, vol. 54, no. 1, pp. 160–163, 2008.

[52] K. Munakata *et al.*, "Detritiation System of Air with Honeycomb Catalyst and Adsorbent," *Fusion Science and Technology*, vol. 60, no. 4, pp. 1440–1443, 2011.

[53] A. Bükki-Deme *et al.*, "Experimental investigation of ZrCo getter beds as candidate process for the tritium extraction systems of the European Test Blanket Modules," *Fusion Science and Technology*, vol. 71, pp. 527–531, 2017.

[54] A. Bender *et al.*, "Extrapolation at DEMO scale of the HCPB TER system based on cryogenic trapping," tech. rep., Karlsruhe Institute of Technology, 2017. Eurofusion report, IDM reference: EFDA_D_2N4MK6.

[55] M. Netušil and P. Ditl, *Natural Gas: Extraction to End Use*, ch. 1. Natural Gas Dehydration, pp. 3–21. IntechOpen, 2012.

[56] Shell, "Design and Operation of Molecular Sieve Units." Visited on 14/02/2019. URL: `https://www.shell.com/business-customers/global-solutions/featured-stories/design-and-operation-of-molecular-sieve-units.html`.

[57] D. Demange *et al.*, "CAPER modifications and first experimental results on highly tritiated water processing with PERMCAT at the Tritium Laboratory Karlsruhe," *Fusion Science and Technology*, vol. 60, no. 4, pp. 1317–1322, 2011.

[58] S. Welte *et al.*, "Characterisation of a multitube PERMCAT reactor in view of a technical facility for highly tritiated water processing at the Tritium Laboratory Karlsruhe," *Fusion Engineering and Design*, vol. 86, pp. 2237–2240, 2011.

[59] S. Welte *et al.*, "Development of a technical scale PERMCAT reactor for processing of highly tritiated water," *Fusion Engineering and Design*, vol. 87, pp. 1045–1049, 2012.

[60] A. Bükki-Deme *et al.*, "PERMCAT experiments with tritium at high helium flow rates relevant for the tritium extraction systems using the CAPER facility at TLK," *Fusion Engineering and Design*, vol. 109-111, pp. 1331–1334, 2016.

[61] M. Incelli *et al.*, "Heavy water decontamination tests through a Pd-Ag membrane reactor: Water Gas Shift and Isotope Swamping performances," *Fusion Engineering and Design*, vol. 124, pp. 692–695, 2017.

[62] M. Simplicio *et al.*, "Permeation of single gases and binary mixtures of hydrogen and helium through a MFI zeolite hollow fibres membrane for application in nuclear fusion," *Separation and Purification Technology*, vol. 122, pp. 199–205, 2014.

[63] O. Borisevich *et al.*, "Experimental study of permeation and selectivity of zeolite membranes for tritium processes," *Fusion Engineering and Design*, vol. 98-99, pp. 1755–1758, 2015.

[64] O. Borisevich *et al.*, "Comparison of MFI-ZSM5 and NaA zeolite-type tubular membranes for the separation of water vapour from helium for tritium processes in future fusion reactors," *Fusion Engineering and Design*, vol. 125, pp. 134–138, 2017.

[65] M. Mulder, *Basic Principles of Membrane Technology*. Springer-Science+Business Media, B. V., 1992.

[66] A. F. Ismail *et al.*, *Gas Separation Membranes: polymeric and inorganic*. Springer, 2015.

[67] R. W. Baker, *Membrane Technology and Applications*. John Wiley & Sons, 2012.

[68] J. Rouquerol *et al.*, "Recommendations for the characterization of porous solids," tech. rep., International Union of Pure and Applied Chemistry, 1994.

[69] R. D. Noble and S. A. Stern, eds., *Membrane Separations Technology: principles and applications*. Elsevier, 1995.

[70] Y. Yampolskii *et al.*, eds., *Materials Science of Membranes for Gas and Vapor Separation*. John Wiley & Sons, Ltd, 2006.

[71] H. P. Hsieh, *Inorganic Membranes for Separation and Reaction*. Elsevier, 1996.

[72] E. Nagy, *Basic equations of the mass transport through a membrane layer*. Elsevier, 2012.

[73] A. J. Burggraaf and L. Cot, eds., *Fundamentals of Inorganic Membrane Science and Technology*. Elsevier, 1996.

[74] A. S. Ziarani *et al.*, "Knudsen's permeability correction for tight porous media," *Transport in Porous Media*, vol. 91, pp. 239–260, 2012.

[75] W. He *et al.*, *Gas Transport in Solid Oxide Fuel Cells*, ch. Gas Diffusion Mechanisms and Models, pp. 9–17. SpringerBriefs in Energy, 2014.

[76] I. Medved *et al.*, "Surface diffusion in porous media: a critical review," *Microporous and Mesoporous Materials*, vol. 142, pp. 405–422, 2011.

[77] D. A. McQuarrie, *Statistical Mechanics*. Viva Books, 2011.

[78] A. J. Burggraaf, "Single gas permeation of thin zeolite (MFI) membranes: theory and analysis of experimental observations," *Journal of Membrane Science*, vol. 155, pp. 45–65, 1999.

[79] L. J. P. van de Broeke *et al.*, "Transport and separation properties of a silicalite-1 membrane - I. operating conditions," *Chemical Engineering Science*, vol. 54, pp. 245–258, 1999.

[80] N. Kosinov *et al.*, "Recent developments in zeolite membranes for gas separation," *Journal of Membrane Science*, vol. 499, pp. 65–79, 2016.

[81] W. J. W. Bakker *et al.*, "Temperature dependence of one-component permeation through a silicalite-1 membrane," *AIChE Journal*, vol. 43, no. 9, pp. 2203–2214, 1997.

[82] R. I. Maisel, *Principles of Adsorption and Reaction on Solid Surfaces*, ch. 4. Adsorption II: Adsorption Isotherms, pp. 239–244. John Wiley & Sons, 1996.

[83] P. Saha and S. Chowdhury, "Insight into adsorption thermodynamics," in *Thermodynamics* (M. Tadashi, ed.), ch. 16, Rijeka: InTech, 2011.

[84] N. Stadie, *Synthesis and Thermodynamic Studies of Physisorptive Energy Storage Materials*. PhD thesis, California Institute of Technology, 2012.

[85] N. Y. Chen *et al.*, *Molecular Transport and Reaction in Zeolites: Design and Application of Shape Selective Catalysis*. Wiley, 1994.

[86] R. Xu *et al.*, *Chemistry of Zeolites and Related Porous Materials: Synthesis and Structure*. Wiley, 2007.

[87] I. Z. Association, "Database of Zeolite Structures." Visited on 21/07/2018. URL: `http://www.iza-structure.org/databases/`.

[88] S. M. Auerbach *et al.*, eds., *Handbook of Zeolite Science and Technology*. Marcel Dekker Inc., 2003.

[89] Z. A. Alothman, "A review: Fundamental aspects of silicate mesoporous materials," *Materials*, vol. 5, pp. 2874–2902, 2012.

[90] A. Tavolaro and E. Drioli, "Zeolite membranes," *Advanced Materials*, vol. 11, no. 12, pp. 975–996, 1999.

[91] J. Weitkamp, "Zeolites and catalysis," *Solid State Ionics*, vol. 131, pp. 175–188, 2000.

[92] C. Feng *et al.*, "Recent progress in zeolite/zeotype membranes," *Journal of Membrane Science and Research*, vol. 1, pp. 49–72, 2015.

[93] B. F. Sels and L. M. Kustov, eds., *Zeolites and Zeolite-like Materials*. Elsevier, 2016.

[94] W. Loewenstein, "The distribution of aluminum in the tetrahedra of silicates and aluminates," *American Mineralogist*, vol. 39, pp. 92–96, 1954.

[95] O. M. Dzhigit *et al.*, "Heats of adsorption of water vapour on X-zeolites containing Li^+, Na^+, K^+, Rb^+ and Cs^+ cations," *Transactions of the Faraday Society*, vol. 67, pp. 458–467, 1971.

[96] T. C. Golden and S. Sircar, "Gas adsorption on silicalite," *Journal of Colloid and Interface Science*, vol. 162, no. 1, pp. 182–188, 1994.

[97] M. Katoh *et al.*, "Infrared studies on nitrogen oxides adsorbed on alkali metal ion-exchanged ZSM-5 zeolites," *Zeolites*, vol. 15, no. 7, pp. 591–596, 1995.

[98] S. Savitz *et al.*, "Calorimetric study of adsorption of alkanes in high-silica zeolites," *The Journal of Physical Chemistry B*, vol. 102, no. 35, pp. 6865–6872, 1998.

[99] S. Savitz *et al.*, "A calorimetric investigation of CO, N_2 and O_2 in alkali-exchanged MFI," *Microporous and Mesoporous Materials*, vol. 37, pp. 33–40, 2000.

[100] D. F. Plant *et al.*, "CO_2 adsorption in alkali cation exchanged Y faujasites: A quantum chemical study compared to experiments," *Chemical Physics Letters*, vol. 426, pp. 387–392, 2006.

[101] R. T. Yang, *Adsorbents: Fundamentals and Applications*. Wiley-Interscience, 2003.

[102] P. L. Llewellyn and G. Maurin, *Introduction to Zeolite Science and Practice (3rd revised edition)*, ch. 17. Gas adsorption on zeolites and related materials, pp. 561–610. Elsevier, 2007.

[103] R. F. Lobo, *Ordered Porous Solids: recent advances and prospects*, ch. 9. Intermolecular forces in zeolite adsorption and catalysis, pp. 239–261. Elsevier, 2009.

[104] G. Maurin, *Adsorption by Powders and Porous Solids: principles, methodology and applications (2nd edition)*, ch. 6. Modelling of Physisorption in Porous Solids, pp. 199–235. Elsevier, 2014.

[105] National Institute of Standards and Technology, "Computational Chemistry Comparison and Benchmark DataBase." Visited on 21/07/2018. URL: `https://cccbdb.nist.gov/introx.asp`.

[106] D. E. Stogryn and A. P. Stogryn, "Molecular multipole moments," *Molecular Physics*, vol. 11, no. 4, pp. 371–393, 1966.

[107] A. L. Ford and J. C. Browne, "Ab initio calculation of the line strengths in the electric dipole vibration-rotation spectrum of the HD molecule," *Physical Review A*, vol. 16, no. 5, pp. 1992–2001, 1977.

[108] W. Thorson *et al.*, "Novel theory of the HD dipole moment. II. Computations," *Physical Review A*, vol. 31, no. 1, pp. 34–42, 1985.

[109] W. Thorson *et al.*, "Novel theory of the HD dipole moment. I. Theory," *Physical Review A*, vol. 31, no. 1, pp. 22–33, 1985.

[110] A. V. Kiselev *et al.*, "Molecular statistical calculation of gas adsorption by silicalite," *Zeolites*, vol. 5, pp. 261–267, 1985.

[111] J. A. Dunne *et al.*, "Calorimetric heats of adsorption and adsorption isotherms. 1. O_2, N_2, Ar, CO_2, CH_4, C_2H_6, and SF_6 on silicalite," *Langmuir*, vol. 12, pp. 5888–5895, 1996.

[112] D. W. Breck *et al.*, "Crystalline zeolites. I. the properties of a new synthetic zeolite, type A," *Journal of the American Chemical Society*, vol. 78, no. 23, pp. 5963–5972, 1956.

[113] A. Saito *et al.*, "High-resolution nitrogen and argon adsorption on ZSM-5 zeolites: effects of cation exchange and Si/Al ratio," *Microporous Materials*, vol. 3, pp. 543–556, 1995.

[114] J. A. Dunne *et al.*, "Calorimetric heats of adsorption and adsorption isotherms. 2. O_2, N_2, Ar, CO_2, CH_4, C_2H_6, and SF_6 on NaX, H-ZSM-5, and Na-ZSM-5 zeolites," *Langmuir*, vol. 12, pp. 5896–5904, 1996.

[115] A. Jayaraman *et al.*, "Adsorption of nitrogen, oxygen and argon on Na-CeX zeolites," *Adsorption*, vol. 8, no. 4, pp. 271–278, 2002.

[116] N. Kazuyuki *et al.*, "High resolution adsorption isotherms of N_2 and Ar for non-porous silicas and MFI zeolites," *Adsorption*, vol. 13, no. 3-4, pp. 351–356, 2007.

[117] R. E. Bazan *et al.*, "Adsorption equilibria of O_2, Ar, Kr and Xe on activated carbon and zeolites: single component and mixture data," *Adsorption*, vol. 17, pp. 371–383, 2011.

[118] E. García-Perez *et al.*, "Unraveling the argon adsorption processes in MFI-type zeolite," *The Journal of Physical Chemistry C*, vol. 112, no. 27, pp. 9976–9979, 2008.

[119] W. Zhu *et al.*, "Water vapour separation from permanent gases by a zeolite-4A membrane," *Journal of Membrane Science*, vol. 253, no. 1-2, pp. 57–66, 2005.

[120] S. G. Sorenson *et al.*, "Influence of zeolite crystal expansion/contraction on NaA zeolite membrane separations," *Journal of Membrane Science*, vol. 366, pp. 413–420, 2011.

[121] L. Cot *et al.*, "Inorganic membranes and solid state sciences," *Solid State Sciences*, vol. 2, pp. 313–334, 2000.

[122] J. Caro *et al.*, "Zeolite membranes - state of their development and perspective," *Microporous and Mesoporous Materials*, vol. 38, pp. 3–24, 2000.

[123] Y. S. Lin, "Microporous and dense inorganic membranes: current status and prospective," *Separation and Purification Technology*, vol. 25, pp. 39–55, 2001.

[124] E. E. McLeary *et al.*, "Zeolite based films, membranes and membrane reactors: Progress and prospects," *Microporous and Mesoporous Materials*, vol. 90, pp. 198–220, 2006.

[125] J. Caro *et al.*, "Zeolite membranes - recent developments and progress," *Microporous and Mesoporous Materials*, vol. 115, pp. 215–233, 2008.

[126] H. Verweij, "Inorganic membranes," *Current Opinion in Chemical Engineering*, vol. 1, pp. 156–162, 2012.

[127] P. Bernardo and G. Clarizia, "30 years of membranes technology for gas separation," *Chemical Engineering Transactions*, vol. 32, pp. 1999–2004, 2013.

[128] Hitachi Zosen Corporation. Visited on 28/07/2018. URL: `http://www.hitachizosen.co.jp/english/products/products009.html`.

[129] P. Gorgojo *et al.*, *Membrane Science and Technology*, ch. 5. Preparation and Characterization of Zeolite Membranes, pp. 135–175. Elsevier B. V., 2008.

[130] S. Morooka *et al.*, "Microporous inorganic membranes for gas separation," *Materials Research Society Bulletin*, vol. 24, no. 3, pp. 25–29, 1999.

[131] M. Yu *et al.*, "Characterizing nonzeolitic pores in MFI membranes," *Industrical & Engineering Chemistry Research*, vol. 47, no. 11, pp. 3943–3948, 2008.

[132] M. Yu *et al.*, "Zeolite membranes: Microstructure characterization and permeation mechanisms," *Accounts of Chemical Research*, vol. 4, no. 11, p. 1, 2011.

[133] S. H. Park *et al.*, "The thermal expansion of the zeolites MFI, AFI, DOH, DDR, and MTN in their calcined and as synthesized forms," *Studies in Surface Science and Catalysis*, vol. 105, pp. 1989–1994, 1997.

[134] P. Lightfoot *et al.*, "The widespread occurrence of negative thermal expansion in zeolites," *Journal of Materials and Chemistry*, vol. 11, pp. 212–216, 2001.

[135] M. Noack *et al.*, "Influence of the Si/Al-ratio on the permeation properties of MFI-membranes," *Microporous and Mesoporous Materials*, vol. 79, pp. 329–337, 2005.

[136] R. Krishna *et al.*, "The Maxwell-Stefan description of mass transport across zeolite membranes," *The Chemical Engineering Journal*, vol. 57, pp. 155–162, 1995.

[137] T. Q. Gardner *et al.*, "Adsorption and diffusion properties of zeolite membranes by transient permeation," *Desalination*, vol. 149, no. 1-3, pp. 435–440, 2002.

[138] J. C. Poshusta *et al.*, "Temperature and pressure effects on CO_2 and CH_4 permeation through MFI zeolite membranes," *Journal of Membrane Science*, vol. 160, pp. 115–125, 1999.

[139] F. Jareman *et al.*, "Modelling of single gas permeation in real MFI membranes," *Journal of Membrane Science*, vol. 236, pp. 81–89, 2004.

[140] H. Richter *et al.*, "Preparation of zeolite membranes on the inner surface of ceramic tubes and capillaries," *Separation and Purification Technology*, vol. 32, no. 1-3, pp. 133–138, 2003.

[141] C. Günther *et al.*, "Zeolite membranes for hydrogen and water separation under harsh conditions," *Chemical Engineering Transactions*, vol. 32, pp. 1963–1968, 2013.

[142] M. Schlösser, *Accurate calibration of the Raman system for the Karlsruhe Tritium Neutrino Experiment*. PhD thesis, Karlsruhe Institute of Technology, 2013.

[143] "Private communication with Fraunhofer IKTS membrane manufacturers," 11/2018.

[144] R. Antunes *et al.*, "Experimental investigation of the ideal selectivity of MFI-ZSM-5 zeolite-type membranes for a first evaluation of the separation of hydrogen isotopologues from helium," *Separation and Purification Technology*, vol. 212, pp. 767–773, 2019.

[145] S. Miachon *et al.*, "Nanocomposite MFI-alumina membranes via pore-plugging synthesis: specific transport and separation properties," *Journal of Membrane Science*, vol. 298, pp. 71–79, 2007.

[146] J. M. van de Graaf *et al.*, "Permeation of weakly adsorbing components through a silicalite-1 membrane," *Chemical Engineering Science*, vol. 54, pp. 1081–1092, 1999.

[147] N. Nishiyama *et al.*, "Evaluation of reproducible high flux silicalite-1 membranes: gas permeation and separation characterization," *Separation and Purification Technology*, vol. 22-23, pp. 295–307, 2001.

[148] C. Bai *et al.*, "Preparation and separation properties of silicalite composite membranes," *Journal of Membrane Science*, vol. 105, pp. 79–87, 1995.

[149] J. Coronas *et al.*, "Characterization and permeation properties of ZSM-5 tubular membranes," *AIChE*, vol. 43, no. 7, pp. 1797–1812, 1997.

[150] S. A. S. Rezai *et al.*, "Water/hydrogen/hexane multicomponent selectivity of thin MFI membranes with different Si/Al ratios," *Microporous and Mesoporous Materials*, vol. 108, pp. 136–142, 2008.

[151] S. Friebe *et al.*, "Deuterium/hydrogen permeation through different molecular sieve membranes: ZIF, LDH, zeolite," *Microporous and Mesoporous Materials*, vol. 216, pp. 127–132, 2015.

[152] L. Dörr *et al.*, "The closed tritium cycle of the Tritium Laboratory Karlsruhe," *Fusion Science and Technology*, vol. 48, pp. 262–267, 2005.

[153] T. Yamanishi *et al.*, "Overview of R&D activities on tritium processing and handling technology in JAEA," *Fusion Engineering and Design*, vol. 87, pp. 890–895, 2012.

[154] S. Welte *et al.*, "Tritum Laboratory Karlsruhe: Administrative and technical framework for isotope laboratory operation," *Fusion Science and Technology*, vol. 67, pp. 635–638, 2015.

[155] E. A. Clark, "Effects of tritium gas exposure on EPDM elastomer," tech. rep., Savannah River National Laboratory, 2009. SRNL report, reference: SRNL-STI-2009-00801 Rev. 0.

[156] E. B. Fox *et al.*, "Polymer performance and aging in a tritium environment," *Fusion Science and Technology*, vol. 71, no. 4, pp. 507–513, 2017.

[157] B. Bornschein *et al.*, "Successul experimental verification of the tokamak exhaust processing concept of ITER with the CAPER facility," *Fusion Science and Technology*, vol. 48, pp. 11–16, 2005.

[158] M. Glugla *et al.*, "Commissioning of the catalytic plasma clean-up facility CAPRICE and first experimental results," *Fusion Technology*, vol. 28, no. 3P1, pp. 625–629, 1995.

[159] D. Demange *et al.*, "CAPER as central and crucial facility to support R&D with tritium at TLK," *Fusion Science and Technology*, vol. 67, no. 2, pp. 308–311, 2015.

[160] S. Welte *et al.*, "Experimental performance test of key components of the KATRIN outer tritium loop," *Fusion Science and Technology*, vol. 71, pp. 316–320, 2017.

[161] Tektronix, "Keithley Series 6400 Picoammeters." Visited on 31/12/2018. URL: `https://www.tek.com/`

`keithley-low-level-sensitive-and-specialty-instruments/keithley-series-6400-picoammeters`.

[162] K. Munakata *et al.*, "Experimental and computational determination of deuterium–tritium mixtures with a small volume ionization chamber," *Fusion Engineering and Design*, vol. 39-40, pp. 937–948, 1998.

[163] R. Wagner *et al.*, "Improvement and characterization of small cross-piece ionization chambers at the Tritium Laboratory Karlsruhe," *Fusion Science and Technology*, vol. 60, pp. 968–971, 2011.

[164] A. I. Parracho *et al.*, "Processing highly tritiated water desorbed from molecular sieve bed using PERMCAT," *Fusion Engineering and Design*, vol. 87, pp. 1277–1281, 2012.

[165] M. Sturm *et al.*, "Monitoring of all hydrogen isotopologues at Tritium Laboratory Karlsruhe using Raman spectroscopy," *Laser Physics*, vol. 20, no. 2, pp. 493–507, 2010.

[166] M. Schlösser *et al.*, "Raman Spectroscopy at the Tritium Laboratory Karlsruhe," *Fusion Science and Technology*, vol. 67, pp. 555–558, 2015.

[167] F. Priester and B. Bornschein, "TriToP - a compatibility experiment with turbomolecular pumps under tritium atmosphere," *Vacuum*, vol. 98, pp. 22–28, 2013.

[168] R. Lässer *et al.*, "Analytic of tritium-containing gaseous species at the Tritium Laboratory Karlsruhe," *Fusion Engineering and Design*, vol. 58-59, pp. 411–415, 2001.

[169] Z. Köllő *et al.*, "Calibrating a gas chromatograph to measure tritium using calorimetry," *Fusion Engineering and Design*, vol. 84, no. 7-11, pp. 1073–1075, 2009.

[170] A. Bükki-Deme *et al.*, "Current status of tritium calorimetry at TLK," *Fusion Science and Technology*, vol. 67, no. 2, pp. 282–285, 2015.

[171] K. S. Weil *et al.*, "Brazing as a means of sealing ceramic membranes for use in advanced coal gasification processes," *Fuel*, vol. 85, pp. 156–162, 2006.

[172] A. F. Sammells and M. V. Mundschau, eds., *Nonporous Inorganic Membranes*, ch. 8. Syngas membrane engineering design and scale-up issues. Application of ceramic oxygen conducting membranes, pp. 215–244. Wiley-VCH, 2006.

[173] A. Basile and K. Ghasemzadeh, eds., *Current trends and future developments on (bio-) membranes*, ch. 15. Silica membranes sealing in high temperatures, pp. 367–381. Elsevier, 2017.

[174] R. Antunes *et al.*, "Numerical analysis of H_2/He gas separation experiments performed with a MFI-type tubular zeolite membrane," *Chemical Engineering Research and Design*, vol. 109, pp. 327–334, 2016.

[175] T. C. Merkel *et al.*, "Power plant post-combustion carbon dioxide capture: An opportunity for membranes," *Journal of Membrane Science*, vol. 359, pp. 126–139, 2010.

[176] R. Pathare and R. Agrawal, "Design of membrane cascades for gas separation," *Journal of Membrane Science*, vol. 364, pp. 263–277, 2010.

[177] W. J. Koros and R. Mahajan, "Pushing the limits on possibilities for large scale gas separation: which strategies?," *Journal of Membrane Science*, vol. 175, pp. 181–196, 2000.

[178] R. Baker, "Future directions of membrane gas separation technology," *Industrial & Engineering Chemistry Research*, vol. 41, no. 6, pp. 1393–1411, 2002.

[179] D. F. Sanders *et al.*, "Energy-efficient polymeric gas separation membranes for a sustainable future: A review," *Polymer*, vol. 54, pp. 4729–4761, 2013.

[180] O. Borisevich *et al.*, "Zeolite membrane cascade for tritium extraction and recovery systems," *Fusion Science and Technology*, vol. 67, no. 2, pp. 262–265, 2015.

[181] K. Cohen and G. Murphy, *The theory of isotope separation as applied to the large-scale production of ^{235}U.* McGraw-Hill, 1951.

[182] S. Villani, ed., *Uranium Enrichment.* Springer-Verlag, 1979.

[183] M. Ohno *et al.*, "Gas separation performance of tapered cascade with membrane," *Journal of Nuclear Science and Technology*, vol. 15, no. 6, pp. 411–420, 1978.

[184] S. A. Stern and S.-C. Wang, "Permeation cascades for the separation of krypton and xenon from nuclear reactor atmospheres," *AIChE*, vol. 26, no. 6, pp. 891–901, 1980.

[185] A. S. Krass *et al.*, *Uranium Enrichment and Nuclear Weapon Proliferation.* Taylor & Francis Ltd, 1983.

[186] K. Sirkar, *Separation of Molecules, Macromolecules and Particles: Principles, Phenomena and Processes.* Cambridge University Press, 2014.

[187] S.-T. Hwang and K. Kammermeyer, *Membranes in Separations*, ch. 8. Engineering Aspects of Membrane Separation, pp. 323–420. John Wiley & Sons, 1975.

[188] J. Xu and R. Agrawal, "Gas separation membrane cascades I. one-compressor cascades with minimal exergy losses due to mixing," *Journal of Membrane Science*, vol. 112, pp. 115–128, 1996.

[189] A. K. Alshehri and Z. Lai, "Attainability and minimum energy of multiple-stage cascade membrane systems," *Journal of Membrane Science*, vol. 495, pp. 284–293, 2015.

[190] L. Zhao *et al.*, "Multi-stage gas separation membrane processes used in post-combustion capture: Energetic and economic analyses," *Journal of Membrane Science*, vol. 359, pp. 160–172, 2010.

[191] M. Binns *et al.*, "Strategies for the simulation of multi-component hollow fibre multi-stage membrane gas separation systems," *Journal of Membrane Science*, vol. 497, pp. 458–471, 2016.

[192] A. Santucci *et al.*, "Recent achievments of the Pd-Ag membrane technologies in tritium extraction system applications," *Fusion Engineering and Design*, 2019. In press: `https://doi.org/10.1016/j.fusengdes.2019.03.162`.

[193] C. Day *et al.*, "Consequences of the technology survey and gap analysis on the EU DEMO R&D programme in tritium, matter injection and vacuum," *Fusion Engineering and Design*, vol. 109-111, pp. 299–308, 2016.

[194] R. Lawless *et al.*, "Tritium plant technology development for a DEMO power plant," *Fusion Science and Technology*, vol. 71, no. 4, pp. 679–686, 2017.

[195] Y. Hörstensmeyer *et al.*, "Analysis of the EU-DEMO fuel cycle elements: Intrinsic impact of technology choices," *Fusion Engineering and Design*, vol. 136, no. Part A, pp. 314–318, 2018.

[196] G. Federici *et al.*, "DEMO design activity in Europe: Progress and Updates," *Fusion Engineering and Design*, vol. 136, pp. 729–741, 2018.

[197] R. J. Silbey *et al.*, *Physical Chemistry*, ch. 1. Zeroth Law of Thermodynamics and Equations of State, pp. 11–21. John Wiley & Sons, 2005.

[198] G. Towler and R. Sinnott, *Chemical Engineering and Design: Principles, Practice and Economics of Plant and Process Design*, ch. 20. Transport and Storage of Fluids, pp. 1207–1265. Elsevier, 2013.

[199] R. K. Rajput, *Thermal Engineering*, ch. 24. Air Compressors, pp. 1182–1190. Laxmi Publications, 2006.

[200] R. Antunes and L. Frances, "Dimensioning of ideal membrane cascade systems for the separation of binary gas mixtures for nuclear fusion applications," *(under review in) Fusion Engineering and Design*, 2019.

[201] D. Demange *et al.*, "Tritium management and anti-permeation strategies for three different breeding blanket options foreseen for the European Power Plant Physics and Technology Demonstration reactor study," *Fusion Engineering and Design*, vol. 89, no. 7-8, pp. 1219–1222, 2014.

[202] I. Ricapito *et al.*, "Technologies and modelling issues for tritium processing in the European Test Blanket Systems and perspectives for DEMO," *Fusion Engineering and Design*, vol. 89, no. 7-8, pp. 1469–1475, 2014.

[203] D. Demange *et al.*, "Tritium extraction technologies and DEMO requirements," *Fusion Engineering and Design*, vol. 109-111, no. Part A, pp. 912–916, 2016.

[204] F. R. Urgorri *et al.*, "Tritium transport modeling at system level for the EUROfusion dual coolant lithium-lead breeding blanket," *Nuclear Fusion*, vol. 57, p. 116045, 2017.

[205] A. Santucci *et al.*, "Tritium migration in HCLL and WCLL blankets: impact of tritium solubility in liquid Pb-17Li," *IEEE Transactions on Plasma Science*, vol. 42, no. 4, pp. 1053–1057, 2014.

[206] M. P. Rohde *et al.*, "Fischer-Tropsch synthesis with in situ H_2O removal - Directions of membrane development," *Microporous and Mesoporous Materials*, vol. 115, no. 1-2, pp. 123–136, 2008.

[207] I. Voigt *et al.*, "Scale-up of ceramic nanofiltration membranes to meet large scale applications," *Separation and Purification Technology*, vol. 215, pp. 329–334, 2019.

[208] H. Hasegawa *et al.*, "Gas separation process for CO_2 removal from natural gas with DDR-type zeolite membrane," *Energy Procedia*, vol. 114, pp. 32–36, 2017.

[209] R. B. Bird *et al.*, *Transport Phenomena*, ch. 6. Interphase Transport in Isothermal Systems, pp. 177–184. John Wiley & Sons, 2002.

[210] National Institute of Standards and Technology, "Thermophysical Properties of Fluid Systems." Visited on 12/02/2019. URL: `https://webbook.nist.gov/chemistry/fluid/`.

[211] K. F. Loughlin, "Water isotherm models for 4A (NaA) zeolite," *Adsorption*, vol. 15, pp. 337–353, 2009.

[212] A. Gabelman, "Adsorption Basics: Part 1," *AIChE*, 2017.

[213] E. Tsotsas and A. Mujumdar, eds., *Modern Drying Technology: Energy Savings (Vol. 4)*, ch. 5. Zeolites for Reducing Drying Energy Use, pp. 163–168. Wiely-VCH, 2012.

[214] Gas Processing & LNG, "Optimal design and operation of molecular sieve gas dehydration units - part 1." Visited on 18/02/2019. URL: `http://gasprocessingnews.com/features/201708/optimal-design-and-operation-of-molecular-sieve-gas-dehydration-units%E2%80%94part-1.aspx`.

[215] K. S. Knaebel, "A "How To" Guide for Adsorber Design," tech. rep., Adsorption Research, Inc., 2016. Available in: `http://www.adsorption.com/wp-content/uploads/2016/04/AdsorberDes2.pdf` (visited on 14/02/2019).

[216] W. L. McCabe *et al.*, *Unit Operation of Chemical Engineering*, ch. 25. Adsorption, pp. 810–837. McGraw-Hill, 1993.

[217] B. Baghapour *et al.*, "A pressure drop study for packed bed adsorption thermal energy storage," *Applied Thermal Engineering*, vol. 138, pp. 731–739, 2018.

[218] University of San Diego - Advanced Energy Technology Group, "Austenitic Stainless Steel (316)." Visited on 19/02/2019. URL: `http://www-ferp.ucsd.edu/LIB/PROPS/PANOS/ss.html`.

[219] L. Qiu *et al.*, "Zeolite 4A: heat capacity and thermodynamic properties," *Solid State Sciences*, vol. 2, pp. 841–846, 2000.

[220] Brounell Limited, "1 kg 4A Molecular sieves." Visited on 20/02/2019. URL: `https://brownell.co.uk/buyonline/desiccant-refills/1kg-molecular-sieves/1kg-4a-molecular-sieves.html`.

[221] M. Tsapatsis, "Toward high-throughput zeolite membranes," *Science*, vol. 34, pp. 767–768, 2011.

[222] L. D. Pace *et al.*, *Radioactive Waste*, ch. 14. Radioactive Waste Management of Fusion Power Plants, pp. 303–328. IntechOpen, 2012.

[223] European Commission, "Funding & tender opportunities." Visited on 21/02/2019. URL: `https://ec.europa.eu/info/funding-tenders/opportunities/portal/screen/support/faq;keywords=/2890`.

[224] M.-C. Desjonquères and D. Spanjaard, *Concepts in Surface Physics*. Springer-Verlag, 1993.

[225] D. M. Ruthven, *Principles of Adsorption and Adsorption Processes*, ch. 2. Physical adsorption and the characterizaiton of porous adsorbents, pp. 29–61. John Wiley & Sons, 1984.

[226] J. N. Israelachvili, *Intermolecular and Surface Forces (3rd edition)*. Academic Press, 2011.

[227] A. J. Stone, *The Theory of Intermolecular Forces*. Oxford University Press, 2013.

[228] R. M. Barrer, "Specificity in physical sorption," *Journal of Colloid and Interface Science*, vol. 21, no. 4, pp. 415–434, 1966.

[229] MKS Instruments Inc., "Gas Correction Factors for Thermal-based Mass Flow controllers." Visited on 13/09/2018. URL: `https://www.mksinst.com/docs/ur/MFCGasCorrection.aspx`.

[230] MKS Instruments Inc., "1179C general purpose mass-flow controller." Visited on 13/09/2018. URL: `https://www.mksinst.com/docs/UR/1179C-DS.pdf`.

[231] L'Essor Français Electronique, "High Accuracy Pressure Sensor." Visited on 13/09/2018. URL: `http://www.efe-sensor.com/products/?produit=PTA220`.

[232] D. Demange *et al.*, "Overview of R&D at TLK for process and analytical issues on tritium management in breeder blankets of ITER and DEMO," *Fusion Engineering and Design*, vol. 87, no. 7-8, pp. 1206–1213, 2012.

[233] Michell Instruments, "PURA Pure Gas Trace Moisture Transmitter." Visited on 28/10/2018. URL: `http://www.michell.com/uk/products/pura.htm`.

[234] J. W. Schmidt and M. R. Moldover, "Dielectric permittivity of eight gases measured with cross capacitors," *International Journal of Thermophysics*, vol. 24, no. 2, pp. 375–403, 2003.

[235] D. P. Fernández *et al.*, "A database for the static dielectric constant of water and steam," *Journal of Physical and Chemical Reference Data*, vol. 24, no. 1, pp. 33–69, 1995.

[236] D. Demange *et al.*, "Micro-Channel Catalytic Reactor integration in CAPER and R&D on Highly Tritiated Water handling and processing," *Fusion Science and Technology*, vol. 67, pp. 312–315, 2015.

[237] M. Yamada *et al.*, "Operation results on safety systems of tritium process laboratory in Japan Atomic Energy Research Institute," *Fusion Science and Technology*, vol. 41, no. 3P2, pp. 593–597, 2002.

[238] Indium Corporation, "Metal Thermal Interface Materials (brochure)." Visited on 14/10/2018. URL: `https://www.indium.com/thermal-interface-materials/`.

[239] Indium Corporation, "Indium & Indium Alloy Wire." Visited on 14/10/2018. URL: `http://www.indium.com/metals/indium/indium-wire/`.

[240] E. A. L. Committee, "Evaluation of the uncertainty of measurement in calibration," tech. rep., European Accreditation, 2013.

[241] J. C. for Guides in Metrology (JCGM/WG 1), "Evaluation of measurement data — guide to the expression of uncertainty in measurement," tech. rep., International Bureau of Weights and Measures, 2008.

[242] J. R. Taylor, *An Introduction to Error Analysis: The Study of Uncertainties in Physical Measurements*. University Science Books, 1997.

[243] D. L. Purich and R. D. Allison, *Hanbook of Biochemical Kinetics*. Academic Press, 2000.

[244] P. Atkins and J. de Paula, *Atkins' Physical Chemistry*, ch. 22. The rates of chemical reactions, pp. 791 – 829. W. H Freeman and Company, 2006.

Appendix A

The physics of adsorption onto zeolites

Physical adsorption or physisorption is governed by weak intermolecular forces where the electronic structure of the molecules is not modified[1] [224]. Therefore, adsorbate-adsorbent interactions in physisorption are mainly due to van der Waals forces (close-range attraction and repulsion). These forces are always present for every sorbate and sorbent (also referred to as "non-specific" forces). Furthermore, electrostatic forces are also present for molecular interactions with charged surfaces which is the case of zeolites (also referred to as "specific" forces). Overall, five interaction terms are typically considered to estimate the total adsorbate-adsorbent potential $\phi(r)$ (in $\mathrm{J\,mol^{-1}}$) as a function of the distance r between the molecules[2]. The potential is defined in equation (A.1) as the sum of the contributions of the terms associated with each force given below [101, 103, 225, 226].

$$\phi(r) = \phi_{\mathrm{D}} + \phi_{\mathrm{R}} + \phi_{\mathrm{ind}} + \phi_{E\mu} + \phi_{EQ} \tag{A.1}$$

- **Dispersion (London) interaction**: this interaction is quantum mechanical in nature and arises from the appearance of an instantaneous dipole in one molecule creating an electrical field that polarizes a nearby molecule. Consequently, an instantaneous dipole-dipole attractive interaction takes place whose potential can be described[3] with equation (A.2), where $\alpha_{\mathrm{p},i}$ and I_i are, respectively, the polarizability and ionisation potential of the interacting molecule i.

$$\phi_{\mathrm{D}} = -\frac{3}{2}\frac{\alpha_{\mathrm{p},1}\alpha_{\mathrm{p},2}}{r^6}\frac{I_1 I_2}{I_1 + I_2} \equiv -\frac{A}{r^6} \tag{A.2}$$

- **Repulsive interaction**: also of quantum nature, this interaction is important when the molecules are closer than an equilibrium distance r_0. The overlap of the occupied electron orbitals is forbidden by Pauli exclusion principle resulting in a

[1] For chemisorption the interaction is strong enough to enable chemical bonds (i.e., covalent or ionic) between the adsorbate and adsorbent molecules.

[2] r should be given by the sum of the van der Waals radii of the interacting molecules.

[3] In reality the estimation of the London force is rather complex as its magnitude is affected by the presence of other molecules. Besides the original expression derived by London (presented in (A.2)) two other expressions can be used for the estimation of this force term (Slater-Kirkwood and Kirkwood-Müller) [101, 225].

repulsive interaction [227]. This interaction increases with the decreasing distance and the corresponding potential is given by equation (A.3). The sum of the potential energies $\phi_D + \phi_R$ leads to the Lennard-Jones potential function, whose derivative is null at $r = r_0$.

$$\phi_R = +\frac{Ar_0^6}{2r^{12}} \equiv +\frac{B}{r^{12}} \tag{A.3}$$

- **Ion − induced dipole interaction**: this interaction exists when an ionic charge q present on the adsorbent's surface (e.g., Na^+ in a zeolite) generates an electric field E which induces a dipole on the incoming molecule with polarizability α_p. The electrostatic potential energy is calculated with equation (A.4). $\epsilon_0 = 8.854 \times 10^{-12}\,C^2\,J^{-1}\,m^{-1}$ is the permittivity of free space.

$$\phi_{ind} = -\frac{1}{2}\alpha_p \frac{q^2}{r^4(4\pi\epsilon_0)^2} \equiv -\frac{1}{2}\alpha_p E^2 \tag{A.4}$$

- **Ion − permanent "point" dipole interaction**: this interaction exists when the adsorbent has charges and the adsorbate has molecules with a permanent dipole μ_{dp} (e.g., H_2O) that interacts with the electric field E produced by the adsorbent ions (with a charge q). The corresponding potential is calculated according to equation (A.5). θ is the angle between the direction of the dipole moment and the electric field. The interaction can be either attractive or repulsive depending on θ.

$$\phi_{E\mu} = -\frac{q\mu_{dp}\cos\theta}{r^2(4\pi\epsilon_0)} \equiv -E\mu_{dp}\cos\theta \tag{A.5}$$

- **Field gradient − electric quadrupole interaction**: the electrostatic energy between the quadrupole moment[4] Q of the adsorbate and the field gradient $\partial E/\partial r$ of charge q is determined with equation (A.6) where θ is the angle between the field gradient and quadrupole moment. This interaction can also be either attractive or repulsive.

$$\phi_{EQ} = -\frac{Qq(3\cos^2\theta - 1)}{4r^3(4\pi\epsilon_0)} \equiv \frac{1}{2}Q\frac{\partial E}{\partial r} \tag{A.6}$$

It can be shown that for low coverage, where the adsorbate-adsorbate interactions can be neglected, and at ambient temperatures the isosteric heat of adsorption is $\Delta H \sim \phi$. For high-silica zeolites (with a reduced number of cations), the adsorption of non-polar molecules dominates (equations (A.2) and (A.3)). Hence, ΔH is expected to increase with the polarizability of the adsorbents and with the decrease of the pore sizes of the host zeolites. This effect has been reported in [98]. The presence of cations implies an additional interaction term with non-polar molecules, given by equation (A.4). For polar molecules (for instance H_2O or NH_3 on chabazite) the electrostatic interaction can be dominant as reported in [228].

[4]The quadrupole moment Q arises from a non-uniform distribution of charge within the molecule.

Appendix B

Description of the facilities used for the experiments

B.1 HyDe loop facility

B.1.1 P&ID

The Pipe and Instrumentation Diagram (P&ID) of the HyDe loop facility used for the permeation experiments without tritium (i.e., He, H_2, D_2 as feeding gases) through two MFI membranes is presented in figure B.1. The pathways for the three gases are evidenced by colours: green for helium, red for protium and orange for deuterium. Blue represents the common path, which is the feed and permeate sides of the membrane. In dark gray the main components used for these experiments are shown: gas bottles, mass-flow controllers RF01/02/03, pressure sensors RP01/02, thermocouples RT01/02, vacuum pumps, vessels BD01/02, the catalyst KT01 and the membrane module MM01.

B.1.2 Description of the instrumentation

The characteristics of the instruments used for the experiments performed in the HyDe loop facility are presented below and summarised in table B.1:

Mass-flow controllers: the MFCs are used to control the flow of the gas feeding the membrane. The principle of operation of the devices installed in the setup (MKS Instruments Inc., 1179C) for flow control or measurement is based on the change of the temperature profile measured on a by-pass capillary tube (sensor tube) where the gas flows. Thus, the reading of the flow is dependent on the specific heat of the flowing gas. These devices are usually calibrated for a specific gas (e.g., N_2), and the actual flow of a different gas can be calculated using the specific heat values of both gases. For MKS devices, gas-conversion factors are available in [229]. In the HyDe loop facility RF01 is calibrated for helium and both RF02 and RF03 are calibrated for H_2 and while RF01 and RF02 were used for the gases with which they were calibrated, RF03 was used for D_2. However, due to the physical similarities of

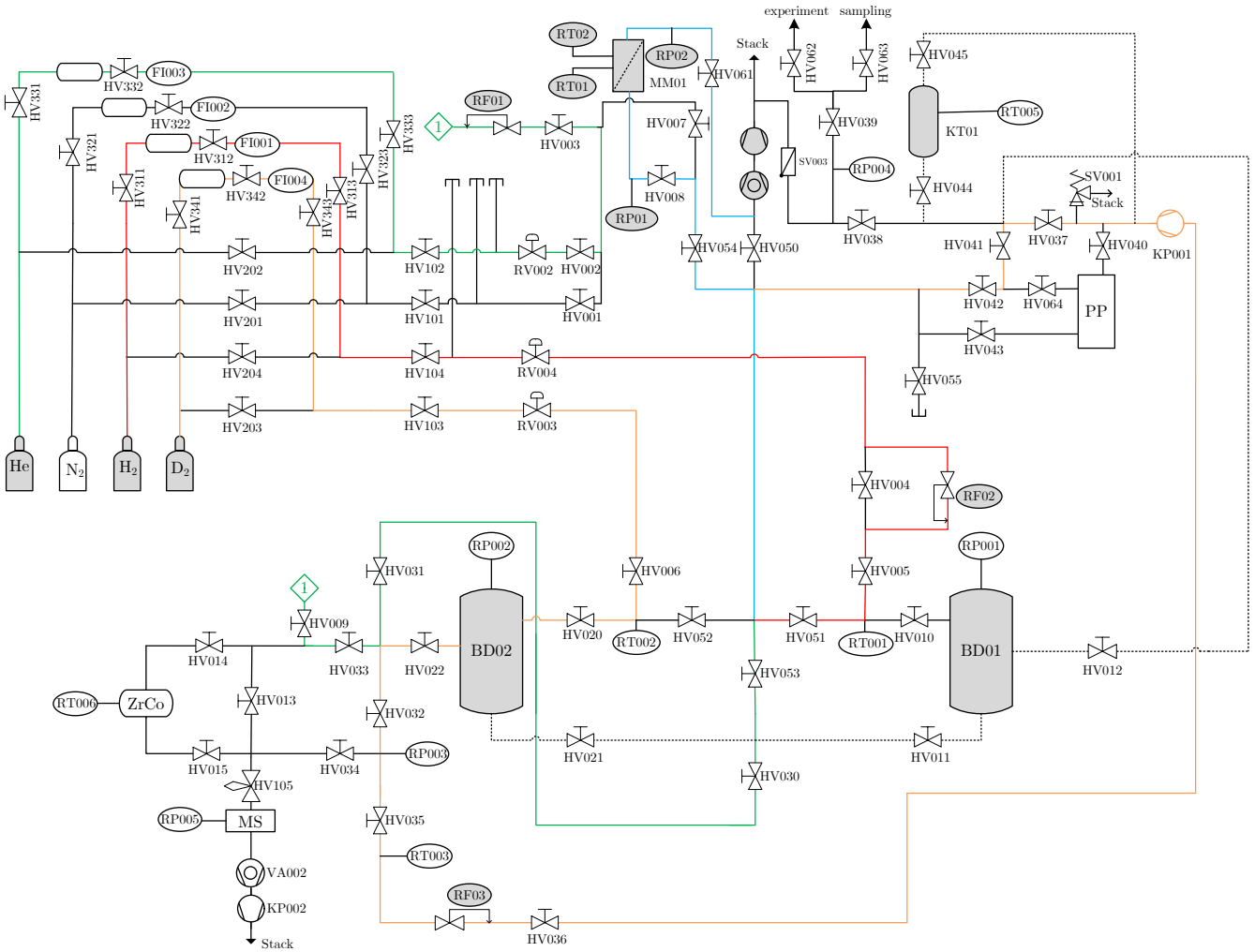

Figure B.1: P&ID of the HyDe loop facility. The flow paths for He, H_2 and D_2 are indicated respectively in green, orange and blue. In light blue the common path for all gases (i.e., feeding and permeate lines) is shown. The main components used for the permeation experiments are presented in gray. BD: vessel, HV: hand valve, KP: circulation pump, KT: catalyst, MM: membrane module, MS: mass spectrometer, PP: permeator, RF: flow controller, RP: pressure sensor, RV: regulation valve (pressure), SV: safety valve, VA: vacuum pump.

Table B.1: Characteristics of the devices used for the permeation experiments through MFI membranes performed at the HyDe loop facility. The flows are given in $\mathrm{mL\,min^{-1}}$ at standard conditions of temperature and pressure or sccm (standard cubic centimeter per minute). The data sheets for the mass-flow controllers and pressure sensors are available in [230] and [231], respectively.

Name	Full Scale (FS)	Physical principle	Accuracy
RF01 ($F_{\mathrm{p,He}}$)	$200\,\mathrm{mL\,min^{-1}}$	thermal-based	$\pm 0.5\,\%$ of FS
RF02 ($F_{\mathrm{p,H2}}$)	$100\,\mathrm{mL\,min^{-1}}$	thermal-based	$\pm 0.5\,\%$ of FS
RF03 ($F_{\mathrm{p,D2}}$)	$500\,\mathrm{mL\,min^{-1}}$	thermal-based	$\pm 0.5\,\%$ of FS
RP01 (p_{f})	3000 mbar	diaphragm deflection	$\pm 0.1\,\%$ of FS
RP02 (p_{p})	3000 mbar	diaphragm deflection	$\pm 0.1\,\%$ of FS
RT01 (T_{m})	$> 1273.15\,\mathrm{K}$	thermoelectric effect	$\pm 1\,\%$ of reading
RT02 (T_{m})	$> 1273.15\,\mathrm{K}$	thermoelectric effect	$\pm 1\,\%$ of reading

both diatomic gases, the correction for the flow is below 1 %, which is within the experimental uncertainty of the measurements. The uncertainties associated with the flow measurements were calculated using the information available in the data sheet of the devices. Due to the high-repeatability of these devices observed during experiments, this uncertainty was considered much lower than 1 %.

Pressure sensors: the pressure sensors RP01 and RP02 are used to measure the feed and permeate absolute pressures. The technology of the sensors used relies on a diaphragm (metallic sensing element), whose deflection measures the pressure of the gas (absolute and not gas-dependent). These high-accuracy sensors were purchased from L'Essor Français Electronique (EFE, PTA225), whose expected accuracies are lower than 0.1 % of their full-scale (3000 mbar for the devices used). The pressure sensors RP001 and RP002 associated, respectively, with vessels BD01 and BD02 are MKS Baratron (type 722A) with a reported accuracy of $\pm 0.5\,\%$ of the reading.

Thermocouples: two thermocouples were installed on the surface of the membrane module for temperature control and measurement. The thermocouples are both of type-K, and their principle of operation is based on a voltage difference which exists between two electrical conductors (e.g., NiCr-NiAl) when they are subjected to a given temperature. Their typical measuring ranges are between $< 273.15\,\mathrm{K}$ up to $> 1273.15\,\mathrm{K}$. These thermocouples were purchased from RS Components Ltd., with accuracies of 1 % in the measuring range.

Heater and control unit: the heating wire (HORST 023006) is connected to a control unit (HORST RC00725), which allows the regulation of the desired membrane temperature using one of the thermocouples mentioned in the previous point.

Vacuum pumps: the pumping train is used for two different purposes: (1) continuous evacuation of the permeate and pressure-difference for permeation through the membrane, (2) cleaning of the lines to ensure the quality of the experiments. For (1), only the rough vacuum-pump MVP 015-2 (diaphragm type) is used, which can provide an ultimate pressure of 5×10^{-1} mbar. During the experiments typical permeate pressures were around 30 mbar. For (2), both diaphragm and turbo-molecular pumps are used in series. The turbo-molecular pump has an ultimate-pressure below 10^{-7} mbar. The two pumps are part of the commercial pumping train Pfeiffer HiCube 80.

The control of all devices and data acquisition were done with LabVIEW.

B.1.3 Production of catalysed mixtures with HD

To produce the desired H_2-HD-D_2 catalysed gas mixture, each vessel is initially filled with H_2 (e.g., BD01) and D_2 (e.g., BD02) up to a certain pressure. The circulation pump KP001 is used to route the gas through the catalyst (1/6" Al_2O_3 pebbles coated with Pt) to promote the production of the isotopologue HD. The final H_2-HD-D_2 gas composition is a function of the initial H_2/D_2 molar ratio, catalyst temperature and equilibration time (refer to Appendix E).

Two permeation experiments with catalysed mixtures were performed with each MFI-ZSM-5 membrane at 298 K to validate the extrapolation presented in section 4.6.3. For these experiments, RF03 was replaced with RF02, with better sensitivity, to ensure a higher accuracy in the calculated permeances. For these experiments, two equilibrated mixtures of H_2-HD-D_2 with 25-50-25 mol% were prepared, using the following procedure:

1. evacuation of the lines using the pumping train for several hours;
2. the two vessels BD001 and BD002 with similar volumes[1] are initially filled with equal pressures (e.g., 1300 mbar) of H_2 and D_2, respectively;
3. a closed-loop circuit including the vessels BD001/BD002, the circulation pump KP001 and the catalyst at 473 K is used to circulate the mixture until an equilibrated mixture is produced (dashed lines in figure B.1).

The circulation rate is limited by RF02, which has a full-scale of 100 mL min^{-1} and therefore the whole gas mixture must be recirculated through the catalyst for, at least, 45 min. Nevertheless, 2 h of recirculation were used to ensure well equilibrated mixtures. The composition of the prepared gas mixture was measured offline with LARA, by sampling it to a dedicated 500 cm^3 gas vessel ("sampling" in figure B.1). To ensure

[1] BD001 has a volume of (1665 ± 9) cm^3, and BD002 has a volume of (1655 ± 8) cm^3 [142].

Table B.2: Composition of the catalysed mixtures prepared in the HyDe loop facility. The RP001 and RP002 values are, respectively, the pressures of the BD001 and BD002 vessels when filled with H_2 and D_2. The composition values were measured with LARA.

Mix. #	RP001 (mbar)	RP002 (mbar)	H_2 (mol%)	HD (mol%)	D_2 (mol%)	Circulation time (min)
1	1240 ± 6	1156 ± 6	26.7 ± 1.2	39.7 ± 1.3	33.6 ± 1.2	40
2	1230 ± 6	1236 ± 6	24.7 ± 1.2	49.5 ± 1.5	25.9 ± 1.1	> 120
3	1360 ± 7	1397 ± 7	25.5 ± 1.2	48.2 ± 1.6	26.2 ± 1.5	> 120
4	1361 ± 7	1358 ± 7	25.5 ± 1.2	49.6 ± 1.4	25.0 ± 1.0	> 120

reproducibility in the procedure described above, several mixtures were prepared with an equimolar mixture of H_2/D_2. The composition of four gas mixtures produced are presented in table B.2. All four mixtures have the same concentration of H_2/D_2 within $\pm 2\,\%$. The mixture 1 was circulated through the catalyst for only 40 min, which, as expected, provides a concentration of H_2-HD-D_2 considerably different from 25-50-25 mol%. In contrast, for longer circulation times (mixtures $\#\,2-4$), the catalysed mixtures measured with LARA had a gas composition close to a fully equilibrated mixture. This procedure demonstrated a good reproducibility for the preparation of catalysed mixtures.

The catalysed mixture was fed into the membrane using the orange path presented in figure B.1. To ensure that the steady-state is reached in ≈ 30 min, a feeding flow of $50\,\mathrm{mL\,min^{-1}}$ was used.

B.2 ZEMTEX facility

B.2.1 Description of the main components used for the experiments

The role of each main device/component installed in the ZEMTEX facility is described in section 5.3. Furthermore, the principles of operation of most of the devices installed inside the glovebox are similar to those used in the HyDe loop facility. Therefore, only the principles of operation of the ionisation chambers, moisture sensors, CuO reactor and molecular-sieve beds are presented here for completeness. The characteristics of all instrumentation installed in ZEMTEX are summarised in table B.3.

Ionisation chambers: the ionisation chambers installed in the ZEMTEX setup are custom-made cross-piece detectors widely used at the TLK [162, 163]. These devices consist of an outer, cylindric anode made of a stainless steel mesh, whereas the cathode is a thin (0.89 mm diameter), conducting (also stainless steel) rod placed in the cylinder axis. Between both electrodes a voltage of 180 V is usually applied.

When the tritiated gas flows through the chamber, electrical charges are produced and collected as a result of the ionising events induced by the radioactive gas. Afterwards the current is measured with a picoammeter. On the one side, these devices have several advantages such as small size and inline operation. On the other side, these devices suffer from memory effect and they are sensible to gas composition [232];

Moisture sensors: the moisture sensors were deployed for online measurement of the moisture content of the streams (relevant for the Q_2O/He experiments). These PURA devices manufactured by Michell Instruments rely on the variations of impedance measured when water molecules are absorbed on an insulating material, placed between two metallic plates [233]. The metallic surface exposed to the gas is a very thin ($< 0.1\,\mu m$), porous surface which allows the permeation of water molecules towards the insulating material. Moreover, since the dielectric constant of the water molecules is much higher than that of the insulating layer and carrier gas[2] the water molecules are easily detected. These devices are especially

Table B.3: Characteristics of the devices used for the experiments in the ZEMTEX/CAPER facility. The flows given in $mL\,min^{-1}$ are at standard conditions of temperature and pressure or sccm (standard cubic centimeter per minute).

Name	Model	Operation range	Accuracy
RF007	MKS 1749A	$30 - 1500\,mmol\,h^{-1}$	$\pm 0.5\,\%$ of FS
RF1006	MKS M200	$2 - 100\,mL\,min^{-1}$	$\pm 0.5\,\%$ of FS
RF3002	Brooks GF80	$10 - 500\,mL\,min^{-1}$	$\pm 0.1\,\%$ of FS
RF3003	Brooks GF80	$10 - 500\,mL\,min^{-1}$	$\pm 0.1\,\%$ of FS
RF3004	Brooks GF80	$30 - 1500\,mL\,min^{-1}$	$\pm 1\,\%$ of reading
RP802	MKS Baratron	$0 - 2000\,hPa$	$\pm 0.5\,\%$ of reading
RP805	MKS Baratron	$0 - 2000\,hPa$	$\pm 0.5\,\%$ of reading
RP842	MKS Baratron	$0 - 100\,hPa$	$\pm 0.5\,\%$ of reading
RP848	MKS Baratron	$0 - 2000\,hPa$	$\pm 0.5\,\%$ of reading
RP866	MKS Baratron	$0 - 2000\,hPa$	$\pm 0.5\,\%$ of reading
RP3001	EFE PTA225	$0 - 2000\,hPa$	$\pm 0.1\,\%$ of FS
All RM	Michell Instr. PURA	$-100 - +20\,°C$	$\pm 0.1\,\%$ of FS
All RT	RS Components Ltd.	$273.15 - 1273.15\,K$	$\pm 1\,\%$ of reading
All RX	KIT custom-made	$0 - 10^9$ pA	$\pm 10 - 20\,\%$ of reading
KP802/803	Senior Flexonics Inc. MB601DC	–	–
VA851	Normetex	–	–
VA852	Senior Flexonics Inc. MB601DC	–	–

[2]For instance, the relative dielectric permittivity of helium is around 1 at relevant temperatures, whereas the relative dielectric permittivity of water is around 78 at 298 K and 55 at 373 K [234, 235].

designed for dry atmospheres with a range of dew point values between $-100\,°C$ and $+20\,°C$. The accuracy of these devices is on the order of 2 % as reported by the manufacturers;

CuO reactor: the CuO reactor is required for the oxidation of the incoming Q_2/He stream through the reaction $CuO(s) + Q_2(g) \rightarrow Cu(s) + Q_2O(g)$. The operation of this reactor is rather simple[3] and for an efficient conversion it should be operated at temperatures around 400 °C. This material, accommodated in a compact stainless steel vessel ($\approx 300\,cm^3$), has been widely used to produce highly tritiated water at the TLK [57, 164]. Although high oxidation efficiencies should be expected, the amount of Q_2 which is converted into Q_2O has been observed to decrease over time;

Molecular sieve bed: as described in section 5.1 the molecular sieve beds are widely used in tritium laboratories, mainly in the tritum retention systems of glove-boxes [152, 237]. Moreover, small volume MSBs ($\approx 150\,cm^3$) have been used for the adsorption of highly tritiated water in different experiments at the TLK [57, 164]. These vessels contain hydrophilic zeolite pebbles (e.g., 3A or 5A) as adsorbents (typically around $100 - 120\,g$) whose usual water adsorption capacities are limited to 20 wt%.

B.2.2 Construction and qualification of a metal-sealed membrane module

B.2.2.1 Selection of the sealing material

Besides the tritium compatibility, the sealing material of the lab-scale module has to fulfill the following requirements: (1) ductility, (2) stability up to 150 °C (423 K) and (3) stability up to 1500 hPa of pressure difference. The criteria (2) and (3) are imposed by the experimental conditions expected along the ZEMTEX campaign. Moreover, due to the brittleness of the zeolite-ceramic membranes, the ductility of the sealing material is important to avoid breaking the membrane. The metallic $50 - 50$ wt% InPb alloy (Indalloy 7) was found to fulfill these requirements [238]. This material has solidus and liquidus temperatures of 184 °C and 210 °C, respectively, which are above the desired maximum membrane temperature. Furthermore, the compressive strengths of indium and lead are on the order of a few MPa.

The actual membrane sealings were prepared out of InPb wire manufactured by Indium Corporation [239]. Qualification tests were performed to measure the pressure difference established across the membrane at different temperatures ($< 150\,°C$). Moreover, the

[3] A micro-reactor is also available in CAPER for water production as described in [236]. However, this device requires a continuous control of O_2 supply and it is reported to produce higher pressure-drops across it when compared to the CuO.

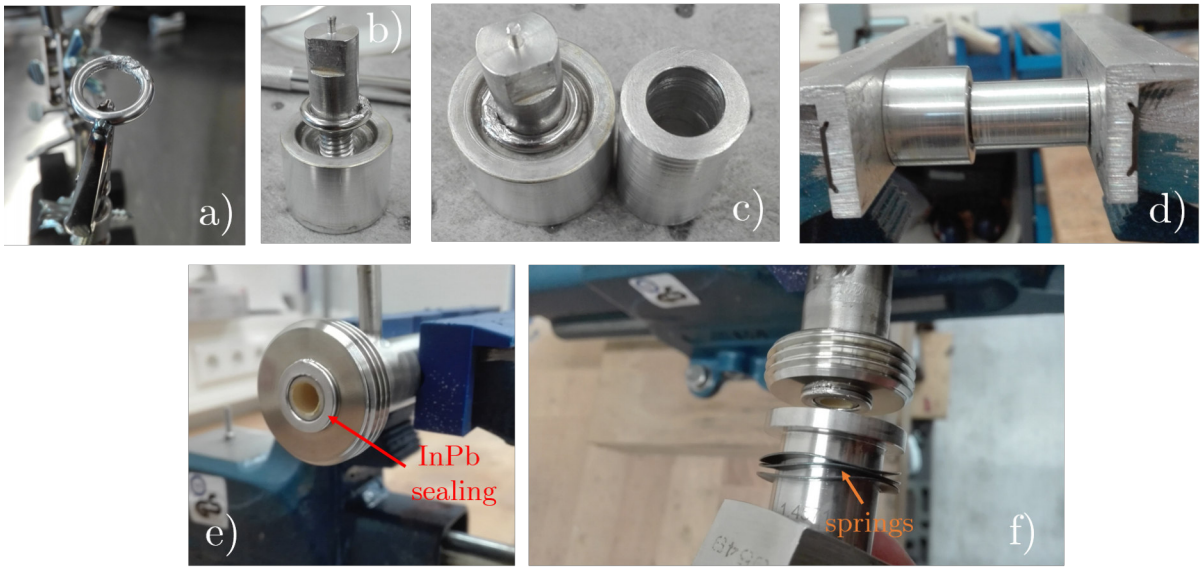

Figure B.2: Photos taken along the preparation and installation of InPb sealings for the zeolite-ceramic membrane accommodated inside the stainless membrane module. a) preparation of O-ring out of InPb wire, b)-d) flattening of the surface, e) installation at the membrane, f) closing of the module with threaded connections with metal springs to avoid high stress and breaking of the membrane.

helium leak-tightness of the whole module was also measured along several thermal cycles.

B.2.2.2 Preparation and installation of the InPb sealing

The main steps for the preparation of the InPb sealings are displayed in figure B.2. First, a InPb O-ring, with the same diameter as the membrane outer diameter ($\approx$ 10 mm), is manually prepared out of the InPb wire (figure B.2a)). Then, two metal cylinders are pressed against each other with the metallic O-ring placed in between them (figure B.2b)-d)). As a result, the O-ring is flattened and ready to be placed at one of the membrane ends (figure B.2e)). The membrane module is closed afterwards using two threaded connections at both ends (figure B.2f))

B.2.2.3 Helium leak-tests (external)

The helium leak-rates of single components in the primary system must not exceed 10^{-9} mbar L s^{-1}. Therefore, after the assembly of the membrane module, helium leak-tests towards the outside were performed for the whole module. The schematic diagram of the apparatus used for these tests is presented in figure B.3. The module, with the membrane sealed with InPb sealings, was placed inside an oven where the temperature was varied between $\approx$ 298 K and $\approx$ 423 K. A leak-detector (Pfeiffer Smart test HLT 570), operated under vacuum mode, was connected to one of the module ports and a cold trap at liquid nitrogen temperatures (77 K) was placed between the leak-detector

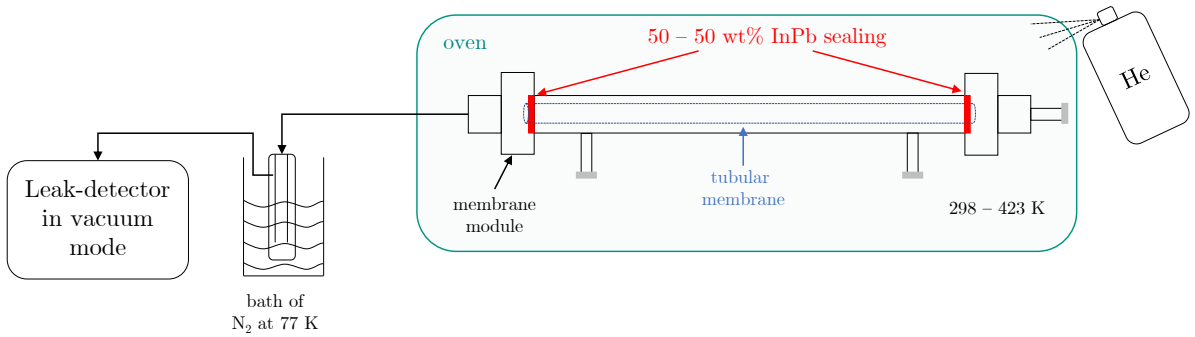

Figure B.3: Schematic diagram of the setup used to perform helium leak-tests with the newly prepared membrane module.

and the module to avoid the contamination of the leak-detector[4]. With background levels of 10^{-10} mbar L s^{-1}, helium (99.9999 mol% purity) was sprayed into the oven and the resulting leak-rates measured. After various temperature cycles and repeated measurements for several days, the highest measured leak-rate was 2×10^{-10} mbar L s^{-1}, well below 10^{-9} mbar L s^{-1}, as required by the TLK regulations for tritium processing components.

B.2.2.4 Hermicity leak-tests (internal)

The objective of these tests is to demonstrate that the metallic sealings are hermetic and suitable for gas separation experiments in which a constant pressure difference between the feed and permeate sides is required. The membrane was installed in the HyDe loop facility and it was tested in dead-end mode. The pressure difference across the membrane was measured for relevant feeding flows ($100 - 200$ mL min^{-1}) and temperatures ($298 - 423$ K). At each temperature, constant plateaus of pressure difference were observed for He, H_2 and D_2 along $\approx 1 - 2$ h. These results are consistent with those obtained with EPDM sealings (retentate closed as in figure 4.4), suggesting no measurable difference in the hermicity of the InPb sealings. In addition, the membrane was tested for more than 20 h at 423 K, demonstrating no appreciable temperature or gas effect in the internal leak-tightness of the membrane, at the pressure ranges of interest. These tests successfully qualified the $50 - 50$ wt% In-Pb sealings as alternative to the EPDM O-rings, fulfilling the tritium compatibility requirement to perform experiments with zeolite membranes under tritiated atmosphere.

[4]All contaminants (e.g., water molecules outgassed from the metallic surfaces) remain at the cold trap and a clean helium gas arrives at the leak-detector (helium liquifies at 4.2 K).

Appendix C

Uncertainty budget for the quantities measured along the experiments

C.1 Procedure to determine the uncertainty of a measurand

The procedure followed to evaluate the experimental uncertainties of all different measured quantities (i.e., gas flows, pressures, temperatures) is inline with the recommendations provided by the document "EA-4/02 M: 2013" [240]. This document is written in accordance with the "Guide to the expression of uncertainty in measurement" (GUM) [241].

Two types of methods exist to evaluate the standard uncertainties of the measurands. The type A method considers the statistical analysis of a series of observations and the type B relies on the information available specific to the measuring device (e.g., certificates of calibration, data sheets). These sources of error should be taken into account for a correct estimation of the uncertainty associated with the measured quantity. In the case of uncorrelated quantities, which is the case for the work presented in this thesis, the final uncertainty δy of the output y is calculated by equation (C.1), where δy_i^2 is one of the m components used for the final uncertainty.

$$\delta y^2 = \sum_{i=1}^{m} \delta y_i^2 \tag{C.1}$$

In a series of measurements with n independently measured data points q, the estimate of the quantity Q is the aritmetic average $\bar{q}$ defined by equation C.2. The corresponding uncertainty $\delta\bar{q}$ is determined by the experimental standard deviation of the mean, given by equation (C.3).

$$\bar{q} = \frac{1}{n}\sum_{j=1}^{n} q_j \tag{C.2}$$

$$\delta\bar{q} = \sqrt{\frac{\frac{1}{n-1}\sum_{j=1}^{n}(q_j - \bar{q})^2}{n}} \tag{C.3}$$

The accuracy of the measuring device reported by the manufacturer (e.g., data sheets) is an example of the information which can be used for the type B source. Usually given with lower (a_-) and upper (a_+) limits, the uncertainty of the measurand x_i is the value $a = a_- = a_+$ divided by $\sqrt{3}$ (representing a rectangular distribution of probability), as presented in equation (C.4).

$$\delta x_i = \frac{a}{\sqrt{3}} \tag{C.4}$$

The expression of the final uncertainty Δ is determined by multiplying δy by a coverage factor k, which expresses a certain coverage probability (or confidence level). For example, for a coverage probability of 95 %, and when the distribution follows a Gaussian, k is equal to 2. When the Gaussian distribution is not representative (e.g., low number of degrees of freedom), the t-student distribution should be used instead. For a large number of degrees of freedom (> 50), $k \to 2$ for a confidence level of 95 %.

C.2 Propagation of uncertainty for the permeance and selectivity

The uncertainty of the quantity f, which is a function of the variables $X_1, X_2, ..., X_i, ...$, is determined by taking into account the individual contributions δX_i. For independent variables, the expanded uncertainty Δf is determined using equation (C.5). The underlying necessary condition to use equation (C.5) is to assume that variables $X_1, X_2, ..., X_i, ...$ are measured independently and the observed values follow a normal distribution [242]. As presented above, δX_i are the standard uncertainties and k is the coverage factor.

$$\Delta f = k\sqrt{\left(\frac{\partial f}{\partial X_1}\delta X_1\right)^2 + \left(\frac{\partial f}{\partial X_2}\delta X_2\right)^2 + ... + \left(\frac{\partial f}{\partial X_i}\delta X_i\right)^2 + ...} \tag{C.5}$$

The permeance is dependent on the gas flow $F_{\mathrm{f},i}$, feed and permeate pressures $p_{\mathrm{f},i}$ and $p_{\mathrm{p},i}$, and membrane surface area A_m. Applying equation (C.5) to the definition of the permeance presented in section 3.1, the expanded uncertainty for the permeance is given by equation (C.6).

$$\Delta \Pi_i = k\Pi_i\sqrt{\left(\frac{\delta F_{\mathrm{f},i}}{F_{\mathrm{f},i}}\right)^2 + \left(\frac{\sqrt{\delta p_{\mathrm{f},i}^2 + \delta p_{\mathrm{p},i}^2}}{p_{\mathrm{f},i} - p_{\mathrm{p},i}}\right)^2 + \left(\frac{\delta A_\mathrm{m}}{A_\mathrm{m}}\right)^2} \tag{C.6}$$

The selectivity is defined by ratio of the permeances of two gases and thus the expression for the expanded uncertainty for $\Delta\alpha^*_{i,j}$ is given by equation (C.7).

$$\Delta\alpha^*_{i,j} = k\alpha^*_{i,j}\sqrt{\left(\frac{\delta \Pi_i}{\Pi_i}\right)^2 + \left(\frac{\delta \Pi_j}{\Pi_j}\right)^2} \tag{C.7}$$

Appendix D

Results of the permeation experiments without tritium

The values and the corresponding uncertainties obtained along the entire experimental campaign of the permeation experiments through MFI-ZSM-5 membranes A and B without tritium (chapter 4) are presented here.

D.1 Linearity between the permeation flow and pressure difference

The experiments to verify the linearity between the imposed permeation flow and measured pressure difference at $\approx 298\,\mathrm{K}$ are presented and discussed in section 4.3. The results obtained for membrane A are presented in table D.1, while the results obtained for membrane B are presented in table D.2. In the plot of figure D.1 the linear fitting for the measured values with membrane B are presented (the corresponding plot for membrane A is presented in the core text, section 4.3). The permeances are also given in these tables, and the constancy of the values demonstrate that the permeance is independent of the pressure difference across the membrane (and hence large diameter defects on the order of $10^2\,\mathrm{nm}$ are absent).

Table D.1: Data from the permeation experiments carried out to verify the linearity between the permeation flow and the pressure difference (membrane A).

Gas	$F_{\mathrm{p},i}$ ($10^{-7}\,\mathrm{mol\,s^{-1}}$)	Δp_i (10^3 Pa)	Π_i ($10^{-9}\,\mathrm{mol\,m^{-2}\,s^{-1}\,Pa^{-1}}$)
He	74 ± 4	6.6 ± 0.2	233 ± 29
	149 ± 4	13.4 ± 0.2	230 ± 14
	224 ± 4	20.4 ± 0.2	226 ± 9
	298 ± 4	27.4 ± 0.2	224 ± 7
	372 ± 4	34.5 ± 0.2	223 ± 5
	447 ± 4	41.8 ± 0.2	221 ± 4
	521 ± 4	49.0 ± 0.2	220 ± 4
	596 ± 4	56.3 ± 0.2	219 ± 3
	671 ± 4	63.6 ± 0.2	218 ± 3
	744 ± 4	70.8 ± 0.2	214 ± 2
H_2	76 ± 2	4.4 ± 0.2	360 ± 41
	151 ± 2	8.1 ± 0.2	382 ± 23
	225 ± 2	11.9 ± 0.2	389 ± 16
	300 ± 2	15.8 ± 0.2	393 ± 12
	374 ± 2	19.6 ± 0.2	396 ± 10
	449 ± 2	23.4 ± 0.2	397 ± 8
	523 ± 2	27.2 ± 0.2	398 ± 7
	598 ± 2	31.0 ± 0.2	399 ± 6
	672 ± 2	34.8 ± 0.2	399 ± 6
	747 ± 2	38.2 ± 0.2	403 ± 2
D_2	80 ± 11	5.6 ± 0.2	296 ± 76
	155 ± 11	11.2 ± 0.2	287 ± 38
	230 ± 11	17.0 ± 0.2	279 ± 25
	303 ± 11	22.4 ± 0.2	279 ± 19
	378 ± 11	28.0 ± 0.2	278 ± 15
	453 ± 11	33.5 ± 0.2	279 ± 13
	527 ± 11	39.2 ± 0.2	278 ± 11
	602 ± 11	44.7 ± 0.2	278 ± 9
	677 ± 11	50.2 ± 0.2	278 ± 8
	752 ± 11	55.5 ± 0.2	279 ± 8

Table D.2: Data from the permeation experiments carried out to verify the linearity between the permeation flow and the pressure difference (membrane B).

Gas	$F_{\mathrm{p},i}$ (10^{-7} mol s^{-1})	Δp_i (10^3 Pa)	Π_i (10^{-9} mol m^{-2} s^{-1} Pa^{-1})
He	74 ± 4	5.2 ± 0.2	296 ± 40
	149 ± 4	10.6 ± 0.2	290 ± 19
	223 ± 4	16.0 ± 0.2	289 ± 13
	298 ± 4	21.4 ± 0.2	288 ± 10
	372 ± 4	26.7 ± 0.2	286 ± 8
	446 ± 4	32.4 ± 0.2	285 ± 6
	521 ± 4	37.9 ± 0.2	283 ± 5
	595 ± 4	43.5 ± 0.2	282 ± 5
	670 ± 4	54.9 ± 0.2	282 ± 4
	744 ± 4	50.5 ± 0.2	280 ± 4
H_2	76 ± 2	3.1 ± 0.2	500 ± 76
	150 ± 2	6.1 ± 0.2	504 ± 39
	225 ± 2	9.2 ± 0.2	505 ± 26
	299 ± 2	12.3 ± 0.2	503 ± 19
	374 ± 2	15.3 ± 0.2	503 ± 15
	448 ± 2	18.4 ± 0.2	503 ± 13
	523 ± 2	21.5 ± 0.2	502 ± 11
	597 ± 2	24.6 ± 0.2	502 ± 10
	671 ± 2	27.6 ± 0.2	502 ± 9
	746 ± 2	30.7 ± 0.2	502 ± 8
D_2	80 ± 11	4.3 ± 0.2	383 ± 100
	155 ± 11	8.5 ± 0.2	374 ± 51
	229 ± 11	12.9 ± 0.2	367 ± 34
	303 ± 11	17.3 ± 0.2	363 ± 25
	378 ± 11	21.7 ± 0.2	360 ± 20
	452 ± 11	26.1 ± 0.2	358 ± 17
	527 ± 11	30.2 ± 0.2	360 ± 14
	601 ± 11	34.7 ± 0.2	357 ± 12
	676 ± 11	39.3 ± 0.2	356 ± 11
	758 ± 11	42.7 ± 0.2	359 ± 11

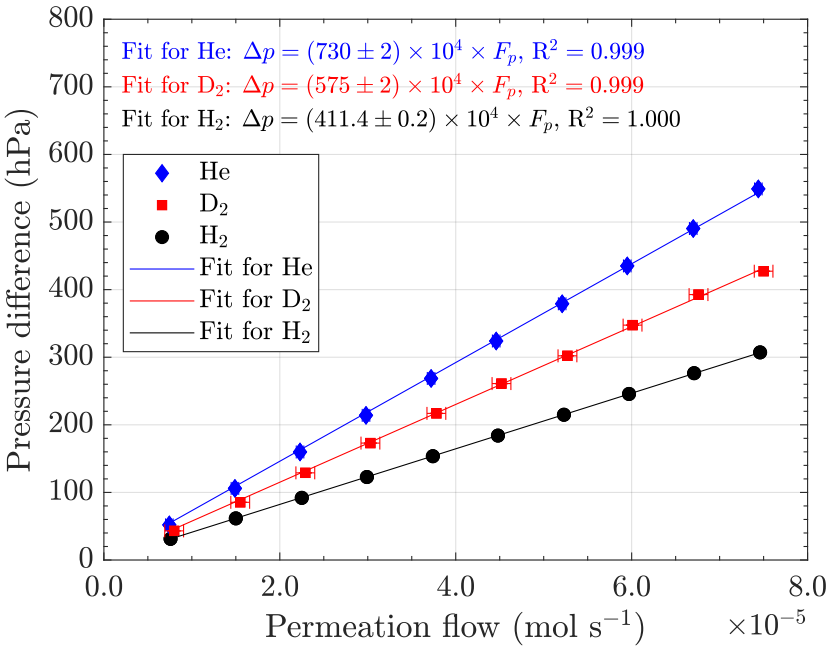

Figure D.1: Linearity between the imposed flow and the measured pressure difference across membrane B. He: blue diamonds, H_2: black circles, D_2: red squares. Obtained at 298 K. The solid lines are linear fits for the corresponding data.

D.2 Single-gas permeances as a function of the membrane temperature

The single-gas permeation experiments as a function of the membrane temperature are discussed in section 4.4. The results obtained for membrane A are presented in table D.3, while the results obtained for membrane B are presented in table D.4.

Table D.3: Data obtained during the experiments performed to measure the single-gas permeances through membrane A. Accuracy of the thermocouples assumed to be 1 % of the measured value.

Gas	$F_{\mathrm{p},i}$ ($10^{-7}\,\mathrm{mol\,s^{-1}}$)	Δp_i (10^3 Pa)	Π_i ($10^{-9}\,\mathrm{mol\,m^{-2}\,s^{-1}\,Pa^{-1}}$)	T_{m} (K)
He	744 ± 4	70.8 ± 0.2	214 ± 2	298 ± 3
	744 ± 4	71.5 ± 0.2	215 ± 2	304 ± 3
	744 ± 4	77.5 ± 0.2	200 ± 1	313 ± 3
	744 ± 4	81.4 ± 0.2	189 ± 2	321 ± 3
	744 ± 4	89.4 ± 0.2	172 ± 2	336 ± 3
	744 ± 4	98.1 ± 0.2	157 ± 2	347 ± 3
	744 ± 4	103.6 ± 0.2	148 ± 2	358 ± 4
	744 ± 4	106.0 ± 0.2	145 ± 1	373 ± 4
	744 ± 4	103.9 ± 0.2	148 ± 2	384 ± 4
	744 ± 4	99.9 ± 0.2	154 ± 2	399 ± 4
	744 ± 4	98.6 ± 0.2	156 ± 2	409 ± 4
H_2	747 ± 2	38.2 ± 0.2	403 ± 2	298 ± 3
	746 ± 2	39.1 ± 0.2	394 ± 5	304 ± 3
	746 ± 2	42.0 ± 0.2	368 ± 4	313 ± 3
	746 ± 2	44.0 ± 0.2	350 ± 6	321 ± 3
	746 ± 2	49.9 ± 0.2	310 ± 3	334 ± 3
	746 ± 2	54.1 ± 0.2	286 ± 4	346 ± 3
	746 ± 2	58.0 ± 0.2	266 ± 2	358 ± 4
	746 ± 2	58.8 ± 0.2	263 ± 1	371 ± 4
	746 ± 2	57.7 ± 0.2	268 ± 3	383 ± 4
	746 ± 2	58.2 ± 0.2	265 ± 1	396 ± 4
	746 ± 2	57.6 ± 0.2	267 ± 2	409 ± 4
D_2	752 ± 11	55.5 ± 0.2	279 ± 8	298 ± 3
	752 ± 11	58.1 ± 0.2	266 ± 7	304 ± 3
	752 ± 11	60.0 ± 0.2	259 ± 7	313 ± 3
	752 ± 11	64.7 ± 0.2	238 ± 6	321 ± 3
	752 ± 11	75.1 ± 0.2	205 ± 5	338 ± 3
	752 ± 11	80.5 ± 0.2	191 ± 5	346 ± 3
	752 ± 11	85.1 ± 0.2	181 ± 5	359 ± 4
	752 ± 11	84.9 ± 0.2	181 ± 5	371 ± 4
	752 ± 11	83.3 ± 0.2	186 ± 5	384 ± 4
	752 ± 11	82.9 ± 0.2	187 ± 5	396 ± 4
	752 ± 11	81.7 ± 0.2	188 ± 5	409 ± 4

Table D.4: Data obtained during the experiments performed to measure the single-gas permeances through membrane B. Accuracy of the thermocouples assumed to be 1 % of the measured value.

Gas	$F_{\mathrm{p},i}$ ($10^{-7}\,\mathrm{mol\,s^{-1}}$)	Δp_i (10^3 Pa)	Π_i ($10^{-9}\,\mathrm{mol\,m^{-2}\,s^{-1}\,Pa^{-1}}$)	T_m (K)
He	744 ± 4	54.9 ± 0.2	280 ± 4	298 ± 3
	744 ± 4	56.6 ± 0.2	271 ± 4	304 ± 3
	744 ± 4	59.7 ± 0.2	257 ± 3	313 ± 3
	744 ± 4	62.9 ± 0.2	244 ± 3	321 ± 3
	744 ± 4	69.4 ± 0.2	221 ± 3	331 ± 3
	744 ± 4	76.6 ± 0.2	200 ± 2	346 ± 3
	744 ± 4	80.8 ± 0.2	190 ± 2	358 ± 4
	744 ± 4	82.3 ± 0.2	187 ± 2	372 ± 4
	744 ± 4	81.6 ± 0.2	188 ± 2	384 ± 4
	744 ± 4	78.7 ± 0.2	194 ± 2	397 ± 4
	744 ± 4	74.8 ± 0.2	205 ± 2	409 ± 4
H_2	746 ± 2	30.4 ± 0.2	507 ± 8	299 ± 3
	746 ± 2	31.4 ± 0.2	491 ± 7	304 ± 3
	746 ± 2	33.4 ± 0.2	462 ± 7	313 ± 3
	746 ± 2	35.4 ± 0.2	435 ± 6	321 ± 3
	746 ± 2	39.0 ± 0.2	396 ± 4	334 ± 3
	746 ± 2	43.2 ± 0.2	357 ± 4	346 ± 3
	746 ± 2	45.6 ± 0.2	338 ± 4	356 ± 4
	746 ± 2	47.0 ± 0.2	327 ± 4	371 ± 4
	746 ± 2	47.3 ± 0.2	325 ± 3	383 ± 4
	746 ± 2	46.6 ± 0.2	331 ± 4	397 ± 4
	746 ± 2	45.4 ± 0.2	340 ± 4	409 ± 4
D_2	750 ± 11	43.1 ± 0.2	359 ± 11	298 ± 3
	750 ± 11	47.5 ± 0.2	352 ± 10	304 ± 3
	750 ± 11	50.7 ± 0.2	325 ± 9	313 ± 3
	750 ± 11	53.4 ± 0.2	311 ± 8	321 ± 3
	750 ± 11	57.1 ± 0.2	289 ± 8	331 ± 3
	750 ± 11	63.7 ± 0.2	253 ± 7	346 ± 3
	750 ± 11	67.2 ± 0.2	240 ± 6	358 ± 4
	750 ± 11	69.0 ± 0.2	233 ± 6	371 ± 4
	750 ± 11	69.1 ± 0.2	233 ± 6	383 ± 4
	750 ± 11	65.1 ± 0.2	236 ± 6	397 ± 4
	750 ± 11	63.7 ± 0.2	241 ± 7	409 ± 4

D.3 Permeation experiments with H_2/D_2 and H_2/He mixtures

The results obtained for the permeation of binary mixtures H_2/D_2 and H_2/He through MFI membranes at different temperatures are discussed in section 4.6.2. The results obtained for membrane A are presented in tables D.5-D.6 (for H_2/D_2) and D.7-D.8 (for H_2/He), while the results obtained for membrane B are presented in tables D.9-D.10 (for H_2/D_2) and D.11-D.12 (for H_2/He).

Figure D.2 presents the calculated global permeances of H_2/He as a function of the molar mass for membrane A at different temperatures. The curves were obtained with the fitting parameters given in table D.13. Figure D.3 presents the calculated global permeances of H_2/D_2 (top plot) and H_2/He (bottom plot) as a function of the molar mass for membrane B at different temperatures. The curves were obtained with the fitting parameters given in table 4.4 for H_2/D_2 and table D.13 for H_2/He.

Table D.5: Data obtained during the permeation of H_2/D_2 mixtures through membrane A. Only presented in the molar range 10−90 mol% (the values obtained with pure gases are taken from the single-gas permeances). Accuracy of the thermocouples assumed to be 1 % of the measured value.

F_{p,H_2} (10^{-7} mol s^{-1})	F_{p,D_2} (10^{-7} mol s^{-1})	Δp (10^3 Pa)	Π (10^{-9} mol m^{-2} s^{-1} Pa^{-1})
	$T_m = (298 \pm 3)$ K		
76 ± 2	677 ± 11	53.2 ± 0.2	292 ± 8
150 ± 2	602 ± 11	51.7 ± 0.2	301 ± 8
225 ± 2	527 ± 11	50.3 ± 0.2	310 ± 9
300 ± 2	453 ± 11	48.8 ± 0.2	319 ± 9
374 ± 2	378 ± 11	47.3 ± 0.2	330 ± 10
449 ± 2	304 ± 11	45.8 ± 0.2	340 ± 10
523 ± 2	229 ± 11	44.1 ± 0.2	353 ± 10
598 ± 2	155 ± 11	42.4 ± 0.2	367 ± 11
672 ± 2	80 ± 11	40.6 ± 0.2	383 ± 12
	$T_m = (321 \pm 3)$ K		
78 ± 2	676 ± 11	63.8 ± 0.2	244 ± 6
151 ± 2	601 ± 11	62.0 ± 0.2	251 ± 6
225 ± 2	527 ± 11	60.2 ± 0.2	258 ± 6
299 ± 2	452 ± 11	58.3 ± 0.2	267 ± 6
374 ± 2	378 ± 11	56.4 ± 0.2	276 ± 6
454 ± 2	297 ± 11	54.5 ± 0.2	285 ± 6
522 ± 2	229 ± 11	52.4 ± 0.2	296 ± 6
597 ± 2	155 ± 11	50.5 ± 0.2	308 ± 6
672 ± 2	81 ± 11	48.5 ± 0.2	321 ± 6
	$T_m = (346 \pm 3)$ K		
76 ± 2	676 ± 11	78.2 ± 0.2	199 ± 5
150 ± 2	602 ± 11	76.0 ± 0.2	204 ± 5
225 ± 2	527 ± 11	73.9 ± 0.2	210 ± 6
295 ± 2	457 ± 11	71.7 ± 0.2	216 ± 6
369 ± 2	383 ± 11	69.3 ± 0.2	224 ± 6
448 ± 2	304 ± 11	66.8 ± 0.2	233 ± 6
523 ± 2	229 ± 11	64.1 ± 0.2	243 ± 7
597 ± 2	155 ± 11	61.8 ± 0.2	252 ± 7
672 ± 2	81 ± 11	59.3 ± 0.2	263 ± 7

Table D.6: Data obtained during the permeation of H_2/D_2 mixtures through membrane A (cont.). Continuation of table D.5. Only presented in the molar range $10 - 90\,\mathrm{mol\%}$ (the values obtained with pure gases are taken from the single-gas permeances). Accuracy of the thermocouples assumed to be 1 % of the measured value.

$F_{\mathrm{p,H_2}}$ $(10^{-7}\,\mathrm{mol\,s^{-1}})$	$F_{\mathrm{p,D_2}}$ $(10^{-7}\,\mathrm{mol\,s^{-1}})$	Δp $(10^3\ \mathrm{Pa})$	Π $(10^{-9}\,\mathrm{mol\,m^{-2}\,s^{-1}\,Pa^{-1}})$
	$T_\mathrm{m} = (371 \pm 4)\,\mathrm{K}$		
76 ± 2	676 ± 11	86.2 ± 0.2	180 ± 5
150 ± 2	601 ± 11	83.8 ± 0.2	186 ± 5
225 ± 2	526 ± 11	81.3 ± 0.2	191 ± 5
299 ± 2	452 ± 11	78.6 ± 0.2	198 ± 5
377 ± 2	377 ± 11	76.0 ± 0.2	205 ± 5
453 ± 2	299 ± 11	73.6 ± 0.2	212 ± 6
523 ± 2	229 ± 11	70.9 ± 0.2	220 ± 6
597 ± 2	155 ± 11	68.2 ± 0.2	229 ± 6
672 ± 2	80 ± 11	65.3 ± 0.2	238 ± 6
	$T_\mathrm{m} = (398 \pm 4)\,\mathrm{K}$		
76 ± 2	676 ± 11	82.5 ± 0.2	188 ± 5
150 ± 2	602 ± 11	80.3 ± 0.2	193 ± 5
224 ± 2	528 ± 11	78.1 ± 0.2	199 ± 5
299 ± 2	452 ± 11	76.0 ± 0.2	204 ± 5
374 ± 2	378 ± 11	73.7 ± 0.2	211 ± 6
448 ± 2	303 ± 11	71.4 ± 0.2	218 ± 6
521 ± 2	228 ± 11	68.4 ± 0.2	226 ± 6
596 ± 2	156 ± 11	65.9 ± 0.2	236 ± 6
672 ± 2	80 ± 11	63.7 ± 0.2	244 ± 7

Table D.7: Data obtained during the permeation of H_2/He mixtures through MFI membrane A. Only presented in the molar range $10 - 90\,\mathrm{mol\%}$ (the values obtained with pure gases are taken from the single-gas permeances). Accuracy of the thermocouples assumed to be 1 % of the measured value.

$F_{\mathrm{p,H_2}}$ $(10^{-7}\,\mathrm{mol\,s^{-1}})$	$F_{\mathrm{p,He}}$ $(10^{-7}\,\mathrm{mol\,s^{-1}})$	Δp $(10^3\ \mathrm{Pa})$	Π $(10^{-9}\,\mathrm{mol\,m^{-2}\,s^{-1}\,Pa^{-1}})$
	$T_\mathrm{m} = (298 \pm 3)\,\mathrm{K}$		
76 ± 2	670 ± 4	69.1 ± 0.2	223 ± 4
150 ± 2	596 ± 4	66.0 ± 0.2	234 ± 4
225 ± 2	521 ± 4	62.8 ± 0.2	246 ± 5
300 ± 2	447 ± 4	59.3 ± 0.2	260 ± 5
374 ± 2	372 ± 4	56.3 ± 0.2	275 ± 5
449 ± 2	298 ± 4	52.8 ± 0.2	266 ± 6
523 ± 2	223 ± 4	49.5 ± 0.2	292 ± 6
598 ± 2	149 ± 4	46.5 ± 0.2	332 ± 7
672 ± 2	74 ± 4	43.0 ± 0.2	359 ± 8
	$T_\mathrm{m} = (321 \pm 3)\,\mathrm{K}$		
76 ± 2	670 ± 6	77.7 ± 0.2	199 ± 3
150 ± 2	595 ± 6	74.1 ± 0.2	208 ± 3
225 ± 2	521 ± 6	70.3 ± 0.2	219 ± 3
299 ± 2	446 ± 5	67.1 ± 0.2	230 ± 3
374 ± 2	372 ± 5	63.5 ± 0.2	243 ± 3
448 ± 2	298 ± 5	60.1 ± 0.2	256 ± 4
523 ± 2	223 ± 4	56.2 ± 0.2	274 ± 4
597 ± 2	149 ± 4	52.9 ± 0.2	291 ± 4
672 ± 2	74 ± 4	48.7 ± 0.2	316 ± 5
	$T_\mathrm{m} = (346 \pm 3)\,\mathrm{K}$		
76 ± 2	670 ± 4	95.2 ± 0.2	161 ± 2
150 ± 2	595 ± 4	91.0 ± 0.2	169 ± 2
225 ± 2	521 ± 4	86.6 ± 0.2	178 ± 2
299 ± 2	446 ± 4	82.2 ± 0.2	188 ± 2
374 ± 2	372 ± 4	77.6 ± 0.2	199 ± 3
448 ± 2	298 ± 4	73.1 ± 0.2	211 ± 3
523 ± 2	223 ± 4	68.6 ± 0.2	224 ± 3
597 ± 2	149 ± 4	64.1 ± 0.2	241 ± 3
672 ± 2	74 ± 4	59.4 ± 0.2	259 ± 4

Table D.8: Data obtained during the permeation of H_2/He mixtures through membrane A (cont.). Continuation of table D.7. Only presented in the molar range $10 - 90\,\mathrm{mol\%}$ (the values obtained with pure gases are taken from the single-gas permeances). Accuracy of the thermocouples assumed to be 1 % of the measured value.

$F_{\mathrm{p,H_2}}$ $(10^{-7}\,\mathrm{mol\,s^{-1}})$	$F_{\mathrm{p,He}}$ $(10^{-7}\,\mathrm{mol\,s^{-1}})$	Δp $(10^3\ \mathrm{Pa})$	Π $(10^{-9}\,\mathrm{mol\,m^{-2}\,s^{-1}\,Pa^{-1}})$
	$T_{\mathrm{m}} = (371 \pm 4)\,\mathrm{K}$		
76 ± 2	670 ± 4	104.0 ± 0.2	148 ± 2
150 ± 2	595 ± 4	99.6 ± 0.2	155 ± 2
225 ± 2	521 ± 4	95.1 ± 0.2	161 ± 2
299 ± 2	446 ± 4	90.5 ± 0.2	170 ± 2
374 ± 2	372 ± 4	85.7 ± 0.2	180 ± 2
448 ± 2	298 ± 4	81.0 ± 0.2	190 ± 2
523 ± 2	223 ± 4	74.5 ± 0.2	207 ± 3
597 ± 2	149 ± 4	69.7 ± 0.2	221 ± 3
672 ± 2	74 ± 4	64.9 ± 0.2	237 ± 3
	$T_{\mathrm{m}} = (398 \pm 4)\,\mathrm{K}$		
76 ± 2	670 ± 6	97.7 ± 0.2	158 ± 2
150 ± 2	595 ± 6	93.3 ± 0.2	165 ± 2
225 ± 3	521 ± 6	89.5 ± 0.2	172 ± 2
299 ± 3	446 ± 5	85.1 ± 0.2	181 ± 2
374 ± 3	372 ± 5	80.7 ± 0.2	191 ± 2
448 ± 4	298 ± 5	76.3 ± 0.2	202 ± 3
523 ± 4	223 ± 4	71.9 ± 0.2	214 ± 3
597 ± 4	149 ± 4	66.9 ± 0.2	231 ± 3
672 ± 5	74 ± 4	63.1 ± 0.2	244 ± 3

Table D.9: Data obtained during the permeation of H_2/D_2 mixtures through membrane B. Only presented in the molar range $10 - 90\,\mathrm{mol\%}$ (the values obtained with pure gases are taken from the single-gas permeances). Accuracy of the thermocouples assumed to be 1 % of the measured value.

$F_{\mathrm{p,H_2}}$ $(10^{-7}\,\mathrm{mol\,s^{-1}})$	$F_{\mathrm{p,D_2}}$ $(10^{-7}\,\mathrm{mol\,s^{-1}})$	Δp $(10^3\ \mathrm{Pa})$	Π $(10^{-9}\,\mathrm{mol\,m^{-2}\,s^{-1}\,Pa^{-1}})$
	$T_\mathrm{m} = (298 \pm 3)\,\mathrm{K}$		
76 ± 2	675 ± 11	42.9 ± 0.2	362 ± 10
150 ± 2	601 ± 11	41.8 ± 0.2	371 ± 11
225 ± 2	526 ± 11	40.6 ± 0.2	382 ± 11
299 ± 2	452 ± 11	39.1 ± 0.2	398 ± 11
374 ± 2	378 ± 11	37.7 ± 0.2	412 ± 12
448 ± 2	303 ± 11	36.3 ± 0.2	427 ± 12
523 ± 2	229 ± 11	35.0 ± 0.2	444 ± 13
597 ± 2	155 ± 11	33.5 ± 0.2	464 ± 14
671 ± 2	80 ± 11	32.0 ± 0.2	485 ± 14
	$T_\mathrm{m} = (321 \pm 3)\,\mathrm{K}$		
76 ± 2	676 ± 11	49.4 ± 0.2	314 ± 9
150 ± 2	601 ± 11	48.0 ± 0.2	323 ± 9
225 ± 2	527 ± 11	46.7 ± 0.2	333 ± 9
299 ± 2	452 ± 11	45.2 ± 0.2	344 ± 10
374 ± 2	378 ± 11	43.7 ± 0.2	355 ± 10
448 ± 2	303 ± 11	42.2 ± 0.2	368 ± 10
523 ± 2	229 ± 11	40.7 ± 0.2	382 ± 11
597 ± 2	155 ± 11	39.0 ± 0.2	398 ± 11
671 ± 2	80 ± 11	37.5 ± 0.2	414 ± 12
	$T_\mathrm{m} = (346 \pm 3)\,\mathrm{K}$		
76 ± 2	676 ± 11	60.0 ± 0.2	260 ± 7
150 ± 2	601 ± 11	58.0 ± 0.2	268 ± 7
225 ± 2	527 ± 11	56.2 ± 0.2	276 ± 8
299 ± 2	452 ± 11	54.5 ± 0.2	285 ± 8
374 ± 2	378 ± 11	52.8 ± 0.2	294 ± 8
448 ± 2	303 ± 11	51.0 ± 0.2	304 ± 8
523 ± 2	229 ± 11	49.1 ± 0.2	316 ± 9
597 ± 2	155 ± 11	47.3 ± 0.2	329 ± 9
671 ± 2	80 ± 11	45.3 ± 0.2	343 ± 10

Table D.10: Data obtained during the permeation of H_2/D_2 mixtures through membrane B (cont.). Continuation of table D.9. Only presented in the molar range $10 - 90\,\mathrm{mol\%}$ (the values obtained with pure gases are taken from the single-gas permeances). Accuracy of the thermocouples assumed to be 1 % of the measured value.

$F_{\mathrm{p,H_2}}$ $(10^{-7}\,\mathrm{mol\,s^{-1}})$	$F_{\mathrm{p,D_2}}$ $(10^{-7}\,\mathrm{mol\,s^{-1}})$	Δp $(10^3\ \mathrm{Pa})$	Π $(10^{-9}\,\mathrm{mol\,m^{-2}\,s^{-1}\,Pa^{-1}})$
	$T_\mathrm{m} = (371 \pm 4)\,\mathrm{K}$		
76 ± 2	676 ± 11	65.4 ± 0.2	237 ± 6
150 ± 2	601 ± 11	63.6 ± 0.2	244 ± 7
225 ± 2	527 ± 11	61.8 ± 0.2	252 ± 7
299 ± 2	452 ± 11	60.0 ± 0.2	259 ± 7
378 ± 2	378 ± 11	57.9 ± 0.2	269 ± 7
448 ± 2	303 ± 11	55.8 ± 0.2	278 ± 8
523 ± 2	229 ± 11	53.7 ± 0.2	289 ± 8
597 ± 2	155 ± 11	51.6 ± 0.2	301 ± 8
671 ± 2	80 ± 11	49.2 ± 0.2	315 ± 9
	$T_\mathrm{m} = (398 \pm 4)\,\mathrm{K}$		
76 ± 2	676 ± 11	64.4 ± 0.2	242 ± 7
150 ± 2	601 ± 11	62.6 ± 0.2	248 ± 7
225 ± 2	527 ± 11	60.8 ± 0.2	255 ± 7
299 ± 2	452 ± 11	59.8 ± 0.2	263 ± 7
374 ± 2	378 ± 11	57.2 ± 0.2	271 ± 7
448 ± 2	303 ± 11	55.2 ± 0.2	281 ± 8
523 ± 2	229 ± 11	53.3 ± 0.2	291 ± 8
597 ± 2	155 ± 11	51.2 ± 0.2	303 ± 8
671 ± 2	80 ± 11	49.3 ± 0.2	315 ± 9

Table D.11: Data obtained during the permeation of H_2/He mixtures through membrane B. Only presented in the molar range 10 − 90 mol% (the values obtained with pure gases are taken from the single-gas permeances). Accuracy of the thermocouples assumed to be 1 % of the measured value.

F_{p,H_2} (10^{-7} mol s^{-1})	$F_{p,He}$ (10^{-7} mol s^{-1})	Δp (10^3 Pa)	Π (10^{-9} mol m^{-2} s^{-1} Pa^{-1})
	$T_m = (298 \pm 3)$ K		
76 ± 2	670 ± 4	52.6 ± 0.2	293 ± 4
150 ± 2	595 ± 4	50.3 ± 0.2	307 ± 4
225 ± 2	521 ± 4	47.8 ± 0.2	322 ± 5
299 ± 2	446 ± 4	45.4 ± 0.2	309 ± 5
374 ± 2	372 ± 4	43.0 ± 0.2	340 ± 6
448 ± 2	298 ± 4	40.5 ± 0.2	380 ± 6
523 ± 2	223 ± 4	38.0 ± 0.2	405 ± 7
597 ± 2	149 ± 4	35.5 ± 0.2	434 ± 7
671 ± 2	74 ± 4	33.0 ± 0.2	466 ± 8
	$T_m = (321 \pm 3)$ K		
76 ± 2	670 ± 4	61.3 ± 0.2	252 ± 3
150 ± 2	595 ± 4	58.5 ± 0.2	264 ± 4
225 ± 2	521 ± 4	55.8 ± 0.2	276 ± 4
299 ± 2	446 ± 4	53.0 ± 0.2	291 ± 4
374 ± 2	372 ± 4	50.2 ± 0.2	307 ± 4
448 ± 2	298 ± 4	47.3 ± 0.2	325 ± 5
523 ± 2	223 ± 4	44.4 ± 0.2	347 ± 5
597 ± 2	149 ± 4	41.6 ± 0.2	370 ± 6
671 ± 2	74 ± 4	38.7 ± 0.2	398 ± 6
	$T_m = (346 \pm 3)$ K		
76 ± 2	670 ± 4	74.4 ± 0.2	207 ± 3
150 ± 2	595 ± 4	71.1 ± 0.2	216 ± 3
225 ± 2	521 ± 4	67.8 ± 0.2	227 ± 3
299 ± 2	446 ± 4	64.4 ± 0.2	240 ± 3
374 ± 2	372 ± 4	61.0 ± 0.2	230 ± 3
448 ± 2	298 ± 4	57.5 ± 0.2	253 ± 4
523 ± 2	223 ± 4	54.0 ± 0.2	286 ± 4
597 ± 2	149 ± 4	50.4 ± 0.2	305 ± 4
671 ± 2	74 ± 4	47.0 ± 0.2	329 ± 5

Table D.12: Data obtained during the permeation of H_2/He mixtures through membrane B (cont.). Continuation of table D.11. Only presented in the molar range $10 - 90\,\mathrm{mol\%}$ (the values obtained with pure gases are taken from the single-gas permeances). Accuracy of the thermocouples assumed to be 1 % of the measured value.

$F_{\mathrm{p,H_2}}$ $(10^{-7}\,\mathrm{mol\,s^{-1}})$	$F_{\mathrm{p,He}}$ $(10^{-7}\,\mathrm{mol\,s^{-1}})$	Δp $(10^3\ \mathrm{Pa})$	Π $(10^{-9}\,\mathrm{mol\,m^{-2}\,s^{-1}\,Pa^{-1}})$
		$T_{\mathrm{m}} = (371 \pm 4)\,\mathrm{K}$	
76 ± 2	670 ± 4	79.2 ± 0.2	194 ± 2
150 ± 2	595 ± 4	75.8 ± 0.2	203 ± 3
225 ± 2	521 ± 4	72.4 ± 0.2	213 ± 3
299 ± 2	446 ± 4	68.9 ± 0.2	224 ± 3
374 ± 2	372 ± 4	65.3 ± 0.2	236 ± 3
448 ± 2	298 ± 4	61.8 ± 0.2	249 ± 3
523 ± 2	223 ± 4	58.2 ± 0.2	265 ± 4
597 ± 2	149 ± 4	54.5 ± 0.2	282 ± 4
672 ± 2	74 ± 4	50.9 ± 0.2	302 ± 4
		$T_{\mathrm{m}} = (398 \pm 4)\,\mathrm{K}$	
76 ± 2	670 ± 4	75.2 ± 0.2	204 ± 3
150 ± 2	595 ± 4	72.2 ± 0.2	213 ± 3
225 ± 2	521 ± 4	69.1 ± 0.2	223 ± 3
299 ± 2	446 ± 4	65.9 ± 0.2	213 ± 3
374 ± 2	372 ± 4	63.6 ± 0.2	234 ± 3
448 ± 2	298 ± 4	60.3 ± 0.2	256 ± 3
523 ± 2	223 ± 4	56.9 ± 0.2	271 ± 4
597 ± 2	149 ± 4	53.5 ± 0.2	288 ± 4
671 ± 2	74 ± 4	50.0 ± 0.2	308 ± 4

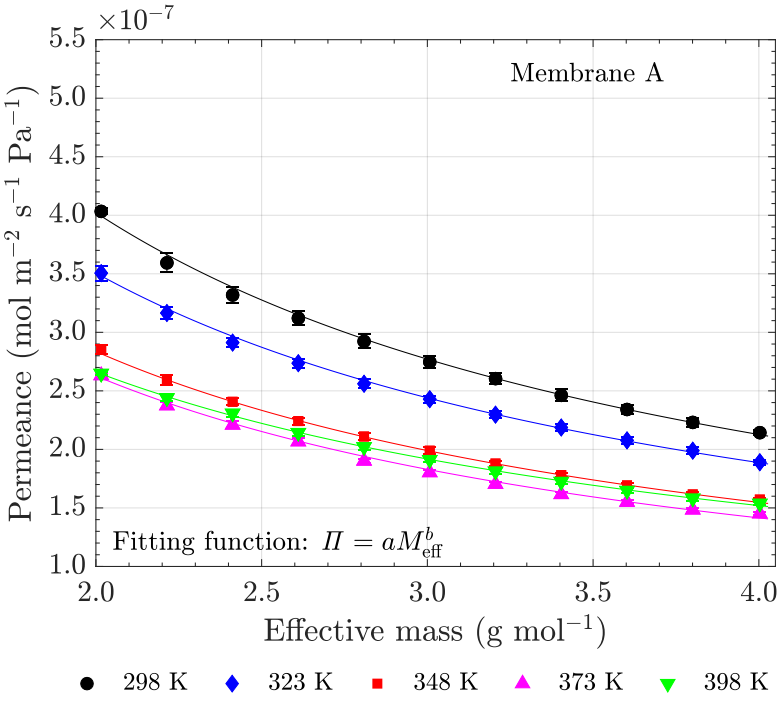

Figure D.2: Permeance of the H_2/He mixture as a function of M_{eff} for different membrane temperatures. Plot obtained for membrane A. The solid lines present the fits using an allometric function. The corresponding fitting parameters are presented in table D.13.

Table D.13: Parameters obtained in the fitting of the permeances of H_2/He as a function of the effective mass for membranes A and B. The corresponding plot is presented in figure D.2. Units: $[a] = 10^{-9}\,\mathrm{mol\,m^{-2}\,s^{-1}\,Pa^{-1}}$, b is dimensionless.

	Membrane A				
	298 K	323 K	348 K	373 K	398 K
a	760 ± 11	652 ± 6	520 ± 4	488 ± 7	466 ± 3
b	-0.919 ± 0.016	-0.894 ± 0.009	-0.874 ± 0.007	-0.893 ± 0.016	-0.808 ± 0.006
R^2	0.997	0.999	0.999	0.997	0.999
	Membrane B				
	298 K	323 K	348 K	373 K	398 K
a	929 ± 1	783 ± 6	645 ± 3	582.8 ± 0.7	561 ± 4
b	-0.865 ± 0.001	-0.848 ± 0.007	-0.849 ± 0.005	-0.821 ± 0.001	-0.758 ± 0.006
R^2	0.999	0.999	0.999	0.999	0.999

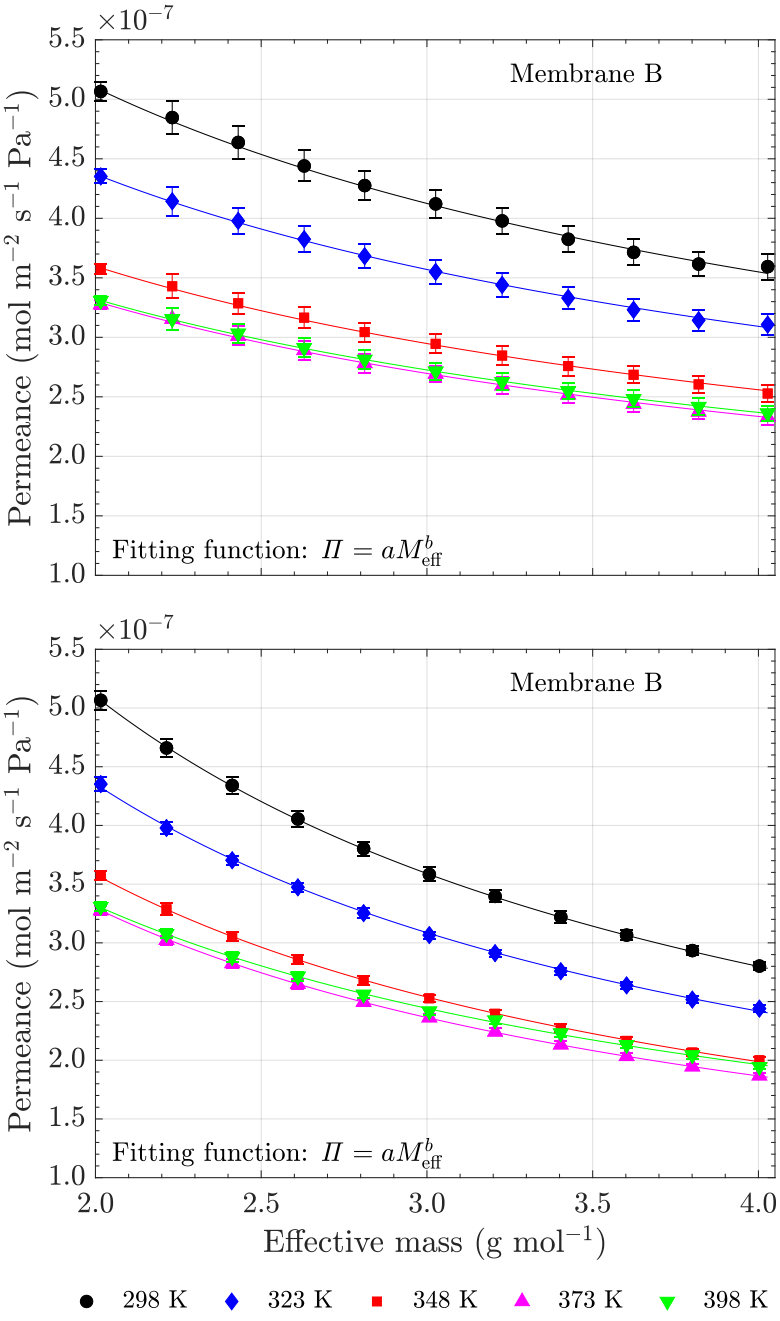

Figure D.3: Permeance of the H_2/D_2 and H_2/He mixtures as a function of M_{eff} for different membrane temperatures. Plots obtained for membrane B. Top: H_2/D_2, bottom: H_2/He. The solid lines present the fits using an allometric function. The corresponding fitting parameters are presented in table 4.4 for H_2/D_2 and table D.13 for H_2/He.

Appendix E

Kinetics for the production of asymmetric isotopologues

Equations (E.1) and (E.2) present the isotopic exchange reactions in which the asymmetric isotopologues HD and DT are produced. The equilibrium constant K_{eq} associated to each of these reactions, also referred to as rate constant for the reaction, is temperature dependent and it determines the concentrations of the gas species at equilibrium according to equation (E.3) [243, 244].

$$\mathrm{H_2} + \mathrm{D_2} \rightleftharpoons 2\,\mathrm{HD} \tag{E.1}$$

$$\mathrm{D_2} + \mathrm{T_2} \rightleftharpoons 2\,\mathrm{DT} \tag{E.2}$$

$$K_{\mathrm{eq}}^{\mathrm{HD}} = \frac{c_{\mathrm{HD,eq}}^2}{c_{\mathrm{H_2,eq}} c_{\mathrm{D_2,eq}}} \tag{E.3}$$

The concentrations of H_2 and D_2 at equilibrium ($c_{\mathrm{H_2,eq}}$ and $c_{\mathrm{D_2,eq}}$, respectively) are calculated using equations (E.4) and (E.5). Replacing these two expressions in (E.3) and solving the second order equation for $c_{\mathrm{HD,eq}}$, the equilibrium concentration of HD is determined according to equation (E.6), where the positive solution ($c_{\mathrm{HD,eq,+}}$) is the only one with physical meaning.

$$c_{\mathrm{H_2,eq}} = 1 - c_{\mathrm{D,in}} - \frac{1}{2} c_{\mathrm{HD,eq}} \tag{E.4}$$

$$c_{\mathrm{D_2,eq}} = c_{\mathrm{D,in}} - \frac{1}{2} c_{\mathrm{HD,eq}} \tag{E.5}$$

$$c_{\mathrm{HD,eq,\pm}} = \frac{-\frac{1}{2} K_{\mathrm{eq}}^{\mathrm{HD}} \pm \sqrt{\frac{1}{4} K_{\mathrm{eq}}^{\mathrm{HD}\,2} - (4 - K_{\mathrm{eq}}^{\mathrm{HD}}) c_{\mathrm{D,in}} (c_{\mathrm{D,in}} - 1) K_{\mathrm{eq}}^{\mathrm{HD}}}}{\frac{1}{2}(4 - K_{\mathrm{eq}}^{\mathrm{HD}})} \tag{E.6}$$

In table E.1, experimentally measured equilibrium constants for the production of HD and DT are presented for different temperatures [26]. The larger the temperature, the higher is the equilibrium constant which reflects a higher amount of produced HD or DT for the same initial isotopic concentration. It should be noted that $K_{\mathrm{eq}} \to 4$ for $T \to \infty$ ($K_{\mathrm{eq}} > 4$ would mean that the atomic fraction of the isotopes was not conserved). Thus, the maximum amount of HD (or DT) which can be produced is 50 mol%, for an initial

equimolar mixture of H_2/D_2 (or D_2/T_2). Figure E.1 shows an example of a plot for a catalysed mixture of H_2-HD-D_2 produced at 473 K.

Table E.1: Calculated gas equilibrium constants for the isotopic exchange reactions $H_2 + D_2 \rightleftharpoons 2\,HD$ and $D_2 + T_2 \rightleftharpoons 2\,DT$. The values are from [26].

T (K)	K_{eq}^{HD} (-)	K_{eq}^{DT} (-)
100	2.26	3.29
200	2.90	3.69
300	3.26	3.82
∞	4.00	4.00

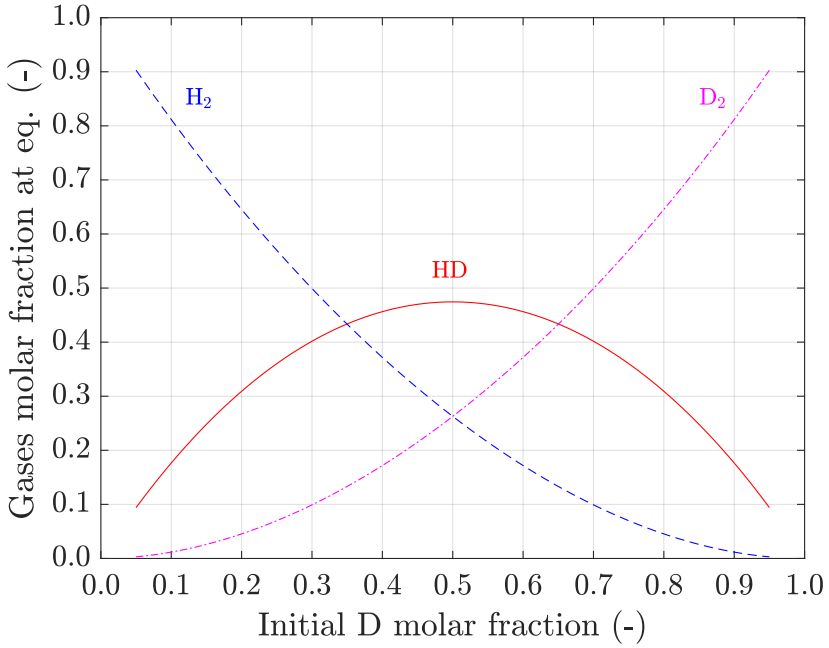

Figure E.1: Molar fraction of H_2, D_2 and HD at equilibrium as function of the initial atomic fraction of D. Plot obtained for 300 K (i.e., $K_{eq}^{HD} = 3.26$).

Appendix F

Results of the permeation and separation experiments with tritium

The values and the corresponding uncertainties obtained along the entire experimental campaign performed with the ZEMTEX setup are given here, complementing the information presented in chapter 5. All the data concerning the mixtures prepared for the permeation experiments (without and with tritium) are presented in section F.1. The measured permeation flows and pressures, and the calculate permeances, are presented in section F.2 for different membrane temperatures. The average flow, pressure and moisture values measured along the Q_2O/He experiments are presented in table F.5.

F.1 Composition of the gas mixtures measured with LARA, RGA and GC

The Q atomic fractions of the eight gas mixtures prepared for the permeation experiments are presented in table F.1. The non-tritiated mixtures #1 and #2, prepared by filling vessel BD807 with H_2 and D_2, was only measured with RGA. The sample #3 is pure D_2 (≥ 99.8 mol% from Air Liquide bottle) and for this reason was not measured with any technique (hence not shown in the table). This pure D_2 gas was sent to the TLK Tritium Transfer System for the preparation of the mixtures $\#4-7$ by adding increasing amounts of tritium into it. In TTS, the composition of each prepared mixture was measured with LARA and, after transferring the gas into BD807 in CAPER, the compositions of the Q_2 mixtures were also measured with GC and RGA. Due to the routing of the Q_2 mixture to TTS and back to CAPER, a slight increase of the H concentration was observed due to the rather long pipework between the TTS and CAPER gloveboxes.

Figure F.1 compares the D_2, DT and T_2 molar fractions of mixture #7 measured with LARA, RGA and GC. The compositions theoretically expected for a fully equilibrated mixture at 300 K are also plotted[1] ($K_{\mathrm{eq}}^{\mathrm{DT}} = 3.82$, Appendix E). All techniques show consistent values with the theory for the concentration of D_2, whereas a larger discrepancy

[1]Neglecting the presence of H due to its low concentration.

Table F.1: Comparison of the atomic fraction of the Q_2 gas mixtures measured with LARA, RGA and GC. These gas mixtures were used for the permeation experiments through the membrane C in the ZEMTEX facility. Typical relative uncertainties for these techniques are within 5 %.

Mix. #	H			D			T		
	LARA	RGA	GC	LARA	RGA	GC	LARA	RGA	GC
1	–	50.9	–	–	49.1	–	–	–	–
2	–	30.2	–	–	69.8	–	–	–	–
4	0.5	–	–	92.0	–	–	7.3	–	–
5	0.6	1.3	0.0	78.5	78.8	80.0	20.7	20.2	20.0
6	5.8	3.6	6.5	59.1	60.7	60.2	35.1	35.7	33.4
7	4.9	2.6	5.2	48.4	52.0	49.8	46.6	45.4	41.0
8	4.2	1.6	4.7	41.1	43.1	40.2	54.6	55.5	51.3

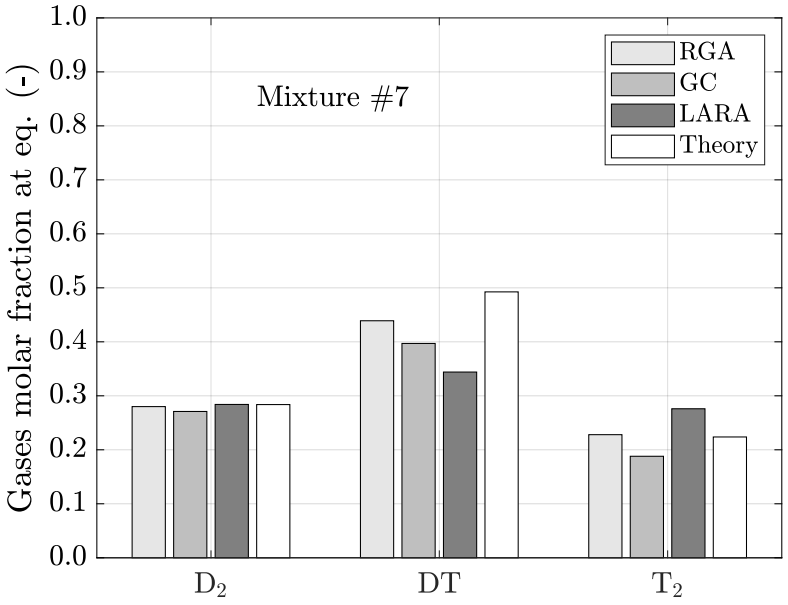

Figure F.1: Comparison of the molar fraction of D_2-DT-T_2 of mixture #7 measured with LARA, GC and RGA. The compositions determined using the theory of a fully equilibrated mixture at 300 K (using equations given in E) are also presented.

exists for DT and T_2 especially with LARA. The reason for this deviation is attributed to the relatively short time between the preparation of the mixture and the measurement with LARA (when prepared in TTS). After sending the gas to CAPER, the circulation of each Q_2 mixture through pumps promoted further equilibration, justifying the approximation of the concentrations of DT and T_2 measured with RGA and GC towards the values expected from the theory.

F.2 Permeances as a function of the membrane temperature

The Q_2 permeation experiments at different temperatures performed with the ZEMTEX setup with membrane C are discussed in section 5.6. Tables F.2-F.3 display the measured flows and pressure differences and the calculated He and Q_2 permeances. The He and Q_2 flows were set respectively with RF3004 and RF1006; the feed and permeate pressures were measured respectively with RP3001 and RP842.

F.3 Separation experiments with Q_2/He

Table F.4 displays the average feed, permeate and retentate flows and pressures measured along the two experimental campaigns for the separation of dry mixtures discussed in section 5.7. The helium flow was imposed with RF007 and the flows of H_2 and Q_2

Table F.2: Data obtained during the experiments performed to determine the He and Q_2 permeances through membrane C. The compositions of the mixtures #1 − #7 are presented in table F.1.

Gas	F_p (10^{-7} mol s^{-1})	Δp (10^3 Pa)	Π_i (10^{-9} mol m^{-2} s^{-1} Pa^{-1})	T_m (K)
He	736 ± 4	58.1 ± 0.3	262 ± 4	293 ± 1
	736 ± 3	61.7 ± 0.2	246 ± 3	318 ± 2
	736 ± 4	66.6 ± 0.3	228 ± 3	326 ± 3
	736 ± 3	74.3 ± 0.2	204 ± 2	348 ± 6
	736 ± 2	77.6 ± 0.1	196 ± 1	371 ± 8
Mix. #1	439 ± 2	22.7 ± 0.1	400 ± 7	291 ± 1
	439 ± 2	25.8 ± 0.1	352 ± 5	318 ± 3
	439 ± 2	27.0 ± 0.1	336 ± 5	326 ± 4
	439 ± 2	30.4 ± 0.1	298 ± 4	349 ± 6
	439 ± 2	32.4 ± 0.1	280 ± 4	371 ± 9
Mix. #2	439 ± 2	24.0 ± 0.1	378 ± 6	291 ± 1
	439 ± 2	27.0 ± 0.1	336 ± 5	318 ± 3
	439 ± 2	28.3 ± 0.1	321 ± 4	326 ± 4
	439 ± 2	31.8 ± 0.1	285 ± 4	349 ± 6
	439 ± 2	33.9 ± 0.1	267 ± 3	371 ± 9
Mix. #3	439 ± 2	26.1 ± 0.1	347 ± 5	291 ± 1
	439 ± 2	29.7 ± 0.1	305 ± 4	318 ± 3
	439 ± 2	31.0 ± 0.1	292 ± 4	326 ± 4
	439 ± 2	34.9 ± 0.1	259 ± 3	349 ± 6
	439 ± 2	37.3 ± 0.1	243 ± 3	372 ± 9
Mix. #4	439 ± 2	26.6 ± 0.1	341 ± 5	291 ± 1
	439 ± 2	30.1 ± 0.1	301 ± 4	318 ± 3
	439 ± 2	31.6 ± 0.1	287 ± 4	326 ± 4
	439 ± 2	35.4 ± 0.1	256 ± 3	349 ± 6
	439 ± 2	37.9 ± 0.1	239 ± 3	371 ± 8
Mix. #5	401 ± 3	25.1 ± 0.2	329 ± 7	291 ± 1
	409 ± 2	28.7 ± 0.1	294 ± 4	318 ± 3
	409 ± 2	30.1 ± 0.1	280 ± 4	326 ± 4
	409 ± 2	33.8 ± 0.1	250 ± 4	349 ± 6
	409 ± 2	36.0 ± 0.1	234 ± 3	371 ± 8
Mix. #6	417 ± 2	26.5 ± 0.1	325 ± 5	292 ± 1
	411 ± 4	29.6 ± 0.1	287 ± 6	319 ± 3
	413 ± 4	30.9 ± 0.1	276 ± 6	326 ± 4
	409 ± 2	34.6 ± 0.1	244 ± 3	349 ± 6
	417 ± 2	37.4 ± 0.1	229 ± 3	372 ± 9
Mix. #7	395 ± 3	26.3 ± 0.1	310 ± 6	293 ± 1
	394 ± 2	29.8 ± 0.1	273 ± 4	319 ± 2
	394 ± 2	30.8 ± 0.1	264 ± 4	326 ± 3
	394 ± 2	34.4 ± 0.1	237 ± 3	349 ± 6
	396 ± 4	36.7 ± 0.1	224 ± 5	371 ± 9

Table F.3: Data obtained during the experiments performed to determine the He and Q_2 permeances through membrane C (cont.). The composition of the mixture #8 is presented in table F.1.

Gas	F_p (10^{-7} mol s^{-1})	Δp (10^3 Pa)	Π_i (10^{-9} mol m^{-2} s^{-1} Pa^{-1})	T_m (K)
Mix. #8	387 ± 2	55.5 ± 0.1	314 ± 5	291 ± 1
	387 ± 2	28.8 ± 0.1	278 ± 4	318 ± 3
	387 ± 2	30.2 ± 0.1	265 ± 4	326 ± 4
	387 ± 2	33.8 ± 0.1	236 ± 3	349 ± 6
	387 ± 2	35.9 ± 0.1	223 ± 3	372 ± 9

Table F.4: Average flows and pressures measured at equilibrium along the separation experiments of H_2/He and Q_2/He. T_m: membrane temperature, $F_{f,i}$: feed flow of species i, p_f and p_p: absolute feed and permeate pressures, F_p and F_r: permeate and retentate flows. The flows are given in standard conditions of temperature and pressure.

T_m (K)	$F_{f,He}$ (mL min^{-1})	F_{f,H_2} | F_{f,Q_2} (mL min^{-1})	p_f (hPa)	F_p (mL min^{-1})	p_p (hPa)	F_r (ml min^{-1})
			H_2/He			
293±1	178.8±0.9	19.9 ± 0.4	477.6±1.3	78.2 ± 1.1	51.5 ± 0.1	133.8±1.1
326±4	178.7±0.9	19.8 ± 0.5	478.8±1.3	69.1 ± 1.0	47.8 ± 0.1	143.5±1.1
349±6	180.3±0.8	19.9 ± 0.4	479.5±1.3	62.7 ± 1.1	44.9 ± 0.1	152.6±1.2
371±9	180.3±0.8	19.8 ± 0.5	479.4±1.3	59.2 ± 1.1	43.6 ± 0.1	155.7±1.1
			Q_2/He			
293±1	179.7±0.9	19.6 ± 0.3	477.3±1.2	75.9 ± 1.1	51.8 ± 0.1	137.4±1.1
326±4	179.7±0.9	19.6 ± 0.3	477.6±1.3	66.0 ± 1.0	47.6 ± 0.5	146.7±1.1
349±6	179.7±0.9	19.6 ± 0.3	478.2±1.3	59.4 ± 1.1	44.9 ± 0.1	154.9±1.2
371±9	179.7±0.9	19.6 ± 0.3	478.0±1.2	56.8 ± 1.1	43.7 ± 0.1	157.1±1.1

were set with RF1006. The absolute feed pressure was measured with RP3001 and the permeate pressure with RP842. The total permeate and retentate flows were measured, respectively, with RF3003 and RF3002.

F.4 Separation experiments with Q_2O/He

The experimental results obtained along the separation experiments with Q_2O/He in the range $1 - 10$ mol% are presented and discussed in section 5.8. Complementing the information given there, table F.5 displays the average flows, pressures and dew points measured along the different experiments. x_{f,Q_2} is the concentration of Q_2 in the feed (given by $F_{f,Q_2}/(F_{f,Q_2} + F_{f,He})$), which is assumed to be equal to the Q_2O concentration as a result of a complete oxidation through the CuO reactor. p_f (RP3001) and p_p (RP842) are respectively the absolute feed and permeate pressures. $T_{dp,f}$ (RM3008) are the dew

points measured at the outlet of the CuO, which are much higher than the dew points measured with RM836 (around −60 °C for all experiments), installed before the CuO reactor. $T_{\mathrm{dp,pb}}$ and $T_{\mathrm{dp,pa}}$ are the dew points measured respectively with RM3011 (before the MSB) and RM3012 (after the MSB) in the permeate, whereas $T_{\mathrm{dp,rb}}$ and $T_{\mathrm{dp,ra}}$ are the values measured with RM3009 (before the MSB) and RM3010 (after the MSB) in the retentate. The considerably lower values measured with RM3010 and RM3012 show the drying effect of the MSB, inside which the water molecules remain adsorbed.

Table F.5: Average flows, pressures and dew points along the separation experiments with D_2O/He and Q_2O/He. $F_{\mathrm{f},i}$: feed flow of gas species i, $x_{\mathrm{f,D_2}}$ and $x_{\mathrm{f,Q_2}}$: feed concentration of D_2 and Q_2 in He (the same as vapor), p_f and p_p: absolute feed and permeate pressures, $T_{\mathrm{dp,f}}$: dew point value after the CuO and before the membrane (i.e., feed side), $T_{\mathrm{dp,pb}}$ and $T_{\mathrm{dp,rb}}$: dew point values before the MSBs in the permeate and retentate, $T_{\mathrm{dp,pa}}$ and $T_{\mathrm{dp,ra}}$: dew point value after the MSBs in the permeate and retentate. The flows are given in standard conditions of temperature and pressure.

#	$F_{\mathrm{f,He}}$ ($\mathrm{mL\,min^{-1}}$)	$F_{\mathrm{f,D_2}} \mid F_{\mathrm{f,Q_2}}$ ($\mathrm{mL\,min^{-1}}$)	$x_{\mathrm{f,D_2}} \mid x_{\mathrm{f,Q_2}}$ (mol%)	p_f (hPa)	p_p (hPa)	$T_{\mathrm{dp,f}}$ (°C)	$T_{\mathrm{dp,pb}}$ (°C)	$T_{\mathrm{dp,pa}}$ (°C)	$T_{\mathrm{dp,rb}}$ (°C)	$T_{\mathrm{dp,ra}}$ (°C)
					D_2O/He					
1	198.5 ± 3.1	1.9 ± 0.3	0.95 ± 0.15	525.2 ± 1.8	57.0 ± 0.2	-25.5 ± 0.9	-36.4 ± 1.0	-82.9 ± 1.8	-32.3 ± 1.0	-92.4 ± 1.3
2	200.8 ± 1.7	4.0 ± 0.3	1.95 ± 0.17	520.0 ± 1.2	56.0 ± 0.2	-19.0 ± 0.6	-30.9 ± 0.7	-83.1 ± 4.2	-27.6 ± 0.8	-87.1 ± 2.1
3	190.0 ± 3.0	9.9 ± 0.3	4.95 ± 0.15	538.5 ± 1.3	55.3 ± 0.2	-5.4 ± 0.6	-21.1 ± 0.6	-84.4 ± 2.7	-18.1 ± 0.6	-91.8 ± 1.2
4	180.0 ± 3.0	20.0 ± 0.3	10.00 ± 0.17	527.7 ± 1.5	52.8 ± 0.4	$+5.6 \pm 0.8$	-16.4 ± 0.8	-78.4 ± 1.0	-15.0 ± 0.8	-88.8 ± 1.2
					Q_2O/He					
5	196.4 ± 3.1	3.9 ± 0.3	1.95 ± 0.16	494.3 ± 1.2	59.0 ± 0.2	-18.8 ± 0.7	-31.1 ± 1.9	-90.3 ± 2.3	-27.1 ± 1.5	-89.3 ± 1.5

Appendix G

Derivation of the equations implemented in the model to simulate membrane cascades

G.1 Separation factors of membrane cascades

In the literature of cascades, three separation factors that mathematically relate the concentrations in the feed $x^k_{\mathrm{f},i}$, permeate $y^k_{\mathrm{p},i}$ and retentate $x^k_{\mathrm{r},i}$ streams are usually defined for each stage as follows [176, 186]:

- **stage separation factor, S_{stg}**: equates the concentrations in the permeate and retentate according to equation (G.1)

$$S_{\mathrm{stg}} = \frac{y^k_{\mathrm{p},i}/(1-y^k_{\mathrm{p},i})}{x^k_{\mathrm{r},i}/(1-x^k_{\mathrm{r},i})} \equiv \frac{Y^k_{\mathrm{p},i}}{X^k_{\mathrm{r},i}} \tag{G.1}$$

- **head separation factor, S_{h}**: equates the concentrations in the permeate and feed according to equation (G.2), which is equal to the separation factor α obtained in the Q_2/He and Q_2O/He separation experiments

$$S_{\mathrm{h}} = \frac{y^k_{\mathrm{p},i}/(1-y^k_{\mathrm{p},i})}{x^k_{\mathrm{f},i}/(1-x^k_{\mathrm{f},i})} \equiv \frac{Y^k_{\mathrm{p},i}}{X^k_{\mathrm{f},i}} \tag{G.2}$$

- **tail separation factor, S_{t}**: equates the concentrations in the feed and retentate according to equation (G.3)

$$S_{\mathrm{t}} = \frac{x^k_{\mathrm{f},i}/(1-x^k_{\mathrm{f},i})}{x^k_{\mathrm{r},i}/(1-x^k_{\mathrm{r},i})} \equiv \frac{X^k_{\mathrm{f},i}}{X^k_{\mathrm{r},i}} \tag{G.3}$$

For a single-entry separator with only one feeding stream, the condition $S_{\mathrm{h}} = S_{\mathrm{t}}$ holds and thus equation (G.4) applies [186]. Consequently, the separation factor α obtained from the experiments is equal to $\sqrt{S_{\mathrm{stg}}}$. Using (G.1)-(G.4), two equations can be found for $y^k_{\mathrm{p},i}$ (equation (G.5)) and $x^k_{\mathrm{r},i}$ (equation (G.6)) as a function of both $x^k_{\mathrm{f},i}$ and S_{stg}. Therefore, for each stage, the permeate and retentate concentrations are calculated using

$x^k_{\mathrm{f},i}$ and S_{stg}.

$$S_{\mathrm{stg}} = S_{\mathrm{h}} \times S_{\mathrm{t}} = S^2_{\mathrm{h}} = S^2_{\mathrm{t}} \tag{G.4}$$

$$y^k_{\mathrm{p},i} = \frac{\sqrt{S_{\mathrm{stg}}} X^k_{\mathrm{f},i}}{1 + \sqrt{S_{\mathrm{stg}}} X^k_{\mathrm{f},i}} \tag{G.5}$$

$$x^k_{\mathrm{r},i} = \frac{X^k_{\mathrm{f},i}/\sqrt{S_{\mathrm{stg}}}}{1 + X^k_{\mathrm{f},i}/\sqrt{S_{\mathrm{stg}}}} \tag{G.6}$$

An alternative expression for S_{stg} as a function of $y^k_{\mathrm{p},i}$, $\alpha^*_{i/j}$ and γ can be found from the permeate flows of species i and j through the membrane[1] (equations (G.7) and (G.8)). For a binary mixture, $y_{\mathrm{p},i} = 1 - y_{\mathrm{p},j}$ and $x_{\mathrm{r},i} = 1 - x_{\mathrm{r},j}$. Hence, dividing equation (G.7) by (G.8), equation (G.9) is obtained, where $\alpha^*_{i,j} = \Pi_i/\Pi_j$ is the selectivity.

$$y^k_{\mathrm{p},i} F^k_{\mathrm{p}} = \Pi_i p_{\mathrm{f}} A_{\mathrm{m}} (x^k_{\mathrm{r},i} - \gamma^{-1} y^k_{\mathrm{p},i}) \tag{G.7}$$

$$y^k_{\mathrm{p},j} F^k_{\mathrm{p}} = \Pi_j p_{\mathrm{f}} A_{\mathrm{m}} (x^k_{\mathrm{r},j} - \gamma^{-1} y^k_{\mathrm{p},j}) \tag{G.8}$$

$$\frac{y^k_{\mathrm{p},i}}{1 - y^k_{\mathrm{p},i}} = \alpha^*_{i,j} \frac{x^k_{\mathrm{r},i} - \gamma^{-1} y^k_{\mathrm{p},i}}{(1 - x^k_{\mathrm{r},i}) - \gamma^{-1}(1 - y^k_{\mathrm{p},i})} \tag{G.9}$$

From the definition of S_{stg} given in equation (G.1), the retentate concentration can be written as $x^k_{\mathrm{r},i} = y^k_{\mathrm{p},i}/[S_{\mathrm{stg}}(1 - y^k_{\mathrm{p},i}) + y^k_{\mathrm{p},i}]$. Replacing this expression in equation (G.9) and after some algebra the following equation for S_{stg} is found.

$$S_{\mathrm{stg}} = \frac{\alpha^*_{i/j} - y^k_{\mathrm{p},i}(\alpha^*_{i/j} - 1)\gamma^{-1}}{1 + (1 - y^k_{\mathrm{p},i})(\alpha^*_{i/j} - 1)\gamma^{-1}} \tag{G.10}$$

G.2 Cut and calculation of the flows along the cascade

The cut is defined as the ratio between the total permeate and feed flows: $\nu^k = F^k_{\mathrm{p}}/F^k_{\mathrm{f}}$. However, a more convenient expression for the cut depending on the species concentrations can be found, starting from the mass-balance equations for the total and component flows given, respectively, by equations (G.11) and (G.12).

$$F^k_{\mathrm{f}} = F^k_{\mathrm{p}} + F^k_{\mathrm{r}} \tag{G.11}$$

$$x^k_{\mathrm{f},i} F^k_{\mathrm{f}} = y^k_{\mathrm{p},i} F^k_{\mathrm{p}} + x^k_{\mathrm{r},i} F^k_{\mathrm{r}} \tag{G.12}$$

On the one side, equation (G.13) is obtained by replacing (G.11) into (G.12). On the other side, since $\nu^k = F^k_{\mathrm{p}}/(F^k_{\mathrm{p}} + F^k_{\mathrm{r}})$, then $F^k_{\mathrm{p}}/F^k_{\mathrm{r}} = \nu^k/(1 - \nu^k)$. Hence, replacing this expression into equation (G.13), the final equation for the cut is provided by

[1] Here the retentate concentration x_{r} is the molar fractions of the species along the membrane on the high pressure side.

equation (G.14).

$$\frac{F_{\mathrm{p}}^{k}}{F_{\mathrm{r}}^{k}} = \frac{x_{\mathrm{r},i}^{k} - x_{\mathrm{f},i}^{k}}{x_{\mathrm{f},i}^{k} - y_{\mathrm{p},i}^{k}} \tag{G.13}$$

$$\nu^{k} = \frac{x_{\mathrm{f},i}^{k} - x_{\mathrm{r},i}^{k}}{y_{\mathrm{p},i}^{k} - x_{\mathrm{r},i}^{k}} \tag{G.14}$$

With the cut values obtained from the concentrations, the flows along the cascade are determined by firstly calculating the total feed flow F_{f}^{k} for each stage. Since the flow feeding stage k is the sum of the permeate flow coming from $k-1$ and retentate flow from $k+1$, the following equation holds: $F_{\mathrm{f}}^{k} = (1-\nu^{\mathrm{k+1}})F_{\mathrm{f}}^{k+1} + \nu^{k-1}F_{\mathrm{f}}^{k-1}$. This expression can be generalised to all stages using equation (G.15), which includes an additional term for the injection stage.

$$F_{\mathrm{f}}^{k} = F_{\mathrm{f}}^{k}\delta^{\mathrm{inj}} + (1-\nu^{\mathrm{k+1}})F_{\mathrm{f}}^{k+1} + \nu^{k-1}F_{\mathrm{f}}^{k-1} \tag{G.15}$$

Equation (G.15) can be written in matrix form $\boldsymbol{F}_{\mathrm{f}}^{\mathrm{inj}} = \boldsymbol{A}^{\nu}\boldsymbol{F}_{\mathrm{f}}$, where $\boldsymbol{F}_{\mathrm{f}}^{\mathrm{inj}}$ is a column vector for the injection flows (all elements zero except for $k = \mathrm{inj}$), $\boldsymbol{F}_{\mathrm{f}}$ is a column vector for all feed flows F_{f}^{k}, and $\boldsymbol{A}^{\nu}$ is a square matrix given by (G.16). Thus, the feed flows $\boldsymbol{F}_{\mathrm{f}}$ are calculated by solving $\boldsymbol{F}_{\mathrm{f}} = \boldsymbol{A}^{\nu^{-1}}\boldsymbol{F}_{\mathrm{f}}^{\mathrm{inj}}$.

$$\boldsymbol{A}^{\nu} = \begin{bmatrix} \vdots & \vdots & 0 & 0 & 0 \\ -\nu^{k-2} & 1 & -(1-\nu^{k}) & 0 & 0 \\ 0 & -\nu^{k-1} & 1 & -(1-\nu^{k+1}) & 0 \\ 0 & 0 & -\nu^{k} & 1 & -(1-\nu^{k+2}) \\ 0 & 0 & 0 & \vdots & \vdots \end{bmatrix} \tag{G.16}$$

Appendix H

Space occupation for the membrane cascade and adsorption columns

The physical space occupied by the membrane cascade and adsorption columns is presented in this section, based on the results presented in chapters 7 and 8. The dimensions of the rooms accommodating these systems consider extra space for tubing and operators.

H.1 Membrane cascade

The front and top views for the space arrangement of the membrane cascade are displayed, respectively, in figure H.1. The stages are proposed to be placed horizontally and distributed in different levels in a dedicated metallic structure. The length of this structure is chosen to be 3.000 m, since the longest stage (stage 3) is 2.730 m-long. With a total area 19.4 m^2, the room accommodating the membrane cascade also includes a dedicated area for the compressors. Considering that the room has to be at least two times taller than the metallic structure (with 1.640 m), the volume of the whole room is estimated to be 63.6 m^3.

H.2 Adsorption columns

The adsorption columns are placed vertically next to each other as presented in top view in figure H.2. The room required to accommodate the three columns is estimated to be around 15.7 m^2. Since each column is 1.9 m high, the building is proposed to be twice as higher. Therefore, the volume of the room is $\approx$ 59.7 m^3.

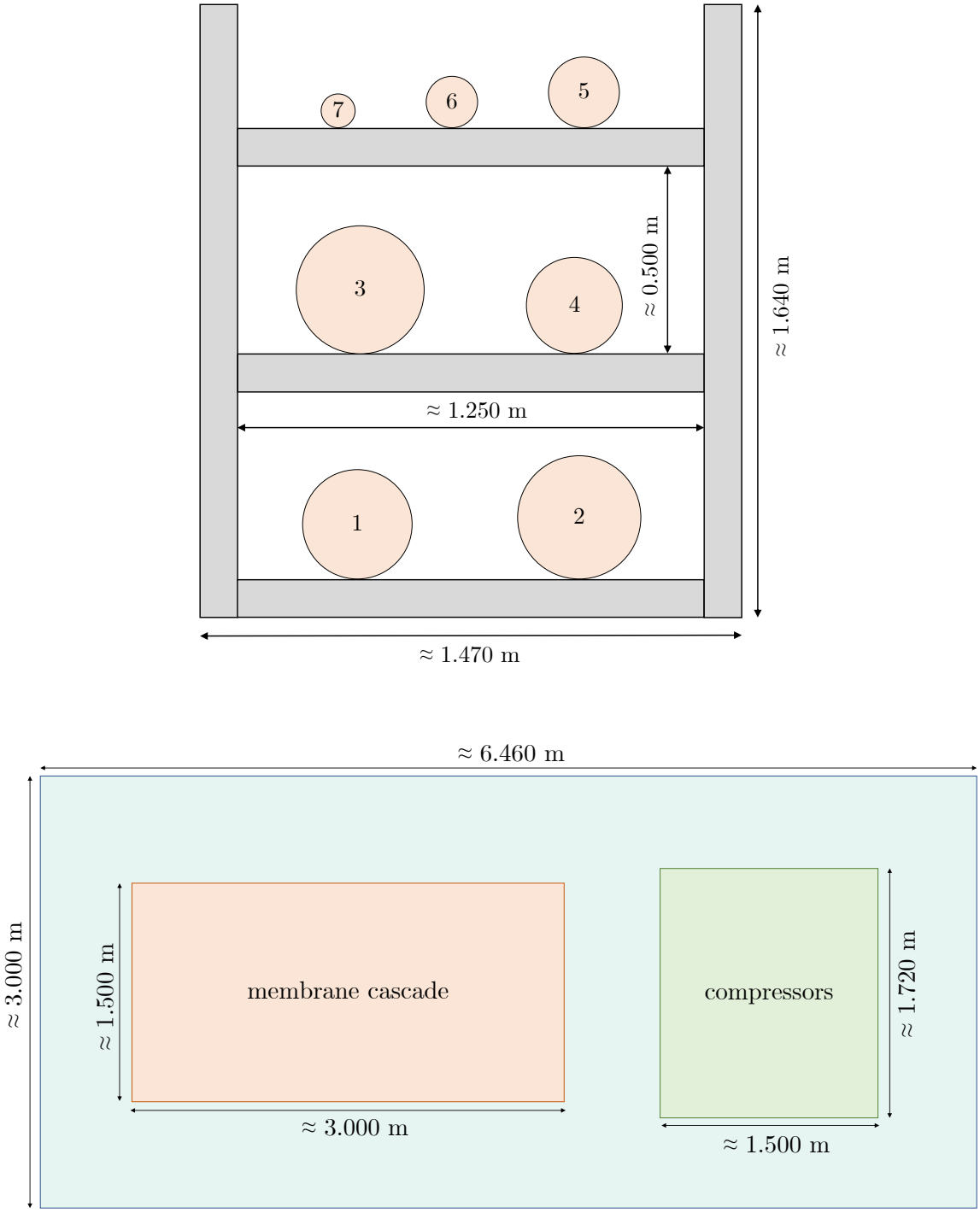

Figure H.1: Space required to accommodate the membrane cascade. Top: front view, bottom: top view. The heaviest stages are placed in the lowest levels of a metallic structure. The area occupied by the membrane cascade is show in orange and in green the area occupied by the compressors.

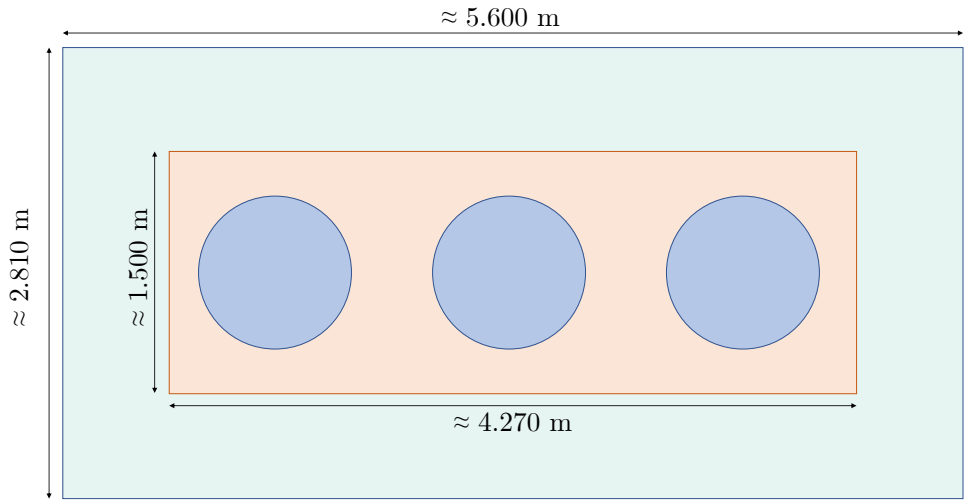

Figure H.2: Top view for the space required to accommodate the adsorption columns.